Thèse de doctorat de l'université Denis Diderot
Spécialité : physique des particules

présentée par

Boris A. POPOV

pour obtenir le titre de docteur de l'université Paris VII

Search for $\nu_\mu \to \nu_\tau$ neutrino oscillations in the $\tau^- \to e^- \bar{\nu}_e \nu_\tau$ decay channel in the NOMAD experiment at CERN.

soutenue le 12 mai 1998 devant le jury composé de :

M. Banner
J. Bouchez
S. Bunyatov
A. Letessier-Selvon
S. Petcov
F. Vannucci

To my Motherland, to France,
and
to my friends from all over the world

Contents

This manuscript is organized in the following way.

In the first chapter the history of neutrino physics and unsolved problems of neutrino masses and mixing are discussed from both theoretical and experimental point of views. It is shown that the investigation of phenomenon known as neutrino oscillations is the only possible way nowadays to detect neutrino masses below $\sim 1\ eV$. Some of the past, present and future experiments searching for neutrino oscillations are reviewed.

The second chapter is devoted to the description of the NOMAD experiment currently searching for $\nu_\mu \to \nu_\tau$ (and $\nu_\mu \to \nu_e$) neutrino oscillations in the neutrino beam from the CERN SPS accelerator. The general idea of this experiment and the performances of the NOMAD subdetectors are presented.

In the third chapter we present the algorithms used for the charged and neutral track reconstruction in the NOMAD setup. Special emphasis is put on the description of the track model used for the charged track reconstruction in the NOMAD drift chambers and on the subdetector matching technique implemented for the particle identification. Algorithms developed for the electron identification and reconstruction are presented.

In the fourth chapter we describe the procedure used for the simulation of the neutrino interactions in the NOMAD setup and show the achieved quality of the reconstruction of the event kinematics.

Finally, in the last chapter the method based on likelihood ratios developed for the ν_e CC selection and $\nu_\mu \to \nu_\tau$ oscillation search in the $\tau^- \to e^- \bar{\nu}_e \nu_\tau$ decay channel is presented. Preliminary results for the data set corresponding to the NOMAD '96 run are given and major current limitations are discussed.

Chapter 1

Introduction

1.1 History of Neutrino

The history of neutrino started in 1930 when W.Pauli invented this particle to explain the continuous electron spectrum in nuclear β-decay [1]. Experimentally the first neutrino (electron antineutrino $\bar{\nu}_e$) was observed only 25 years later in the Savannah River reactor experiment directed by Reines and Cowan [2]. The second type of neutrino, the muon neutrino ν_μ, was discovered in 1962 in the experiment lead by Lederman, Schwartz and Steinberger [3] using the first high energy neutrino beam [4] at the Brookhaven accelerator [5]. This result was the first confirmation of the family structure of the fundamental fermions.

The third family of leptons was established via the observation of τ production at the SPEAR e^+e^- accelerator [6]. As to the corresponding third generation of neutrino ν_τ, it has not yet been directly detected through its interactions with matter. But the evidence for its existence was deduced from the momenta distribution of secondary particles in τ decays, τ lifetime measurements [7] and from the observed W-boson partial production cross section ratios $\sigma(W \to e\nu_e)/\sigma(W \to \mu\nu_\mu)/\sigma(W \to \tau\nu_\tau)$ [8]. The existence of ν_τ was also confirmed indirectly by LEP experiments giving 2.991 ± 0.016 [9] for the number of light ($m_\nu < M_Z/2$) neutrino types from the invisible width of the Z^0-boson.

Since the construction of the first intense neutrino beams these particles are heavily used as probes of the structure of matter and of the weak interactions. Difficulty of their experimental observation is related to the fact that neutrinos reveal themselves only via weak interactions. But this is at the same time the reason for the interest in neutrino physics where weak interactions are completely separated from the other type of interactions. Many neutrino experiments have contributed to build the so-called Standard Model, the theory of electro-weak interactions [10]. Among the most important results are the discovery of the negative helicity of neutrinos [11], the interpretation of the linear rise of the total neutrino-nucleon cross-section by the quark structure of matter [12] and the discovery of neutral currents by the Gargamelle bubble chamber at CERN [13].

There has been an obvious progress in neutrino physics during the last decades. Moreover, there are more than 50 different experiments involving neutrinos which are currently running. Nevertheless neutrinos are still the least known particles among the well-established fundamental fermions and several very important questions about their intrinsic properties remain open. The most important among them:

- - are neutrinos massive?
- - do their families mix by analogy to the quark sector?

1.2 Neutrino Masses

1.2.1 Experimental aspects

The question of neutrino masses was addressed by a large number of experiments using kinematical techniques to provide direct measurements of neutrino masses. Unfortunately, no evidence of massive neutrinos has been found up to now. The best current upper limits are summarized in the Table 1.1

Table 1.1: Experimental upper limits on neutrino masses from direct measurements.

Limit	Method	Experiment
$m_{\nu_e} < 3.9\ eV$ (95% CL)	end point of e^- energy spectrum from tritium decay	Troitsk [14]
$m_{\nu_\mu} < 0.17\ MeV$ (90% CL)	$\pi^+ \to \mu^+ \nu_\mu$ decay at rest	PSI [15]
$m_{\nu_\tau} < 23.1\ MeV$ (95% CL)	$\tau \to 5\pi\ (\pi^0)\ \nu_\tau$	ALEPH [16]

One should point out that the great majority of experiments measuring the region near the end point of the β-spectrum of tritium give negative values for $m^2_{\nu_e}$ due to anomalies which are not yet understood. For example, the result of the Troitsk experiment giving the most stringent upper limit was initially presented as $m^2_{\nu_e} = -22 \pm 4.8\ (eV^2)$, while a better treatment of the shape of the measured part of the beta spectrum gives $m^2_{\nu_e} = 1.5 \pm 5.9 \pm 3.6\ (eV^2)$ [14].

Using the energy-momentum conservation in the two-body $\pi \to \mu$ decay at rest and measuring the momentum of the outgoing muon, one can derive the following expression for the ν_μ mass:

$$m^2_{\nu_\mu} = m^2_\pi - m^2_\mu - 2m_\pi \sqrt{p^2_\mu + m^2_\mu}$$

The experiment at PSI also gave a negative value $m^2_{\nu_\mu} = -0.016 \pm 0.023\ (MeV^2)$, where the largest uncertainty comes from the knowledge of the pion mass m_π [15].

Limit on the ν_τ mass has been derived (using a two dimensional likelihood fit of the visible energy and the invariant mass distribution) from the study of the decay

$$\tau \to 5\pi\ (\pi^0)\ \nu_\tau$$

where the available phase space for the neutrino is significantly reduced compared to the other decay channels [16].

It is becoming clear now that the end of the road has been reached in these experimental efforts unless a new generation of techniques is forthcoming.

1.2.2 Theoretical aspects

Let us look at the problem of neutrino masses from the theoretical point of view.

The Standard Model assumes massless neutrinos, as well as the existence of left-handed neutrinos and right-handed antineutrinos only. However, it does not give any reason why neutrinos are massless. The masses of the other leptons are introduced as additional parameters into the theory. Nevertheless, several models beyond the Standard Model provide a mechanism to generate neutrino masses [17].

In order to introduce a neutrino mass one has to extend the Lagrangian of the weak interaction by an additional mass term which has to be hermitian and invariant under Lorentz transformations.

For the weak interactions it is convenient to deal with chiral projections $\nu_{L,R}$ of the neutrino field operator ν:

$$\nu_L \;=\; \frac{1}{2}(1-\gamma_5)\nu \;=\; \nu_-$$

and

$$\nu_R \;=\; \frac{1}{2}(1+\gamma_5)\nu \;=\; \nu_+$$

Mass terms always transform left- and right-handed neutrinos into each other. This can be seen by the fact that it is possible to find massive particles in opposite helicity states, depending on the frame chosen. Experimentally observed neutrinos of one family are the left-handed neutrinos ν_L and their CP partners right-handed antineutrinos ($\bar{\nu}_R$).

Dirac and Majorana neutrinos

Before going into details, let us consider the difference between two possible neutrino representations: Dirac and Majorana neutrinos. This difference can be illustrated with the help of the following example [18].

Suppose there exists a massive neutrino with negative helicity ν_-. If the theory under consideration is CPT invariant, then there exists also the CPT mirror image of ν_-, an antineutrino with positive helicity $\bar{\nu}_+$:

$$\underbrace{(\nu_- \quad , \quad \bar{\nu}_+)}_{CPT}$$

But since the neutrino ν_- has a mass its velocity is smaller than the speed of light so an observer can move faster. Then in the frame of this observer, the neutrino is running the other way around but it is still spinning the same way. In other words it is possible to convert with a Lorentz boost a neutrino with negative helicity into a neutrino with positive helicity ν_+.

$$\overbrace{\underbrace{(\nu_- \quad , \quad \bar{\nu}_+)}_{CPT} \qquad (\qquad\quad , \quad \nu_+)}^{Lorentz\ boost}$$

The question is whether these two states with positive helicity (ν_+ and $\bar{\nu}_+$) are the same (do they interact in the same way)?

- If we assume that ν_+ is not the same particle as $\bar{\nu}_+$, then ν_+ has its own CPT mirror image $\bar{\nu}_-$. This new state can be connected to $\bar{\nu}_+$ by a Lorentz boost.

  $$\overbrace{\underbrace{(\nu_- \quad , \quad \bar{\nu}_+)}_{CPT} \qquad \underbrace{(\bar{\nu}_- \quad , \quad \nu_+)}_{CPT}}^{Lorentz\ boost}$$

  So, we have four states with the same mass. This set of states is called a Dirac neutrino. In general a Dirac neutrino can have an electric dipole moment and a magnetic dipole moment, but they are proportional to the mass of the neutrino [19]:

  $$\mu_\nu = \frac{3eG_F m_\nu}{8\pi^2\sqrt{2}} = 3.2 \times 10^{-19}(m_\nu/1eV)\mu_B,$$

  (where G_F is the Fermi constant and $\mu_B = \dfrac{e}{2m_e}$ is the Bohr magneton) and consequently much too small to give rise to experimentally observable phenomena[1].

- If we assume that ν_+ is identical to $\bar{\nu}_+$ then there are only two states with the same mass left.

$$(\overbrace{\underbrace{\nu_- \quad , \quad \nu_+}_{CPT}}^{Lorentz\ boost})$$

This set of states is called a Majorana neutrino.

In the rest frame a CPT transformation applied to either of the two spin states reverses its spin. Then a 180 degrees rotation brings the neutrino back to the original state. In other words a CPT transformation is equivalent to a Lorentz boost for Majorana neutrinos. That is the meaning of the expression saying that a Majorana neutrino is its own antiparticle.

Consequently Majorana neutrinos have no magnetic dipole moment and no electric dipole moment.

If neutrinos are Majorana particles, then it is also possible for a ν_μ interacting with matter to produce a μ^+ rather than a μ^-. But the probability for a given ν_m component of the ν_μ to be produced with positive helicity is proportional to $(m_{\nu_m}/E_m^*)^2$, where E_m^* is the energy of the ν_m in the rest frame of the decaying hadron (π or K meson). Unfortunately, since the value $(m_{\nu_m}/E_m^*)^2$ is likely to be extremely small this effect cannot be observed experimentally.

If neutrinos were Majorana particles they would be unique among the known fermions due to the fact that Majorana masses cannot be generated by an ordinary Higgs doublet as it is the case for Dirac masses.

We have to emphasize once again that the distinction between Dirac and Majorana neutrinos disappear in the case of massless neutrinos.

Let us see now how one can introduce neutrino mass terms in the Lagrangian of weak interactions.

- **Dirac mass term**

The simplest way to describe the mass is to introduce the right-handed neutrinos although they have not been seen so far. The mass term in the Lagrangian is

$$\mathcal{L}_{Dirac} = -(\bar{\nu}_L M \nu_R + \bar{\nu}_R M^\dagger \nu_L)$$

where $\nu_{L,R}$ are given by

$$\nu_{L,R} = \begin{pmatrix} \nu_e \\ \nu_\mu \\ \nu_\tau \end{pmatrix}_{L,R}$$

In general M is a 3×3 complex mass matrix, and hence there is no guarantee that mass eigenvalues are positive. One needs to bi-diagonalize M using two unitary matrices U and V:

$$U^+ M V = m_D = \begin{pmatrix} m_1 & 0 & 0 \\ 0 & m_2 & 0 \\ 0 & 0 & m_3 \end{pmatrix}$$

[1]The best experimental upper limit on the ν_e magnetic moment is $\mu < 1.8 \times 10^{-10}\mu_B$ at 90% CL [9].

where U and V relate the mass eigenstates $\nu_L^{(m)}$, $\nu_R^{(m)}$ and weak eigenstates ν_L, ν_R

$$\begin{aligned}\nu_L &= U\nu_L^{(m)} \\ \nu_R &= V\nu_R^{(m)}\end{aligned}$$

The diagonalized mass Lagrangian is

$$\mathcal{L}_{Dirac} = -\bar{\nu}_L^{(m)} m_D \nu_R^{(m)} + h.c.$$

Physically, since only ν_L is involved in weak interactions, the matrix U is the analog of the Cabibbo, Kobayashi and Maskawa (CKM) mixing matrix.

The total lepton number $l = l_e + l_\mu + l_\tau$ is conserved in case of a pure Dirac mass term.

The two important questions to this approach are: why do not we have any proof of the ν_R existence and why is the mass scale so small?

- **Majorana mass term**
  The Majorana neutrino mass can be described by the use of ν_L only

$$\mathcal{L}_{Majorana} = -\frac{1}{2}\bar{\nu}_L^c M \nu_L + h.c.$$

where $\bar{\nu}_L^c$ is a right-handed neutrino.

Since $\bar{\nu}_L^c M \nu_L = \bar{\nu}_L^c M^T \nu_L$, we have $M = M^T$, i.e. M is symmetric and diagonalization can be done by a single unitary matrix U in this case. Again, with

$$\nu_L = U\nu_L^{(m)}$$

we can rewrite

$$\mathcal{L}_{Majorana} = -\frac{1}{2}(\bar{\nu}_L^c m_D \nu_L + \bar{\nu}_L m_D \nu_L^c)$$

Defining $\nu_{Majorana} = \nu_L + \nu_L^c$, we obtain

$$\mathcal{L}_{Majorana} = -\frac{1}{2}\bar{\nu}_{Majorana}\, m_D\, \nu_{Majorana}$$

The major difference with respect to the previous Dirac case is that the lepton number is violated by two units. To understand that this fact is not in contradiction with existing experimental data (as it was mentioned above), let us recall the origin of the introduction of lepton number [18]. It was observed experimentally that the neutral particle which is emitted simultaneously with a μ^+ in π^+ decay interacts with matter producing a μ^- and never μ^+. This neutral particle was called ν_μ. Something similar happens for π^-: the neutral particle (called $\bar{\nu}_\mu$) which is emitted simultaneously with a μ^- interacts with matter producing a μ^+ and never μ^-. The conventional explanation of these facts is that

  - ν_μ and $\bar{\nu}_\mu$ are distinct from each other;
  - there is a quantum number which is conserved during these interactions - the lepton number. If we assign the lepton number $+1$ to μ^- and ν_μ and -1 to μ^+ and $\bar{\nu}_\mu$, then ν_μ can only produce μ^- in matter;

However, there is no evidence that this explanation is correct. The existence of the lepton number is not necessary. An alternative explanation arises from the fact that the neutral particle produced in π^+ decay has a left-handed helicity, while the neutral particle produced in π^- decay has a right-handed helicity. Now, suppose that the parity-violating weak interaction is such that every neutrino with a right-handed helicity interacts giving a μ^+, while every neutrino with a left-handed helicity interacts giving a μ^-. In this case we do not need to introduce a conserved lepton number. The helicity constraints are sufficient to account for all the observed facts. If this is the true explanation, then, ν_μ and $\bar{\nu}_\mu$ are, respectively, just the left and right helicity states of a single particle - the Majorana neutrino as it was already introduced above.

- **Dirac-Majorana mass term, see-saw mechanism**
Let us consider now the mixed mass term of the most general Dirac-Majorana type. In case of only one generation, the Lagrangian of interest is

$$\mathcal{L}_{D-M} = -m_D \bar{\nu}_L \nu_R - \frac{1}{2}(m_L \bar{\nu}_L^c \nu_L + m_R \bar{\nu}_R^c \nu_R) + h.c.$$

where m_D is Dirac mass and m_L, m_R are Majorana masses.

If we define a left-handed neutrino state ν as

$$\nu = \begin{pmatrix} \nu_L \\ \nu_R^c \end{pmatrix}$$

the Dirac-Majorana Lagrangian looks like that of Majorana alone:

$$\mathcal{L}_{D-M} = -\frac{1}{2}\bar{\nu}^c \mathcal{M} \nu + h.c.$$

where the mass matrix $\mathcal{M}$ is

$$\mathcal{M} = \begin{pmatrix} m_L & m_D \\ m_D & m_R \end{pmatrix}$$

It is to be noted that the state ν is not a mass eigenstate. Diagonalizing $\mathcal{M}$ yields

$$m_1 = \frac{m_L + m_R}{2} - \frac{1}{2}\sqrt{4m_D^2 + (m_R - m_L)^2}$$
$$m_2 = \frac{m_L + m_R}{2} + \frac{1}{2}\sqrt{4m_D^2 + (m_R - m_L)^2}$$

Now, the mass eigenstate $\nu^{(m)}$ can be defined as

$$\nu^{(m)} = \begin{pmatrix} \nu_1 \\ \nu_2 \end{pmatrix} = U\nu = \begin{pmatrix} \cos\theta \cdot \nu_L - \sin\theta \cdot \nu_R^c \\ \sin\theta \cdot \nu_L + \cos\theta \cdot \nu_R^c \end{pmatrix}$$

where the mixing angle is given by $tan2\theta = \frac{2m_D}{(m_R - m_L)}$. There are two interesting cases

  - first, when $m_D >> m_L, m_R$. In this case m_1 and m_2 are almost degenerate in mass ($|m_1| \approx |m_2| \approx m_D$) and we have $\theta \approx 45^0$. This case practically corresponds to a one four-component Dirac neutrino. ν_1 and ν_2 have equal masses, opposite CP parities and the mixing is maximum.
  - second, when $m_R >> m_D, m_L$. If we assume $m_L = 0$ for simplicity, then

$$|m_1| \approx \frac{m_D^2}{m_R}$$

$$|m_2| \approx m_R$$

implying that m_1 is naturally small and m_2 is large. Since $\theta \approx 0^0$, ν_L and ν_R^c are practically decoupled. This is the so-called see-saw mechanism [20]. Note, that m_D has the standard model mass scale whereas m_R is the mass scale of the right-handed neutrino associated with GUT models [21].

The essential feature of the scheme with a combined Dirac-Majorana mass term is the appearance of “sterile” fields which are not present in the standard weak interaction Lagrangian. Then, the mixing between “active” and “sterile” neutrinos is possible. “Active” neutrinos are those which take part in the standard weak interactions. In case of pure Dirac or pure Majorana mass terms only mixing between “active” neutrinos is allowed.

If we generalize the above approach to the three generations

$$m_1 \approx \frac{m_D^2}{m_R} \longrightarrow \bar{m}_1 \approx \bar{m}_D \bar{M}^{-1} \bar{m}_D^T$$

where all barred objects are 3×3 matrices and as before we assume $|(\bar{m}_D)_{i,j}| \ll |\bar{M}_{i,j}|$. Now we have a 6×6 mass matrix given by

$$\mathcal{M} = \begin{pmatrix} 0 & \bar{m}_D \\ \bar{m}_D & \bar{M}_R \end{pmatrix}$$

At this point two possibilities can be considered

- There is no mass hierarchy among the right-handed neutrinos. That is

$$\bar{M}_R \approx M_R \begin{pmatrix} 1 & 0 & 0 \\ 0 & 1 & 0 \\ 0 & 0 & 1 \end{pmatrix}$$

  implying

$$m(\nu_1) : m(\nu_2) : m(\nu_3) = \frac{m_u^2}{M_R} : \frac{m_c^2}{M_R} : \frac{m_t^2}{M_R} \left(\text{or } \frac{m_e^2}{M_R} : \frac{m_\mu^2}{M_R} : \frac{m_\tau^2}{M_R} \right)$$

  where m_u, m_c and m_t are the masses of ”top” quarks (u, c, t) of the corresponding families and m_e, m_μ, m_τ are the masses of the corresponding leptons (electron, muon, tau). This relation is called the quadratic see-saw mechanism.

- The other possibility is the case where the right-handed neutrinos have the mass hierarchy similar to that of the known ”top” quarks

$$\bar{M}_R \approx M_R \begin{pmatrix} \frac{m_u}{m} & 0 & 0 \\ 0 & \frac{m_c}{m} & 0 \\ 0 & 0 & \frac{m_t}{m} \end{pmatrix}$$

  In this case we have

$$m(\nu_1) : m(\nu_2) : m(\nu_3) = \frac{m_u}{M_R} : \frac{m_c}{M_R} : \frac{m_t}{M_R} \left(\text{or } \frac{m_e}{M_R} : \frac{m_\mu}{M_R} : \frac{m_\tau}{M_R} \right)$$

  which is called the linear see-saw mechanism.

The see-saw mechanism is the only one known that allows to explain in a natural way the smallness of neutrino masses with respect to the masses of all the other fundamental fermions.

For a detailed review on the subject of neutrino masses see [22].

1.3 Neutrinos and Astrophysics

Besides the importance of neutrino masses in the theory of weak interactions, there exists also a deep interest in neutrino physics from cosmology. The indirect observation of dark matter in the dynamics of galaxies indicates that the major part of their mass resides in a form which does not emit light.

According to the Big Bang hypothesis neutrinos were produced and interacted during the first short time interval. But as the Universe expanded, they found few particles to interact with and were left as a uniform sea. Neutrinos decoupled at a temperature T_D, when the expansion rate of the Universe became larger than their interaction rate ($T_D \approx 5\ MeV$). The density of such relic neutrinos is calculated to be 113 particles of each 3 types per cm^3 [23]. The other sources of neutrinos in the Universe are supernovae (produce $\sim 10^{58}$ ν's of about 10 MeV per explosion) and stars (the Sun gives $\sim$ 3% of its power in the form of ν's). If neutrinos are massive and stable they can contribute significantly to the mass of the Universe. The current upper limit from cosmology on the sum of all 3 types of ν depends on two parameters - the Hubble constant H_0 and the present energy density of the Universe ρ_0 [21]:

$$\sum_{\mathrm{i=e}}^{\tau} m_{\nu_i} \ \leq 100 \cdot \Omega \cdot h^2 \ (eV)$$

where h and Ω are defined via $H_0 \equiv h \cdot 100\ [(km/sec)/Mpc]$ and $\rho_0 \equiv \Omega \cdot \rho_c$, ρ_c is the critical density corresponding to a flat Universe

$$\rho_c = \frac{3H_0^2}{8\pi G}$$

The limit on the sum of the masses of all neutrino flavours is

$$\sum_{\mathrm{i=e}}^{\tau} m_{\nu_i} \ < \ 15 \div 65\ eV$$

The above limit applies only when neutrinos are stable or much longer lived than the age of the Universe.

1.4 Neutrino Oscillations

A very interesting phenomenon being searched for experimentally is called neutrino oscillations. It was introduced by B.Pontecorvo in 1957 [24] by analogy to the $K^0 - \bar{K}^0$ system. Under the assumption of massive neutrinos and mixing of their families, neutrino interaction with matter is described by flavour eigenstates $|\nu_\alpha>$, while neutrino propagation in space-time is governed by mass eigenstates $|\nu_i>$. As it was already shown before, in this case the flavour eigenstates can be represented as a superposition of the mass eigenstates

$$|\nu_\alpha> = \sum_{\mathrm{i=1}}^{\mathrm{n}} U_{\alpha i}|\nu_i>$$

where U is a unitary mixing matrix analogous to the Cabibbo-Kobayashi-Maskawa mixing matrix for quarks and n is the number of neutrino families ($n = 3$ for ν_e, ν_μ, ν_τ).

In other words the flavour of a neutrino along its propagation can be changed because of the interference between different mass states.

One should point out that there might be an essential difference between quark and neutrino mixing since the electrical charges of quarks differ from zero, whereas those of neutrinos are zero. Consequently, quarks are Dirac particles while neutrinos may be either Dirac particles (there is a conserved lepton charge in this case) or truly neutral Majorana particles (no conserved lepton charge). By studying only neutrino oscillations one can not distinguish the Dirac case from the Majorana case.

In 1962 the formalism describing neutrino oscillations in case of two types of neutrinos (ν_e and ν_μ) was proposed [25]

$$\begin{aligned} \nu_e &= \nu_1 \cdot \cos\theta \; + \; \nu_2 \cdot \sin\theta \\ \nu_\mu &= -\nu_1 \cdot \sin\theta \; + \; \nu_2 \cdot \cos\theta \end{aligned}$$

where ν_1 and ν_2 are mass eigenstates, ν_e and ν_μ are the observed particles, i.e. weak interaction eigenstates.

The probability of neutrino oscillations (Fig. 1.1) is given by

$$P_{\nu_\beta,\nu_\alpha} \;=\; P(\nu_\alpha \leftrightarrow \nu_\beta) \;=\; \sin^2(2\theta) \times \sin^2(1.27\Delta m^2 \frac{L}{E})$$

where $\Delta m^2 = m_2^2 - m_1^2$ $[eV^2]$ is the difference of the squares of the masses of the appropriate neutrino eigenstates, L $[m]$ is the source-detector distance, E $[MeV]$ is the energy of the neutrino. This formula is valid regardless of whether Dirac or Majorana neutrinos are involved.

One can define the oscillation length as $L_{osc} = 2.5 \times \frac{E}{\Delta m^2}$. The sensitivity of an experiment is normally judged by its L/E ratio. Neutrino oscillations could be observed if the mixing angle is large enough and the oscillation length is less or of the order of the source-detector distance ($L_{osc} \leq L$) which can be rewritten as $\Delta m^2 \geq \frac{E}{L}$. To search for low mass differences (Δm^2) the distance (L) should be large and the energy of the neutrino (E) has to be small.

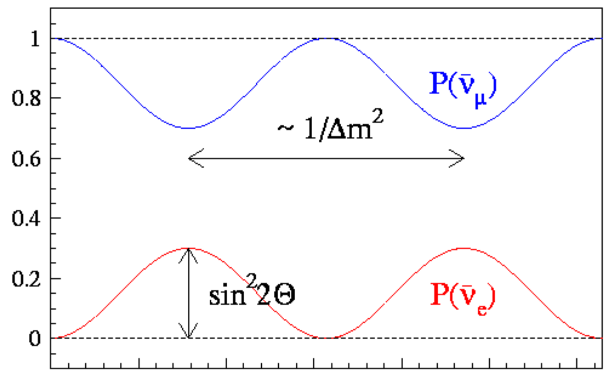

Figure 1.1: Probability of neutrino oscillations in case of 2 neutrino flavours.

The important consequence of the formula above is that neutrino oscillation experiments cannot measure individual neutrino masses, but only differences of squared masses.

With the rising evidence for ν_τ existence this approach was extended to 3 types of neutrinos but it was originally shown [26] that the results should not be significantly different[2].

As a consequence, although there are three neutrino flavours, data were analyzed assuming oscillations between just two of them.

[2]However, the results depend strongly on the assumed mass hierarchy.

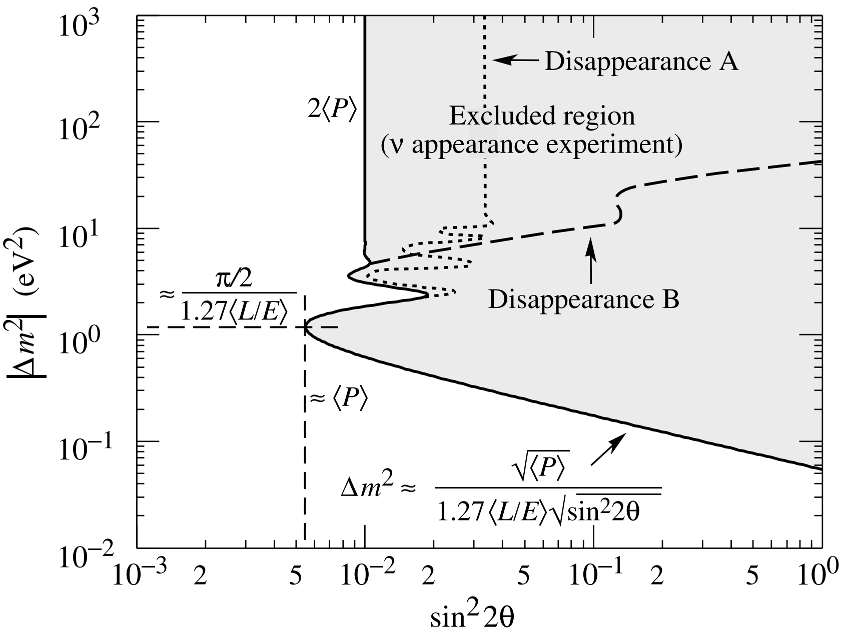

Figure 1.2: Exclusion plot for a toy experiment (from [9]). Shown here are possible areas of neutrino oscillation parameters excluded by different experimental techniques: appearance and disappearance experiments (see later).

Experimental results are usually presented as an area on the 2-dimensional $\{\sin^2(2\theta),\ \Delta m^2\}$ plot. An example of such plot is given in the Figure 1.2 for a toy experiment using unrealistic assumption that $b = 1.27\frac{L}{E}$ has a Gaussian distribution with standard deviation σ_b about a central value[3] b_0.

One should note that

- since the fast oscillations are completely washed out by the resolution for large Δm^2, $\sin^2(2\theta) = 2 < P >$ in this region;
- the maximum exclusion to the left is approximately $< P >$ and it occurs at $\Delta m^2 = \frac{\pi}{2b_0}$;
- the intercept at $\sin^2(2\theta) = 1$ is at $\sqrt{< P >}/b_0$.

Currently it is commonly believed that all the experimental results should be analyzed in the 3-neutrino approach. Moreover, there exist a strong recommendation from the Particle Data Group saying that "in a comprehensive analysis of all current data on limits on neutrino oscillations, one should use a three-generation mixing framework" [27]. We will come back to this discussion later.

At this point we can state that the observation of neutrino oscillations could provide positive answers to both questions about neutrino mass and neutrino mixing. Moreover, it is the only possible technique nowadays to detect neutrino masses below $\sim 1\ eV$.

[3]In a real experiment L and E have some spread and one must average the probability P over the appropriate distributions.

1.5 Neutrino Oscillation Experiments

Experiments looking for neutrino oscillations have been carried out using accelerators, nuclear power plants, cosmic rays, the Sun and even the supernova SN 1987A as neutrino sources.

There are two types of experiments to search for neutrino oscillations. In experiments of the first type (exclusive) one is looking for the appearance of neutrinos of a given flavour ν_β ($\beta = e, \mu, \tau$) at some distance from the source of neutrinos of a different flavour ν_α ($\alpha = e, \mu$; $\alpha \neq \beta$). In experiments of the second type (inclusive) at some distance from the source of neutrinos of a definite flavour one detects neutrinos of the same flavour looking for disappearance of the original neutrinos. In the first case experiments answer the question whether the probability $P_{\nu_\beta,\nu_\alpha}(\alpha \neq \beta)$ is different from zero. In the second case experiments test if the probability $P_{\nu_\alpha,\nu_\alpha} = 1 - \sum_{\alpha \neq \beta} P_{\nu_\beta,\nu_\alpha}$ is not equal to unity.

The method looking for the appearance of "unexpected" neutrinos can be very sensitive to small mixing angles as it is in principle sufficient to detect a small number of events induced by "unexpected" neutrino flavour.

The other method is less sensitive to small mixing angles being in general limited by the statistics and systematical uncertainties in the absolute intensity of the neutrino source used, the neutrino spectrum and the detection efficiency. However, this technique is the only one sensitive to neutrino oscillations into any neutrino species. Even oscillations into "sterile" neutrinos (neutrinos that do not take part in the standard weak interactions) can be measured with this kind of experiment.

The nature (and the amount) of a given neutrino ν_β ($\beta = e, \mu, \tau$) is measured in terms of the charged leptons l_β which come out of charged current (CC) neutrino scattering $\nu_\beta X \to l_\beta X'$. In appearance experiments of $\nu_\alpha \to \nu_\beta$ type the expected number of charged leptons l_β is given by

$$N(\nu_\alpha \to l_\beta; L) \ = \ n_T \int_0^\infty dE \int_0^{q_{max}} dq \ \varepsilon(q) F_\alpha(E) \frac{d\sigma_\beta(E,q)}{dq} P(\nu_\alpha \to \nu_\beta; E, L)$$

whereas in disappearance experiments the attenuation of the original neutrino beam is being measured

$$N_{\alpha\alpha}(L) \ - \ N(\nu_\alpha \to l_\alpha; L) \ = \ n_T \int_0^\infty dE \int_0^{q_{max}} dq \ \varepsilon(q) F_\alpha(E) \frac{d\sigma_\alpha(E,q)}{dq} \times$$

$$(1 \ - \ P(\nu_\alpha \to \nu_\alpha; E, L))$$

where

$$N_{\alpha\beta}(L) \ = \ n_T \int_0^\infty dE \int_0^{q_{max}} dq \ \varepsilon(q) F_\alpha(E) \frac{d\sigma_\beta(E,q)}{dq} \ ,$$

$F_\alpha(E)$ is the flux of neutrino ν_α, n_T is the density of target nucleons, $\varepsilon(q)$ is the detection efficiency for the charged lepton l_β as a function of its energy q, $\frac{d\sigma_\beta(E,q)}{dq}$ is the differential cross section of the interaction $\nu_\beta X \to l_\beta X'$ and $P(\nu_\alpha \to \nu_\beta; E, L) = | < \nu_\alpha(0) | \nu_\beta(L) > |^2$ is the probability of $\nu_\alpha \to \nu_\beta$ transition for a neutrino of energy E after traveling a distance L.

Different techniques are used to cover various regions of phase space expressed in terms of Δm^2 and $\sin^2(2\theta)$. Accelerator experiments give limits down to $\Delta m^2 \sim 0.1 \div 1 \ eV^2$. Reactor experiments cover the region of $\Delta m^2 \sim 10^{-2} \ eV^2$. Atmospheric neutrino experiments allow to reach: $\Delta m^2 \sim 10^{-4} \ eV^2$. Solar neutrino experiments test the region of very small Δm^2: $\sim 10^{-4} \div 10^{-11} \ eV^2$

We present here a breaf review of neutrino oscillation experiments.

1.5.1 Solar Neutrino Experiments

At present there are several indications in favour of non-zero neutrino mass and mixing. The first one comes from the Solar neutrino experiments: Homestake, GALLEX, SAGE and (SUPER)KAMIOKANDE. The results of these experiments are usually compared with the predictions of the Standard Solar Model (SSM) [28, 29, 30, 31] - a physical description of the Sun based on stellar evolution equations.

There are several nuclear fusion reactions occurring in the Sun core, all having the effect of transforming four protons into ^4He nucleus:

$$4p \rightarrow \, ^4He \, + \, 2e^+ \, + \, 2\nu_e \, + \, 26.73 \, MeV \, - \, E_\nu \, ,$$

where E_ν represents the energy taken away by neutrinos ($< E_\nu > \sim 0.6 \, MeV$). Thus, the average energy produced by this reaction and emitted by the Sun in the form of electromagnetic radiation is $Q \approx 26.1 \, MeV$. The Sun luminosity is measured to be $L_\odot = 3.846 \times 10^{26} \, W = 2.4 \times 10^{39} \, MeV/s$ [9]. It is possible to calculate roughly the rate of ν_e emission from the Sun:

$$\frac{dN(\nu_e)}{dt} = 2\frac{L_\odot}{Q} \approx 1.8 \times 10^{38} s^{-1}$$

and, using the average distance between the Sun and the Earth ($D = 1.496 \times 10^{11} \, m$), the solar neutrino flux on the Earth:

$$\Phi_\nu \approx 6.4 \times 10^{10} cm^{-2} s^{-1}$$

There are two main nuclear reaction cycles in the Sun core:

- The pp cycle responsible for 98.5% of the Sun luminosity. It involves the following reactions:

$$p \, + \, p \rightarrow \, e^+ \, + \, \nu_e \, + \, d$$

$$p \, + \, d \rightarrow \, \gamma \, + \, ^3He$$

$$^3He \, + \, ^3He \rightarrow \, ^4He \, + \, p \, + \, p$$

These reactions represent 85% of the pp cycle. In the remaining 15% of cases the last reaction is replaced by the following sequence of reactions:

$$^3He \, + \, ^4He \rightarrow \, \gamma \, + \, ^7Be$$

$$\gamma \, + \, ^7Be \rightarrow \, \nu_e \, + \, ^7Li$$

$$p \, + \, ^7Li \rightarrow \, ^4He \, + \, ^4He$$

The last two reactions in this chain in 0.19% of cases are replaced by

$$p \, + \, ^7Be \rightarrow \, \gamma \, + \, ^8B$$

$$^8B \rightarrow \, ^8Be \, + \, e^+ \, + \, \nu_e$$

$$^8B \rightarrow \, ^4He \, + \, ^4He$$

Let us denote the neutrinos produced in the corresponding reactions by ν_{pp}, ν_{Be} and ν_B. We have to point out that ν_{pp} and ν_B have a continuous energy spectrum while ν_{Be} is monoenergetic because it is produced in a two-body final state reaction (see Table 1.2)

Table 1.2: Main components of the solar neutrino flux on the Earth (as predicted by different SSM).

Solar Model		BP 92	TCL	BP 95	DS
Flux Component	Energy	[28]	[29]	[30]	[31]
pp flux ($\Phi \times 10^{10}/cm^2/s$)	$\leq 420\ keV$	6.00 ± 0.12	6.02	5.91 ± 0.06	6.1
^7Be flux ($\Phi \times 10^{9}/cm^2/s$)	$= 860\ keV$	4.89 ± 0.88	4.33	$5.15^{+0.31}_{-0.36}$	3.71
^8B flux ($\Phi \times 10^{6}/cm^2/s$)	$\leq 15\ MeV$	5.70 ± 0.82	4.4 ± 1.1	$6.62^{+0.93}_{-1.13}$	2.49

- The CNO cycle which involves heavier elements consists of the following chain of reactions:

$$p\ +\ ^{15}N \rightarrow\ ^{12}C\ +\ ^{4}He$$
$$p\ +\ ^{12}C \rightarrow\ \gamma\ +\ ^{13}N$$
$$^{13}N \rightarrow\ ^{13}C\ +\ e^{+}\ +\ \nu_e$$
$$p\ +\ ^{13}C \rightarrow\ \gamma\ +\ ^{14}N$$
$$p\ +\ ^{14}N \rightarrow\ \gamma\ +\ ^{15}O$$
$$^{15}O \rightarrow\ ^{15}N\ +\ e^{+}\ +\ \nu_e$$

and

$$p\ +\ ^{15}N \rightarrow\ \gamma\ +\ ^{16}O$$
$$p\ +\ ^{16}O \rightarrow\ \gamma\ +\ ^{17}F$$
$$^{17}F \rightarrow\ ^{17}O\ +\ e^{+}\ +\ \nu_e$$
$$p\ +\ ^{17}O \rightarrow\ ^{14}N\ +\ ^{4}He$$

The differences in the solar models reflect different choices (personal judgement of authors) of the best experimental measurements of the laboratory cross-sections and the best extrapolation from laboratory energies to the stellar energies. Differences in the neutrino fluxes predicted by various models are small for the pp neutrinos, $\sim 30\%$ for the ^7Be neutrinos and up to a factor of two for the ^8B neutrinos (see Table 1.2).

The solar neutrino spectrum is depicted in Fig. 1.3

It should be pointed out that, while solar neutrinos arrive on the Earth $\sim 500\ s$ after being produced, it takes of the order of $10^6\ years$ for the energy produced in the same reactions to be transported from the Sun core to the surface. Thus, the Sun luminosity which is measured at present is associated with neutrinos which reached the Earth $\sim 10^6\ years$ ago. This is not considered to be a problem in the SSM because the Sun is a star with no appreciable change of properties over $\sim 10^8\ years$.

Let us review briefly the solar neutrino experiments.

- The Homestake ^{37}Cl experiment [32]

  It is the pioneering work in searching for solar neutrinos. The detector is a radiochemical device based on the measurement of the production rate of radioactive ^{37}Ar produced by the neutrino induced reaction

$$\nu_e\ +\ ^{37}Cl\ \rightarrow\ ^{37}Ar\ +\ e^{-}$$

  This technique was first proposed by B.Pontecorvo in 1946 [33].

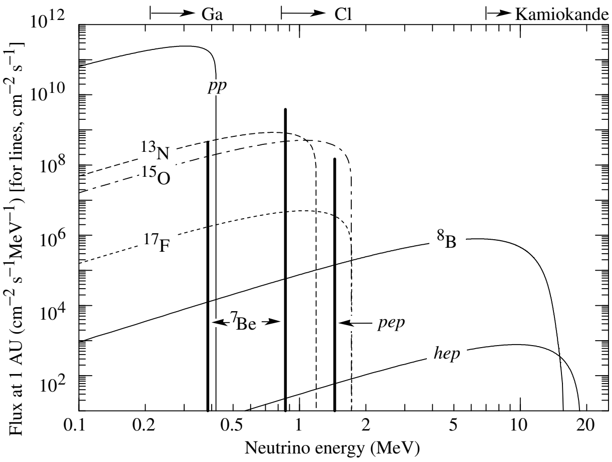

Figure 1.3: Solar neutrino flux (in $cm^{-2}s^{-1}$ for monoenergetic lines and in $cm^{-2}s^{-1}MeV^{-1}$ for continuous spectra). The thresholds corresponding to different detection techniques are also shown.

Due to the energy threshold of 814 keV for this reaction, the detector is sensitive mainly to the ^8B and ^7Be solar neutrinos.

The tank of 390 m^3 filled with 615 t of liquid C_2Cl_4 is located 4850 ft deep underground in the Homestake mine (USA) to reduce the background from protons produced by cosmic rays ($p\ +\ ^{37}Cl\ \rightarrow\ ^{37}Ar\ +\ n$).

Every few months Ar is extracted from the tank by N_2 flux. After separation and purification it is sent to a proportional counter where the reaction $e^-\ +\ ^{37}Ar\ \rightarrow\ \nu_e\ +\ ^{37}Cl$ with half life-time of $\tau_{1/2} = 34\ days$ is observed via the detection of X-ray or Auger electron. The extraction efficiency is measured by injecting a known amount of ^{37}Ar in the tank. The average daily ^{37}Ar production rate ($\sim 0.5\ atoms/day$) illustrates the difficulty of the experiment.

The measured solar neutrino flux was found to be significantly smaller than the one predicted by the SSM. This discrepancy has been known for many years and is called the "solar neutrino problem".

- Gallium experiments

  Two ^{71}Ga radiochemical experiments are dedicated to the measurement of the solar neutrino flux with the aim of testing the Standard Solar Model and trying to solve the "solar neutrino problem". They use similar technique and measure for the first time the *pp* component of solar neutrinos via the reaction

$$\nu_e\ +\ ^{71}Ga\ \rightarrow\ ^{71}Ge\ +\ e^-$$

  with a threshold of 233 keV (first proposed by V.Kuzmin [34]). By analogy to the ^{37}Cl experiment, the detection of neutrino captures is carried out by chemical separation of the ^{71}Ge product and the measurement of its decay. ^{71}Ge is unstable with respect to electron capture ($t_{1/2} = 11.43\ days$) and, therefore, the amount of extracted Ge can be determined from its activity measured in small proportional counters.

  The advantage of this technique is that the detector performance can be tested with an artificial ^{51}Cr neutrino source emitting electron neutrinos with energy

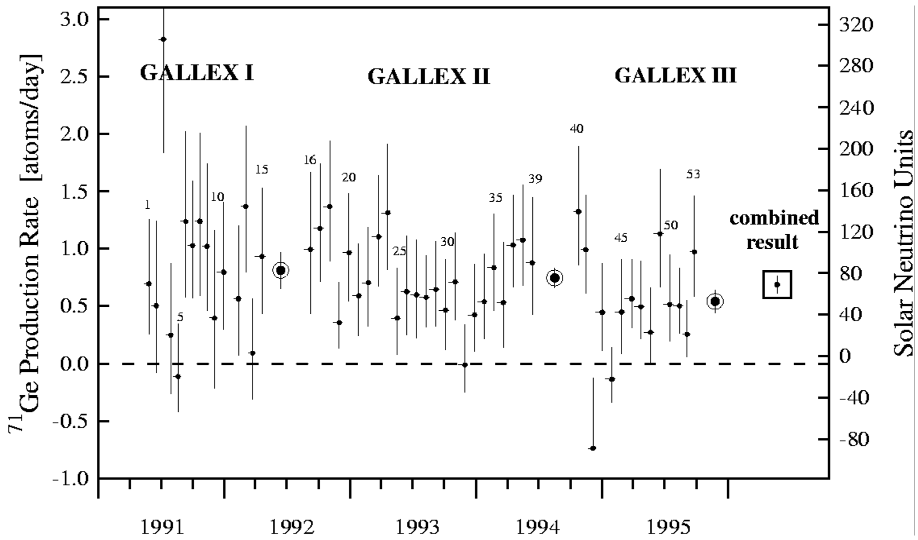

Figure 1.4: Results for the solar neutrino runs of GALLEX I, GALLEX II and GALLEX III. The left hand scale is the measured ^{71}Ge production rate; the right hand scale, the net solar neutrino production rate (in SNU, where 1 SNU corresponds to 10^{-36} captures s^{-1} $atom^{-1}$) after subtraction of side reaction contributions.

of 746 keV. The energy of these neutrinos is similar to the solar ^7Be neutrinos and thus provides an ideal check of the experimental procedure.

To protect detectors from the cosmic radiation one must install them deep underground.

The specific features of the 2 existing experiments are given below.

– GALLEX [35]

  The GALLEX experiment is installed in the Gran Sasso laboratory (Italy). The target consists of 30.3 t of gallium, containing 12 t of ^{71}Ga dissolved in $HCl + H_2O$. Results for the solar neutrino runs of GALLEX I, GALLEX II and GALLEX III are presented in the Fig. 1.4.

  The result of the ^{51}Cr neutrino source (0.93 ± 0.08) [36] indicates that the deficit of solar neutrino flux observed by GALLEX cannot be attributed to experimental artifacts and demonstrates the absence of any significant unexpected systematic errors at the 10% level.

– SAGE (Soviet - American Gallium Experiment) [37]

  The target for the reaction is in the form of liquid gallium metal (55 t) located deep underground in the Baksan Neutrino Observatory in the Caucasus mountains. About once a month the neutrino induced Ge is extracted from the Ga.

  The result from the ^{51}Cr source ($0.95 \pm 0.11^{+0.05}_{-0.08}$) [38] provides evidence for the reliability of the solar neutrino flux measurements in the experiment.

While there were some discrepancies after analyses of the first exposures, both experiments give consistent results now. The measured solar neutrino flux is again smaller than the SSM prediction.

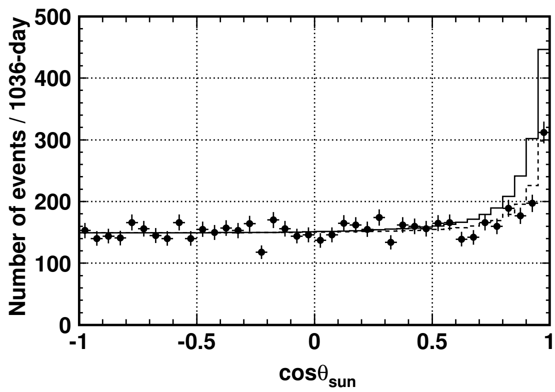

Figure 1.5: The $\cos\theta_{SUN}$ distribution for the final data sample in KAMIOKANDE detector (1036 days) confirms the solar origin of detected neutrinos. The solid line shows the prediction of SSM [30] and the dashed line shows the best fit to the data assuming a flat background distribution.

- The KAMIOKANDE (KAMIOKA Nucleon Decay Experiment) [41]

  KAMIOKANDE is a water imaging Cherenkov detector located in the Kamioka metal mine (Japan) 1 km underground which was originally designed for the proton decay search. The inner detector consists of a cylindrical tank with a diameter of 15.6 m and a height of 11.2 m filled with 2140 $tons$ of water and viewed by 940 photomultipliers[4] (50 cm diameter). It "sees" solar neutrinos in real time through their elastic scattering on electrons

$$\nu_e \ + \ e^- \ \rightarrow \ \nu_e \ + \ e^-$$

  providing the possibility to measure the direction of Cherenkov radiation (which allows to determine the incoming ν direction and to check if it points to the Sun, see Figure 1.5) and the recoiling electron energy (which is reflecting the incident neutrino energy). Elastic scattering by other neutrino species (ν_μ and ν_τ) also takes place but its cross section is six times lower than for ν_e. The sensitivity of KAMIOKANDE to detect electrons goes down to 5 MeV. However, to suppress background events from natural radioactivity of the detector itself and those induced by cosmic ray muons, the practical threshold is pushed to 7 MeV. As a result KAMIOKANDE is sensitive only to the ^8B component of solar neutrinos.

- The SUPERKAMIOKANDE

  The new SUPERKAMIOKANDE setup is a 50000 $tons$ water Cherenkov detector located 150 m to the south from the old KAMIOKANDE facility. It uses the same technique to detect solar neutrinos. The detector consists of inner and outer parts. The latter one serves as a veto counter for the incoming cosmic ray muons as well as a shield layer against γ-rays and neutrons coming from the rocks. The inner detector is the central part (32000 $tons$) of water viewed by 11200 PMT's and is completely surrounded by the outer detector with a water layer of about 2.7 m thickness. This inner detector is used to detect interactions of solar, atmospheric and hopefully supernova neutrinos.

[4] PMT's

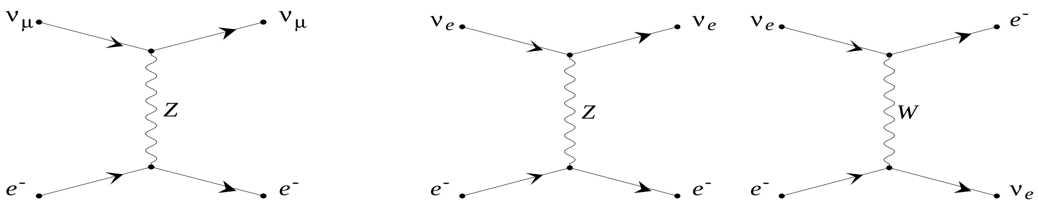

Figure 1.6: Difference between ν_μ (ν_τ) and ν_e interacting with electrons in matter.

The advantage of the SUPERKAMIOKANDE detector is a possibility to use a low energy electron beam from a small linear accelerator for calibration and detector studies.

The most important results from all 5 experiments using different detection techniques is that all of them have seen a deficit of the expected rates compared to the SSM [28, 29, 30]. The results are summerized in the Table 1.3. The solar neutrino flux is normally measured in Solar Neutrino Units[5].

Table 1.3: Results of solar neutrino experiments compared to the SSM predictions.

SSM Prediction			BP 92	TCL	BP 95	DS
Experiment	Threshold	Measured Flux	[28]	[29]	[30]	[31]
Homestake (SNU)	814 keV	$2.55 \pm 0.17 \pm 0.18$	8.1 ± 1.0	6.4 ± 1.4	$9.3^{+1.2}_{-1.4}$	4.1 ± 1.2
GALLEX (SNU)	233 keV	$69.7 \pm 6.7^{+3.9}_{-4.5}$	132 ± 7	122.5 ± 7.0	137^{+8}_{-7}	115 ± 6
SAGE (SNU)	233 keV	$69 \pm 10^{+5}_{-7}$	132 ± 7	122.5 ± 7.0	137^{+8}_{-7}	115 ± 6
Kamioka ($10^6 cm^{-2} s^{-1}$)	7 MeV	$2.80 \pm 0.19 \pm 0.33$	5.7 ± 0.8	4.4 ± 1.1	$6.62^{+0.9}_{-1.1}$	2.49
SuperK ($10^6 cm^{-2} s^{-1}$)	7 MeV	$2.44 \pm 0.06^{+0.25}_{-0.09}$	5.7 ± 0.8	4.4 ± 1.1	$6.62^{+0.9}_{-1.1}$	2.49

It should be noted that the amount of deficit is different for the different experiments. It has also been demonstrated that the deficit is most prominent for the medium energy neutrinos which come mainly from ^7Be reaction.

There were many trials to explain such a strange behaviour of solar neutrinos.

For example, there were attempts to construct so-called non-standard solar models which, in most cases, were yielding lower core temperatures resulting in a much lower ^8B neutrino flux. Recently, however, helioseismology has made great progress and starts to impose strong constraints on the solar model calculations.

MSW effect

As first shown by Mikheev, Smirnov [42] and Wolfenstein [43], the matter effect (in the Sun) can lead to a resonant amplification in the oscillation amplitude.

The main effect of neutrino interactions inside the Sun is elastic forward scattering on electrons. In analogy to optics, the integral of scattered waves can be described by introducing a refraction index n_α ($\alpha = e, \mu, \tau$), leading to a change in neutrino phase velocities. Since the solar matter is non-symmetric with respect to ν_e and $\nu_{\mu,\tau}$ (because ν_e interacts with an electron via both W and Z^0 exchange while $\nu_{\mu,\tau}$ interact only via Z^0 exchange, see Fig. 1.6) it follows that $n_e \neq n_{\mu,\tau}$. Therefore an additional phase difference occurs.

As a result of this difference, the eigenstates which propagate in solar matter without mixing (the "solar eigenstates") differ from those which propagate without

[5] 1 SNU = 10^{-36} captures s^{-1} $atom^{-1}$.

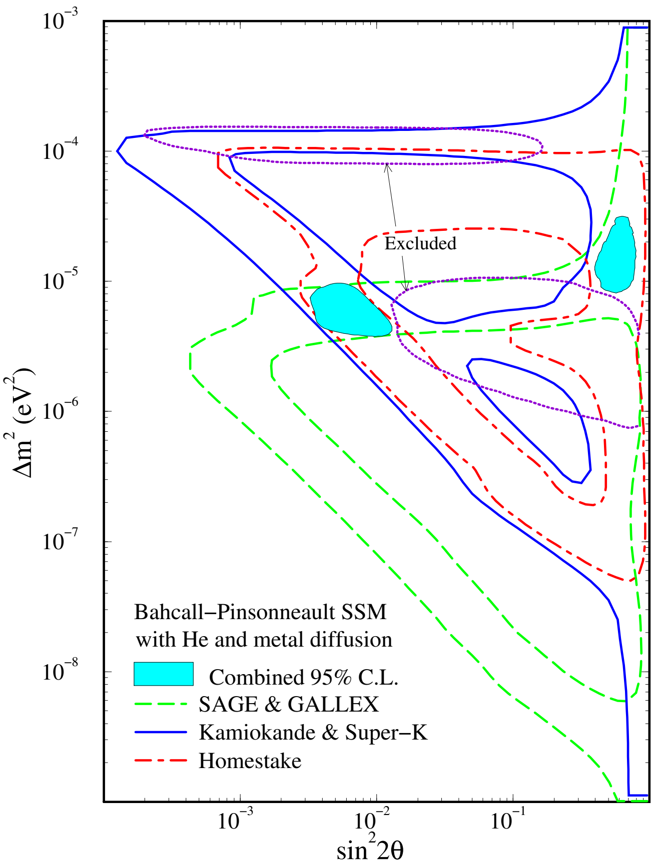

Figure 1.7: The result of the MSW solution (from [44]) in terms of the parameter space (shaded regions) allowed by the combined observations at 95% CL assuming the Bahcall-Pinsonneault SSM with He diffusion [30]. The constraints from Homestake, combined Kamiokande and SuperKamiokande, and combined SAGE and GALLEX are shown by dot-dashed, solid and dashed lines respectively. Also shown are the regions excluded by the Kamiokande spectrum and day-night data (dotted lines).

mixing in vacuum (the mass eigenstates). The mixing angle θ_M in the solar matter (the rotation angle between $\nu_e - \nu_\mu$ and the solar eigenstates) is related to the mixing angle θ_v in vacuum (the rotation angle between $\nu_e - \nu_\mu$ and the mass eigenstates) by:

$$\sin^2(2\theta_M) = \frac{\sin^2(2\theta_v)}{(\cos(2\theta_v) - \frac{L_v}{L_0})^2 + \sin^2(2\theta_v)},$$

where L_v is the oscillation length in vacuum and L_0 is a length characteristic of the motion of neutrinos through the Sun matter which is defined as

$$L_0 = \frac{2\pi}{\sqrt{2} G_F N_e},$$

G_F is the Fermi constant and N_e is the number of electrons per unit volume in the Sun.

The equation above has a resonant behaviour. Thus a very appreciable $\nu_e \to \nu_\mu$ transition may occur in the Sun even for small θ_v.

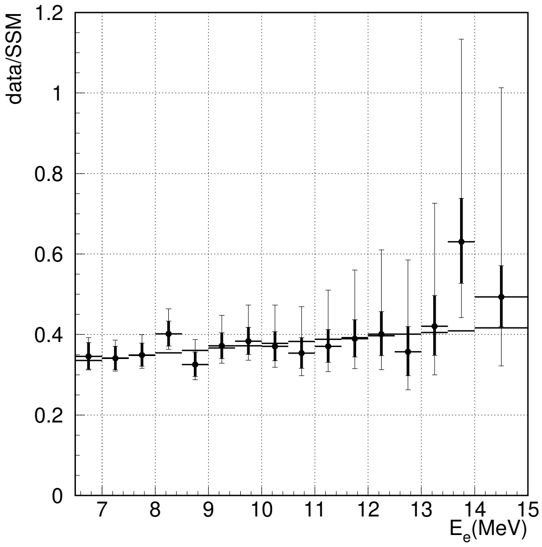

Figure 1.8: Preliminary measurement by SUPERKAMIOKANDE of the ratio of the number of observed events over the corresponding number of expected events from SSM (Data/SSM) versus electron energy. Thick (thin) error bars correspond to statistical (systematic) ones. The curve indicates what one would expect from the MSW small angle solution.

This effect, called Mikheev - Smirnov - Wolfenstain (MSW) effect, can explain the deficit of the measured solar neutrino flux compared to the SSM predictions. There are 2 consistent MSW solutions for all experiments (see Fig 1.7): the so-called "small angle solution" at $\sin^2(2\theta) \sim 8 \times 10^{-3}$ and $\Delta m^2 \sim 5 \times 10^{-6}\ eV^2$ and the "large angle solution" at $\sin^2(2\theta) \sim 0.6$ and $\Delta m^2 \sim 1.6 \times 10^{-5}\ eV^2$.

Vacuum oscillations with the parameters $\Delta m^2 \sim 6 \times 10^{-11}\ eV^2$ and $\sin^2(2\theta) \sim 0.9$ could also explain the observations of the solar neutrino experiments [44].

Future projects

New attempts to shed light on the mystery of solar neutrinos will be made in the nearest future: measurement of the energy spectrum of the solar neutrinos and measurement of solar neutrino flux using neutral current reactions which are not flavour sensitive.

The SUPERKAMIOKANDE detector intends to measure (after at least two years of data taking) the precise shape of the ^8B solar neutrino spectrum independent of the absolute flux value (preliminary results can be seen in the Figure 1.8). Another important measurement is a study of the difference in the ^8B neutrino fluxes between day and night. The reason is that the large-angle MSW solution of the solar neutrino problem predicts a small excess in the nighttime which is caused by the fact that oscillated neutrinos (ν_μ and ν_τ) can be reconverted to the original ν_e due to the regeneration in the Earth. A preliminary result [45] reported by the SUPERKAMIOKANDE collaboration indicates that there is no day-night effect within experimental uncertainties:

$$\frac{D-N}{D+N} = -0.017 \pm 0.026(stat.) \pm 0.017(syst.)$$

SNO (Sudbury Neutrino Observatory, Canada) [39] is a 1000 *tons* heavy water

Cerenkov detector for ^8B neutrinos. The goal of this experiment is to detect the neutral current reaction $\nu + d \to p + n + \nu$ apart from $\nu_e + d \to p + p + e^-$. The former reaction registers ν_μ as well as ν_e and allows to measure the total flux of solar neutrinos on the Earth.

BOREXINO [40] is a 300 *tons* liquid scintillation detector being constructed at Gran Sasso in order to directly observe the ^7Be neutrino line or to confirm its absence. The expected threshold for this detector is 250 keV.

1.5.2 Atmospheric Neutrino Experiments

Atmospheric neutrinos are produced through decays of charged pions and kaons which are secondary particles of the cosmic ray interactions in the atmosphere. Most of these hadrons decay before interacting due to the low density at high altitude.

The following decay chain is the main source of atmospheric neutrinos

$$p(He) \ + \ \text{air nucleus} \ \to \ \pi^\pm \ + \ X$$

$$\pi^\pm \ \to \ \mu^\pm + \ \overset{(-)}{\nu}_\mu$$

$$\mu^\pm \ \to \ e^\pm + \ \overset{(-)}{\nu}_e \ + \ \overset{(-)}{\nu}_\mu$$

Thus, it is expected that the flux ratio of $\frac{(\bar{\nu}_\mu+\nu_\mu)}{(\bar{\nu}_e+\nu_e)}$ is ≈ 2. All the available flux calculations are in agreement within 5% for the flavour ratio of neutrinos with energies $0.4 < E_\nu(GeV) < 1$ [46]. Significant differences in normalization ($\sim 40\%$) arise primary from different treatment of pion production by interactions of protons in the atmosphere. When dealing with the ratio $\frac{(\bar{\nu}_\mu+\nu_\mu)}{(\bar{\nu}_e+\nu_e)}$ most of the systematic uncertainties cancel or are largely reduced.

In the atmospheric neutrino experiments the fluxes of electron and muon neutrinos resulting from cosmic ray interactions with atmosphere are measured. The atmospheric neutrinos have energies ranging from $\sim 100\ MeV$ to a few GeV.

Six underground experiments have measured the atmospheric neutrino flux by detecting quasi-elastic interactions:

$$\nu_e(\nu_\mu) \ + \ n \ \to \ e^-(\mu^-) \ + \ p$$

$$\bar{\nu}_e(\bar{\nu}_\mu) \ + \ p \ \to \ e^+(\mu^+) \ + \ n$$

Three of these experiments (KAMIOKANDE [47], IMB [48] and SUPERKAMIOKANDE [45]) use large volume water tanks to detect the Cherenkov light produced by relativistic particles in water. The other three experiments (FREJUS[6] [49], NUSEX [50] and SOUDAN 2 [51]) are calorimeters with high longitudinal and transverse segmentation.

Observed events are classified as two types: (1) fully contained events in which all the tracks are contained in the detector and the incident neutrino energy is well estimated; (2) partially contained events in which some of the tracks escape the detector and the visible energy is less than the incident one.

Muons appear in all the detectors as single penetrating tracks, while electrons produce electromagnetic showers consisting of many short tracks which can be easily identified in the calorimeters and result in diffuse Cherenkov light rings in the water detectors.

The comparison between the measured and predicted (ν_μ/ν_e) ratio for all the experiments is shown in the Table 1.4.

[6]The result of FREJUS experiment includes both contained and semicontained events.

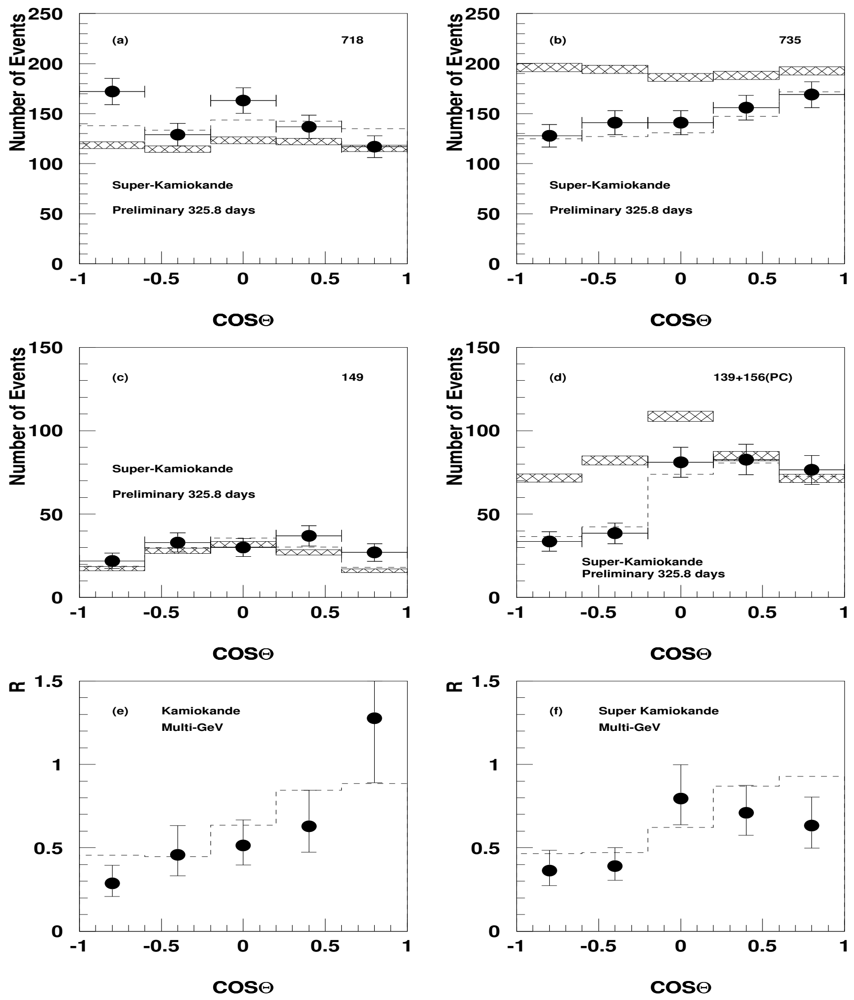

Figure 1.9: Zenith angle ($\cos\Theta$) distributions observed by SUPERKAMIOKANDE (from [45]). (a) electron-like sub-GeV fully-contained 1-ring events corresponding to 326 day observation (718 events). Crossed bands are those expected from no oscillation hypothesis and their widths show the statistical accuracy of the Monte-Carlo simulations. The dashed lines indicate those expected from the assumption of $\nu_\mu \to \nu_\tau$ oscillation with $\Delta m^2 = 5\times10^{-3}\ eV^2$ and $\sin^2 2\theta = 1$; (b) same as (a) for muon-like sub-GeV fully-contained 1-ring events (326 days, 735 events); (c) same as (a) for electron-like multi-GeV fully-contained events (326 days, 149 events); (d) same as (a) for muon-like multi-GeV fully-contained events (326 days, 139 events) plus partially-contained events (293 days, 156 events). (e) Multi-GeV R observed in KAMIOKANDE; (f) same as (e) for SUPERKAMIOKANDE.

Table 1.4: Comparison between measured and calculated (ν_μ/ν_e) ratio for atmospheric neutrino experiments.

Experiment	Detector mass (kt) $\times$ time of exposure (years)	$\frac{(\nu_\mu/\nu_e)_{measured}}{(\nu_\mu/\nu_e)_{predicted}}$
KAMIOKA (sub-GeV)	4.92	$0.60\ ^{+0.07}_{-0.06} \pm 0.05$
KAMIOKA (multi-GeV)	8.2	$0.57\ ^{+0.08}_{-0.07} \pm 0.07$
IMB	7.7	$0.54 \pm 0.05 \pm 0.07$
FREJUS	2.0	$1.00 \pm 0.15 \pm 0.08$
NUSEX	0.4	$0.96\ ^{+0.28}_{-0.32}$
SOUDAN 2	1.52	$0.72 \pm 0.19\ ^{+0.05}_{-0.07}$
SUPERK (sub-GeV)	20	$0.635\ \pm 0.033 \pm 0.053$
SUPERK (multi-GeV)	20	$0.604\ ^{+0.065}_{-0.058} \pm 0.067$

The average of all the experiments after adding the statistical and systematic errors in quadrature is

$$R = \frac{(\nu_\mu/\nu_e)_{measured}}{(\nu_\mu/\nu_e)_{predicted}} \approx 0.62 \pm 0.04$$

The deviation of R from unity is known as the "atmospheric neutrino anomaly". (SUPER)KAMIOKANDE and IMB see less ν_μ induced events than expected. The hypothesis that neutrino oscillations are at the origin of this effect has been significantly reinforced by the observation of the zenith angle dependence of R in KAMIOKANDE [47] and SUPERKAMIOKANDE (see Figure 1.9). The zenith angle is a direct measure of the neutrino path length and neutrino oscillations may manifest themselves as a possible distortion of the zenith angle distribution.

If interpreted as neutrino oscillations ($\nu_\mu \to \nu_e$ or $\nu_\mu \to \nu_\tau$) this result implies neutrino oscillation parameters $\Delta m^2 \sim (10^{-3} \div 10^{-2})$ and $\sin^2(2\theta) \sim 1$.

In conclusion, one can say that the solar neutrino deficit and the atmospheric neutrino anomaly are the most exciting unsolved problems both for particle physics and astrophysics.

1.5.3 Reactor Neutrino Experiments

The study of neutrino interactions at nuclear reactors is an important part of the general field of neutrino physics. Nuclear reactors are the most powerful terrestrial sources of electron antineutrinos. A reactor with a typical thermal power of $3-4\ GW$ emits approximately $6 \times 10^{20} \bar{\nu}_e\ s^{-1}$ with energies up to 10 MeV. However, due to the low-energy spectrum of these neutrinos, the only possible oscillation search is via the disappearance $\bar{\nu}_e \to \bar{\nu}_x$ experiment. Therefore the sensitivity for the mixing amplitude $\sin^2(2\theta)$ is limited by systematic errors in the source strength, the cross-section of neutrino interactions, the detector efficiency, etc.

As explained above, reactor neutrino experiments are suitable for a search for $\bar{\nu}_e \to \bar{\nu}_x$ neutrino oscillations using the disappearance technique. The most stringent constraint is provided by the Bugey [52] experiment performed at the Bugey nuclear power plant (France). High statistics measurements of neutrino spectra were carried out at 15, 40 and 95 m from a 2.8 GW reactor using detection modules filled with ^6Li-loaded liquid scintillator. The minimum excluded values of the Δm^2 and $\sin^2(2\theta)$ parameters are $1 \times 10^{-2}\ eV^2$ and 2×10^{-2} (at 90% CL) respectively (see Fig. 1.11).

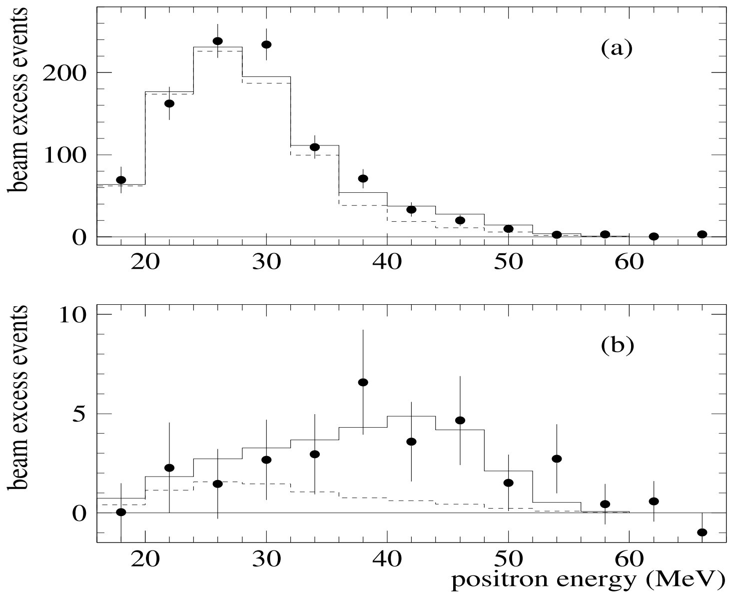

Figure 1.10: The positron energy distribution for the LSND events (a) before and (b) after selection. Shown in the figure are the beam-excess data, estimated background (dashed) and expected distribution for neutrino oscillations at large Δm^2 plus estimated background (solid).

1.5.4 Accelerator Neutrino Experiments

Accelerators produce mainly ν_μ ($\bar{\nu}_\mu$) beams from $\pi^\pm$, $K^{\pm,0}$ and $\mu^\pm$ decays. The ν_e ($\bar{\nu}_e$) component is usually small and poorly determined. Accelerator neutrino experiments use both appearance and disappearance techniques to look for neutrino oscillations.

At the moment there is only one accelerator experiment whose result could be interpreted as an evidence for neutrino oscillations - the LSND experiment [54] at Los-Alamos (USA). Neutrino production from π and μ decays at rest from the LAMPF beam stop is expected to arise almost entirely from $\pi^+ \to \mu^+\nu_\mu$ and $\mu^+ \to e^+\bar{\nu}_\mu\nu_e$. Neutrinos from π^- and μ^- are suppressed due to the smaller π^- yield and to the high capture probability in Fe and Cu of the beam stop. Thus, observation of significant $\bar{\nu}_e$ production would be a hint for new physics. The LSND detector is looking for the $\bar{\nu}_\mu \to \bar{\nu}_e$ transition. It consists of a 8.5 m long and 5.5 m in diameter cylindrical tank filled with 180 *tons* of liquid scintillator. Both Cherenkov and scintillation light can be detected with the help of PMT's. The mean source-detector distance is 29 m. The signature of a $\bar{\nu}_e$ interaction in the detector is the reaction $\bar{\nu}_e + p \to e^+ + n$ followed by $n + p \to d + \gamma(2.2\ MeV)$. This signature is therefore two-fold: a relatively high energy positron ($> 20\ MeV$) and a 2.2 MeV photon which is in time (0.5 ms) and in position (2 m) coincidence with the positron.

The largest irreducible background for the $\bar{\nu}_\mu \to \bar{\nu}_e$ oscillation search is that due

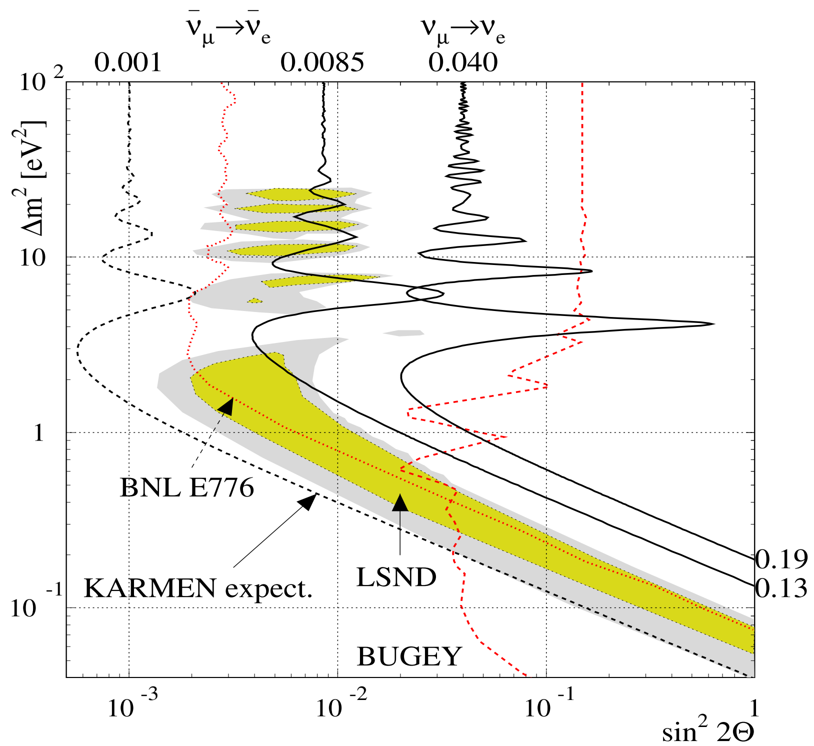

Figure 1.11: Areas of oscillation parameters allowed by the LSND result (shaded areas) and excluded by the KARMEN collaboration (solid lines). The expected sensitivity of the KARMEN experiment after the upgrade is shown together with the limits established by other experiments (BNL E776 and Bugey).

to a contamination of 8×10^{-4} $\bar{\nu}_e$ in the beam. The LSND collaboration reports a raw e^+ excess for $36 < E(MeV) < 60$ at the level of 3σ effect (see Fig. 1.10). If this excess is interpreted as neutrino oscillations, it corresponds to the oscillation probability of $P_{\bar{\nu}_\mu,\bar{\nu}_e} = (0.31 \pm 0.12 \pm 0.05)\%$.

This result was confirmed lately by studying $\nu_\mu \to \nu_e$ neutrino oscillations using ν_μ's from π^+ decays in flight [55]. The ν_e appearance is detected via the reaction $\nu_e C \to e^- X$. A total of 40 beam-on high energy electron events ($60 < E_e(MeV) < 200$) consistent with this signature was observed which is significantly above the 21.9 ± 2.1 events expected from the ν_e contamination in the beam and the beam-off background. If interpreted as an oscillation signal, the observed oscillation probability $(2.6 \pm 1.0 \pm 0.5) \times 10^{-3}$ is consistent with the previously reported result.

The KARMEN experiment [56] at the pulsed spallation neutron facility ISIS (Rutherford Appleton Laboratory, England) uses the same technique as LSND. A high resolution 56 *tons* liquid scintillator calorimeter is located 17.6 m from the proton beam stop. No positive evidence for neutrino oscillations has been observed setting the upper limit on $\sin^2(2\theta) < 8.5 \times 10^{-3}$ for $\bar{\nu}_\mu \to \bar{\nu}_e$ oscillations and $\sin^2(2\theta) < 4.0 \times 10^{-2}$ for $\nu_\mu \to \nu_e$ oscillations at 90% CL for large Δm^2 (Fig. 1.11).

This result is mainly limited by a relatively high background from cosmic rays. The KARMEN detector was upgraded recently to install additional veto counters and started to take data in this new configuration planning to cover the area of oscillation parameters favoured by the LSND collaboration after two years of running. Preliminary result obtained for $\bar{\nu}_\mu \to \bar{\nu}_e$ oscillation search using upgraded KARMEN detector is $\sin^2(2\theta) < 6.2 \times 10^{-3}$ for large Δm^2 at 90% CL [57].

Let us mention also the experiment E531 [58] carried out at the Fermilab (USA) wide band neutrino beam giving the most stringent limits for $\nu_\mu \to \nu_\tau$ oscillations so far. This experiment was devoted to the measurement of charmed particles lifetimes using a nuclear emulsion target. Due to a very good spatial resolution ($\sim \mu m$) such a detector was able to see decays of short lived particles produced in neutrino interactions. It was therefore possible to look for a possible presence of τ lepton decays produced by ν_τ via CC interactions. Drift chambers, a time of flight system, electromagnetic and hadron calorimeters were used for particle identification and measurement of their energies. Because of possible background due to scattering, a kink (single prong) in emulsion was not considered as a τ decay candidate if the secondary track had a momentum perpendicular to the parent direction (p_T) less than 125 MeV. Finally, a momentum cut at $p > 2.5\ GeV$ on the potential τ candidate was applied. The search for τ^- decay signature yielded no candidates[7] allowing to establish the following limits on the $\nu_\mu \to \nu_\tau$ ($\nu_e \to \nu_\tau$) oscillation parameters at 90% CL: $\Delta m^2 < 0.9\ (9)\ eV^2$ for maximal mixing and $\sin^2(2\theta) < 4 \times 10^{-3}$ (0.12) at $\Delta m^2 = 50\ eV^2$.

1.6 Related phenomena

There is a number of phenomena which should be present in nature if neutrinos have masses and if there is mixing in the lepton sector:

- Decay of heavy neutrinos ν_H.

  The phenomenon of neutrino decay is an inevitable consequence of the mixing of heavy neutrinos. Several experiments were looking for decays of heavy neutrinos using different detection techniques.

  For example, an interesting experiment was performed during the total eclipse of October 24, 1995 [59]. A radiative decay of solar neutrinos ($\nu_H \to \nu_i + \gamma$) emitting a photon in the visible range was searched for. No signal was found and the limit on the proper lifetime of the corresponding neutrino was established: $\tau_{\nu_H} > 97\ s$.

  If heavy neutrinos are produced in π- and K-meson decays, then their masses cannot exceed $m_{\pi,K} - m_e$. In the mass range $0 < m_{\nu_H} < m_K - m_e$ the following decay channels of heavy neutrinos are open [60]:

$$\begin{aligned}
\nu_H &\to \gamma\nu \\
\nu_H &\to \gamma\gamma\nu \\
\nu_H &\to e^+e^-\nu_e \\
\nu_H &\to \mu^+e^-\nu_\mu \\
\nu_H &\to \mu^-e^+\nu_e \\
\nu_H &\to \pi^+e^- \\
\nu_H &\to \mu^+\mu^-\nu_\mu \\
\nu_H &\to \pi^+\mu^-
\end{aligned}$$

  The production and decay of heavy neutrinos at high energy accelerators were investigated using CHARM [61], PS191 [62] and BEBC [63] detectors at CERN and in the beam-dump experiment with the IHEP-JINR Neutrino Detector [64] at Protvino. No evidence of heavy neutrino existence was found allowing to set limits on the mixing matrix elements $|U_{eH}|^2$, $|U_{eH}| \cdot |U_{\mu H}|$ (see Fig. 1.12 as an example) and $|U_{\mu H}|^2$. The best upper limits at 90% CL from accelerator experiments are $|U_{eH}|^2 \sim 10^{-7}$, $|U_{eH}| \cdot |U_{\mu H}| \sim 4 \cdot 10^{-7}$

[7] There were three surviving events before the last momentum cut.

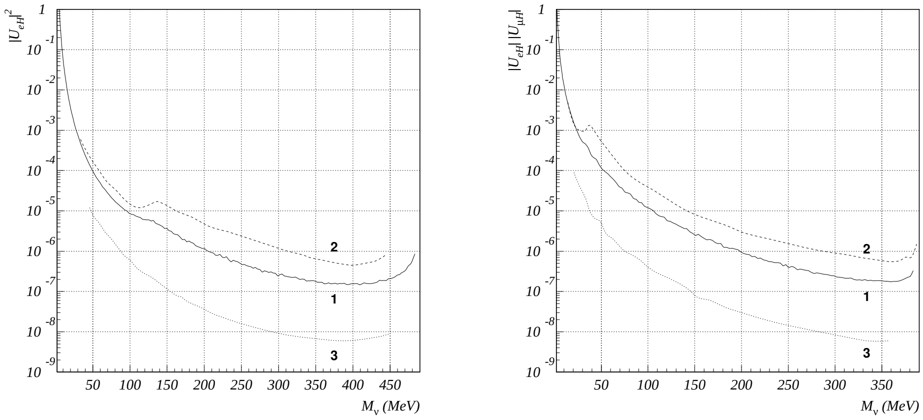

Figure 1.12: The best upper limits (at 90% CL) from accelerator experiments on the mixing matrix elements $|U_{eH}|^2$ and $|U_{eH}| \cdot |U_{\mu H}|$: (1) IHEP-JINR Neutrino Detector [64], (2) CHARM [61], (3) PS191 [62].

for $m_{\nu_H} \sim 100\ MeV$ and $|U_{eH}|^2 \sim 2 \cdot 10^{-9}$, $|U_{eH}| \cdot |U_{\mu H}| \sim 6 \cdot 10^{-9}$ for $m_{\nu_H} \sim 350\ MeV$

- Lepton number nonconserving processes, for example, muon decays: $\mu \to e\gamma$, $\mu \to 3e$.
  The hypothesis of massive neutrinos leads also to these decays which are absolutely forbidden in the framework of the standard weak interactions.

  The best current upper limits on the probabilities of these processes are $\Gamma_{\mu\to e\gamma}/\Gamma_{tot} < 4.9 \times 10^{-11}$ and $\Gamma_{\mu\to 3e}/\Gamma_{tot} < 1.0 \times 10^{-12}$ at 90% CL [9].

- Neutrinoless double β decay.
  The $0\nu - \beta\beta$ decay can occur under the following conditions:

  - the electron neutrino is a Majorana particle;
  - ν_e is massive and/or there exists a right-handed component in the weak interactions.

  Let us stress that the only feasible experiment up to now which can help in solving the problem of the distinction between Dirac and Majorana neutrinos is neutrinoless double β decay.

  The most stringent upper bound on the Majorana mass at present is provided by the Heidelberg-Moscow experiment: $m_\nu < 0.47\ eV$ at 90% CL [65].

1.7 Three neutrino approach

From the measurements at LEP of the invisible width of the Z boson (Fig. 1.13) it follows that only three flavours of neutrinos exist in nature. However, LEP data do not provide a constraint on the number of massive light neutrinos. The number of massive neutrinos depends on the neutrino mixing scheme. If the total lepton number is conserved, neutrinos are Dirac particles and the number of massive neutrinos is equal to the number of neutrino flavours. If the total lepton number is not conserved and only left-handed neutrino fields enter in the total Lagrangian (Majorana mass term), neutrinos with definite mass are Majorana particles and the number of massive neutrinos is again equal to the number of neutrino flavours. In

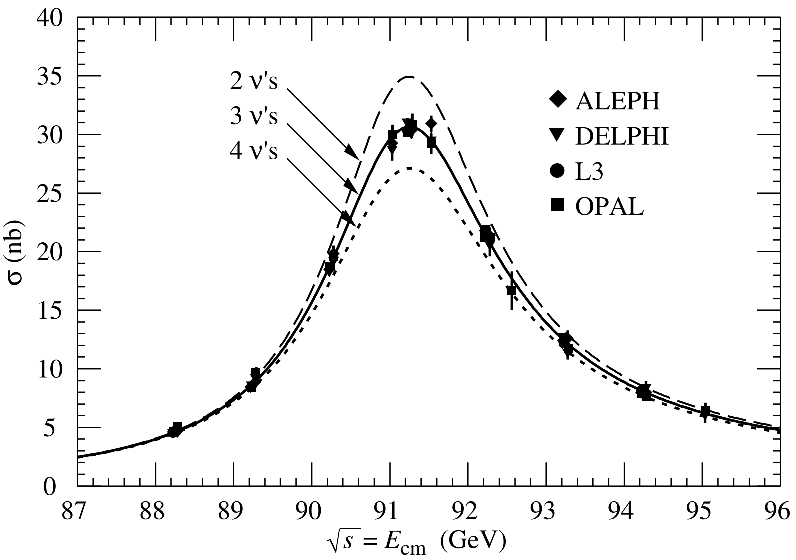

Figure 1.13: Data from the ALEPH, DELPHI, L3 and OPAL experiments at LEP (CERN) for the cross section of the e^+e^- annihilation into hadronic final states near the Z^0 peak as a function of c.m. energy. The curves show the prediction of the Standard Model in case of 2, 3 and 4 light neutrino flavours.

the most general case of neutrino mixing, left-handed and right-handed neutrino flavours enter in the mass term and the total lepton number is not conserved (Dirac and Majorana mass term). In this case massive neutrinos are Majorana particles and the number of particles with definite mass is twice the number of neutrino flavours.

It is to be stressed once again that if the number of massive neutrinos is more than three, oscillations between "active" and "sterile" neutrinos are possible.

Let us derive the oscillation equations in case of three neutrinos assuming some mass hierarchy. We choose the natural mass hierarchy ($m_1 \ll m_2 \ll m_3$). If neutrino masses are generated with the see-saw mechanism, this hierarchy is a consequence of the hierarchy of the lepton or quark masses. The squared mass difference $\Delta m^2_{21} = m_2^2 - m_1^2$ is small and can be relevant for an explanation of the deficit of solar ν_e's as suggested by the MSW solution of the solar neutrino problem. Thus for all experiments with terrestrial neutrinos we have $\Delta m^2_{21} L/2p \ll 1$, where L is the distance between the neutrino source and the detector and p is the neutrino momentum.

Under these assumptions the amplitude of $\nu_\alpha \to \nu_\beta$ transition can be written as

$$\mathcal{A}_{\nu_\alpha \to \nu_\beta} = e^{-iE_1 t} \sum_{j=1,3} U_{\beta j} U^*_{\alpha j} e^{-i(E_j - E_1)t} = e^{-iE_1 t} \left[\sum_{j=1,2} U_{\beta j} U^*_{\alpha j} + U_{\beta 3} U^*_{\alpha 3} \exp\left(-i \frac{\Delta m^2 L}{2p} \right) \right]$$

with $\Delta m^2 = \Delta m^2_{31} = m_3^2 - m_1^2$ and $E_k = \sqrt{p^2 + m_k^2} \approx p + \frac{m_k^2}{2p}$. Taking into account the unitarity of the mixing matrix

$$\sum_{j=1,2} U_{\beta j} U^*_{\alpha j} = \delta_{\alpha\beta} - U_{\beta 3} U^*_{\alpha 3}$$

we obtain for the probability of $\nu_\alpha \to \nu_\beta$ transition with $\beta \neq \alpha$

$$P_{\nu_\alpha \to \nu_\beta} = \frac{1}{2} A_{\nu_\alpha \to \nu_\beta} \left(1 - \cos\left(\frac{\Delta m^2 L}{2p}\right)\right)$$

where

$$A_{\nu_\alpha \to \nu_\beta} = A_{\nu_\beta \to \nu_\alpha} = 4|U_{\beta 3}|^2 |U_{\alpha 3}|^2$$

The expression for the probability of ν_α to survive can be derived from the conservation of the total probability

$$P_{\nu_\alpha \to \nu_\alpha} = 1 - \sum_{\beta \neq \alpha} P_{\nu_\alpha \to \nu_\beta} = 1 - \frac{1}{2} B_{\nu_\alpha \to \nu_\alpha} \left(1 - \cos\left(\frac{\Delta m^2 L}{2p}\right)\right)$$

where the oscillation amplitude $B_{\nu_\alpha \to \nu_\alpha}$ is given by

$$B_{\nu_\alpha \to \nu_\alpha} = \sum_{\beta \neq \alpha} A_{\nu_\alpha \to \nu_\beta}$$

Using the unitarity of the mixing matrix we state that

$$B_{\nu_\alpha \to \nu_\alpha} = 4|U_{\alpha 3}|^2 (1 - |U_{\alpha 3}|^2)$$

Let us emphasize that in this model

- oscillations of terrestrial neutrinos are characterized by three parameters: the mass difference squared ($\Delta m^2 = m_3^2 - m_1^2$) and the squared moduli of the two mixing matrix elements ($|U_{e3}|^2$ and $|U_{\mu 3}|^2$);
- oscillations in all channels are characterized by the same oscillation length and the amplitudes of $\nu_\alpha \to \nu_\alpha$ and $\nu_\alpha \to \nu_\beta$ transitions are related between each other;
- the probabilities of $\nu_\alpha \to \nu_\beta$ and $\bar{\nu}_\alpha \to \bar{\nu}_\beta$ oscillations are equal

  $$P_{\nu_\alpha \to \nu_\beta} = P_{\bar{\nu}_\alpha \to \bar{\nu}_\beta}$$

  This relation is a consequence of the fact that the oscillation probabilities depend only on the squared moduli of the elements of the mixing matrix. In the general case of mixing of three massive neutrinos this equation holds for $\alpha \neq \beta$ only if CP is conserved in the lepton sector. For $\alpha = \beta$ it is a consequence of CPT invariance.

1.8 Possible range of neutrino oscillation parameters

Unfortunately, the experimental situation in the field of neutrino oscillation is extremely confused (see Figure 1.14). It is difficult or almost impossible to describe all the observations by a single model in a natural way. Still, using the existing hints in favour of neutrino oscillations and theoretical issues one can try to predict the most interesting range of neutrino masses and mixing to be looked at[8].

[8] On the other hand, the situation is so confused that any additional information would be of great interest.

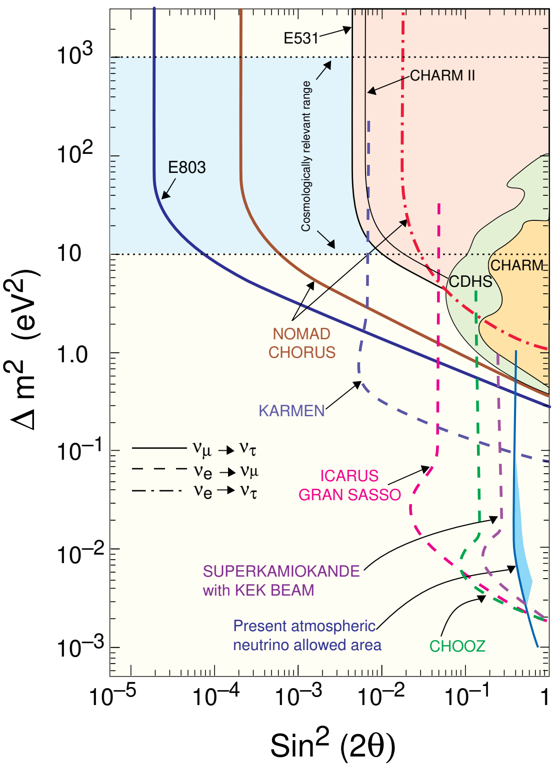

Figure 1.14: Current status of neutrino oscillation searches and expected sensitivity of future experiments.

Assuming a natural mass hierarchy and keeping in mind that the MSW solution probably implies $\Delta m_{21}^2 = m_2^2 - m_1^2 \sim m_2^2$ of the order of 10^{-5} eV^2, one can invoke the see-saw mechanism and predict the ν_τ mass to be in the range of $1 \div 50$ eV^2 which is consistent with cosmological requirements.

This region of mass is being investigated by 2 experiments currently running at the CERN SPS wide band neutrino beam: CHORUS and NOMAD.

The CHORUS (CERN Hybrid Oscillation apparatUS) experiment [66] (see Figure 1.15) is using the largest emulsion target ever built (800 kg) to search for $\nu_\mu \to \nu_\tau$ oscillations in the SPS neutrino beam.

The experiment explores the domain of $\Delta m^2 > 10$ eV^2 for mixing parameter $\sin^2(2\theta)$ down to 2×10^{-4}. The main advantage compared to the earlier E531 experiment is the usage of a nearly 10 times larger emulsion target providing a unique 3-dimensional spatial resolution of ~ 1 μm in association with a high precision scintillation tracker (Figure 1.16).

The analysis of such a large amount of emulsion has become possible with the latest developments of automatic emulsion scanning methods. The hybrid detector provides tracking capabilities around the emulsion target, muon identification and means for the measurement of secondary particles momenta, signs of their charges, total visible energy and missing transverse momentum. This is needed to localize vertices of candidate events and to give a starting point for the kink search in the emulsion for the automatic scanning microscope. The measurement of event kinematics is used for the event preselection. The current state of the analysis is reported in [67]. A subset of neutrino interactions collected during '94 and '95

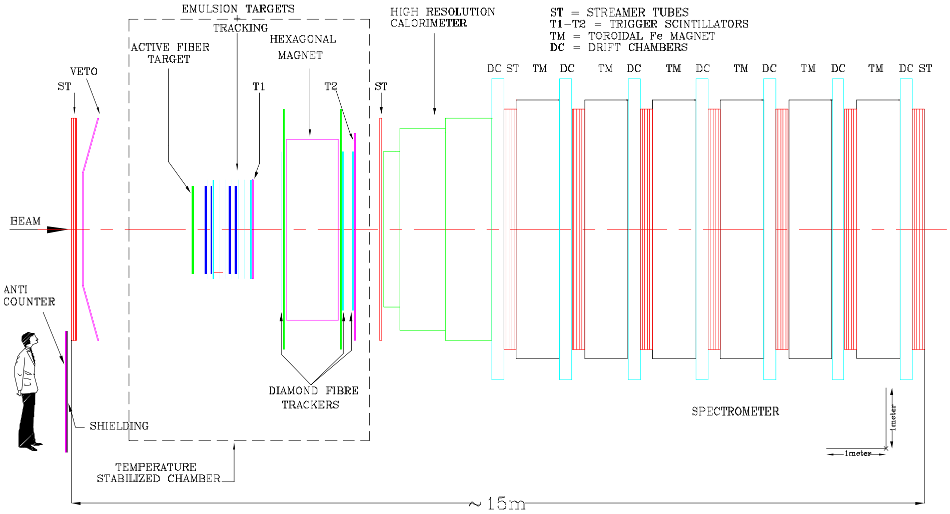

Figure 1.15: General view of the CHORUS setup.

runs has been analyzed, looking for ν_τ charged current interactions where the τ lepton decays to $\mu^- \nu_\tau \bar{\nu}_\mu$. In a sample of 31423 ν_μ charged current interactions, no ν_τ candidates were found. For large Δm^2 values, a limit on the mixing angle of $\sin^2(2\theta)_{\mu\tau} < 3.5 \times 10^{-3}$ at 90% CL can be set, thus improving the previous best result of E531 experiment.

1.9 Future experiments

Experimental neutrino physics is an active and relatively fast evolving field. A large number of neutrino oscillations experiments are running, under construction or being planned and discussed.

Present indications in favour of neutrino oscillations come from the solar neutrino experiments, the atmospheric neutrinos and the LSND result. The explanations in terms of neutrino oscillations correspond to 3 very different mass scales. It is clear that in a 3-family scheme at least one of these indications has to be either wrong or incorrectly interpreted since only 2 different mass scales should be present. To clarify the situation it is crucial to confirm these results with other experiments using, if possible, different techniques.

It has become common now to classify neutrino oscillation experiments according to their L/E_ν ratio.

1.9.1 Short baseline

An extended neutrino program will be started at Fermilab when the NuMI (Neutrino at the Main Injector) facility will be put into operation.

The COSMOS (COsmologically Significant Mass Oscillation Search) experiment (E803) [68] plans to take data for 4 years starting in 2001 and expects to reach a sensitivity of $\sin^2(2\theta_{\mu\tau}) \approx 1.4 \times 10^{-5}$ and to get down to $\Delta m^2 \approx 0.08\ eV^2$ using a detector very similar to CHORUS but with better momentum resolution ($\sim 3\%$) provided by fiber trackers.

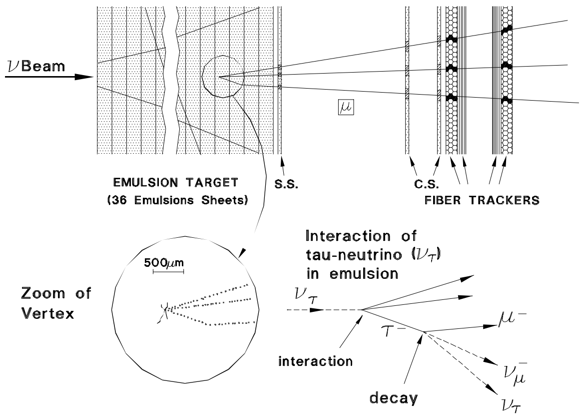

Figure 1.16: Emulsion target of the CHORUS experiment with an illustration of the concept of the τ^- decay detection technique.

A similar project at CERN (TOSCA [69]) consists in using nuclear emulsions in combination with a high acceptance spectrometer (silicon trackers and honeycomb chambers).

1.9.2 Medium baseline

In order to check the LSND indication one needs neutrino experiments with $L/E_\nu \sim 1\ km/GeV$. A unique possibility exists at CERN since the neutrino beam with average energy of $< E_{\nu_\mu} >\sim 24\ GeV$ from the SPS, after entering the Jura mountain, gets out $\sim 17\ km$ away from the source at a place where a detector could be installed [70].

1.9.3 Long baseline

The range of neutrino oscillation parameters that can explain the atmospheric neutrino problem ($\Delta m^2 \sim 10^{-2}\ eV^2$) is accessible to experiments involving human made neutrinos. One needs experiments with $L/E_\nu \geq 250\ km/GeV$.

CHOOZ (France) [71] is an experiment devoted to the search for neutrino $\bar{\nu}_e \to \bar{\nu}_x$ oscillations in the region of $\Delta m^2 \geq 10^{-3}\ eV^2$ using neutrinos produced in commercial nuclear reactors. The detector is located at a distance of 1 km from the neutrino source at a depth of 300 m of water equivalent to screen the cosmic radiation background. The detector fiducial mass is 5 $tons$ of liquid scintillator. The expected event rate in the absence of oscillations is ~ 30 events per day taking into account the detection efficiency.

The CHOOZ experiment has already reported its first results [72]. From the statistical agreement between detected and expected event rates (see Fig. 1.17), there is no evidence (at 90% CL) for neutrino oscillations in the $\bar{\nu}_e$ disappearance mode for a parameter region given by $\Delta m^2 > 0.9 \times 10^{-3}\ eV^2$ for maximum mixing and $\sin^2(2\theta) > 0.18$ for large Δm^2.

A very similar reactor experiment will be performed at Palo Verde (Arizona, USA) [73].

There are several long baseline projects involving usage of the ν_μ beams produced at accelerators.

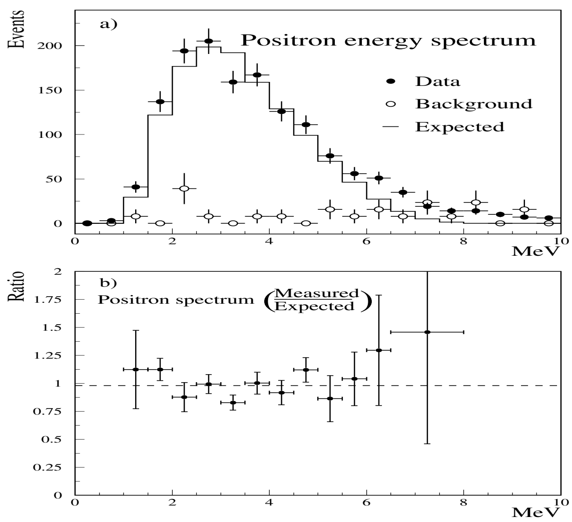

Figure 1.17: Initial results from the CHOOZ experiment.

The first experiment which is approved and financed is K2K (E362) in Japan [74]. It plans to use a neutrino beam from KEK to SUPERKAMIOKANDE ($\sim 225\ km$ away). Due to the fact that the neutrino beam energy is typically $1 \div 2\ GeV$, most of the neutrino reactions are either quasi-elastic or single-pion production, which are easily handled with a water Cherenkov detector. The signature for $\nu_\mu \rightarrow \nu_e$ oscillations will be the appearance of ν_e CC events while for $\nu_\mu \rightarrow \nu_\tau$ oscillations the disappearance of ν_μ CC events (the energy of the beam is below the τ production threshold) with respect to the expectations obtained from near ($\sim 0.6\ km$) and intermediate ($\sim 24.4\ km$) detectors. For 10^{20} p.o.t ($\sim$ 2 years of data taking) one expects $\sim$ 400 CC events in the absence of oscillations that would be reduced to 150 in the presence of $\nu_\mu \rightarrow \nu_\tau$ oscillations with $\Delta m^2 \sim 10^{-2} eV^2$ and maximal mixing. The sensitivity to the mixing parameter $\sin^2(2\theta)$ is of the order of $\sin^2(2\theta) \geq 0.4(0.2)$ for $\nu_\mu \rightarrow \nu_\tau(\nu_e)$ oscillations.

The second project uses a neutrino beam from the Fermilab main injector to be sent to a new large, specially designed detector MINOS (Main Injector Neutrino Oscillation Search) [75] located 730 km away in the Soudan mine. A near detector of similar structure will also be constructed. Due to a very high intensity of proton beam the far detector with a fiducial mass of $\sim 10\ kt$ could register $\sim 3 \times 10^4$ events/year. This experiment is sensitive to a relatively small mixing parameter $\sin^2(2\theta) \geq 0.02$ for Δm^2 above $\sim 3 \times 10^{-3}\ eV^2$.

The discussion about the possibility to construct a special beam line from CERN to the Gran Sasso laboratory ($\sim 730\ km$) and to use the ICARUS detector for the oscillation search [76] is still under way.

There are also many other proposals devoted to the neutrino oscillation searches.

1.10 Summary

The problem of neutrino mass and mixing is the central issue of today's neutrino physics. The study of this problem is associated with the search of new scales in physics. The investigation of the neutrino masses is also connected with the hopes to understand the nature of the dark matter in the Universe.

The observation of neutrino oscillations would provide positive answers to both questions about neutrino mass and mixing. Currently experimental evidences from several sources suggest (with a different degree of confidence) that neutrino oscillations may take place. The deficit of measured solar neutrino flux relative to the expectations from the standard solar models and the deficit of ν_μ's produced by cosmic ray interactions in the atmosphere find a natural (although not unique) explanation in this phenomenon. Furthermore, there is a claim by the LSND collaboration of the direct observation of $\bar{\nu}_\mu \to \bar{\nu}_e$ and $\nu_\mu \to \nu_e$ transitions.

The Standard Model limits itself to massless neutrinos while large variety of theoretical models beyond the Standard Model predict different patterns for neutrino masses and mixing parameters. For these reasons many searches for neutrino oscillations in different regions of the parameter phase space $\{\sin^2(2\theta),\ \Delta m^2\}$ are being performed and planned using natural and human-made neutrino sources.

One of such experiments - the NOMAD experiment which is presently taking data at the CERN SPS accelerator - is supposed to shed light on the possible $\nu_\mu \to \nu_\tau$ mixing for the cosmologically significant neutrino mass difference. The description of the NOMAD experiment will be given in the next chapter.

Chapter 2

The NOMAD experiment

2.1 General idea

The main goal of the NOMAD (Neutrino Oscillation MAgnetic Detector, WA-96) experiment [77] is to search for the appearance of tau neutrinos (ν_τ) in the CERN SPS wideband predominantly ν_μ neutrino beam.

The NOMAD detector [78][1] was designed to measure and identify most of the particles, charged and neutral, produced in neutrino interactions within the detector. The active target is a set of drift chambers with a fiducial mass of about 2.7 $tons$ and a low average density (98.6 kg/m^3). The detector is located in a dipole magnetic field of 0.4 T which allows the determination of the momenta of charged tracks via their curvature, with minimal degradation due to multiple scattering. The active target is followed by a transition radiation detector to tag electrons, an electromagnetic calorimeter including a preshower detector, a hadronic calorimeter and muon chambers.

In three years of running at the CERN SPS, NOMAD should collect data with more than 1 million charged current (CC) ν_μ events.

The possible presence of ν_τ in the beam is being searched for via its CC interaction: $\nu_\tau + N \to \tau^- + X$. Given the lifetime of the τ^- and the average energy of the CERN SPS neutrino beam, the τ^- travels about 1 mm before decaying. The spatial resolution of NOMAD, while good, is not sufficient to recognize such short tracks. Instead, the decays of the τ^- are identified using kinematical criteria, based on a good measurement of the missing transverse momentum in the final state ($\vec{p}_T^{\,miss}$). The presence of at least one neutrino in the final state allows the usage of momentum balance in the plane perpendicular to the beam direction to select ν_τ CC candidates from copious $\overset{(-)}{\nu}_{e,\mu}$ CC and NC background [79]. By studying correlations between the sizes and directions of three vectors in the transverse plane ($\vec{p}_T^{\,miss}$, $\vec{p}_T^{\,lep}$ and $\vec{p}_T^{\,had}$) we can distinguish events containing τ^- decays from different sources of background assuming that the event kinematics is well reconstructed. Let us consider the $\tau^- \to e^-\nu_\tau\bar{\nu}_e$ decay channel as an example (see Fig. 2.1). Since we have two escaping neutrinos in the final state, we expect the missing $\vec{p}_T^{\,miss}$ vector to point roughly in the same direction as the primary electron candidate ($\vec{p}_T^{\,e}$) and their sum to be opposite to the hadronic vector direction ($\vec{p}_T^{\,had}$) in the transverse plane. While the background from ν_e CC interactions behave differently. First of all, if we are able to reconstruct correctly the event kinematics, $\vec{p}_T^{\,miss}$ vector should be small and randomly distributed in the transverse plane, while the $\vec{p}_T^{\,e}$ vector is expected to be back-to-back with the hadronic vector $\vec{p}_T^{\,had}$. In order to fight against background originating from NC events one can use an isolation cut

[1]The publication was extensively used for the preparation of this chapter.

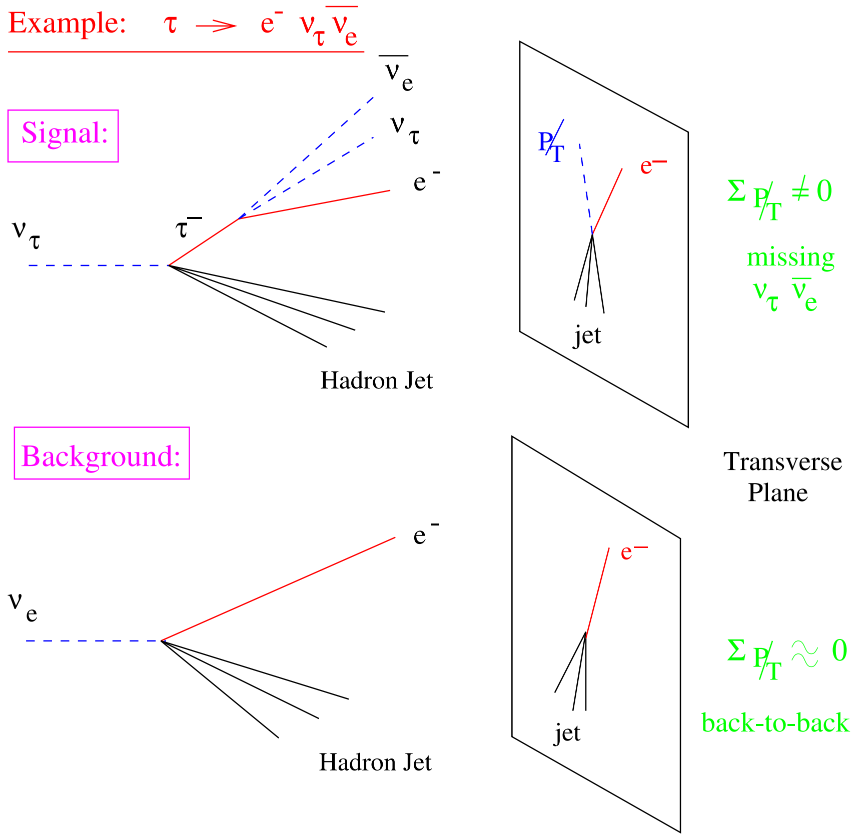

Figure 2.1: Comparison of the event kinematics for ν_τ CC event followed by $\tau^- \to e^-\nu_\tau\bar{\nu}_e$ decay and ν_e CC event.

requiring that the primary electron candidate should be well separated from the rest of the hadrons.

The background contamination from ν_τ in the original beam was estimated to be well below the sensitivity of the experiment.

This technique is a complementary approach to the one adopted by the CHORUS collaboration [66] which is based on the detection of the kink from τ^- decays in nuclear emulsion (where this kink can be actually seen).

In order to be sensitive to a large fraction of the τ^- decay modes and to be able to select events with high efficiency and low backgrounds, the NOMAD detector must satisfy the following requirements:

- be as hermetic as possible to provide a good measurement of event kinematics;
- measure the momenta of charged particles in the drift chamber target with good precision;
- identify and measure muons, electrons and photons with high efficiency and good purity.

As will be discussed below the NOMAD detector has achieved these goals. It is able to search for τ^- decays into two leptonic channels: $e^-\nu_\tau\bar{\nu}_e$, $\mu^-\nu_\tau\bar{\nu}_\mu$ and into three hadronic ones: $\pi^-\nu_\tau$, $\rho^-\nu_\tau$ and $\pi^-\pi^-\pi^+ n\pi^0\nu_\tau$, i.e. about 86% of the τ decays:

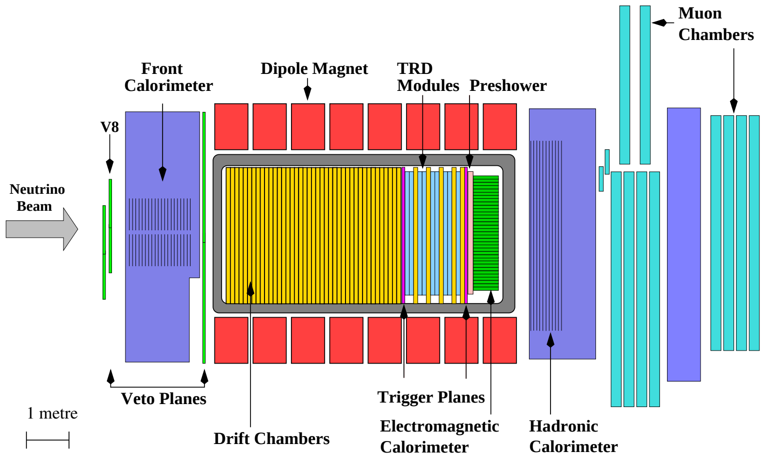

Figure 2.2: A sideview of the NOMAD detector

Decay Mode	Branching Ratio
$\tau^- \to e^- \nu_\tau \bar{\nu}_e$	17.8%
$\tau^- \to \mu^- \nu_\tau \bar{\nu}_\mu$	17.4%
$\tau^- \to \pi^- \nu_\tau$	12%
$\tau^- \to \rho^- \nu_\tau$	25%
$\tau^- \to \pi^- \pi^- \pi^+ n\pi^0 \nu_\tau$	14%
Total	$\sim$ 86%

The advantage of using both leptonic and hadronic decay channels of the τ^- consists in the possibility to perform a cross-check since the background conditions for these decay modes are crucially different.

As can be computed from the average energy of the neutrino beam and the distance between the neutrino production point and the position of the NOMAD detector, the experiment is especially sensitive to the cosmologically interesting ν_τ mass range: $\Delta m^2 \sim 10 \div 100\ eV^2$.

In addition to searching for neutrino oscillations, the large sample of data in a detector with a target density of a hydrogen bubble chamber permits NOMAD to explore many other processes involving neutrinos.

Let us describe the CERN SPS neutrino beam, the NOMAD subdetectors and their performances.

2.2 The Detector and Beam

The NOMAD detector is shown schematically in Figure 2.2 (sideview) and Figure 2.3 (topview). It consists of a number of subdetectors most of which are located in a dipole magnet with a field volume of $7.5 \times 3.5 \times 3.5\ m^3$. The magnetic field is horizontal, perpendicular to the neutrino beam direction, and has the value of $0.4\ T$.

Refering to Figure 2.2, one can define the coordinate system adopted for NOMAD: it has the X-axis into the plane of that figure, the Y-axis directed up towards the top of the detector and the Z-axis horizontal, approximately along the direction

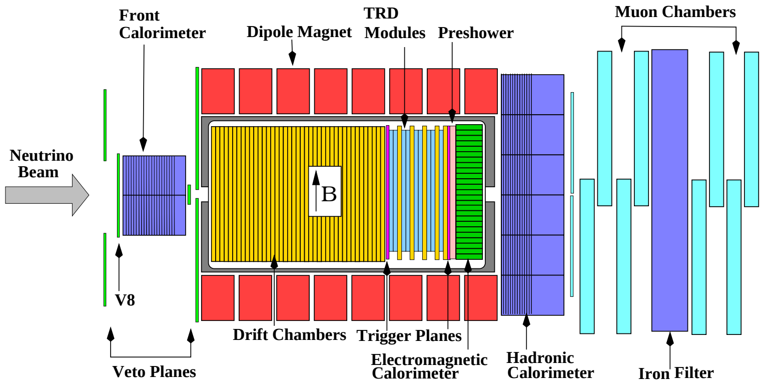

Figure 2.3: A topview of the NOMAD detector

of the neutrino beam. One should keep in mind that the neutrino beam is inclined by 42.5278 $mrad$ (or $2^o 26' 12''$) in the YZ-plane with respect to the chosen Z-axis. The system of coordinates with Z-axis along the neutrino beam direction is used for the analysis.

2.2.1 The Neutrino Beam

The NOMAD detector is located at the CERN West Area Neutrino Facility (WANF) and is exposed to the SPS wide band neutrino beam which consists predominantly of ν_μ. The beam line has been re-optimized for the NOMAD and CHORUS experiments. Figure 2.4 shows a schematic layout of the WANF beam line.

The neutrinos are primarily produced from the decays in flight of the secondary π and K mesons originating from 450 GeV protons impinging on a beryllium target (made of 11 rods 10 cm long and 3 mm in diameter each separated by 9 cm gaps). The secondary pions and kaons are focused by a pair of coaxial magnetic lenses - the horn and reflector. These secondary hadrons are allowed to decay in a 290 m long vacuum tunnel. Shielding made of iron and earth follows to range out the muons and absorb the hadrons.

The NOMAD (CHORUS) detectors are located at about 835 m (823 m) from the target. The average distance between the meson decay point and the NOMAD setup is 620 m.

The SPS cycle repeats every 14.4 s. The protons are extracted from the SPS in two 4 ms long spills (fast/slow extraction) separated by a 2.6 s ‘flat top’. The proton beam has a Gaussian shape with $\sigma \approx 0.5$ mm at the target. This new beam line has been operating now for more than three years with record intensities up to 1.5×10^{13} protons in each of the two spills.

Figure 2.5 shows the predicted neutrino energy spectra which were obtained from a detailed GEANT [80] simulation of the beam line at the position of the NOMAD detector and for a fiducial area of 2.6×2.6 m^2. The fluxes are given per 10^9 protons hitting the target (p.o.t.).

The parameters of the various neutrino components are summarized in the Table 2.1. The neutrino beam simulation is affected by uncertainties due mostly to the limited knowledge of the π and K yields from the hadronic interactions in the beryllium target. The measurement by the SPY collaboration [81] of the production rates of π and K mesons and their ratio from 450 GeV protons hitting a beryllium target will reduce these uncertainties in the neutrino flux.

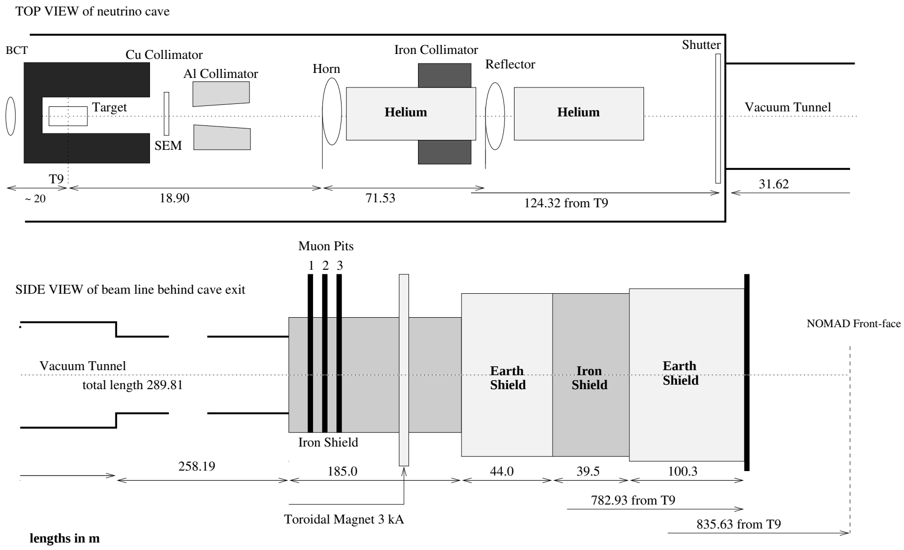

Figure 2.4: Schematic layout of the WANF beam line pointing out its main elements. Not drawn to scale.

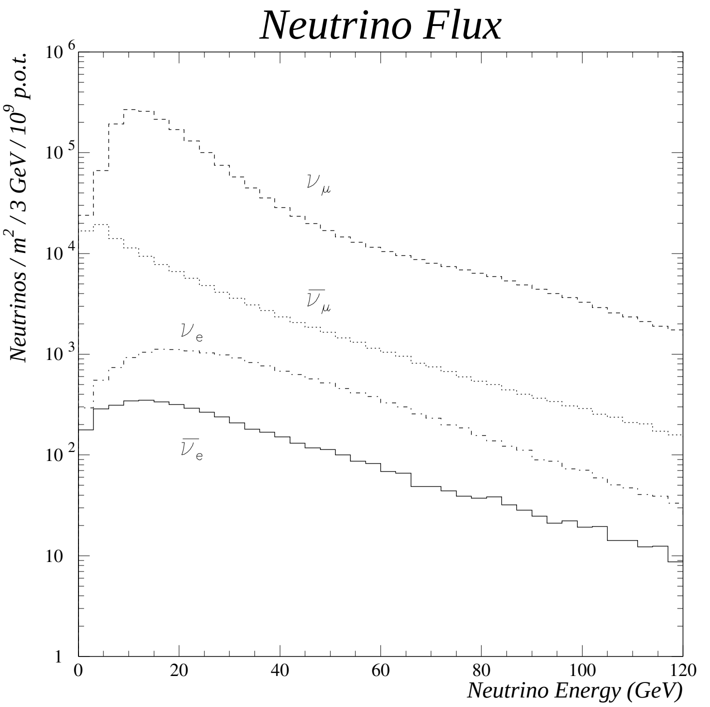

Figure 2.5: The predicted energy spectra of neutrinos at NOMAD.

Table 2.1: Monte-Carlo predictions for the average neutrino energy, relative beam composition and expected number of CC interactions in NOMAD in a fiducial area of 2.6 $\times$ 2.6 m^2 (for 2.4×10^{19} p.o.t.)

	Average E_ν (GeV)	Relative Abundance	Number of ν CC interactions
ν_μ	23.6	1.000	1.15×10^6
$\overline{\nu}_\mu$	22.7	0.07	0.39×10^5
$\nu_{\rm e}$	37.0	0.01	0.17×10^5
$\overline{\nu}_{\rm e}$	33.2	0.003	0.22×10^4

The intrinsic ν_τ component in the beam, from the prompt reaction:

$$p \ + \ N \ \rightarrow \ D_s^\pm \ + \ X, \ D_s^\pm \ \rightarrow \ \tau^\pm \ + \ \overset{(-)}{\nu}_\tau$$

followed by $\tau^\pm \ \rightarrow \ \overset{(-)}{\nu}_\tau \ + \ X$ has been calculated to be negligible [82, 83]. The relative number of ν_τ produced from the above reaction chain and interacting via CC in the fiducial volume of NOMAD has been estimated to be $\sim 5 \ \times \ 10^{-6}$ the number of ν_μ CC events. After selection criteria, the resulting intrinsic ν_τ signal is much less than 1 observed event in the total duration of the NOMAD experiment.

2.3 The NOMAD subdetectors

Let us describe the NOMAD subdetectors in more details. We will follow the neutrino beam direction.

2.3.1 Veto Counters

The veto system consists of an arrangement of 59 scintillation counters covering an area of 5×5 m^2 at the upstream end of the NOMAD detector. The scintillators have a thickness of 2 cm, width 21 cm, and are of two lengths, 300 cm and 210 cm. Most (56) of the counters are viewed at both ends by photomultipliers; the remaining (3) counters have single–ended readout. The counters are arranged in a geometry which provides optimal rejection of charged particles produced upstream of NOMAD, of those produced in neutrino interactions in the iron detector support and of large angle cosmic rays travelling in the same and in the opposite direction to the neutrino beam. A small fraction of interactions in the central region of the iron cannot be excluded, as the support frame for the steel structure (the 'basket') in which the central detector is mounted passes through the space in which scintillators would ideally be placed. Similarly, interactions in the upstream part of the magnet coil are not vetoed, but can be distinguished from target interactions by reconstruction of the event vertex.

The charged particle rejection efficiency of the NOMAD veto is constantly monitored and has remained stable at a level of 96-97%.

2.3.2 Forward Calorimeter

The NOMAD detector is suspended from iron pillars (the 'I's) at the two ends of the magnet. The front pillar was instrumented with scintillators to provide an additional massive active target for neutrino interactions. Physics topics to

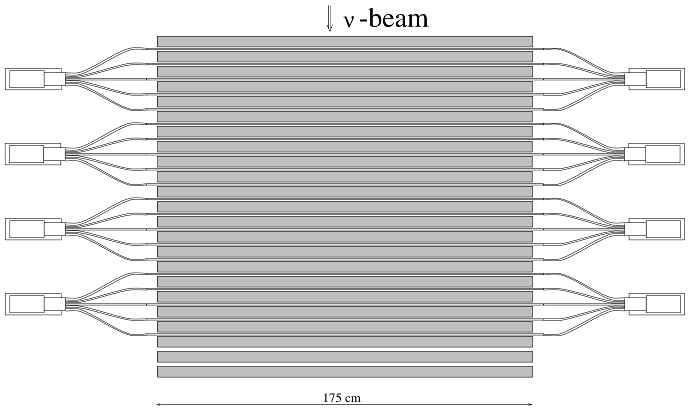

Figure 2.6: Top view of the FCAL

be addressed by this forward calorimeter (FCAL) include multi-muon physics and searches for neutral heavy objects produced in neutrino interactions.

The FCAL consists of 23 iron plates which are 4.9 cm thick and separated by 1.8 cm gaps. Twenty out of the 22 gaps are instrumented with long scintillators which are read out on both ends by 3 inch photomultipliers. The dimensions of the scintillators are 175 $cm \times 18.5$ $cm \times 0.6$ cm. To achieve an optimal light collection and a reasonable number of electronic channels five scintillators along the beam axis are ganged together by means of twisted light guides and form a module. Ten of such modules are placed above each other and form a stack. Along the beam axis are four such stacks. The area of the FCAL 'seen' by the neutrino beam is 175 $cm \times 190$ cm (see Figure 2.6). The detector has a depth of about 5 nuclear interaction lengths and a total mass of about 17.7 $tons$.

For neutrino interactions in the first stack of the FCAL, the equivalent hadronic energy of a mip (minimum-ionizing particle) has been determined to be 430 MeV.

2.3.3 Drift Chambers

The drift chambers, which provide at the same time the target for neutrino interactions and the tracking device, are a crucial part of the NOMAD detector. They were designed with the conflicting requirements that their walls should be as heavy as possible in order to have a significant number of neutrino interactions and as light as possible in order to minimize the effects of multiple scattering, secondary particle interactions, photon conversions and bremsstrahlung for electrons. To keep the total number of radiation lengths as small as possible for a given target mass, the chambers are made of low density and low atomic number materials: there is less than 1% of a radiation length between 2 consecutive measurement planes.

The chambers (figure 2.7) are built on panels made of Aramid fibres in a honeycomb structure. These panels are sandwiched between two Kevlar-epoxy resin skins. These skins give the mechanical rigidity and flatness necessary over the large (3×3 m^2) surface area. Each drift chamber consists of four panels. The three 8-mm gaps between the panels are filled with an argon - ethane (40% - 60%) mixture at atmospheric pressure. Because the panels are not completely gas tight, the gas is circulating permanently in a closed circuit with a purifier section that removes oxygen and water vapour.

The three gaps are equipped with sense wires making angles of +5, 0 and -5 degrees with respect to the magnetic field direction. Potential wires, made of

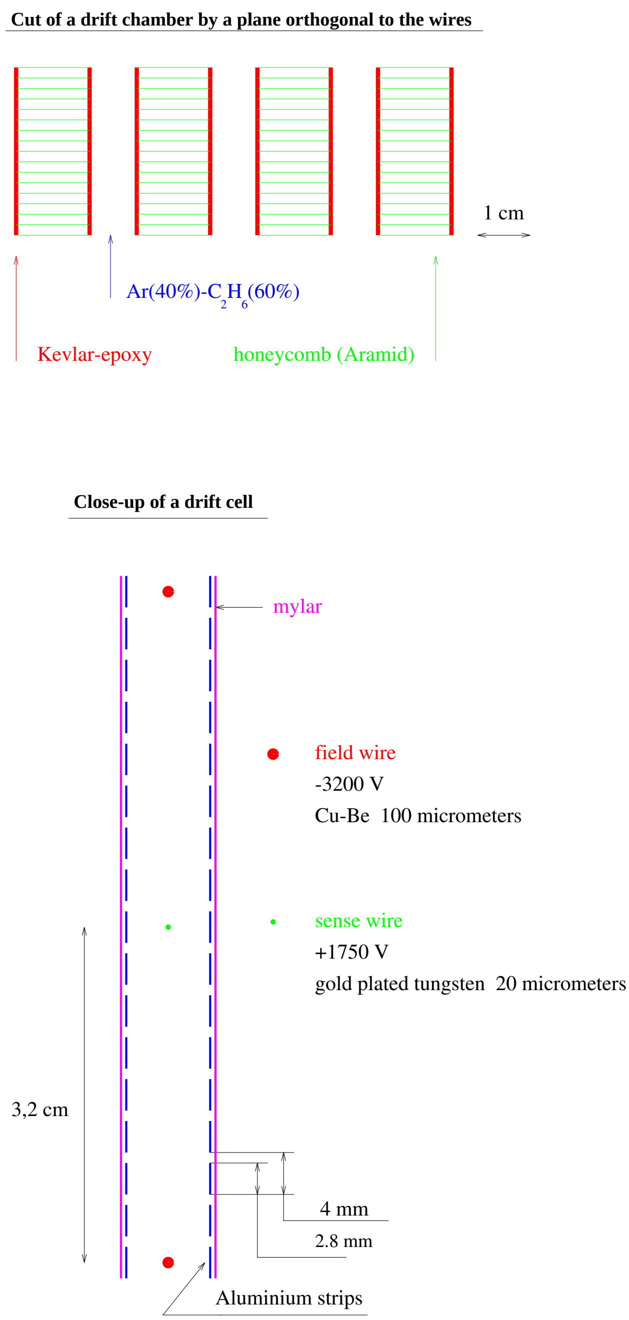

Figure 2.7: An overview of the drift chamber layout

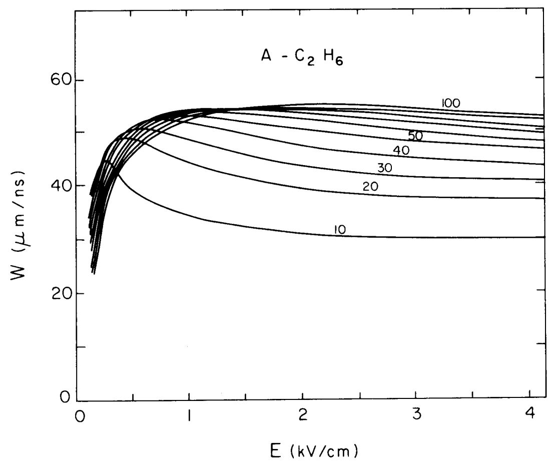

Figure 2.8: Drift velocity as a function of the electric field and the argon - ethane gas mixture at atmospheric pressure. Different curves correspond to different percentage of ethane in the gas mixture.

$Cu - Be$ with a diameter of 100 μm, are interleaved with the sense wires, made of gold-plated tungsten with a diameter of 20 μm. These wires are equally spaced vertically to provide drift cells of ± 3.2 cm around each sense wire. The chambers are placed inside the magnet, field shaping aluminium strips (2.8 mm wide, 12 μm thick, separated by 1.2 mm) are printed on mylar and are glued to the panels. The 3 m long wires are glued to support rods at 3 places to keep the anode–cathode gap constant at 4 mm and decrease the electrostatic and gravitational displacements of these wires. The gap is maintained at 8 mm using 9 spacers. The potentials on the strips provide a drift field of 1 kV/cm. With this electric field and the gas mixture, the ionization electrons drift with a velocity of about 50 $\mu m/ns$ (Fig. 2.8). In order to compensate for the Lorentz angle and to keep the drift direction parallel to the planes when the magnetic field is turned on, the potentials on the strips are set at different values on the two sides of each gap.

As can be seen from the Fig. 2.9, non linearities occur at both ends of the drift cell which has a width of 3.2 cm in the NOMAD drift chambers:

- Close to the anode wire the field is central and not constant. This extends to several mm. Primary ionization fluctuations indicate that for a track within $\pm$ 300 μm from the anode wire, the time is independent from the drift distance;

- The drift cell is closed by a potential wire which is at the same voltage as the facing strip. The electric field then vanishes close to the end of the cell.

The transverse dimension of the chambers is approximately $3 \times 3\, m^2$ and they fill completely the available space inside the magnet coil. The total number of chambers in the complete detector is 49 corresponding to 147 sense wire planes and a total of 6500 wires. The target chambers are combined in 11 modules of four chambers each in the front part of the detector. Five additional chambers are installed individually in the TRD region to provide a precise information about track extrapolations to the TRD planes, preshower (PRS) and electromagnetic calorimeter (ECAL).

Each chamber contributes 0.02 radiation length. The fiducial mass of the chambers totals 2.7 $tons$ over an area of $2.6 \times 2.6\, m^2$. As shown in [84] the NOMAD target is close to be isoscalar ($N_{protons} : N_{neutrons} = 52.4\% : 47.6\%$).

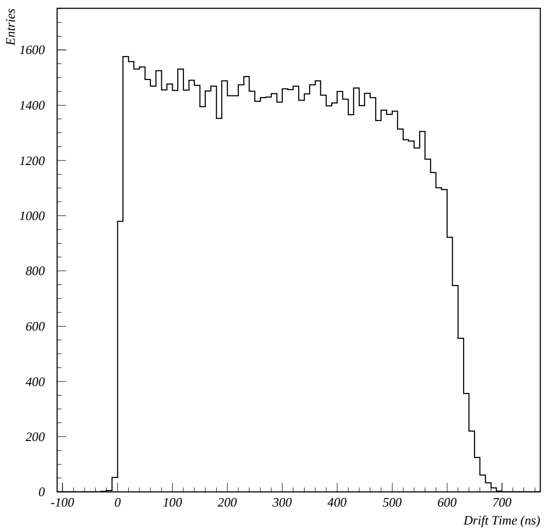

Figure 2.9: Raw drift time distribution.

The chambers are operated at a voltage 100 V above the beginning of the plateau, which was found 200 V wide. Under these conditions, the typical wire efficiency is 0.97, most of the loss being due to the supporting rods. Wire signals are fed to a preamplifier and a fast discriminator, allowing track separation down to 1 mm. Discriminator output signals are sent to Lecroy 1876 TDC's with a bin width of 1 ns. These TDC's measure a time difference with a common stop technique:

$$\Delta t = t_{stop} - t_{start},$$

where

$$t_{start} = t_{interaction} + \Delta t_{tof} + \Delta t_{drift} + \Delta t_{wire} + \Delta t_{elect}$$

which takes into account the interaction time ($t_{interaction}$), the time of flight of the measured particle between the interaction point and the measured plane (Δt_{tof}), the drift time of electrons (Δt_{drift}), the signal propagation along the sense wire (Δt_{wire}) and the signal propagation in the electronic circuits (Δt_{elect}).

$$t_{stop} = t_{interaction} + \Delta t_{tof\_trig} + \Delta t_{delay}$$

consists of the time of flight of the triggering particle (Δt_{tof_trig}) and a delay (Δt_{delay}) long enough that the stop signal arrives after all start signals. Finally, the time measured by the TDC is

$$\Delta t = (\Delta t_{tof\_trig} + \Delta t_{delay}) - (\Delta t_{tof} + \Delta t_{drift} + \Delta t_{wire} + \Delta t_{elect})$$

This time can be corrected for the Δt_{elect} and Δt_{wire} (if the x coordinate of the hit along the wire is known), so that the true drift time is extracted.

To provide the information about the relative (with respect to a corresponding wire) coordinate of a particle, the drift time should be converted into the distance with the help of the so-called time-to-distance relation[2].

[2]The actual hit position is computed taking into account the wire position and shape.

The generalized coordinate c is obtained from the coordinate c_w of the wire and from the drift distance d, which is a function of both the drift time Δt_{drift} and the local angle ϕ between the direction of the track projected onto the wire plane and the direction of the drift velocity. The drift distance is either added to or subtracted from c_w. This is known as the up-down ambiguity:

$$c = c_w \pm d(\Delta t_{drift}, \phi)$$

Unfortunately, this ambiguity should be resolved at the level of track construction and fit.

A special alignment procedure [85] was set up to measure wire positions and shapes, the time-to-distance relationship and other relevant quantities using muons crossing the NOMAD detector.

In the drift chamber system, the position of a track is derived from a drift time measurement and a wire position. The alignment process consists in determining as best as one can all the quantities that enter in this conversion:

- the wire positions and shapes;
- the time to distance relationship and its dependence on the angle of the track in the drift cell;
- the systematic offsets that affect the drift times measured by means of TDC's.

In the NOMAD drift chamber system, the delay introduced by electronics and cables (Δt_{elect}) can in principle be measured by a pulser system. This pulser is made of a gate generator that is fanned to all the chamber planes and then distributed to the wires via a strip that runs on the chamber side and excites capacitively the wires. This system has also been used to check that the equipment functions correctly. With about 1000 pulses, an average of the arrival time of the pulse in the TDC's can be computed, and misfunctionning channels can be identified.

The velocity of the signal propagation along the wire was measured from the data and was found to be 26 cm/ns. This knowledge allows to correct for the time of the signal propagation along the wire Δt_{wire}, if the x coordinate of the hit is known.

Due to the fact that drift chamber planes can work under different gas[3] and high voltage conditions, it was decided to determine the time-to-distance relation for each plane independently. One should keep in mind that the precise determination of the drift velocity[4] is important because a mistake of the order of one percent could lead to a bias in the spatial resolution of the order of several hundred microns ($d_{max} \cdot \frac{\Delta v}{v} = 3.2cm \cdot 0.01 \approx 300\mu m$).

Global alignment uses reconstructed track residuals, i.e. track-to-hit (signed) distance and tries to minimize any systematic offset (see [86] for details). The proposed procedure analyzes the residuals of reconstructed tracks and computes systematic shifts of averages of these residuals. Then, the corresponding parameters are updated and the reconstruction rerun. This process is iterated several times (typical value is 15) until it stabilizes.

The DC track reconstruction is governed by a large number of parameters among which 2 directly impact on the track to hit residuals: the road width for a track search and the allowed χ^2 increment when adding a point during a track expansion. These parameters could vary at different steps of the alignment procedure requiring several iterations.

[3] Due to different nitrogen contamination caused by different leak rates.

[4] No dependence of drift velocity on the presence of the magnetic field (after applying the compensating voltage on strips) was found in our data.

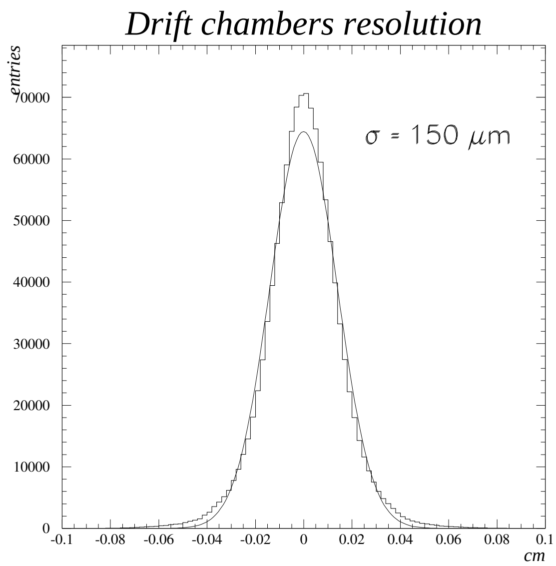

Figure 2.10: Residuals for a sample of straight tracks in the drift chambers.

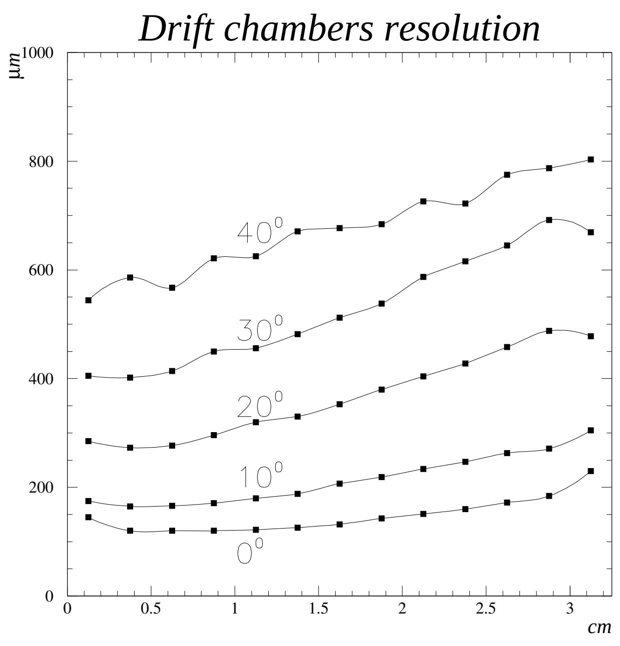

Figure 2.11: The dependence of the track residuals on the drift distance and the polar angle.

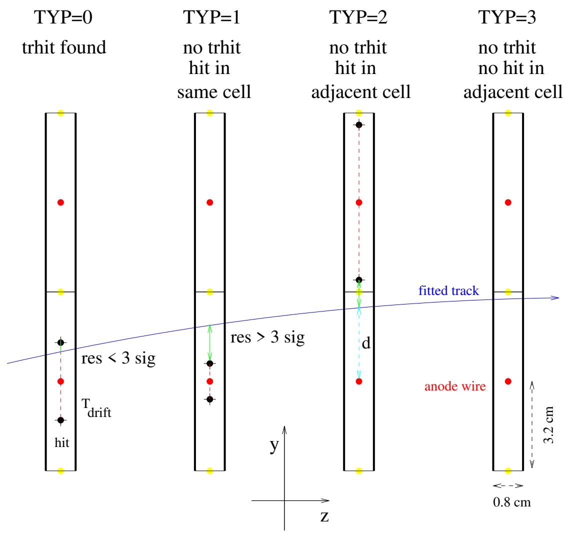

Figure 2.12: The definitions which are used for the drift chamber efficiency studies. See text for details.

The distribution of residuals which has been obtained after careful alignment of all wires (fitted in several segments along the wires to take mechanical defects and electrostatic effects into account) as well as a detailed description of the time-to-distance relation is shown in Figure 2.10. This distribution has a sigma of about 150 microns and confirms the good spatial resolution of the NOMAD drift chambers. The dependence of the resolution on the drift distance and the polar angle is shown in Figure 2.11.

The drift chamber efficiency and its dependence on the track angle and track position in the drift cell was carefully studied using muons crossing the detector between two neutrino spills [87]. All the drift chamber planes touched by the reconstructed track were considered. In each plane we have defined the drift cell crossed by the track and events were classified into 4 categories. The definitions which were used are illustrated in the Fig. 2.12. The event of the first class (TYP=0) occurs when there is a hit in the crossed cell and this hit lies within 3σ (where σ is a combination of the drift chamber resolution and of the contribution due to the effect of multiple scattering) from the predicted track position in this measurement plane. The second class (TYP=1) contains events in which there is a hit in the crossed cell but it was not included in the track since it lies more than 3σ away from the predicted track position. The third class (TYP=2) contains events in which there is no hit in the crossed cell but there exists a hit in the adjacent cell or there is a hit in the adjacent cell which is closer to the predicted track position than another hit in the crossed cell. Finally, the last class (TYP=3) contains events with no hits in both crossed and adjacent cells.

With the help of this classification we can define minimal and maximal efficiencies:

$$\varepsilon_{min} = \frac{\text{events with TYP=0}}{\text{all events}}$$

$$\varepsilon_{max} = \frac{\text{events with TYP=0,1,2}}{\text{all events}}$$

The inefficiency (1-ε_{min}) was calculated as a function of the x-coordinate (along the wire). The results are given in the Fig. 2.13. This distribution can be well fitted by a constant ($\approx 2.4\%$) and three Gaussians with a width of $\approx 6\ mm$ centered at the supporting rod's positions. As a result we can state that the efficiency in the region between wire supporting rods is $\varepsilon_{min} \approx 97.6\%$ which is consistent with our expectations and we confirm that the inefficiency is caused mainly by the presence of the rods.

Further studies show that the major loss of efficiency is not due to the absence of the hit in a measurement plane but due to non-Gaussian tails in the residual distributions. If one extends the road for the hit collection during the track reconstruction a maximal drift chamber efficiency up to $\varepsilon_{max} \approx 99.7\%$ can be obtained.

One can also study the regions of inefficiency along the drift cell (Fig. 2.14) to make sure that we understand correctly the behavior of the drift electrons. The only unrecoverable loss of efficiency corresponds to the (type=3) events. It varies from $\approx 0.1\%$ at the beginning of the cell to $\approx 1\%$ at the end. One can see also that the efficiency loss in the first bin for the (type=0) events can be compensated by adding the events of the (type=1) class. This fact can be explained by the presence of large non-Gaussian tails in the residual distribution especially in the region close to the wire. As expected, (type=2) events occur if the track passes at the edge of the drift cell.

Unfortunately, there are other hardware effects which could cause efficiency losses: planes with short circuits between strips, disconnected field wires, misalignment of a wire with respect to the facing layer of strips. These effects have also been studied and the following conclusion can be drawn (see Fig. 2.15):
- planes with short circuits between strips: efficiency loss $\approx 42\%$,
- disconnected field wires: efficiency loss $\approx 12\%$,
- misaligned strip layers: efficiency loss $\approx 10 \div 15\%$.

To have an idea about the hardware performance of the NOMAD drift chambers we present here an overall situation during the '96 run data taking period: among 147 planes in total 1 or 2 planes were switched off due to unrecoverable problems (such as a broken wire), 2 or 3 planes suffered from short circuits between strips and 3 planes had field wires disconnected.

A potential problem was present in the drift chamber response which is related to the presence of afterpulses (or bounces): some of the hits can be accompanied by one or several other hits on the same wire [88]. If we plot the time difference between the hit included in a given track and the other hit on the same wire we see the following distribution (Fig. 2.16,left). One can observe two contributions: the first one is symmetric in time and the second one is concentrated at $\sim 50\ ns$ after the first digitization. The former contribution was attributed to the emission of low-energy δ-rays which produce random hits in the drift cell crossed by the track, while the latter contribution was associated with the smearing of the electron cloud consisting of several clusters which could trigger another digitization after the arrival of the first electron.

Having subtracted the symmetric part caused by δ-rays we obtain the following distribution (Fig. 2.16,right). The additional difficulty is related to the fact that the rate of the afterpulses depends on the track angle and track position in the drift cell. This study allowed to include the effect of afterpulses in the simulation program.

The knowledge gained by the studies of resolution, efficiency and the presence of afterpulses is used during the reconstruction in the drift chambers. The dependence of the resolution on the drift distance and track angle was parametrized and implemented at the level of track search and fit. A special bounce filter was developed to cope with the presence of afterpulses for the hit selection.

The momentum resolution provided by the drift chambers is a function of momentum and track length. For charged hadrons and muons traveling normal to the

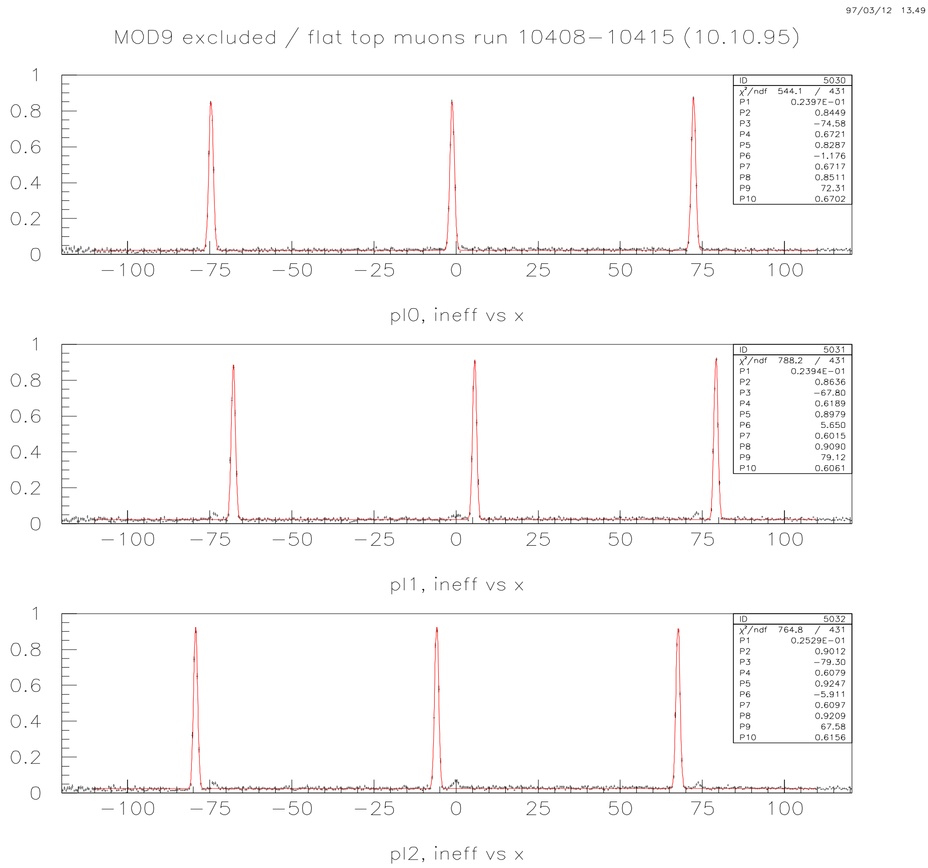

Figure 2.13: The inefficiency (1-ε_{min}) as a function of the x-coordinate (along the wire). Peaks correspond to the wire supporting rods. This distribution can be well fitted by a constant ($\approx$ 2.4%) and three Gaussians with a width of ≈ 6 mm cented at the rod's positions. The small bumps in the second (pl1) and third (pl2) planes are due to the spacers used as chamber supports.

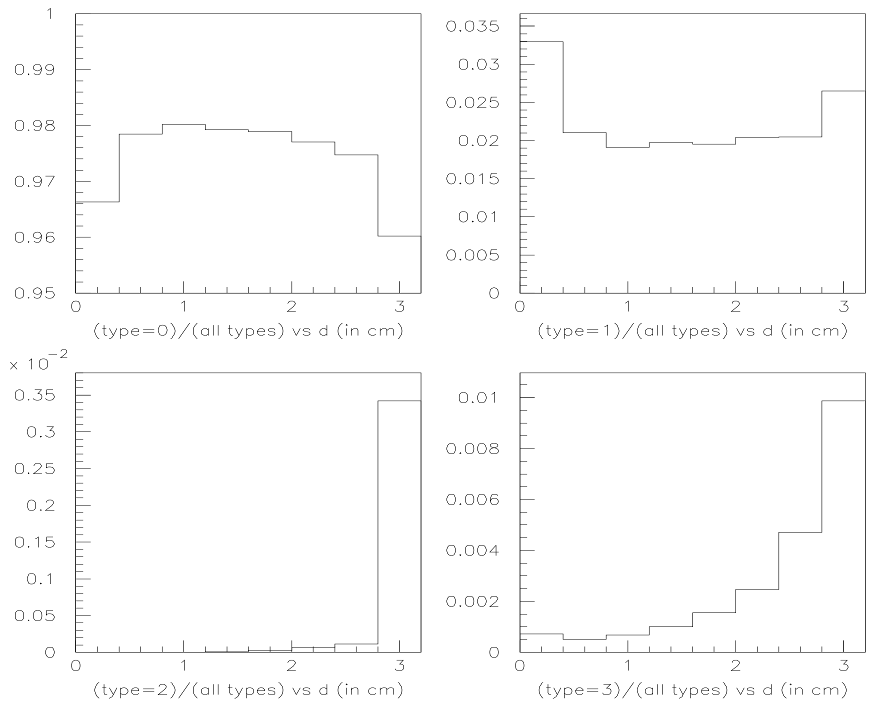

Figure 2.14: The dependence of efficiency on the track position in the drift cell. Inefficiency regions are at the edges of the drift cell as expected.

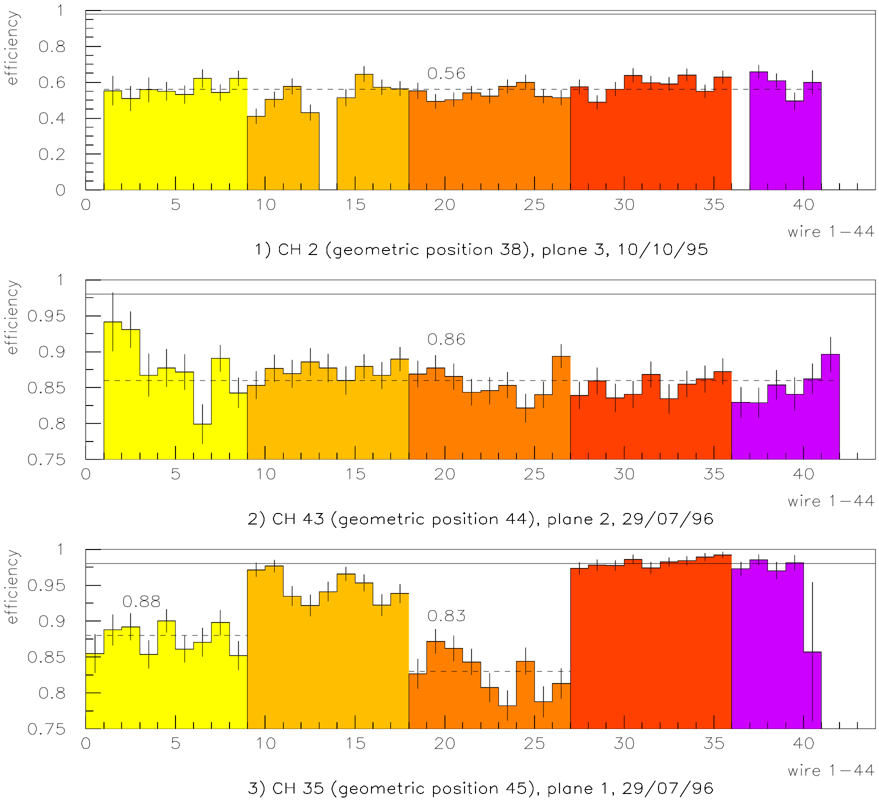

Figure 2.15: Examples of hardware efficiency losses in the drift chamber planes. The horizontal solid line shows $\varepsilon = 0.98$ level for normal chambers. The different shaded areas indicate different layers of cathode strips. We can state that for
(1) planes with short circuits between strips: efficiency loss $\approx 42\%$;
(2) disconnected field wires: efficiency loss $\approx 12\%$;
(3) misaligned strip layers: efficiency loss $\approx 10 \div 15\%$.

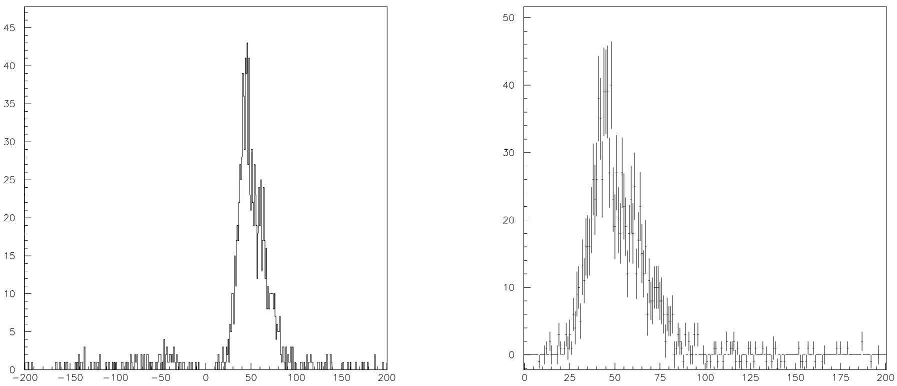

Figure 2.16: Example of the time difference (in ns) between the other hit on the same wire and the hit included in a given track before (left) and after (right) the subtraction of symmetric δ-rays contribution.

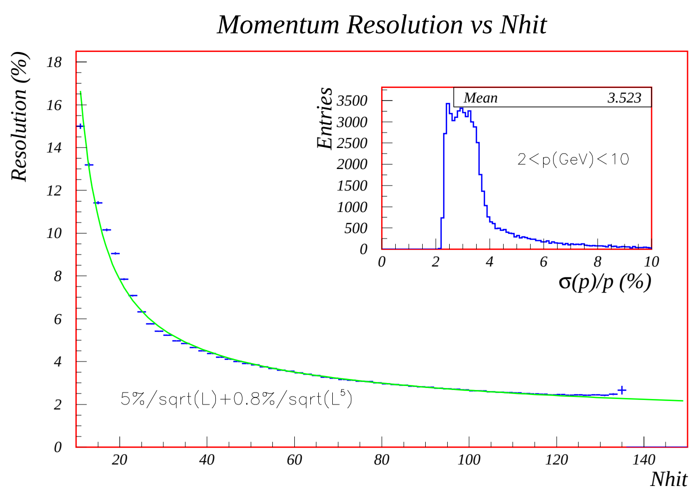

Figure 2.17: Momentum resolution as a function of the track length (number of hits in the fiducial volume of drift chambers).

plane of the chambers, it is parametrized by:

$$\frac{\sigma_p}{p} \approx \frac{0.05}{\sqrt{L}} \oplus \frac{0.008 \times p}{\sqrt{L^5}}$$

where the momentum p is in GeV and the track length L in m. The first term is the contribution from multiple scattering and the second term comes from the single hit resolution of the chambers. For a momentum of 10 GeV, the multiple scattering contribution is the larger one when the track length is longer than 1.3 m.

Fig. 2.17 shows the resolution as a function of the track length as measured from our real data sample. The momentum resolution 3.5% in the momentum range of interest ($2 < p(GeV) < 10$) is achieved.

For electrons, the tracking is more difficult because they radiate photons via the bremsstrahlung process when traversing the tracking system. This results sometimes in a drastically changing curvature. In this case, the resolution is worse and the electron energy is measured by combining information from the drift chambers and the electromagnetic calorimeter as it will be described later.

2.3.4 Trigger Counters

Two trigger planes are installed in the NOMAD detector to provide an efficient selection of neutrino interactions inside the fiducial volume. The first plane follows the active target and the second plane is positioned behind the TRD region. Both of them cover a fiducial area of 280 cm × 286 cm and consist of 32 scintillation counters with single-ended photomultiplier readout. The scintillators have a thickness of 0.5 cm and a width of 19.9 cm. Twenty-eight of the counters are installed horizontally and have a length of 124 cm. In order to increase the fiducial area of the trigger planes, four counters of a length 130 cm are installed vertically to cover the lightguides of the horizontal counters.

The scintillators are connected to photomultipliers (with an intrinsic time resolution of 1 ns) which are oriented parallel to the magnetic field. The field of 0.4 T only reduces the response of these photomultipliers by 30%.

A coincidence between the two planes is required for a valid trigger.

The average efficiency of the trigger counters for single tracks has been determined with the data and found to be $(97.5 \pm 0.1)\%$ [89].

2.3.5 Transition Radiation Detector

The NOMAD Transition Radiation Detector (TRD) [90] was designed to separate electrons from hadrons with a rejection power greater than 10^3 keeping 90% electron identification efficiency. It is placed after the first trigger plane and consists of 9 individual modules. Each of them includes a radiator followed by a detection plane. The first 8 TRD modules are paired into 4 doublets.

In order to provide a precise track extrapolation from the drift chamber target to the calorimeter, five drift chambers are embedded in the TRD, one after each TRD doublet and one after the last TRD module, see Figures 2.2 and 2.3.

The design of the detector was optimised taking into account two main experimental constraints: limited longitudinal space inside the NOMAD magnet and less than 1% of radiation length per each TRD module[5]. The chosen design of the TRD module is the following one (see figure 2.18):

- The radiator is a set of 315 polypropylene foils, each 15 μm thick and 3×3 m^2 in area, separated by 250 μm air gaps. Foils are stretched on the aluminium

[5] Less than 2% of X_0 between two DC measurement planes.

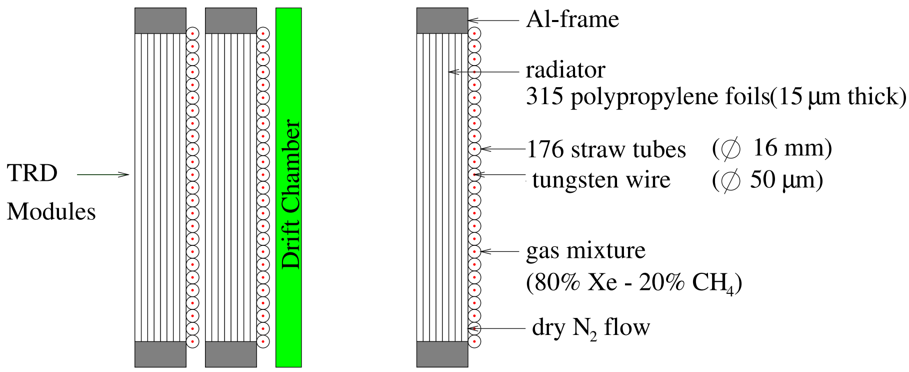

Figure 2.18: A schematic top view of a section of the TRD

frame and embossed to insure a regular spacing in spite of their large size and of electrostatic effects;

- The detection plane consists of 176 vertical straw tubes, each 3 m long and 16 mm in diameter, separated by 0.2 mm. The straw tubes are fed in parallel with a xenon − methane (80% − 20%) gas mixture. They are made of two shifted 12.5 μm thick ribbons of aluminised (115 nm of aluminium) mylar rolled and glued along a 16 mm diameter helix. The sensitive anode is a 50 μm diameter golden tungsten wire stretched with a tension of 100 g. In order to protect the gas mixture in the straw tubes from water and oxygen contamination, each TRD module is enclosed by two aluminised mylar skins with a permanent flow of dry N_2 inside them.

The calibration of the TRD is continuously performed with the help of a radioactive ^{55}Fe source (E_γ=5.89 keV) attached horizontally in the middle of each detection plane. A self-trigger system is used to record ^{55}Fe signals in each straw between every neutrino spill. ^{55}Fe source signals reflect all the changes in the running conditions (high voltage, temperature, pressure, gas mixture composition, etc.), thus allowing efficient monitoring and calibration of the TRD.

The electron identification in TRD is based on the difference of energy deposited in the straw tubes by particles of different Lorentz factors $\gamma = E/m$ (see Fig. 2.19). Charged particles with $\gamma < 500$ deposit energy in the xenon − methane gas mixture predominantly by ionization losses, whereas relativistic charged particles ($\gamma > 500$, mainly electrons in NOMAD) produce also transition radiation X-rays at the interfaces of the foils [91, 92]. As a results, a few photons in a keV range are produced by an electron crossing a radiator ($< N_\gamma >\sim 3$ with $< E_\gamma >\sim 14$ keV for 10 GeV e^-).

About 60% of the photons emitted in the radiator are absorbed in the detection planes due to a large cross-section of Xe for a few keV photons. Transition radiation X-ray energy deposition is added to the ionization losses of the parent particle in the same straw tube, because the angular distribution of the emitted photons is peaked around the initial particle direction (the mean angle of emission is about $1/\gamma$).

A pion rejection factor of the order of 1000 is obtained with the 9 TRD modules, while retaining an electron efficiency of 90% [93] as will be described later.

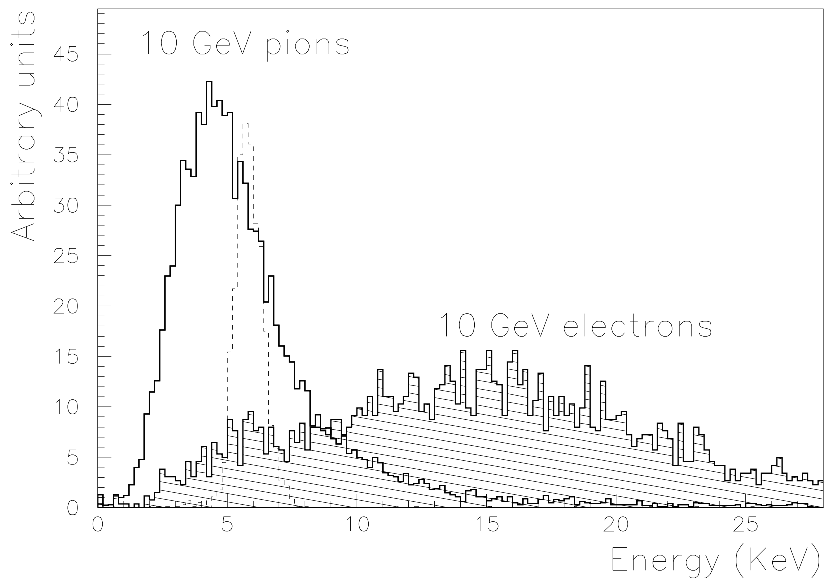

Figure 2.19: Signal amplitudes in a TRD straw for 10 GeV pions and electrons (from test beam measurements). The dashed line corresponds to the ^{55}Fe (5.89 keV) calibration source.

2.3.6 Preshower Detector

The preshower (PRS), which is located just in front of the electromagnetic calorimeter, is composed of two planes of proportional tubes (286 horizontal and 288 vertical tubes) preceded by a 9 mm (1.6 X_o) lead-antimony (96% - 4%) converter, see figure 2.20.

The proportional tubes are made of extruded aluminium profiles and are glued to two aluminium end plates of 0.5 mm thickness. Each tube has a square cross-section of 9×9 mm^2 and the walls are 1 mm thick. The 30 μm gold-tungsten anode is strung to a tension of 50 g and secured at each end. In order to avoid wire vibrations, the anodes are also glued in the middle of the preshower on small spacers. The proportional tubes operate at a voltage of 1500 V with a mixture of Ar : CO_2 (80%:20%).

Signals from each tube are fed into charge preamplifiers.

A large sample of straight through muons is collected during the flat top of the SPS cycle. These muons have been used to monitor the preshower gains against pressure and temperature variations. The global variation of the gain induced by pressure and temperature fluctuations can be calculated on a run by run basis. The electronic gains for each channel are taken into account, allowing the final determination of the individual gas gain. The dispersion of these gas gains is found to be 6% for the 574 tubes and is mainly due to the inhomogeneity of the gas flow inside the preshower.

The fine granularity of the preshower assists in understanding the signals in the electromagnetic calorimeter blocks caused by adjacent particles. Once the clusters with an associated charged track have been constructed, the remaining ones might

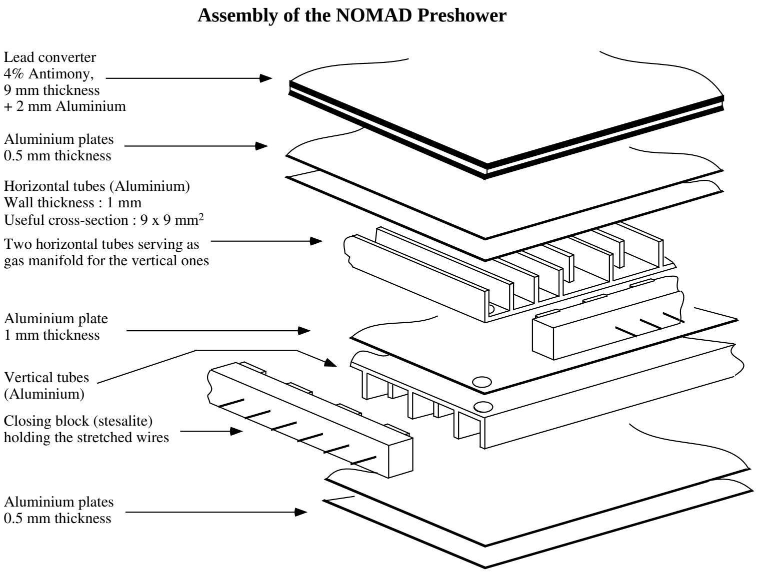

Figure 2.20: A detailed view of the NOMAD preshower detector.

be attributed to photons which have converted[6]. The preshower is used to determine the impact point of converted photons and contribute to the electron identification.

2.3.7 Electromagnetic Calorimeter

The physics goals of NOMAD rely strongly on electron identification, as well as on a very accurate determination of the total transverse momentum in an event.

While electron identification is performed using mainly the Transition Radiation Detector, the measurement of its energy as well as the determination of the neutral component of the transverse momentum requires a large acceptance electromagnetic calorimeter with good energy resolution. In addition, the electromagnetic calorimeter (ECAL), used in conjunction with the Preshower Detector should improve (by at least two orders of magnitude) the electron identification provided by the TRD.

The need to detect electromagnetic showers induced by photons and electrons with energies ranging from about 100 MeV up to 100 GeV requires a large dynamic range in the calorimeter response; a lead-glass detector has been chosen for its good energy resolution and uniformity of response. The presence of the magnetic field transverse to the counter axis requires a special geometry for the calorimeter. A detailed description of ECAL can be found in [94]. The performances of ECAL, when exposed to test beams of electrons, pions and muons are reported in [95].

ECAL consists of 875 lead-glass Čerenkov counters 19 radiation lengths deep and with a rectangular cross section of $79 \times 112\ mm^2$. The direction of the magnetic field (0.4 T) is perpendicular to the counter axis, imposing severe constraints on the mechanical assembly of the light detection system (Figure 2.21). The back face of the lead-glass blocks coupled to the light detectors (two-stage photomultipliers, tetrodes, with a typical gain of 40 in the operating conditions of NOMAD) was cut at 45^o with respect to the block axis, in such a way that the symmetry axis of the tetrodes forms an angle of 45^o with respect to the field direction, thus minimizing the signal reduction caused by the magnetic field. This has been found to be

[6] $\sim 70\%$ of photons convert in PRS.

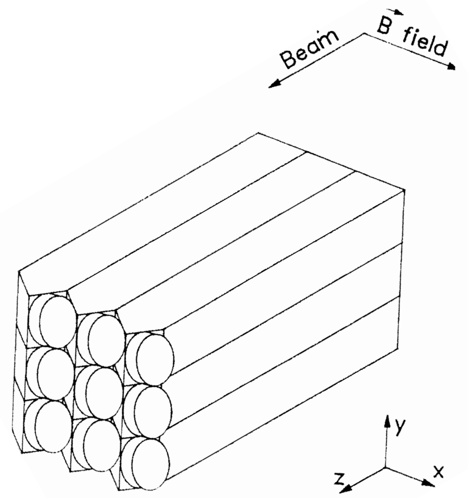

Figure 2.21: Schematic view of some lead-glass counters with phototetrodes.

less than 20% and to be very constant and uniform. A low-noise electronic chain, composed of a charge preamplifier followed by a shaper and a peak sensing ADC with a resolution of 12 bits, provides a calorimeter response in a large dynamic range of more than 3×10^4.

A fast signal is also provided for time measurements in order to reject energy depositions not associated with the event trigger and for using the ECAL at the trigger level, with a resolution of a few ns for energy depositions larger than 1 GeV.

Monitoring of the lead-glass response is performed using blue Light Emitting Diodes (LED, two per block) mounted on the same face of the block on which the tetrodes are positioned; a detailed description of this monitoring system is given elsewhere [96]. The stability of this system has been shown to be within $\pm 1\%$ over periods of several months.

Before the final assembly in NOMAD, each lead-glass block was calibrated in a test beam using 10 GeV electrons. The response to the LED pulses, measured together with that to electrons of known energy ($\Delta p/p$=1%), was recorded and used later on to convert the calibration obtained under the test beam conditions (without magnetic field) to the NOMAD operating conditions. The effect of the magnetic field on the calibration is taken into account by making LED measurements with the magnetic field on and off.

The linearity of the calorimeter response to electrons was verified using test beam measurements in the energy range $1.5 \div 80$ GeV. Deviations from linearity are less than 1.5% and can be easily corrected with a logarithmic algorithm. A detailed study of the energy resolution was performed. After the deconvolution of the electronic noise from the data, a two-parameter fit of the energy resolution $\Delta E/E$ = a + b/$\sqrt{E}$, where E is in GeV, gives a = (1.04 ± 0.01) % and b = (3.22 ± 0.07) %.

The uniformity of the ECAL response as a function of the impact point of the

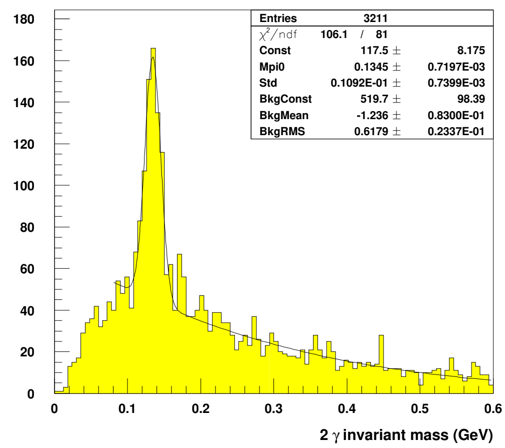

Figure 2.22: The invariant mass distribution of two photons reconstructed in the electromagnetic calorimeter shows a clear peak from π^0.

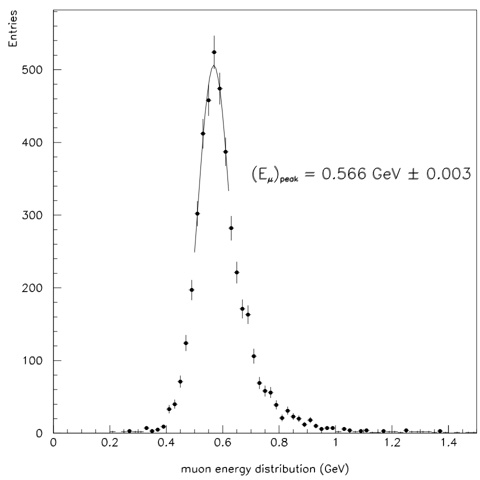

Figure 2.23: The signal in the ECAL from muons crossing the detector during normal data taking. A correction has been applied to account for the differences in impact angle of the muons at the calorimeter front face.

incoming electrons has been measured to be $\pm 0.5\%$; the response to electrons entering at normal incidence in the gaps between adjacent blocks has shown that ECAL is "hermetic" at more than 99%. A weak dependence of the total energy release from the incidence angle θ of the incoming electrons has been found both in the test beam measurements and in the Monte-Carlo simulations: this dependence, which has been empirically parametrized as $E(\theta) = E \times \sqrt{\cos(\theta)}$, can be attributed to the small variation with angle of the Cerenkov light collection efficiency.

The calibration and the calorimeter response to low energy photons has been checked by measuring the π^0 mass produced both in a test beam setup and in the experiment (Fig 2.22). The test beam data gave $m_\pi = 133.7 \pm 1.2\ MeV$ with a $\sigma_m = 16\ MeV$.

The calorimeter response to muons corresponds to an average energy of $(0.502 \pm 0.003)\ GeV$ without the corrections needed to take into account the lead-glass block geometry and the asymmetry in the light detection introduced by the phototetrode position[7]. The muon signals were found to be stable within $\pm 1\%$ over a 2 year period providing a good check on the stability of the calorimeter response. Figure 2.23 shows a typical spectrum of the energy deposited by muons crossing ECAL. This muon monitoring is complementary to the LED monitoring which is continuously running during normal data taking.

Triggers based on the ECAL energy deposition are currently being acquired together with the 'normal' neutrino triggers described later. The large mass of ECAL ($\sim 20\ tons$) gives a trigger rate of ~ 2.5/neutrino spill. The large acceptance makes such events very useful for physics purposes as well as for monitoring of the beam conditions.

2.3.8 Hadronic Calorimeter

The hadron calorimeter (HCAL) is intended to refine the measurement of missing transverse momentum by identifying neutral hadrons and measuring their energies and directions, and by providing a measurement of charged hadronic energy complementary to that derived from momentum measurements in the drift chambers.

The HCAL is an iron–scintillator sampling calorimeter. The NOMAD detector is suspended from iron pillars (the 'I's) at the two ends of the magnet. The downstream pillar was instrumented with scintillators to construct the HCAL with an active area 3.6 m wide by 3.5 m high.

The 'I's consist of 23 iron plates 4.9 cm thick separated by 1.8 cm gaps, and six of these modules form a wall 5.4 m wide, 5.8 m high, and 1.5 m from front face to rear face. This wall acts as a filter for the large muon chambers downstream and as a support for the 'basket' which contains most of the NOMAD detector. It provides also the absorber for the hadron calorimeter.

A schematic frontview of HCAL is given in Figure 2.24. The active elements of the calorimeter are scintillator paddles 3.6 m long, 1 cm thick, and (on average) 18.3 cm wide. The scintillation light is directed to a 5 $inch$ phototube at each end of the module.

The output from each phototube is split. One signal is delayed and sent to a charge–integrating ADC, while the second is discriminated and sent to a multihit TDC. The ADC signals are used for energy and position measurements, while the TDC signals are used to determine event timing. The energy deposited in a given module is obtained from the geometric mean of the two phototube signals, and the horizontal position of the energy deposition is determined from the attenuation length of the scintillator and the ratio of the phototube signals. Figure 2.25 shows the difference between the predicted position and the position measured by the

[7] The corrected value is $(0.566 \pm 0.003)\ GeV$. See Fig. 2.23.

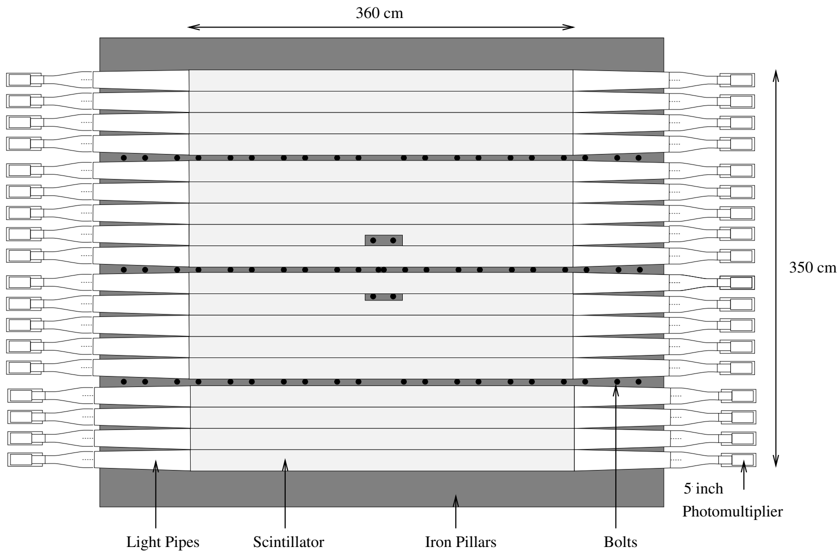

Figure 2.24: A front view of HCAL; see the text for details.

hadron calorimeter for minimum ionizing muons passing through a single module; the typical position resolution is of the order of 20 cm.

Vertical positions are determined from the pattern of energy sharing between the modules. There is a high probability that hadrons will begin to shower in the approximately 2.1 λ_{int} of material upstream of the hadron calorimeter, and so the total hadronic energy is taken to be a weighted sum of the energies deposited in the hadron and electromagnetic calorimeters.

2.3.9 Muon Chambers

The NOMAD muon detector consists of 10 drift chambers previously used in the UA1 experiment [97]. Each chamber has an active area of $3.75 \times 5.55\, m^2$ with two planes of drift tubes in the horizontal and two in the vertical directions. In total there are 1210 drift tubes, each with a maximum drift distance of 7 cm.

The chambers are arranged in pairs (modules) for track segment reconstruction. The first muon station consists of three modules and is placed behind the hadron calorimeter. It is followed by an 80 cm thick iron absorber and a second muon station of two modules, see Figures 2.2 and 2.3.

The chambers are operated with an Argon:Ethane (40% : 60%) gas mixture. Their performance is monitored continuously using high energy muons passing through the detector. The average position resolution for hits is in the range 350 μm to 600 μm depending on the gas quality, see figure 2.26.

The average hit efficiency is 92.5% and the dominant source of the inefficiency (6.5%) is due to the dead areas between the drift tubes. Before the beginning of 1995 run there was a small gap between the muon chambers in station 1. Starting from the 1996 run this gap was closed with several small scintillation counters, the 'muon veto' (see Figure 2.2).

Track segments are reconstructed separately for each station from (typically) 3 or 4 hits per projection, see Figure 2.27. The measured efficiency for the reconstruction of track segments is 97%.

Muons are identified if they penetrate more than 8 interaction lengths (λ_{int}) of

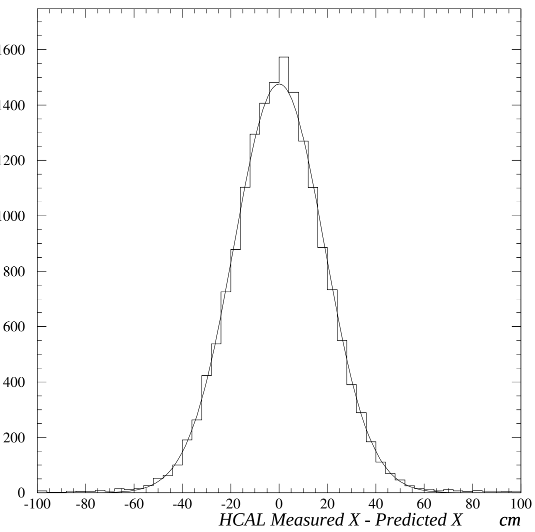

Figure 2.25: Horizontal position resolution for muons passing through a single hadron calorimeter module.

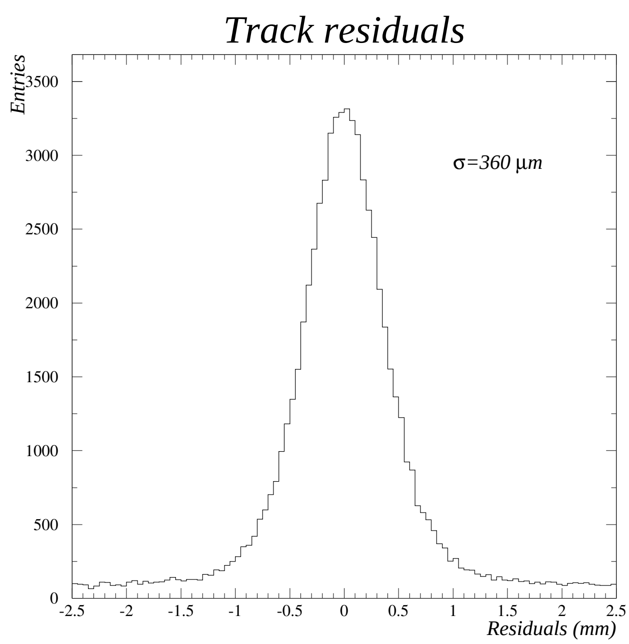

Figure 2.26: Residuals for 4–point segments (tracks) in the muon chambers for good running conditions.

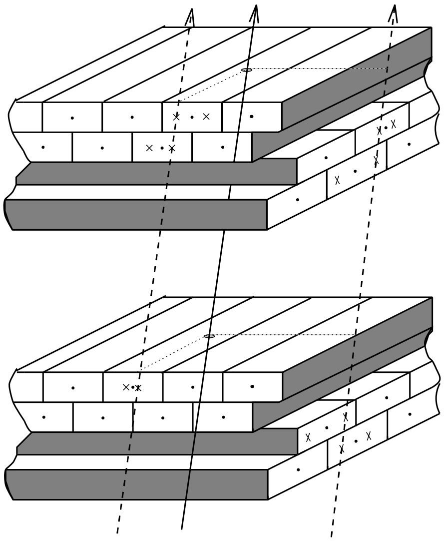

Figure 2.27: A cut through a muon chamber module illustrating the drift tube arrangement, and the typical hit pattern left by a throughgoing muon (continuous arrow) and the track segment reconstructed in projections (dashed arrows).

absorber material in order to reach muon station 1, or 13 λ_{int} for muon station 2. For perpendicular incidence, the momentum thresholds to reach the muon chambers (with 50% probability) are measured to be 2.3 GeV for station 1, and 3.7 GeV for station 2.

The geometrical acceptance to hit either of the two stations is about 98%. This number applies to primary muons from charged current interactions, averaged over their production point in the NOMAD target, and does not include muons which 'range out' in the absorber material.

2.4 Triggering

The following triggers were set up for the study of neutrino interactions in NOMAD:

- $\overline{V} \times T_1 \times T_2$. This trigger allows a study of neutrino interactions in the drift chamber target region. At least one hit in both trigger planes T_1 and T_2 is required. To prevent triggering on through-going muons, no hit should have occurred in the veto counters (V). The rate for this trigger is $\sim 5.5/10^{13}$ *p.o.t.* Of these triggers, about 0.5 are potentially interesting candidates for neutrino interactions in the drift chambers. The remaining triggers consist of 'cosmics' (about 1), non-vetoed muons (1.5) and neutrino interactions in the magnet (2.5).

- $\overline{V_8} \times FCAL$. Neutrino interactions in the forward calorimeter with an energy deposition of at least 3 mip fire this trigger. Through-going muons are vetoed by the veto subset V_8. About 6.5 neutrino interactions occur in the FCAL for 10^{13} *p.o.t.*

- $\overline{V_8} \times T_1 \times T_2 \times FCAL'$. This trigger is set up to study quasielastic like events in the FCAL. Such events allow a relative flux measurement of the neutrino beam as a function of the neutrino energy. For this trigger, a threshold of 1 *mip* energy deposition in the FCAL is requested. The rate for this trigger is $\sim 1.5/10^{13}$ *p.o.t.*

- $\overline{T_1 \times T_2} \times ECAL$. The electromagnetic calorimeter is also used as a target. Different physics topics are addressed using events from this trigger; among them are $\nu_\mu \to \nu_e$ and $\nu_\mu \to \nu_\tau$ oscillations. An energy deposition of more than ~ 1.5 *mip* in the ECAL enables this trigger, which has an average rate of $\sim 2/10^{13}$ *p.o.t.*

- RANDOM. A random trigger which allows a study of detector occupancy was constructed in the following way: a prescaled $\overline{V} \times T_1 \times T_2$ trigger was taken and delayed by 23 μs (corresponding to 1 SPS turn).

Approximately 15 neutrino candidate triggers are taken in each neutrino spill.

In addition various triggers are installed in the 2.6 s long flat top between the two neutrino bursts (with VT_1T_2 logics). These are used for:

- The calibration of the different subdetectors;

- A measurement of the trigger counter efficiency.

One of the triggers is a selection of electrons (from muon decay or delta rays) which allows a study of the behaviour of electrons in the detector as will be discussed later. In total, about 60 triggers are taken in each flat top.

In the neutrino spills, the data acquisition has a typical deadtime of $\sim 10\%$ arising from digitizations. The data taking time lost due to down-time and inter-run transitions was estimated to be less than 3%.

2.5 Summary

It was illustrated that the performances of the NOMAD subdetectors are in good agreement with our expectations.

As can be seen from the description of the NOMAD detector, the experiment provides a unique possibility to study the properties of neutrino interactions with a quality of bubble chamber experiments (concerning the reconstruction of tracks and particle identification) and with a statistics comparable with the one obtained using coarse grained calorimeters.

The large sample of data in a detector with a target density of a hydrogen bubble chamber will permit NOMAD to explore not only neutrino oscillations but also many other processes involving neutrinos.

We can now come to the problem of the correct usage of subdetector's responses to perform the event reconstruction in the NOMAD setup.

Chapter 3

Event reconstruction in NOMAD

In order to use the event kinematics for the oscillation search one should perform the event reconstruction in the best possible way.

The main purpose of the reconstruction program in any experiment of high energy physics is

- to measure the momentum of charged particles;
- to measure the energy (and the direction, if possible) of neutral particles;
- to determine the particle type (provide particle identification).

In NOMAD the trajectories of charged particles are reconstructed from the coordinate measurements provided by the drift chambers system. At the next stage the charged tracks are used to perform the pattern recognition in the other subdetectors. The electromagnetic showers induced by photons are measured by the system of preshower and electromagnetic calorimeter. The particle identification is provided by the combined information from all the NOMAD subdetectors.

3.1 Charged track reconstruction

The task of any reconstruction program is two-fold. First of all, it should perform pattern recognition, that is to decide which individual measurements provided by a detector should be associated together to form an object representing a particle trajectory. Pattern recognition in the tracking detectors (such as drift chambers) is called a track search. At the next stage fitting procedure should be applied to this set of measurements in order to extract the parameters describing the trajectory out of which the physical quantities can be computed. For example, the momentum of a charged particle is determined from a measurement of the curvature of its trajectory in a known stationary magnetic field. The results of the track search have to be confirmed or rejected by the track fit and possible ambiguities should also be solved. The fitting procedure requires a track model, i.e. a mathematical way to represent a trajectory of a particle. The track can be uniquely described at any point by 6 parameters (3 spatial coordinates, 2 directions and the curvature or the absolute value of the momentum with the proper sign). In addition to the estimated track parameters their covariance matrix should be available to be used at the next step of analysis. If the particle travels in vacuum it is sufficient to know these parameters in a single point since the trajectory is then the solution of the equation of motion with these parameters as the initial values. As soon as the particle interacts with matter, the trajectory is no longer the exact solution due to the fact that this interaction is a random process. That is why we have to take into account effects of energy losses and multiple scattering together with measurement errors due to the detector resolution when performing the track fit.

From the above discussion it is obvious that track search and fit are important parts of the data analysis.

3.1.1 Track finding and fitting algorithms

The reconstruction program for the NOMAD drift chambers [98] is extremely important for the performance and sensitivity of the experiment. A very high efficiency of the track reconstruction is required in order to provide good measurement of event kinematics for the oscillation search. We have also to be sure that the measured track parameters do not deviate significantly from the true particles momenta, that is the reconstruction program should provide good momentum resolution. To solve this problem and given the fact that in the NOMAD setup the amount of matter crossed by a particle between two measurement planes can not be neglected, the effects of energy losses and multiple scattering should be carefully taken into account.

In the following we will mention briefly the main features of the track search method, introduce the track fit algorithm and describe the track model used in some details.

Before this description let us present some of our implementation choices which proved to be useful during the development phase.

3.1.2 Implementation choices

The DC reconstruction program is a software package written in *C* language in an object oriented way. Large number of entry points is provided to an external user. This approach allows to build new applications in an easy and straightforward way.

The DC reconstruction software includes track/vertex search and fit, graphical display, data access routines and tools for storage of the results of the reconstruction. It provides:

- standalone reconstruction for on-line monitoring and off-line processing;
- toolbox for calibration (alignment);
- entry points for the second stage ("phase 2") reconstruction.

Special efforts have been made to allow the usage of this software on different platforms which is very important for an international collaboration. The code has been tested under VMS, OSF1, SunOS, Solaris, HP-UX, AIX and Linux operating systems.

It was decided to use access routines in order to retrieve any information from ZEBRA [99] banks or C-structures. This approach allowed to keep the higher level code unchanged when there was a necessity to modify low level structures.

All the objects on which the program operates are represented as a *C* structures. For example, a track in terms of the program is just a list of associated hits.

The track reconstruction is driven by a set of parameters which are stored in the *C* structure called `DcGlobal`.

At an early stage of the program development a graphical interface was built to draw the results of the reconstruction on a high-resolution screen. It was found to be extremely important to look at the performance of the pattern recognition algorithms in order to study possible improvements. Most of the parameters which drive the reconstruction in the drift chambers (`DcGlobal` structure) were adjusted in this way.

3.1.3 Track finding

The track finding algorithm is described in detail elsewere [100]. We will present here the overall strategy. The track finding consists of four steps: triplet building-up, helix search, hit collection and track construction (fit, clean-up and expansion).

Hits

A hit is a single digitization (measurement of a coordinate) in one of the planes of a drift chamber. In our implementation a structure is associated to each of those digitizations. Hit structure carries the information about the chamber, the plane and the wire which recorded the measurement and about the raw drift time given by the TDC. To accurately convert this time into a drift distance one needs information such as the position of the hit along the wire and the angle at which the particle crossed the measurement plane. Such information is only available at the later stage of the reconstruction process and we use central values as an initial guess. Later in the program this conversion will be improved with the solution of the up-down ambiguity.

Track hits

A drift chamber hit acquires many attributes once included into a track. For example, the sign or the drift distance (since the time-to-distance relationship depends on the crossing angle). Due to the fact that a hit could belong in principle to several tracks, these attributes should not be stored inside a hit. We thus resorted to defining a special object which was called *trhit*. It contains the quantities needed at each measurement plane for fitting, i.e. local track parameters, local covariance matrix, etc. These objects actually ensure the connection between track and hits as the chosen name tries to indicate.

Triplets

As it was mentioned above, the NOMAD drift chambers are made of 3 sensitive planes measuring U, Y and V coordinates, where U and V are rotated by $+5$ and -5 degrees with respect to Y. The U and V "frames" are defined so that U and V are 0 when X and Y are 0:

$$U = Y \cdot \cos 5^\circ - X \cdot \sin 5^\circ$$

$$V = Y \cdot \cos 5^\circ + X \cdot \sin 5^\circ$$

In order to perform the pattern recognition we need to combine the information about the track position provided by the 3 sensitive planes of one chamber into a space measurement.

Let us define a triplet as a combination of 3 hits in the planes of a given chamber. It represents the first attempt to solve the up-down ambiguity and contains the 3-dimensional information about the particle trajectory in a given Z reference plane. The most sensitive criterion to discriminate hits belonging to the same track is the quantity:

$$\Delta = U + V - 2 \cdot Y \cdot \cos 5^\circ \approx 2 \cdot \Delta z \cdot \tan\gamma \cdot \sin 5^\circ$$

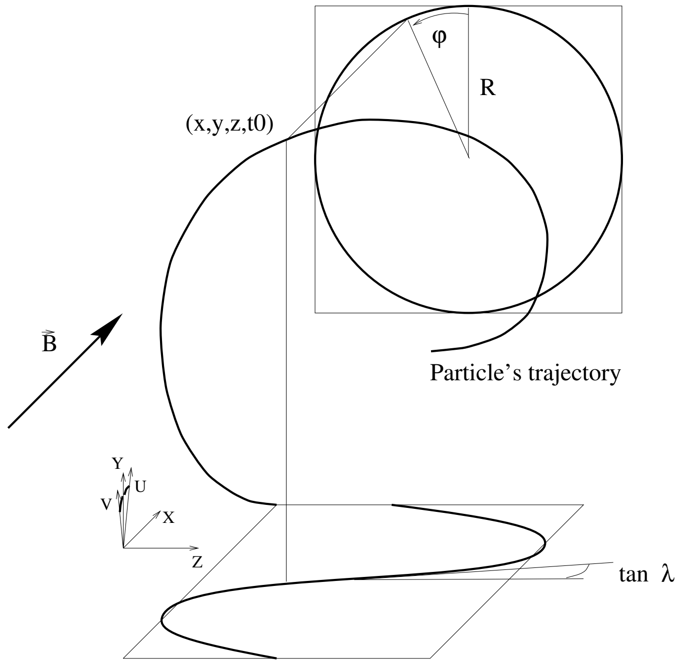

Figure 3.1: Definition of the helix parameters used to describe charged particle trajectory in the NOMAD setup.

that is proportional to the local track slope in the (xz) plane ($\tan\gamma$) and the distance between two measurement planes (Δz). It tends to be small for straight tracks going perpendicular to the DC planes and amounts to around 3 mm for a slope of 1.

As each U, Y or V coordinate depends on the drift distance sign (thereafter referred to as the "sign"), each three-hit combination allows eight different triplets to be built. A triplet is then defined as a combination of three hits (U, Y and V), three signs, and the Δ value.

To build triplets a cut on $|\Delta|$ is applied. Various filters can be used to select the best triplet candidates, for example: consider only the first one (in terms of $|\Delta|$) for a given Y hit, ignore triplets if more than one can be built for one of its hits, etc. These two filters exhibit efficiency-purity performances of 70%-70% and 45%-85%. The first is the one implemented in the current software version. The cut on $|\Delta|$ is driven by `DcGlobal.Dmax1` parameter (typical value is 3 cm).

On top of these a posteriori cuts, one could imagine to mask hits to the triplet search (in order to prevent the building-up of wrong triplets) if they lie in a too crowded region, if there is a bounce hit on the same wire or if the drift time is too small.

The computer time needed for the triplet build-up goes as N^3_{hits} but remains on average a small contribution to the overall reconstruction time budget.

Triplets are used to initiate the DC track search.

Helix search

Having three triplets in hand, one is able to test whether they belong to the same helix trajectory [1] and compute helix parameters if it is the case.

The chosen helix parameters are x, y, $1/R$, $\tan\lambda$, ϕ, t_0 (see Fig. 3.1). x and y are self explanatory, λ is the dip angle, ϕ is the angle of the helix tangent in the

[1] The track model will be described in details later.

(yz) plane, negative for upwards going tracks, R is the signed radius in the (yz) plane. t_0 is the time subtracted to the hit drift time to compute the drift distance. This parameter had to be introduced to be able to cope with trigger time jitter and to fit off-time (with respect to the main triggers) tracks.

Let us consider three triplets labeled "0", "1" and "2" and let us calculate the helix parameters assuming they lie on a circle in the (yz) plane with center (y_c, z_c) and radius R is given by:

$$R^2 = (y_0 - y_c)^2 + (z_0 - z_c)^2 = (y_1 - y_c)^2 + (z_1 - z_c)^2 = (y_2 - y_c)^2 + (z_2 - z_c)^2$$

Using this equation we can build two new ones

$$2y_c \cdot (y_1 - y_0) + 2z_c \cdot (z_1 - z_0) = (y_1^2 - y_0^2) + (z_1^2 - z_0^2)$$

$$2y_c \cdot (y_2 - y_0) + 2z_c \cdot (z_2 - z_0) = (y_2^2 - y_0^2) + (z_2^2 - z_0^2)$$

and, subtracting one from the other, we get

$$2y_c \cdot \left[\frac{y_1 - y_0}{z_1 - z_0} - \frac{y_2 - y_0}{z_2 - z_0}\right] = \frac{(y_1^2 - y_0^2) + (z_1^2 - z_0^2)}{z_1 - z_0} - \frac{(y_2^2 - y_0^2) + (z_2^2 - z_0^2)}{z_2 - z_0}$$

Introducing $\Delta y_{ij} = y_i - y_j$, $\Delta z_{ij} = z_i - z_j$ and $A = \Delta y_{10}\Delta z_{20} - \Delta y_{20}\Delta z_{10}$ we obtain

$$y_c = y_0 + \frac{1}{2A} \cdot [\Delta z_{20} \cdot (\Delta y_{10}^2 + \Delta z_{10}^2) - \Delta z_{10} \cdot (\Delta y_{20}^2 + \Delta z_{20}^2)]$$

Analogously,

$$z_c = z_0 - \frac{1}{2A} \cdot [\Delta y_{20} \cdot (\Delta z_{10}^2 + \Delta y_{10}^2) - \Delta y_{10} \cdot (\Delta z_{20}^2 + \Delta y_{20}^2)]$$

Introducing $S_{ij} = \Delta y_{ij}^2 + \Delta z_{ij}^2$ we can write

$$R^2 = (y_0 - y_c)^2 + (z_0 - z_c)^2 = \frac{1}{4A^2} \cdot S_{10} \cdot S_{20} \cdot S_{21}$$

Then

$$\cos\phi_0 = \frac{y_0 - y_c}{R} = \frac{1}{\sqrt{S_{10}S_{20}S_{21}}}(S_{20}\Delta z_{10} - S_{10}\Delta z_{20})$$

and

$$\sin\phi_0 = \frac{z_0 - z_c}{R} = \frac{1}{\sqrt{S_{10}S_{20}S_{21}}}(S_{10}\Delta y_{20} - S_{20}\Delta y_{10})$$

With 9 measurements and 6 parameters one has 3 constraints to test whether three triplets belong to the same helix trajectory. At the moment, we only cut on the x residual (checking that the three triplets are roughly aligned in x), which is the most sensitive quantity when the three triplets belong to chambers far apart:

$$x^{extrap} = x_1 + (\phi_2 - \phi_1) \cdot \frac{x_3 - x_1}{\phi_3 - \phi_1}$$

$$|x^{extrap} - x_2| < \texttt{DcGlobal.Maxdx}$$

To compute fully the helix parameters one has to iterate the calculation of the local slopes and drift distances since the time-to-distance relation depends on the local track angle. To avoid unnecessary calculations we do not compute the helix parameters if the 3 triplets form more than a half turn or if the initial x misalignment is more than `DcGlobal.Maxdx` parameter (typical value is 3 cm).

Hit collection

Having the helix parameters in hand, one can collect hits in a road around the helix extrapolation. This procedure is controlled with the help of the global variable `DcGlobal.Roadwidth`, ranging from about $\sim 2\ mm$ to $3\ mm$. The collection stops when:

- too many measurement planes are crossed without match. This is driven by the global parameter `DcGlobal.Maxhole` (typical value is 3);
- two or more hits are found within a control road (it is then dangerous to choose without a good track position prediction in hand). The control road width is set with the global variable `DcGlobal.Dangerousroad`. Zero value indicates that we do not wish to stop even when crossing a crowded region.

Track candidate search

Given three chambers into which triplets have been built a track construction function is called. When 3 triplets pass the `DcGlobal.Maxdx` cut (that is the x residual is less than the global variable `DcGlobal.Maxdx`) they are sent to the construction function. If this function returns a constructed track it is "improved" (see next paragraph) and added to a track list. Otherwise the track candidate is deleted. This approach allows to change drastically the track search algorithm without modification of the library. As an example, the DC track search based on the usage of TRD hits was developed [101] (in which case the track construction function is quite different). Additional track search algorithms have been built which take into account the information about the reconstructed vertices [100].

Track improvement

Having a track candidate one can now fit it, check the drift time sign assignment, remove undesirable points and try to expand this track. The function responsible for this task takes as an argument the one-point χ^2 above which a point will be excluded from the track, or under which it will be included during the track expansion (`DcGlobal.Maxpointchi2` parameter, typical value is 10).

3.1.4 Fit algorithm

Having performed the patten recognition, we can now try to fit constructed tracks to determine the track parameters, i.e. charged particles momenta. The Kalman filter technique was adapted to fulfil this task.

The Kalman filter

The Kalman filter is a mathematical name assigned to least-squares stepwise parameter estimation technique. Originally developed in the early 60's to predict rocket trajectories from a set of their past positions, it can be used to handle multiple scattering while estimating track parameters. We will try to briefly shed light on the features of the Kalman filter for track fitting and refer to the literature for more details [102, 103].

Consider a setup in which the track position measurement devices are interleaved with matter[2]. Following the Gauss-Markov theorem, the best (linear) estimate of the track parameters is obtained via a least squares fit using the actual covariance matrix of the involved measurements. It means that we have to combine the

[2]This is of course always the case but somehow more for the NOMAD detector.

drift chamber resolution and the effect of multiple scattering when computing the covariance matrix. When the multiple scattering is taken into account, this covariance matrix is no longer diagonal. In the traditional least squares global fit, this ($N_{meas} \times N_{meas}$) matrix has to be computed and inverted. In NOMAD experiment where N_{meas} is $50 \div 100$ this inversion is not only time consuming but also numerically unstable. Another disadvantage of the traditional fit is the fact that it provides the track parameters only at the fixed reference plane, for example at the beginning of the track. In order to find the best track parameters at the end of the track one has to perform a completely independent fit using the new reference plane. Due to multiple scattering, the results of these two fits are not related by the track model and cannot be obtained from one another.

The Kalman filter technique is a stepwise technique (a step being the propagation from one measurement to the next one and its inclusion in the fit) which could eventually handle an infinite number of measurements and gives, mathematically speaking, exactly the same result as a standard least squares minimization. In the framework of track fitting, it essentially avoids big matrix inversion and provides almost for free an optimal estimate of track parameters at any location, allowing the detection of outlying measurements, extrapolation and interpolation into other subdetectors.

Let us describe the Kalman filter method by considering a linear discrete dynamic system which is in each point of (discrete) time (t_k) characterized by a state vector x_k. The evolution of this state vector in time is described by a time-independent transformation, the system equation:

$$x_k = f_k(x_{k-1}) + w_k$$

where f_k is a deterministic function (track model in our case) and w_k is a random disturbance of the system, the so-called process noise (multiple scattering in our case).

The state vector does not need to be observed directly. In most cases a function of the state vector is observed, corrupted by measurement noise[3]:

$$m_k = h_k(x_k) + \varepsilon_k$$

where m_k is the vector of observations at time t_k (in NOMAD we measure only one coordinate in a given Z reference plane). We shall assume in the following that w_k and ε_k are independent random vectors and have mean 0 and a finite covariance matrix.

Linearizing the system in the vicinity of x_{k-1}, one obtains:

$$\begin{aligned} f_k(x_{k-1}) &= F_k \cdot x_{k-1} \\ h_k(x_k) &= H_k \cdot x_k \end{aligned}$$

We can now define keywords used in the Kalman filter estimation technique:

- **Prediction** is the estimation of the state vector at a "future" time, that is the estimation of the state vector at time or position $(i+1)$ using all the measurements up to m_i.

- **Filtering** is estimating "present" state vector based upon all "past" measurements, i.e. estimating track parameters using measurements[4] up to m_i (or from m_i on). In other words the filtering includes the measurement at time or position i into the prediction at this time or position.

[3] The difference between the true value of a measured physical or geometrical quantity and the value recorded by the detector is called the measurement error.

[4] One has to assume that the measurements are ordered with respect to time to handle multiple scattering because the covariance matrix of measurement residuals depends on this order. Without multiple scattering, the ordering does not affect the filter result as in the case of a global fit.

- **Filter.** The algorithm which performs filtering is called a filter and is built incrementally: filtering m_1 to m_i consists in filtering m_1 to m_{i-1}, propagating the track from m_{i-1} to m_i and including m_i. A filter can proceed forward (i increases) or backward (i decreases).

- **Smoothing** means using all the measurements to provide a track parameter estimate at any position. Because of multiple scattering the track parameter estimates at various locations are not related through the track model. In fact, these estimates are solutions of different least-squares problems: the χ^2 to be minimized depends on the position at which the track parameters are to be computed. The smoothed estimate can be obtained as a weighted mean of two filtered estimates: the first one using m_1 to m_i (forward), the other using m_N to m_{i+1} (backward).

One can understand the basic idea of the Kalman filter in the following way. If there is an estimate of the state vector at time t_{k-1}, it is extrapolated to time t_k by means of the system equation. The estimate at time t_k is then computed as the weighted mean of the predicted state vector and of the measurement at time t_k, according to the measurement equation. The information contained in this estimate can be passed back to all previous estimates by means of a second filter running backwards or by the smoother.

The main formulae for prediction, filtering and smoothing in a linear dynamic system are the following:

System equation:

$$x_k^{true} \; = \; F_k \cdot x_{k-1}^{true} \; + \; w_k$$
$$E\{w_k\} \; = \; 0, \quad cov\{w_k\} \; = \; Q_k \quad (1 \leq k \leq n)$$

Measurement equation:

$$m_k \; = \; H_k \cdot x_k^{true} \; + \; \varepsilon_k$$
$$E\{\varepsilon_k\} \; = \; 0, \quad cov\{\varepsilon_k\} \; = \; V_k \; = \; G_k^{-1} \quad (1 \leq k \leq n)$$

where the matrices Q_k and V_k represent the process noise (multiple scattering) and measurement noise (detector resolution) respectively.

Notations:

- x_k^{true} is a true value of the state vector at time t_k

- $\tilde{x}_k^j$ is an estimate of x_k^{true} using measurements up to time j ($j < k$: prediction, $j = k$: filtered estimate, $j > k$: smoothed estimate, $\tilde{x}_k^k = \tilde{x}_k$)

- $C_k^j = cov\{\tilde{x}_k^j - x_k^{true}\}$

- $r_k^j = m_k - H_k \cdot \tilde{x}_k^j$ is the residual

- $R_k^j = cov\{r_k^j\}$

In the predicted state vector j is usually equal to $(k-1)$, in the smoothed state vector j is usually equal to n.

Prediction:

- Extrapolation of the state vector:
  $\tilde{x}_k^{k-1} = F_k \, \tilde{x}_{k-1}$

- Extrapolation of the covariance matrix:
  $C_k^{k-1} = F_k C_{k-1} F_k^T + Q_k$

- Predicted residuals:
  $r_k^{k-1} = m_k - H_k \tilde{x}_k^{k-1}$

- Covariance matrix of the predicted residuals:
  $R_k^{k-1} = V_k + H_k C_k^{k-1} H_k^T$

Filter (Weighted means formalism):

- Filtered state vector:
  $\tilde{x}_k = C_k[(C_k^{k-1})^{-1} \tilde{x}_k^{k-1} + H_k^T G_k m_k]$

- Covariance matrix of the filtered state vector:
  $C_k = [(C_k^{k-1})^{-1} + H_k^T G_k H_k]^{-1}$

- χ^2 increment:
  $\chi^2_{k,F} = r_k^T G_k^{-1} r_k + (\tilde{x}_k - \tilde{x}_k^{k-1})^T (C_k^{k-1})^{-1} (\tilde{x}_k - \tilde{x}_k^{k-1})$

Smoother:

- Smoothed state vector:
  $\tilde{x}_k^n = \tilde{x}_k + A_k(\tilde{x}_{k+1}^n - \tilde{x}_{k+1}^k)$

- Smoother matrix:
  $A_k = C_k F_{k+1}^T (C_{k+1}^k)^{-1}$

- Covariance matrix of the smoothed state vector:
  $C_k^n = C_k + A_k(C_{k+1}^n - C_{k+1}^k) A_k^T$

- Smoothed residuals:
  $r_k^n = m_k - H_k \tilde{x}_k^n = r_k - H_k(\tilde{x}_k^n - \tilde{x}_k)$

- Covariance matrix of the smoothed residuals:
  $R_k^n = R_k - H_k A_k (C_{k+1}^n - C_{k+1}^k) A_k^T H_k^T = V_k - H_k C_k^n H_k^T$

Using the Kalman filter the computer time consumed for a track fit is proportional to the number of hits on the track, while with the global technique it is proportional to the cube of the same number in case of multiple scattering.

Implementation of the track fit for the NOMAD drift chambers

The track fit proceeds in 3 steps: forward filtering, backward filtering and smoothing. The smoothing provides the best possible track position estimate at any measurement location, thus allowing to remove efficiently wrong associations.

The fitting routine performs those 3 steps until the fit procedure converges. The convergence criterion is a χ^2 modification between 2 fits of less than `Converge` parameter (typical value is 0.1). If `Converge` is 0 no convergence criterion is applied.

The Kalman filter technique was implemented in two different ways: using weight and covariance matrices. The latter one was found faster since it allows to avoid several matrix inversions per iteration when the effect of multiple scattering is taken into account.

A set of formulae was found to be useful to speed up the calculations: if W and V are symmetric matrices and T is a nonsingular matrix of the same order as V and W, the following relations hold

$$(V^{-1} + W^{-1})^{-1} = V(W + V)^{-1} W$$

$$(TV^{-1}T + W^{-1})^{-1} = V(V + TWT)^{-1} W$$

At the end of the fitting procedure the quality of each track candidate is checked looking at the number of hits (it should be greater than `DcGlobal.Minhit`) and track efficiency[5] ($\varepsilon >$ `DcGlobal.Efficiency`). All badly reconstructed track candidates are discarded and used hits are released for other attempts to build a good track.

For clean track candidates (free from outliers and background) if the measurements covariance matrix entering the fit has been properly evaluated the value of the track chi-squared follows approximately a χ^2 distribution with the number of degrees of freedom being equal to the number of measurements minus the number of adjusted parameters.

In order to be able to compare the χ^2 of tracks of different length N_{hit} (where N_{hit} is the number of hits included in this track), one usually calculates the probability to find a χ^2 larger than a given value:

$$P(\chi^{'\,2} > \chi^2) = \int_{\chi^2}^{\infty} p_n(\chi^{'\,2})\; d\chi^{'\,2}$$

where p_n is the probability density function (p.d.f.) of a χ^2 distribution for n degrees of freedom. For clean tracks P is uniformly distributed between 0 and 1. In the presence of background one finds some enhancement near $P \to 0$.

3.1.5 Calibration

In order to provide good position resolution DC system has to be carefully calibrated. This is important and CPU consuming task given a huge amount of parameters to be adjusted (5 per wire, 9 per plane and 1 per chamber) over large fiducial area ($3 \times 3 \times 5\ m^3$). To perform this task the alignment procedure described earlier was developed.

All the calibration constants obtained via the alignment procedure (about 40000 in total) are stored in the NOMAD data base (under HEPDB [104]) and are decoded automatically when the reconstruction program encounters the beginning of a new run [105].

Additional information about on-line running conditions (HV, disconnected planes, dead wires, gas flow, etc.) is also available and is used during the reconstruction.

The results of the DC reconstruction can be stored in ZEBRA structures and can be reloaded in order to save computer time needed to recompute the track parameters.

An example of raw event from real data can be seen on the Fig. 3.2. Having applied the DC reconstruction and particle identification via subdetector matching package (see later) we obtain the following results (Fig. 3.3).

3.1.6 Track model

Use of the correct track model is important for the performance of the fitting procedure.

The track model describes the dependence of the measurements on the initial values in the ideal case of no measurement errors and no interaction of the particle with matter.

The trajectory of a charged particle in a (static) magnetic field is determined by the following equation of motion:

$$d^2\vec{x}/d^2s = (kq/p) \cdot (d\vec{x}/ds) \times B(\vec{x}(s)),$$

[5]The track efficiency is defined as the ratio of the number of hits included in a given track over the number of sensitive planes crossed.

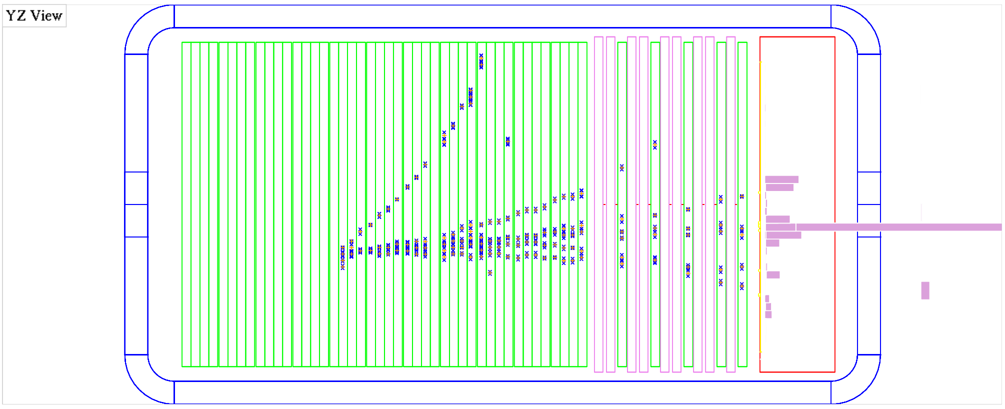

Figure 3.2: Run 8744 Event 228 from real data. One can easily see a dead drift chamber plane in the middle of the detector.

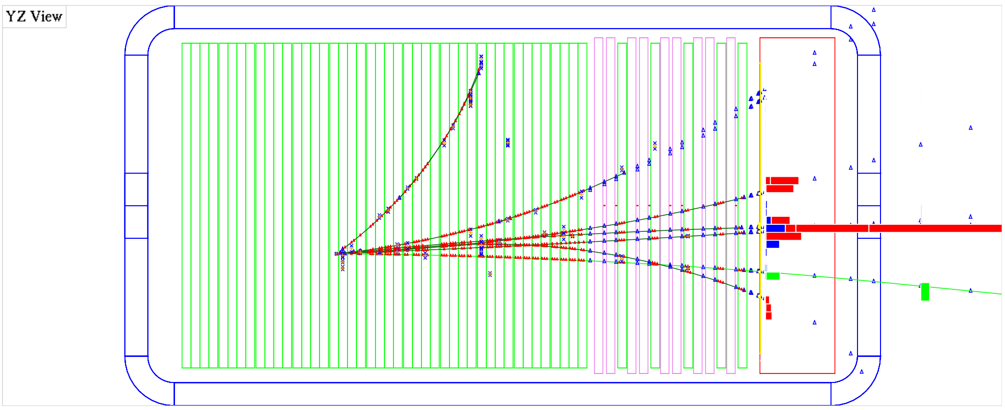

Figure 3.3: Run 8744 Event 228 from real data after performing DC reconstruction and particle identification via subdetector matching package (see later).

where s is the path length, k - a constant of proportionality, q - the charge of the particle (signed), p - the absolute value of the momentum of the particle and $B(\vec{x})$ - the static magnetic field.

During its flight through the detector a particle encounters various influences coming from the materials of which the detector is built. There are effects which can be taken into account in a deterministic way: mean energy loss and mean multiple scattering. They depend in general on the mass of the particle, its momentum, the thickness of the material traversed and, of course, on the kind of the material.

Let us describe the parametrization used for the track fit and the associated algebra:

- The extrapolation step which is assumed to be small enough not to modify significantly the track parameters;
- The matrix of derivatives of the extrapolation step (the F matrix in the Kalman filter notations);
- The multiple scattering matrix (the Q matrix in the Kalman filter notations);
- The energy loss computation (ionization and bremsstrahlung losses).

We will concentrate on the so-called "helix" model which is valid for a charged particle traveling in a magnetic field; however the case of a "linear" model was also implemented to allow the extrapolation of neutral tracks and charged tracks in areas without magnetic field.

The track model assumed for the first stage of the reconstruction in the drift chambers corresponds to the one of a pion[6].

Definition of parameters

The following set of parameters (see Fig. 3.1) was chosen to be fitted to measurements (hits) in the current version of the drift chambers reconstruction program [98]:

- x - coordinate of the track position in a given reference z plane;
- y - coordinate of the track position in a given reference z plane;
- $\frac{1}{R}$ - curvature of the track (the sign is opposite to the particle charge);
- $\tan\lambda$ - the tangent of the dip angle;
- ϕ - the angle of track tangent in (yz) plane ($\tan\phi = -\frac{dy}{dz}$);
- t - the time at which a particle crosses a given reference z plane.

The relation between the momentum p and the radius R is:

$$p(GeV) = 0.003 \cdot B(T) \cdot R(cm)/\cos\lambda$$

reflecting the choice of the system (distance is measured in cm, momentum in GeV, magnetic field in $Tesla$, time in ns).

One should point out that the sign of $(1/R)$ only reflects the particle charge if the time runs the right way along the track. The sign convention used implies that $R\phi$ increases with time along the assumed time direction (which is the one given by the order of the hits in the track).

We call p the vector of parameters: $(x,\ y,\ \frac{1}{R},\ \tan\lambda,\ \phi,\ t)$.

[6]It means that calculations of particle's trajectory, energy losses and multiple scattering effects assume the pion mass.

The extrapolation step: simplified case

Using ϕ as the running parameter, the integral of the equation of motion in the constant magnetic field along the x-axis can be written in the following way:

$$\begin{aligned} x &= x_0 + R \cdot \tan\lambda \cdot (\phi - \phi_0) \\ y &= y_0 + R \cdot (\cos\phi - \cos\phi_0) \\ z &= z_0 + R \cdot (\sin\phi - \sin\phi_0) \end{aligned}$$

where R and $\tan\lambda$ remain constant along the trajectory.

To get the matrix of derivatives (called F in [102] and [103]) needed to extrapolate the parameter covariance matrix, one should first express the parameters p_1 as functions of the parameters p_0, defining the location of p_i as the intersection of the helix with a vertical plane (xy) at $z = z_i$.

$$\sin\phi_1 = \sin\phi_0 + (z_1 - z_0) \cdot (1/R)$$

To simplify the calculations we assume that R and $\tan\lambda$ are constant over the elementary extrapolation step. This is a valid assumption since the extrapolation is always done going from one measurement plane to the next one and the distance between two consecutive measurement planes varies from 2.5 cm to 3.5 cm in the NOMAD setup allowing to neglect the amount of matter crossed (given the low average density of the active target). The effect of energy losses is taken into account at the new track position as will be described later.

Among all possible ϕ_1 values the first crossing is chosen in the requested time direction. From the ϕ_1 value at a new point all other parameters can readily be computed:

$$\begin{aligned} x_1 &= x_0 + \tan\lambda_0 \cdot R_0 \cdot (\phi_1 - \phi_0) \\ y_1 &= y_0 + R_0 \cdot (\cos\phi_1 - \cos\phi_0) \\ \tan\lambda_1 &= \tan\lambda_0 \\ t_1 &= t_0 + R_0 \cdot (\phi_1 - \phi_0)/(\beta\cos\lambda_0) \end{aligned}$$

In the last equation β reads for the particle velocity and $R \cdot \Delta\phi$ (where $\Delta\phi = \phi_1 - \phi_0$) has the right sign following our convention.

The matrix of derivatives (F)

The extrapolation matrix F between two measurement planes (from position "0" to position "1") is defined as the derivative of the extrapolation result p_1 with respect to the input parameters p_0:

$$F = \frac{dp_1}{dp_0}$$

Computing the derivatives of p_1 components with respect to p_0 components is tedious and requires some care, since ϕ_1, which is itself a parameter, is used in the above formulae to compute x_1, y_1, t_1 values at the point "1". Differentiating $\sin\phi_1$ yields:

$$\cos\phi_1 \cdot d\phi_1 = \cos\phi_0 \cdot d\phi_0 + (z_1 - z_0) \cdot d(R_0^{-1})$$

and hence:

$$\begin{aligned} \frac{\partial\phi_1}{\partial\phi_0} &= \frac{\cos\phi_0}{\cos\phi_1}, \\ \frac{\partial\phi_1}{\partial R_0^{-1}} &= \frac{z_1 - z_0}{\cos\phi_1} \end{aligned}$$

The other (non vanishing) derivatives read (where we use the following definitions $\Delta\phi = \phi_1 - \phi_0$ and $\Delta z = z_1 - z_0$):

$$
\begin{aligned}
\frac{\partial x_1}{\partial x_0} &= 1 \\
\frac{\partial x_1}{\partial R_0^{-1}} &= \frac{\tan\lambda}{R^{-1}} \cdot \left(\frac{\Delta z}{\cos\phi_1} - \frac{\Delta\phi}{R^{-1}} \right) \\
\frac{\partial x_1}{\partial \tan\lambda_0} &= \frac{\Delta\phi}{R^{-1}} \\
\frac{\partial x_1}{\partial \phi_0} &= \frac{\tan\lambda}{R^{-1}} \cdot \left(\frac{\cos\phi_0}{\cos\phi_1} - 1 \right) \\
\frac{\partial y_1}{\partial y_0} &= 1 \\
\frac{\partial y_1}{\partial R_0^{-1}} &= \frac{1}{R^{-1}} \cdot \left(\frac{\cos\phi_0 - \cos\phi_1}{R^{-1}} - \frac{\sin\phi_1 \Delta z}{\cos\phi_1} \right) \\
\frac{\partial y_1}{\partial \phi_0} &= \frac{\sin\phi_0 - \frac{\sin\phi_1 \cos\phi_0}{\cos\phi_1}}{R^{-1}} \\
\frac{\partial R_1^{-1}}{\partial R_0^{-1}} &= 1 \\
\frac{\partial \tan\lambda_1}{\partial \tan\lambda_0} &= 1
\end{aligned}
$$

The derivative of time of flight with respect to the arc length has been neglected, because once a track is fitted the uncertainty on this parameter amounts to about half a ns for a track crossing the whole central detector, and the uncertainty on the arc length amounts to much less than 15 cm. This approximation yields:

$$\frac{\partial t_1}{\partial t_0} = 1$$

Let us stress that for the validity of all the formulae given above the relation $F \cdot F^{-1} \equiv 1$ should hold which implies that one is obliged to use $R^{-1} = \frac{1}{2}(R_0^{-1} + R_1^{-1})$ and $\tan\lambda = \frac{1}{2}(\tan\lambda_0 + \tan\lambda_1)$ when performing these calculations.

3.1.7 Multiple scattering

The main source of random perturbations of a charged track is the multiple Coulomb scattering, that is an elastic scattering of a particle off nuclei of matter.

One of the most important criterion on the quality of the reconstruction program is a good track parameter resolution. Beyond the usage of the correct track model, accounting for multiple scattering in the fit procedure certainly reduces the parameter variances[7]. For this purpose one needs to compute the parameter variance contribution due to multiple scattering when extrapolating from one point to another and use this information during the track fit [102].

Let θ_1 and θ_2 be independent multiple scattering angles in two perpendicular planes (one of them contain the particle's trajectory and the other one is perpendicular to it). After some calculations one can find the relations between our helix parameters (λ and ϕ) and the multiple scattering angles (θ_1 and θ_2):

$$\delta\lambda = \theta_1, \qquad \delta\phi = \frac{\theta_2}{\cos\lambda}$$

[7]This mainly comes from the Gauss-Markov theorem.

These relations can be obtained through the following calculations. Let us define two orthogonal unitary vectors

$$\vec{e}_1 \;=\; \begin{pmatrix} \sin\lambda \\ -\cos\lambda\cdot\sin\phi \\ \cos\lambda\cdot\cos\phi \end{pmatrix} \qquad \text{and} \qquad \vec{e}_2 \;=\; \begin{pmatrix} 0 \\ \cos\phi \\ \sin\phi \end{pmatrix}$$

The third vector can be constructed via:

$$\vec{e}_3 \;=\vec{e}_1\times\vec{e}_2 \;=\; \begin{pmatrix} \cos\lambda \\ \sin\lambda\cdot\sin\phi \\ -\sin\lambda\cdot\cos\phi \end{pmatrix}$$

The multiple scattering effect will change the vector $\vec{e}_1$ to

$$\vec{e}_1\prime \;=\; \vec{e}_1 \;+\; \theta_2\cdot\vec{e}_2 \;+\; \theta_1\cdot\vec{e}_3$$

Using the first two components of this vector, we can state that :

$$\sin\lambda' \;=\; \sin\lambda \;+\; \theta_1\cdot\;\cos\lambda$$

or $\delta\lambda=\theta_1$.
Analogously, from

$$-\cos\lambda'\cdot\sin\phi' \;=\; -\cos\lambda\cdot\sin\phi \;+\; \theta_2\cdot\cos\phi \;+\; \theta_1\cdot\sin\lambda\cdot\sin\phi$$

and

$$-\cos\lambda'\cdot\sin\phi' = -\cos\lambda\cdot\sin\phi' \;+\; \theta_1\cdot\sin\lambda\cdot\sin\phi' =$$
$$-\cos\lambda\cdot\sin\phi\;-\cos\lambda\cdot\delta\phi\cdot\cos\phi\;+\;\theta_1\cdot\sin\lambda\cdot\sin\phi+...$$

it follows that $\delta\phi=\frac{\theta_2}{\cos\lambda}$.

To compute the multiple scattering effect we need two rows of F which correspond to the variations in $\tan\lambda$ and ϕ:

$$F_{\tan\lambda}=\frac{dp_1}{d(\tan\lambda_0)} \qquad \text{and} \qquad F_\phi=\frac{dp_1}{d\phi_0},$$

where

$$F_{\tan\lambda}=(R\cdot(\phi_1-\phi_0),\ 0,\ 0,\ 1,\ 0,\ 0)$$

and

$$F_\phi=(R\cdot\tan\lambda\cdot(\frac{\cos\phi_0}{\cos\phi_1}-1),\ R\cdot(\sin\phi_0-\tan\phi_1\cdot\cos\phi_0),\ 0,\ 0,\ \frac{\cos\phi_0}{\cos\phi_1},\ 0)$$

Taking this into account and using the simplest formula for the standard deviation of the multiple scattering angle distribution [107]

$$\theta=\frac{0.0136\ (GeV)}{\beta p}\cdot\sqrt{\frac{s}{X_0}}\cdot\left(1+0.038\cdot ln\left(\frac{s}{X_0}\right)\right)\approx\frac{0.0136\ (GeV)}{\beta p}\cdot\sqrt{\frac{s}{X_0}}$$

(where s is the arc length along the particle path and X_0 is the radiation length) one can calculate the covariance matrix Q_{MS} due to multiple scattering integrating over the helix trajectory of a particle. For example, the elements of this matrix which originate from a change in $\tan\lambda$ can be expressed in the following way

$$V_{\tan\lambda}(p(i),p(j))=\int_{\phi_0}^{\phi_1}F_{\tan\lambda}(p(i))F_{\tan\lambda}(p(j))(\frac{d\tan\lambda}{d\lambda})^2d\sigma^2(\theta_1)=$$
$$\int_{\phi_0}^{\phi_1}F_{\tan\lambda}(p(i))F_{\tan\lambda}(p(j))\cdot k\cdot(\frac{d\tan\lambda}{d\lambda})^2ds$$

If $i = j$, it is the variance, if $i \neq j$, it is the correlation term.

In other words,

$$V_{\tan\lambda}(x,x) = \int_{\phi_0}^{\phi_1} R^2(\phi_1 - \phi(s))^2 \epsilon_{\tan\lambda}(s) ds \text{ , where}$$

$$ds = \frac{Rd\phi}{\cos\lambda} \text{ , } \epsilon_{\tan\lambda} = k \cdot (\frac{d\tan\lambda}{d\lambda})^2 \text{ , } \frac{d\tan\lambda}{d\lambda} = \frac{1}{\cos^2\lambda} \text{ , } k = (\frac{0.0136GeV}{\beta p})^2 \cdot \frac{1}{X_0}$$

The continues and uniform matter distribution between the positions "0" and "1" is assumed throughout these computations.

One can set $A = \frac{Rk}{\cos^5\lambda}$ and compute all terms of the multiple scattering matrix due to the variation of λ:

$$\begin{aligned} V_{\tan\lambda}(x,x) &= A \int_{\phi_0}^{\phi_1} R^2(\phi_1 - \phi)^2 d\phi = \frac{AR^2}{3}(\phi_1 - \phi_0)^3 \\ V_{\tan\lambda}(\tan\lambda, \tan\lambda) &= A(\phi_1 - \phi_0) \\ V_{\tan\lambda}(x, \tan\lambda) &= \frac{AR}{2}(\phi_1 - \phi_0)^2 \end{aligned}$$

One can then check the overall normalization by computing, for example:

$$V(\lambda) = \cos^4\lambda \cdot V(\tan\lambda) = \frac{kR(\phi_1 - \phi_0)}{\cos\lambda} = ks$$

This matches the well known formula quoted above.

Analogously we can perform the calculations of the covariance matrix due to the variance in ϕ ($B = A \cdot \cos^2\lambda$)

$$\begin{aligned} V_\phi(x,x) &= \frac{BR^2\tan^2\lambda}{2\cos^2\phi_1} \times [-3\sin\phi_1 \cdot \cos\phi_1 + 2\cos^2\phi_1 \cdot (\phi_1 - \phi_0) + (\phi_1 - \phi_0) \\ &\quad - \sin\phi_0 \cdot \cos\phi_0 + 4\sin\phi_0 \cdot \cos\phi_1] \\ V_\phi(y,y) &= -\frac{BR^2}{2\cos^2\phi_1} \times [2\sin\phi_1 \cdot \cos\phi_1 \cdot \cos^2\phi_0 - \sin\phi_1 \cdot \cos\phi_1 \\ &\quad -2\sin\phi_0 \cdot \cos\phi_0 \cdot \cos^2\phi_1 + \sin\phi_0 \cdot \cos\phi_0 - (\phi_1 - \phi_0)] \\ V_\phi(\phi,\phi) &= \frac{B}{2\cos^2\phi_1} \times [\sin\phi_1 \cdot \cos\phi_1 - \sin\phi_0 \cdot \cos\phi_0 + (\phi_1 - \phi_0)] \\ V_\phi(x,y) &= -\frac{BR^2\tan\lambda}{2\cos^2\phi_1} \times [2\sin\phi_1 \cdot \cos\phi_1 \cdot \sin\phi_0 - \sin\phi_0 \cdot \cos\phi_0 \cdot \sin\phi_1 \\ &\quad + \sin\phi_1 \cdot (\phi_1 - \phi_0) + 2\cos^2\phi_1 \cdot \cos\phi_0 - \cos\phi_1 \cdot \cos^2\phi_0 - \cos\phi_1] \\ V_\phi(x,\phi) &= \frac{BR\tan\lambda}{2\cos^2\phi_1} \times [-\sin\phi_1 \cdot \cos\phi_1 + 2\cos\phi_1 \cdot \sin\phi_0 \\ &\quad - \sin\phi_0 \cdot \cos\phi_0 + (\phi_1 - \phi_0)] \\ V_\phi(y,\phi) &= \frac{BR}{2\cos^2\phi_1} \times [\cos^2\phi_0 \cdot \cos\phi_1 - \cos\phi_1 + \sin\phi_0 \cdot \cos\phi_0 \cdot \sin\phi_1 \\ &\quad - \sin\phi_1 \cdot (\phi_1 - \phi_0)] \end{aligned}$$

These results were obtained with the help of the REDUCE program [108] for analytical computations.

In case we want to transport the multiple scattering matrix in the opposite direction (from "1" to "0") along the same trajectory: $Q_{10} = F_{10}Q_{01}F_{10}$, where $F_{ji} = \frac{\delta p_i}{\delta p_j}$. The simpler way to obtain the same result is to change the sign of the Q matrix.

3.1.8 Energy losses

Ionization losses

In order to reach an agreement between the treatment of energy losses in the Monte–Carlo simulation program [80] and the DC reconstruction program in the wide interval of momenta (from several tens of MeV up to several hundred GeV) for all charged particles (except electrons[8]) we decided to use the following formula for the ionization energy losses [109]

$$-\left(\frac{dE}{dx}\right)_{il} = Kz^2\rho\frac{Z}{A}\frac{1}{\beta^2}\left[\frac{1}{2}\ln\left(\frac{(2m_ec^2\gamma^2\beta^2)^2}{I^2(1+2\gamma m_e/M+(m_e/M)^2)}\right)-\beta^2-\frac{\delta}{2}\right]$$

where $K = 4\pi N_A r_e^2 m_e c^2$, z is the charge of the particle, M its mass, ρ the density of the detector and I the average ionization potential. The density correction[9] ($\frac{\delta}{2}$) has been parametrized as described in [80] through formulae depending on I, ρ, γ and Z.

In order to calculate the parameters which depend on the detector composition, the table of density ρ and radiation length X_0 obtained from the detailed GEANT simulation of the NOMAD detector (GENOM package [110]) is used. The value of $\frac{Z}{A}$ versus Z as it comes from the average isotopic composition is also stored. The approximate formula $I = 16Z^{0.9}$ is used to calculate the ionization potential.

The effect of energy loss is implemented as a change of curvature 1/R for a given step. Transition from the standard Bethe formula to the implemented one is done through the following chain of formulae:

$$\frac{d(1/R)}{dx} = -\frac{1}{R^2}\frac{dR}{dx}$$

using $p = 0.003BR/\cos\lambda$ and $\frac{dp}{dx} = \frac{1}{\beta}\frac{dE}{dx}$ (since $E\,dE = p\,dp$), one gets

$$\frac{d(1/R)}{dx} = -\frac{1}{R^2}\frac{\cos\lambda}{0.003B\beta}\frac{dE}{dx}$$

We can also reformulate this expression stating that

$$\frac{d(1/R)}{dE} = -\frac{1}{R^2}\frac{\cos\lambda}{0.003B\beta}$$

Then, over a step of length $\Delta x = R\Delta\phi/\cos\lambda$ the increment to 1/R reads:

$$\Delta(1/R) = \frac{d(1/R)}{dE}\frac{dE}{dx}\Delta x = \frac{(1/R)}{0.003B\beta}\frac{dE}{dx}\Delta\phi$$

One has to check the sign of this $1/R$ increment for the 4 sign combinations of $1/R$ and $\Delta\phi$. Noting that the sign of $\Delta(1/R)$ should be identical to the sign of $1/R$ and that $R\Delta\phi$ is positive, one simply adds an absolute value:

$$\Delta(1/R) = \frac{d(1/R)}{dE}\frac{dE}{dx}\Delta x = \frac{|1/R|}{0.003B\beta}\frac{dE}{dx}\Delta\phi$$

with $\Delta\phi = \phi_{end} - \phi_{start}$.

[8] Estimation of energy losses for electrons is more complicated because of bremsstrahlung effect.

[9] Correction terms ($-\beta^2$) and ($-\frac{\delta}{2}$) are added for completeness. Neither of these effects is important in our case.

Bremsstrahlung losses

The energy loss due to bremsstrahlung (brem) for electrons and positrons[10] was also taken into account:

$$-\left(\frac{dE}{dx}\right)_{brem} = \frac{E}{X_0}$$

where E is the energy of electron and X_0 is the radiation length. One should remember that for electrons the brem energy losses start to dominate over the ionization losses for the energies above the critical energy [27]

$$E_c \approx \frac{800\ MeV}{Z + 1.2}$$

which means that in the NOMAD detector the brem energy losses are important for any electron trajectory above $\sim 100\ MeV$ (any reconstructable track).

Ideally, one would like to define a threshold above which an electron track would be broken and the emitted brem photon would be detected in the electromagnetic calorimeter. In practice, it turn out to be impossible to calculate this threshold since it depends on too many different parameters (such as electron energy, track length, quality of DC alignment, pedestals in the electromagnetic calorimeter, etc.). Thus, we decided to include the whole spectrum of the brem energy losses (E is the reconstructed energy of the electron candidate) in the electron track model.

Following the same steps as in the above calculations of ionization losses, one finds:

$$\Delta(1/R) = \frac{\Delta\phi}{\beta^2 X_0 \cos\lambda},$$

where one could readily approximate $\beta = 1$. For the global sign, a comparison with the above case indicates that the formula is correct.

Now we can try to build an analog of the Q_{MS} matrix which would take into account variations of parameters due to a change in curvature $(1/R)$ during the bremsstrahlung process.

Under the assumption of $1/k$ dependence of the spectrum of the emitted bremsstrahlung photons ($dN/dk = a/k$, where k is the energy of photon), we can calculate the variance of the electron momentum due to the bremsstrahlung effect.

$$\sigma_k^2 =< k^2 > - < k >^2$$

$$< k >= \int_0^E \frac{dN}{dk} \cdot k \cdot dk = a \cdot E = \frac{s}{X_0} \cdot E$$

$$< k^2 >= \int_0^E \frac{dN}{dk} \cdot k^2 \cdot dk = a \cdot \frac{E^2}{2}$$

That is

$$\sigma_k = E \cdot \sqrt{\frac{a}{2} - a^2} = E \cdot \sqrt{\frac{s}{2X_0} - \frac{s^2}{X_0^2}} \approx E \cdot \sqrt{\frac{s}{2X_0}}$$

where s is a step length (normally small).

Using momentum conservation ($\sigma_k = \sigma_p$), we obtain

$$\sigma_{1/R} = \frac{3 \cdot 10^{-3} \cdot B}{p^2} \cdot \sigma_p \approx \frac{3 \cdot 10^{-3} \cdot B}{E^2} \cdot \sigma_E \approx \frac{3 \cdot 10^{-3} \cdot B}{E^2} \cdot \sqrt{\frac{s}{2X_0}}$$

Finally, using the variance on $1/R$ due to bremsstrahlung and taking into account the derivatives in the form

[10] In the following description the term electron implies also to a positron.

$$\begin{aligned}
F_{1/R} \quad = \quad & (R\tan\lambda(\frac{\Delta z}{\cos\phi_1} - R(\phi_1-\phi_0)), \\
& R^2(\cos\phi_0 - \cos\phi_1) - \frac{\sin\phi_1 \Delta z R}{\cos\phi_1}, \\
& 1, \\
& 0, \\
& \frac{\Delta z}{\cos\phi_1}, \\
& 0)
\end{aligned}$$

we can follow the same technique as the one used for the Q_{MS} computation and obtain elements of the analogous Q_{brem} matrix:

$$\begin{aligned}
V_{1/R}(x,x) &= \alpha R^2\tan^2\lambda\cdot\left[\left(\frac{\Delta z}{\cos\phi_1}\right)^2(\phi_1-\phi_0) - \frac{\Delta z R}{\cos\phi_1}(\phi_1-\phi_0)^2 + \frac{R^2}{3}(\phi_1-\phi_0)^3\right] \\
V_{1/R}(y,y) &= \alpha\frac{R^4}{2\cos^2\phi_1}\cdot[4\sin\phi_1\cos\phi_1\sin\phi_0\frac{\Delta z}{R} - 3\sin\phi_1\cos^3\phi_1 + \\
& 4\sin\phi_1\cos^2\phi_1\frac{\Delta z}{R}(\phi_1-\phi_0) + 4\sin\phi_0\cos^3\phi_1 - \sin\phi_0\cos^2\phi_1\cos\phi_0 + \\
& 2\cos^4\phi_1(\phi_1-\phi_0) + 4\cos^3\phi_1\frac{\Delta z}{R} - 2\cos^2\phi_1\left(\frac{\Delta z}{R}\right)^2(\phi_1-\phi_0) + \\
& \cos^2\phi_1(\phi_1-\phi_0) - 4\cos\phi_1\frac{\Delta z}{R} + 2\left(\frac{\Delta z}{R}\right)^2(\phi_1-\phi_0)] \\
V_{1/R}(1/R,1/R) &= \alpha(\phi_1-\phi_0) \\
V_{1/R}(\phi,\phi) &= \alpha\left(\frac{\Delta z}{\cos\phi_1}\right)^2(\phi_1-\phi_0) \\
V_{1/R}(x,y) &= \alpha\frac{R^4\tan\lambda}{2\cos^2\phi_1}\cdot[\sin\phi_1\cos\phi_1\frac{\Delta z}{R}[(\phi_1-\phi_0)^2+2] - 2\sin\phi_1\left(\frac{\Delta z}{R}\right)^2(\phi_1-\phi_0) + \\
& 2\sin\phi_0\cos^2\phi_1(\phi_1-\phi_0) - 2\sin\phi_0\cos\phi_1\frac{\Delta z}{R} + \cos^3\phi_1[(\phi_1-\phi_0)^2+2] - \\
& 2\cos^2\phi_1\cos\phi_0 - 2\cos^2\phi_1\frac{\Delta z}{R}(\phi_1-\phi_0)] \\
V_{1/R}(x,1/R) &= \alpha R\tan\lambda\cdot\left[\frac{\Delta z}{\cos\phi_1}(\phi_1-\phi_0) - \frac{R}{2}(\phi_1-\phi_0)^2\right] \\
V_{1/R}(x,\phi) &= \frac{\Delta z}{\cos\phi_1}\times V_{1/R}(x,1/R) \\
V_{1/R}(y,1/R) &= \alpha[R^2(\sin\phi_1-\sin\phi_0) - (R^2\cos\phi_1 + R\Delta z\tan\phi_1)(\phi_1-\phi_0)] \\
V_{1/R}(y,\phi) &= \frac{\Delta z}{\cos\phi_1}\times V_{1/R}(y,1/R) \\
V_{1/R}(1/R,\phi) &= \alpha\frac{\Delta z}{\cos\phi_1}(\phi_1-\phi_0)
\end{aligned}$$

where

$$\alpha = \frac{(3 \cdot 10^{-3} \cdot B)^2 R}{2E^2 X_0 \cos\lambda} = \left[\frac{1}{cm^2}\right]$$

3.1.9 Extrapolator package

Based on the procedure discussed above we have developed an extrapolator package [111] which is heavily used during the track fit, allows to perform the vertex reconstruction and to make the associations between reconstructed objects in NOMAD subdetectors (tracks, clusters, segments, hits, etc). The extrapolator is also used to provide the global detector alignment and calibration, full event reconstruction and particle identification. The precision of the extrapolation is a function of the extrapolation step which was chosen to be 0.5 cm for regions inside the magnetic field and 10 cm in the fieldless areas.

An complementary set of parameters $(\frac{1}{p}, x, y, \frac{p_x}{p_z}, \frac{p_y}{p_z})$ is used to perform extrapolation in the areas without magnetic field. It is also more convenient for the vertex search and fit. The switch from one set of parameters to another one is done automatically depending on the geometrical position of a track and on the strength of the magnetic field.

The magnetic field inside the NOMAD magnet was measured and parametrized by polynomial functions. As a result we can use this magnetic field map during track extrapolation in the NOMAD setup. It was shown that one can consider the magnetic field to be uniform along x (the variations of the field inside the fiducial volume are of the order of a few percent) and neglect the two other components of the field.

To minimize the amount of computations a special DC interface to the extrapolator package was developed. In particular, each track owns a list of extrapolations and updates it according to user requests in such a way that already made computations are not redone. If a track is refitted (as it should be done when its identity radically changes) all previously existed extrapolations are dropped and new ones are created.

Another feature of the track extrapolation which turned out to be useful is the protection against the extrapolation in case a track is fitted as a parent to a vertex with outgoing tracks. Implementation of this approach allowed to provide better matching between NOMAD subdetectors for broken tracks which is important for robust and efficient electron identification since it allows to avoid double counting[11].

3.1.10 Performances of the NOMAD DC reconstruction program.

The chi-squared (χ^2) of the track fit is an important test. In the linear case with normal noise it is exactly χ^2-distributed with $(n-m)$ degrees of freedom, where n is the number of independent measurements and m is the number of estimated parameters. Its importance as a test is based on the fact that it tells us whether the hypothesis that this set of measurements does indeed correspond to a single track should be rejected or accepted. If multiple scattering is well understood and if the detector measurement errors are properly tuned, the distribution of the chi-squared of the fit is in fact χ^2-distributed to a very good approximation. As almost any kind of background has a tendency to increase the χ^2 value, a cut on it is a simple way of detecting mistakes made by the track search.

Implementation of the effects discussed above in the reconstruction program gave us an opportunity to improve the momentum resolution and obtain reasonable

[11] For example, it prevents one from building ghost TRD tracks and applying in vain TRD double track algorithm (see later) which could lead to losses in electron identification efficiency.

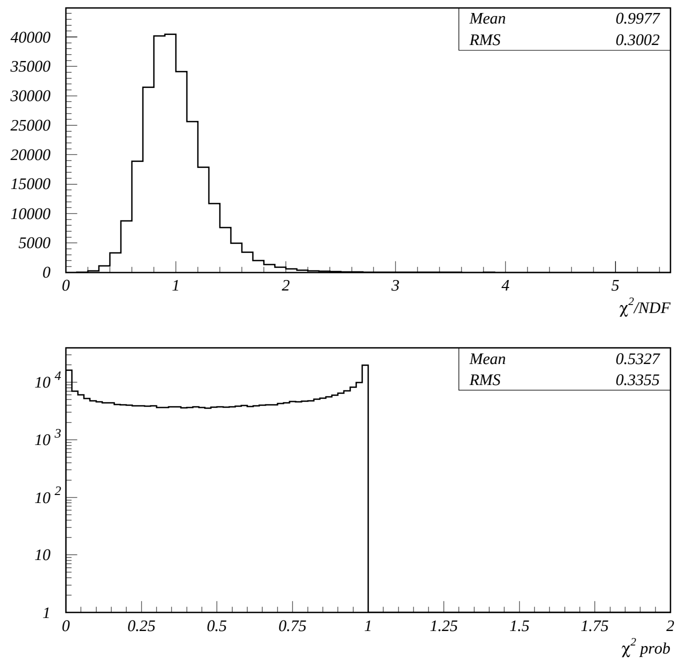

Figure 3.4: Chi-squared and chi-squared probability distributions for muon tracks in the real data.

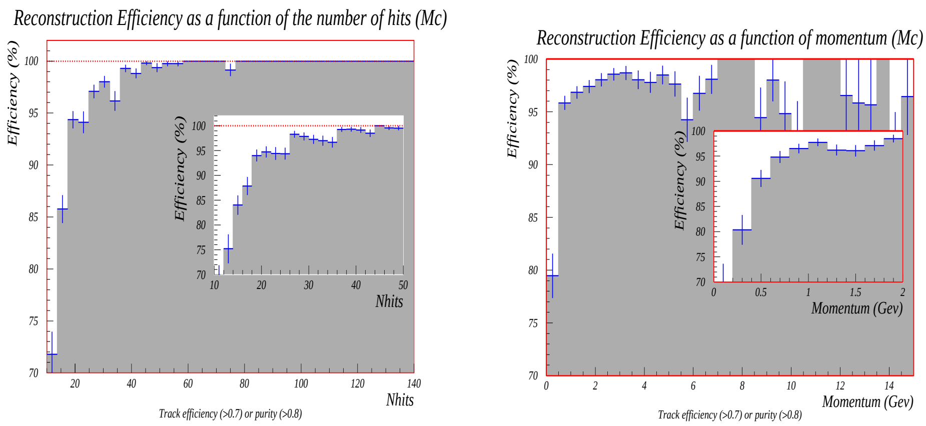

Figure 3.5: The dependence of track reconstruction efficiency on the number of hits in a track (left) and track momentum (right).

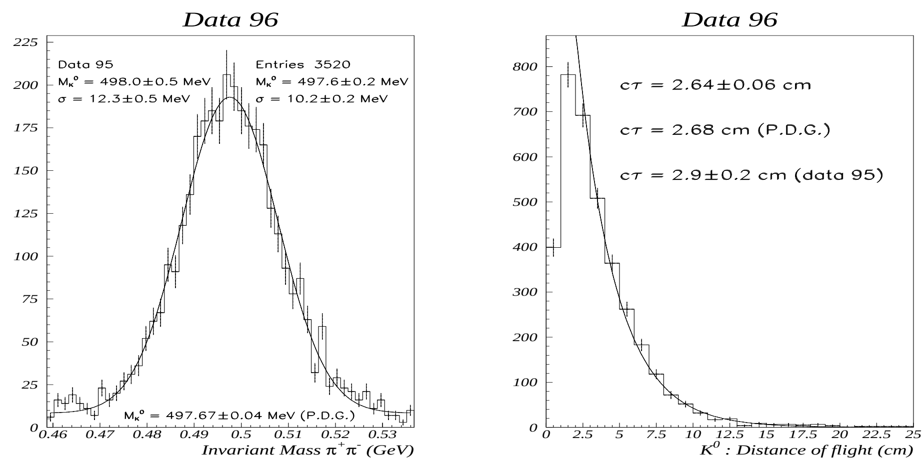

Figure 3.6: Quality of K_S^0 reconstruction in the NOMAD '96 data sample (invariant mass peak and distance of flight). The values obtained with the data from the '95 run are also given for comparison.

distribution for the track χ^2 per degree of freedom (NDF) - χ^2/NDF. As a result the distribution of the reconstructed track probability is almost flat (Fig. 3.4).

Usage of the robust track search algorithm and of the correct track model allowed to reach a high level of reconstruction efficiency. We present here the dependence of the track reconstruction efficiency on the number of hits in a track and on the track momentum (Fig. 3.5) as estimated using Monte-Carlo simulation program. As can be seen from these plots the overall efficiency of the DC reconstruction program is better than 95%. The major losses are due to the low momenta short tracks usually emitted at large angles.

A very powerful tool to check the momentum resolution in the real data was proposed which consists in using the secondary vertices of V^0 type: the widths of the reconstructed K_S^0 (Fig. 3.6) and Λ^0 (Fig. 3.7) mass peaks are directly related to the track momentum resolution. It was found that the measured widths (11 MeV and 4 MeV) are consistent with the estimated momentum resolution $\frac{\sigma_p}{p} \sim 3.5\%$ (Fig. 2.17).

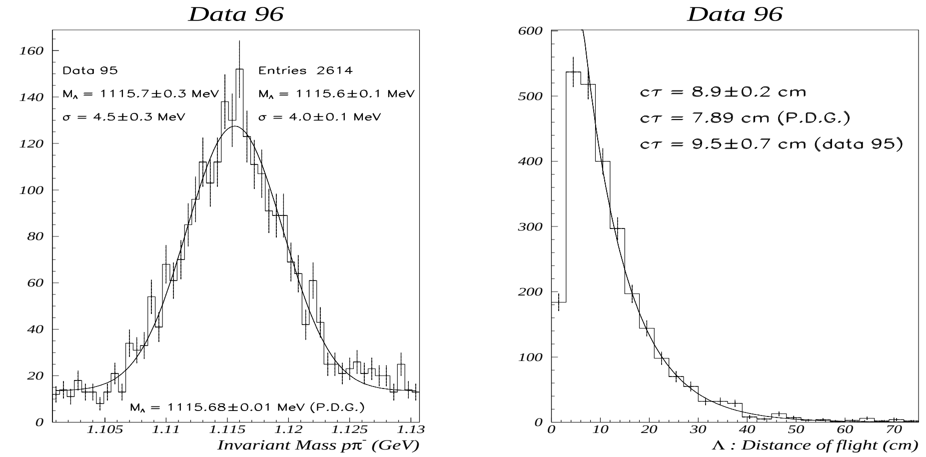

Figure 3.7: Quality of Λ^0 reconstruction in the NOMAD '96 data sample (invariant mass peak and distance of flight). The values obtained with the data from the '95 run are also given for comparison.

3.1.11 Vertex reconstruction

The vertex reconstruction in the NOMAD detector is performed with the help of the vertex finding and fitting package [112] which uses reconstructed DC tracks.

The major tasks of the vertex package are

- determine the event topology (deciding upon which tracks should belong to which vertex);
- perform a fit in order to determine the position of the vertex and the parameters of each track at the vertex;
- recognize the type of a given vertex (primary, secondary, V^0, etc.).

The Kalman filter technique is used to allow fast vertex fit and a simple way to add or remove tracks from an existing vertex without completely refitting it.

Let us mention here the main results of the vertex reconstruction in the NOMAD detector. The detailed information can be found in [86].

Most neutrino interactions in the NOMAD active target occur in the passive panels of the drift chambers. Interaction vertices are reconstructed by extrapolating the tracks of charged particles measured in the chambers. Figure 3.8 shows the distribution of primary vertices in a plane perpendicular to the beam. A fiducial cut of $-120 \leq\ x, y\ \leq 120\ cm$ is imposed. The gradual diminishing of the beam intensity with radius can be easily seen. The nine square spots of high intensity are caused by spacers which are built into the chambers in order to increase their rigidity.

Figure 3.9 shows the distribution of primary vertices along the beam direction. The information from the 11 drift chamber modules has been folded to cover the region of $\sim 10\ cm$ around the centre of each chamber. One can easily see that the bulk of neutrino interactions occurs in the wall of the drift chambers, as expected. The eight 'spikes' in this distribution correspond to the kevlar skins of the drift chambers (see figure 2.7). Regions in z with a low interaction rate correspond to the three gas-filled drift gaps and the honeycomb panels.

The vertex position resolution was checked using MC simulation. The results are presented in Fig. 3.10. We can achieve the resolution of 600 μm, 90 μm and 860 μm in x, y and z respectively.

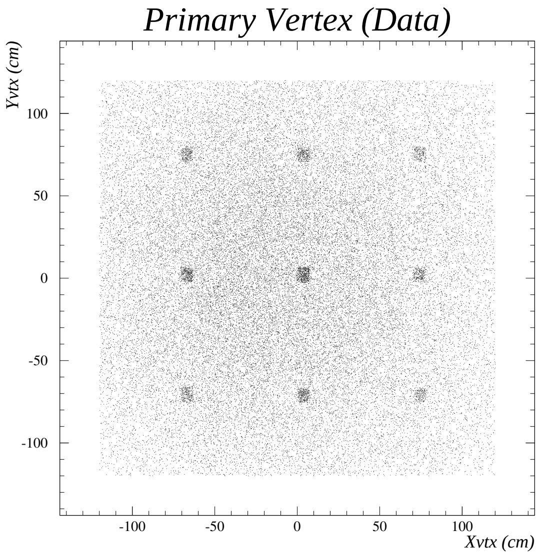

Figure 3.8: The positions of reconstructed neutrino interaction vertices from real data in a plane perpendicular to the beam direction; see text for details.

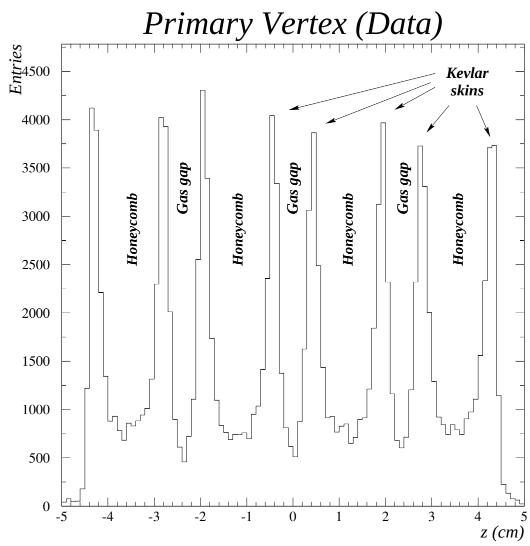

Figure 3.9: The positions of reconstructed neutrino interaction vertices in the real data as measured along the beam direction; see text for details.

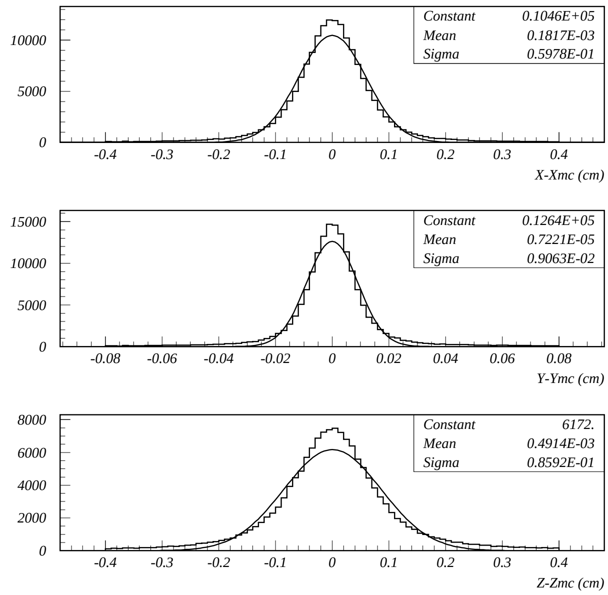

Figure 3.10: The vertex position resolution for reconstructed ν_μ CC MC events. The resolution is 600 μm, 90 μm and 860 μm for x, y and z respectively.

3.2 Particle identification in NOMAD

The physics goals of NOMAD require efficient and robust particle identification (ID). This task was solved with the help of the subdetector matching package described below.

3.2.1 Subdetector matching

Matching of subdetectors information consists in linking together different measurements made by them. The linking being subject to matching criteria that depend both on the considered subdetector and on the current state of the matching itself. Thus the matching procedure must handle feedback in a convenient and flexible way. Moreover one can imagine that the knowledge about a given subdetector measurement imposes some modifications to other subdetector's data. Such modification would occur, for example, when clusterization in calorimeters is making use of the DC tracks and eventually of the associated particle type if it is known. Another example is related to the treatment of electron trajectory in the NOMAD detector: if one has identified a DC track as being an electron then hard bremsstrahlung photons could be looked for and neutral tracks could be created inside the drift chambers requiring further matching with preshower and electromagnetic calorimeter.

Matching process

Matching subdetector's first stage reconstructions (also called "phase 1") mainly consists in trying associations of such reconstructed objects and choosing acceptable combinations to build higher level objects (that happen to be tracks, charged or neutral).

When designing an algorithm that tries all these combinations, one mainly faces two questions:

- since the main output of the matching is particle identification, one should foresee some feedback to the first level processes, for example:
  - the track extrapolation has to account for bremsstrahlung energy losses when the track is identified as an electron. This could require a refit of the reconstructed DC track;
  - π and K decays produce muons that one would like to identify as not being primary ones. A kink finder algorithm could be run on tracks identified as muons;
  - a charged track which is considered as a hadron candidate (not identified as an electron by TRD; depositing energy in the HCAL, or less than its momentum in the ECAL) may require a different cluster finding algorithm (with different patterns) than an electron [113].

  Since this list cannot be a priori complete, one should implement a general feedback mechanism, which is only used when there is a physics requirement.

- Since prototyping of both matching and identification criteria is required, one should avoid as much as possible to hardwire would-be final algorithms. This should ease the merge of subparts of the matching algorithms developed separately.

The steering of the matching process is performed by the so-called matching engine, the program which calls the declared (during the initialization phase) matching routines for each subdetector and checks that they act according to the established rules.

Matching routines

All the matching algorithms are implemented as a set of matching routines (one per subdetector).

The result of matching (MatchObject (MO)) is a collection of subdetector objects (detector object (DO)). A DO may contain more than a single reference to subdetector “phase 1” objects, one can store there a mismatch distance (or more generally a mismatch χ^2), it can also contain references to several subdetector “phase 1” objects: one cluster per projection in the PRS, 2 segments in projections per muon chamber module, etc.

During matching ambiguities may obviously appear. It was decided that a given DO cannot appear in several MO’s (a matching routine trying to do so would trigger a printout and no action would be done). If a subdetector needs to handle ambiguities, then it has to create as many DO’s (with different DO identifiers) as needed which possibly carry or point to the same first stage information. This forces matching routines to do something specific when ambiguities arise. When two DO’s in two MO’s are exclusive one of the other, the physics topics of NOMAD imply that there should be a way either to choose or to detect it[12].

More detailed description on the implementation of the subdetector matching in the NOMAD software can be found in [114].

[12] As an example, we could consider an event where two DC tracks extrapolate to 2 muon chamber segments that share most of their hits (mostly with different signs). If no care is taken, the event becomes a dimuon.

Some distributions

We present here some results making use of the DC track extrapolation into the other subdetectors: TRD, PRS and ECAL (Fig. 2.23). They allow to control the quality of subdetector responses and should be considered as an illustration of the proposed method. For example, we can check the TRD alignment and uniformity of response, study the dependence of the TRD signal on the track momentum and angle (Fig. 3.11). Matching of reconstructed charged tracks with PRS clusters allows to verify the PRS alignment (Fig. 3.12).

Graphics

Most of the reconstruction failures and inefficient matching algorithms can be ruled out by visualizing a few events on a graphic screen. A display is also needed to debug ill matched MC samples. If the clarity of the displayed information has to be a major concern, one should also pay attention to the possibility of accessing detailed information easily. We have been using a rather flexible generic display [115] based on OnX [116] and Ci [117] packages, and a simple and generic method to "dump" drawn objects to a terminal.

3.2.2 Muon identification

Muon identification in NOMAD is an essential and very important task. It is used, for example, for classification of events.

The muon momentum is measured in the drift chambers with a precision of typically 3% for momenta below 20 GeV, where the error is dominated by multiple scattering. For larger momenta the error slowly rises as measurement errors start to dominate, but the muon charge can be reliably measured for momenta up to 200 GeV (see Fig. 3.13).

Track segments are reconstructed from the hits in the muon chambers and the extrapolated central drift chamber tracks are matched to these segments. If this matching satisfies certain quality criteria (e.g. cuts on matching distance and χ^2), which may vary for different analyses, then the track is identified a muon. For a detailed description of the muon matching algorithm see [118]. As can be seen from Figure 3.14, the muon reconstruction efficiency is essentially momentum independent above 5 GeV.

A muon typically leaves a signal in the ECAL which is equivalent to a 500 MeV electromagnetic shower, and a signal in the HCAL equivalent to a 1.4 GeV hadronic shower[13].

It is very important for many NOMAD analyses to identify events which do not contain a primary muon. Very low momentum muons can only be recognized using kinematical criteria. For higher momentum tracks the consistency of the ECAL and HCAL energy deposition can be checked. For muons well above the threshold to reach the chambers, and inside the muon chamber geometrical acceptance, the efficiency to detect at least 2 out of 8-16 possible hits is essentially 100%. As an example, requiring that no muon chamber hits be associated to candidate hadrons within a certain road, and that the energy deposition in the ECAL and HCAL be consistent with a non-minimum-ionizing particle, a residual muon contamination of about 10^{-3} can be achieved for hadrons with $p > 4$ GeV with 90% efficiency.

[13] In both cases, the actual energy depositions are somewhat lower since the calibrations are optimized to measure the energy deposited by electromagnetic and hadronic showers respectively.

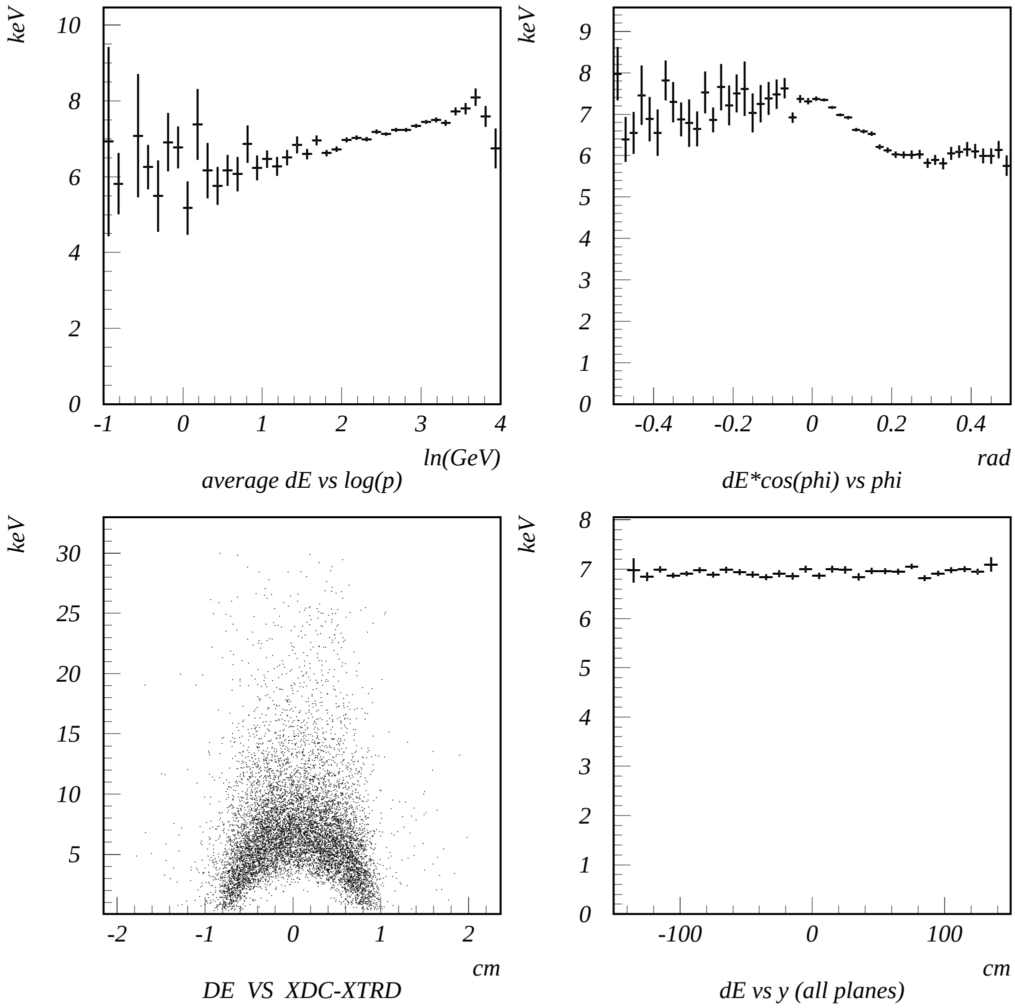

Figure 3.11: Average muon energy loss in one TRD straw (Xenon filled) as a function of momentum: the relativistic rise is clearly visible. Average energy loss as a function of ϕ (opposite of the tangent angle in the vertical plane). Energy loss versus the distance to wire. Average energy loss as a function of y: no obvious dependence.

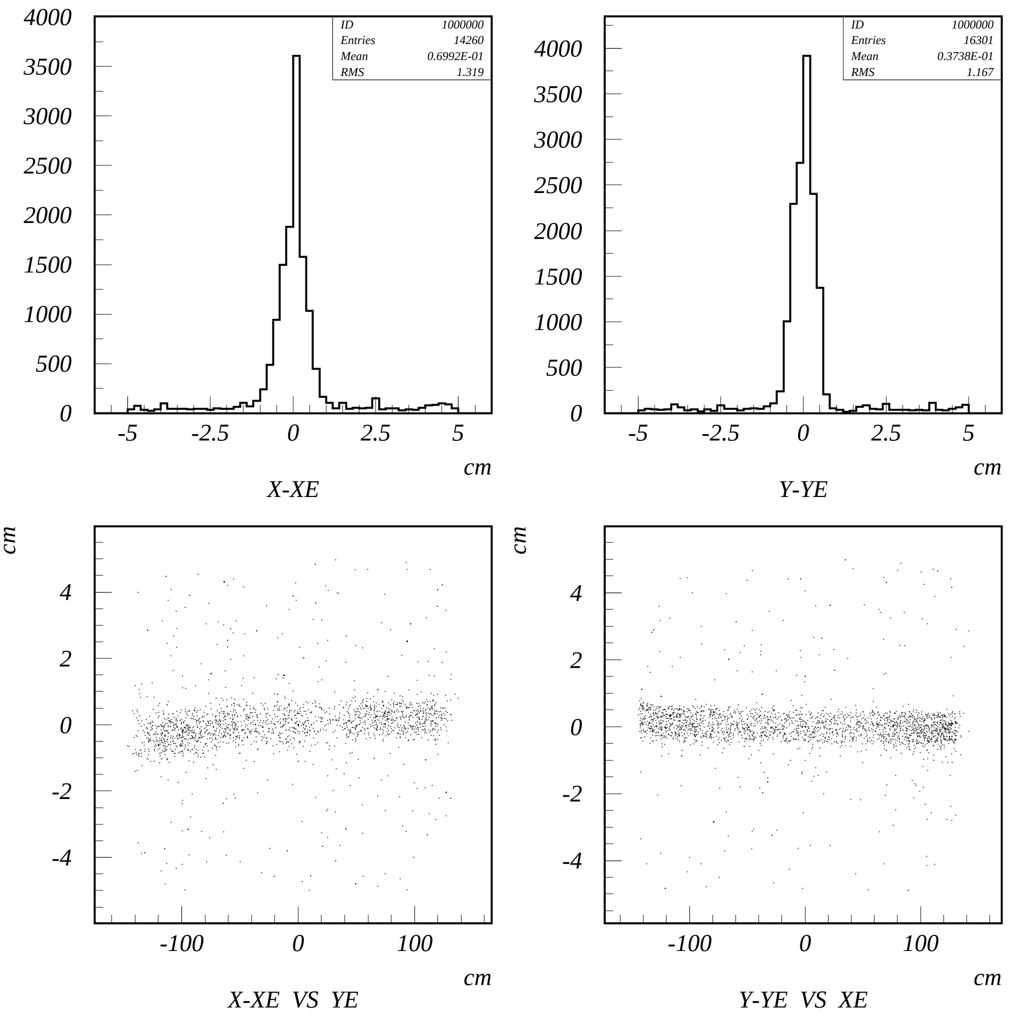

Figure 3.12: Example of PRS alignment for a given run. Residual from the extrapolated DC track position to the PRS cluster in x and y after a displacement of -0.4 cm (x) and -1.3 cm (y) of the PRS. At the bottom, residuals in one coordinate as a function of the other: obviously, the PRS is rotated with respect to the DC frame (by about 0.5 cm over 240 cm).

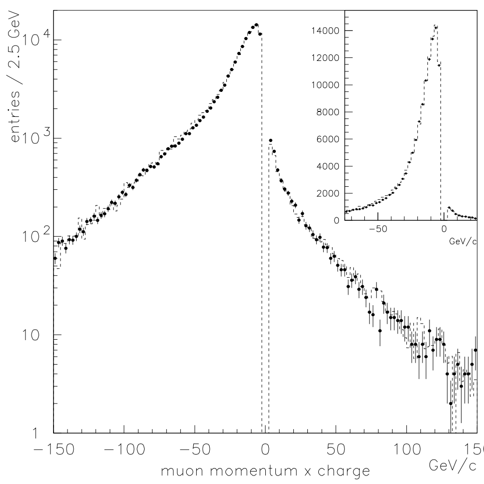

Figure 3.13: Inclusive muon momentum spectrum signed by the charge of the track (comparison of real data and Monte-Carlo simulation).

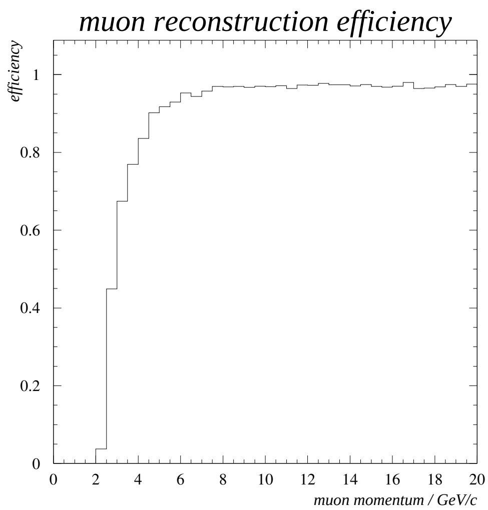

Figure 3.14: Muon reconstruction efficiency as a function of the muon momentum for ν_μ CC events. This includes tracking, vertex association, the probability for a muon to emerge from the iron absorbers, the geometrical efficiency and the matching efficiency (multiple scattering).

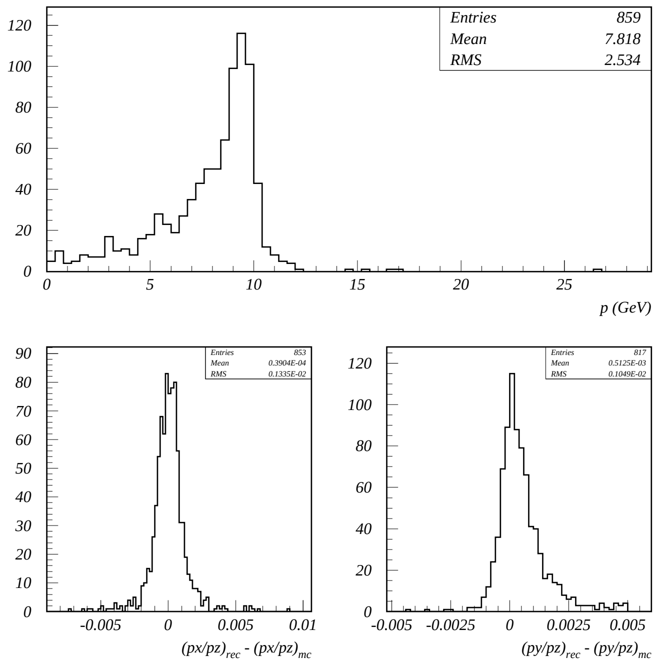

Figure 3.15: Simulated 10 GeV electrons reconstructed using a standard track model ("pion" hypothesis) during the track fit. One can see that both the initial electron momentum and the direction in the bending plane (YZ) are biased.

3.3 Electron identification

The idea of the NOMAD experiment arose from the findings about the possibility of selecting efficiently $\tau^- \rightarrow e^-\nu_\tau\bar{\nu}_e$ events while at the same time keeping the background at a very low level (a few events). This method requires a clean electron identification and measurement. The proposed detector was therefore designed according to the needs of this particular analysis. The use of the hadronic decay modes was explored only later. However the setup that had been proposed turned out to be well adapted to these modes also. Moreover, the possibility of cross-checking the results found in different τ^- decay channels is particularly interesting due to different background conditions.

Nevertheless, the electron decay channel of tau is still believed to be the most powerful tool for the oscillation search in NOMAD. Unfortunately, many potential sources of background coming from isolated e^- exist and have to be taken care of. These are ν_e CC interactions, asymmetric photon conversions, π^0 and η Dalitz decays, Compton and knock-on electrons, μ^-, K_{e3} and π_{e2} decays in flight (the first two being the most important ones).

The search for oscillation signal in the $\tau \rightarrow e$ decay channel requires both efficient electron identification and good reconstruction of the initial electron momentum and direction.

Unfortunately, when the standard approach ("pion" hypothesis during the track fit) is used to treat the electron trajectory both the direction and momentum of this particle at the primary vertex can be biased (see Fig. 3.15). In such a case the use of event kinematics for the oscillation search in the electron decay channel is

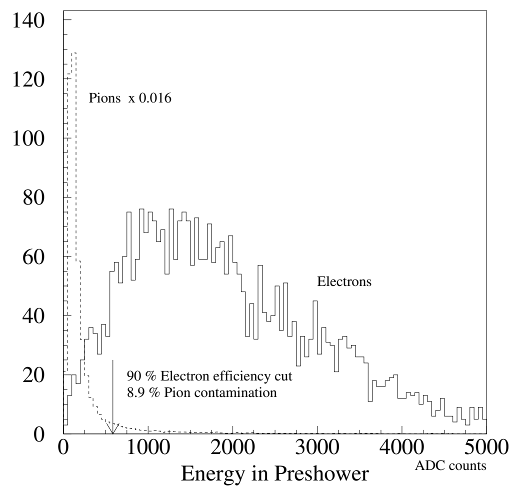

Figure 3.16: Comparison of the preshower response to pions and electrons (test beam measurements).

limited. In other words a special procedure to identify and reconstruct an electron trajectory in NOMAD should be developed. This procedure turned out to be rather complicated and we will try to describe the solutions which were adapted to solve some of the major difficulties.

First of all, we have to identify electrons with good efficiency at the same time keeping the background contamination from misidentified hadrons at the level of $< 3 \times 10^{-6}$. This requirement comes from the total statistics which will be available in NOMAD at the end of data taking (1.15×10^6 of ν_μ CC events and 3.9×10^5 of ν_μ NC events).

3.3.1 Electron identification in NOMAD

Information from the transition radiation detector, preshower and electromagnetic calorimeter is combined to separate electrons from other charged particles. The corresponding algorithms were developed using extensive test beam measurements.

Using the Preshower and the Electromagnetic Calorimeter

A preshower prototype consisting of two layers of 10 tubes each was exposed to beams of electrons and pions at the CERN PS and SPS accelerators [119]. In such a way it was possible to determine the π rejection factor using the PRS signal for a given electron recognition efficiency. It was shown that using the PRS alone for electrons with energy above 4 GeV, it is possible to obtain an electron efficiency of 90% with a π contamination of less than 10% (Fig. 3.16).

The π/e separation is substantially improved when ECAL is used in association with the PRS. In a test beam configuration a particle is accepted as an electron only if the ECAL signal is compatible with the beam energy, within the resolution of ECAL. Combining this requirement with the PRS algorithm a rejection factor of 10^{-3} is obtained in the energy range of $2 \div 10$ GeV, while retaining an overall efficiency to detect electrons at 90%, see Figure 3.17.

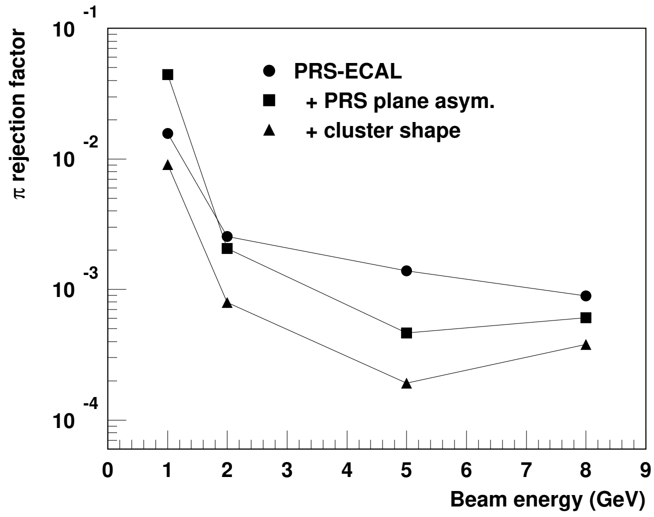

Figure 3.17: The combined pion rejection using PRS and ECAL (test beam measurements).

An additional rejection factor of 2–3 can be obtained using the information on the distribution of energy between the ECAL towers (electromagnetic shower profile) [121].

Unfortunately, these results obtained from test beam measurements are not directly applicable to the real running conditions due to the presence of overlaps in all the relevant subdetectors in case of complicated neutrino interactions.

Using the Transition Radiation Detector

The TRD was designed to separate electrons from other charged particles. The corresponding method is based on the difference in response of the TRD to electrons with respect to other charged particles in the momentum range from 0.5 GeV to 50 GeV. Figure 3.18 shows the response of one TRD straw when crossed by 10 GeV electrons and pions.

Discrimination between the two hypothesis is done computing a likelihood ratio $\mathcal{L}$ (see Fig. 3.19) computed from the responses of all the straws crossed by an incident particle.

$$\mathcal{L} = \sum_{i=1}^{N} ln \frac{P(\varepsilon_i \mid e)}{P(\varepsilon_i \mid \pi)} \tag{3.1}$$

where:

- N is the total number of straw tubes crossed by the charged particle and included in the TRD track ($N \leq 9$);
- ε_i is the energy deposited in the i-th straw tube along the e^- trajectory;
- $P(\varepsilon_i \mid e)$ and $P(\varepsilon_i \mid \pi)$ are the probabilities for an electron e and a pion[14] π to deposit the energy ε_i in the i-th TRD plane.

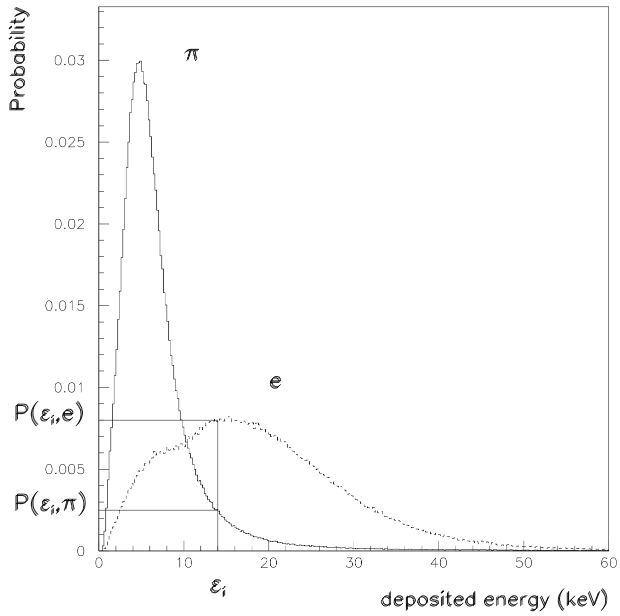

Figure 3.18: Energy deposited in a TRD straw by 10 GeV electrons and pions. (Monte-Carlo simulation).

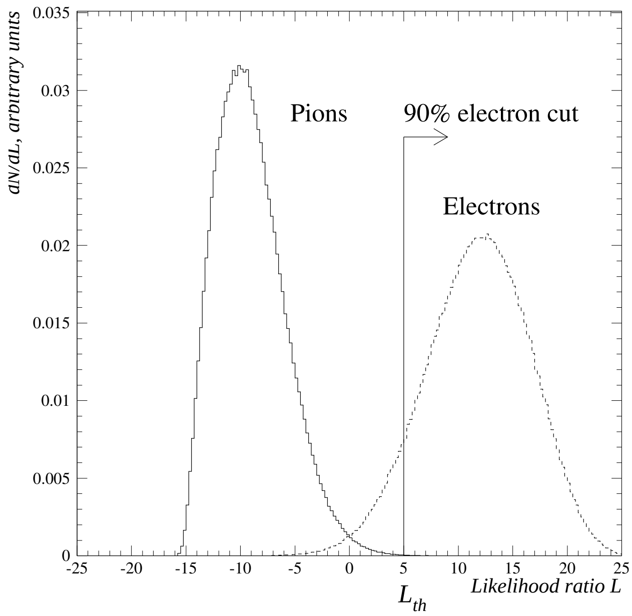

Figure 3.19: The likelihood ratio distributions for pions and electrons of 10 GeV crossing 9 TRD modules (Monte-Carlo simulation).

As can be seen from Fig. 3.19, the desired electron efficiency defines a threshold on the likelihood ratio and gives the rejection power against charged hadrons.

The transition radiation and ionisation loss spectra for energy depositions in the straws were obtained by simulations and were confirmed by test beam measurements.

With a 90% electron detection efficiency, the NOMAD TRD reaches a 10^{-3} rejection factor for isolated tracks in the $0.5 \div 50\ GeV$ momentum range [93].

From the description of the algorithm one can see that a correct association of TRD tubes to a studied track is extremely important for the robust and efficient electron identification.

3.3.2 Building of TRD tracks out of extrapolated DC tracks

This task was solved using extrapolated DC tracks and a matching technique. During the event reconstruction in NOMAD detector there is a strong interference between DC and TRD information. At the early stage of "phase 1" reconstruction the information about the x coordinate as measured by the reconstructed TRD tracks is used to help building DC tracks [101] in the so-called TRD region of the active target.

The standalone TRD reconstruction program [120] was designed to build tracks in TRD which are then associated to DC tracks to provide particle identification [90]. Unfortunately, in case of complicated neutrino interactions with high multiplicity it could happen that several particles cross the same set of TRD straw tubes (TRD overlap). If this information is lost (which is the case if one uses standalone TRD reconstruction only) then the particle identification can be wrong since the energies deposited by several particles are summed up and the probability of misidentification is significantly higher. This problem was solved partially by using reconstructed DC tracks to collect TRD hits along the extrapolation road and construct TRD tracks[15]. For example, there could be two or more TRD tracks built out of the same TRD straw tube hits. In such a case a special algorithm [90] which takes into account all the available information about particles momenta, number of shared hits, etc. can be applied. This approach improves significantly the purity of identified electrons/positrons. For example, this technique together with the TRD double track algorithm decreases the number of $\pi\&\pi$ overlaps misidentified as $e\&e$ from 95% to ~1% [90].

As a result we can state that combining the information from the NOMAD subdetectors (DC, TRD, PRS and ECAL) we can reach the required rejection power against hadrons keeping the electron identification efficiency at a reasonable level.

3.4 Electron reconstruction

The proposed matching algorithm is especially useful for identification and reconstruction of electron/positron trajectory in the NOMAD setup.

3.4.1 Special treatment of electron trajectory

Several different approaches have been tried for electron identification and reconstruction. The simplest one is when an electron is reconstructed as one piece at the

[14]The term pion implies any charged particle except an electron.

[15]This is done at the level of matching making use of the good precision on the extrapolated DC track position (of the order of 1 mm, Fig. 3.20) which is much better than the diameter of the TRD straw tube.

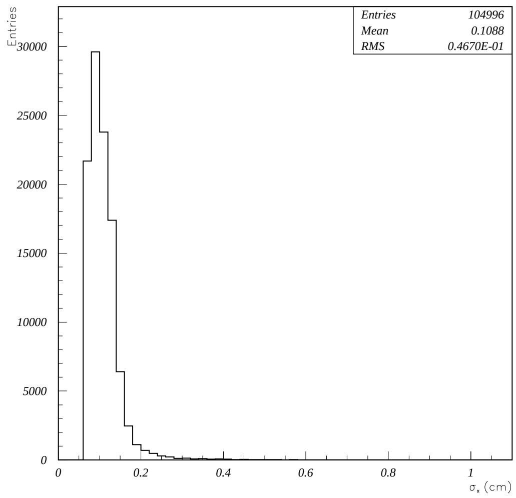

Figure 3.20: Uncertainty on the x coordinate of the extrapolated DC track position in a TRD measurement plane is of the order of 1 mm which is much better than the diameter of the TRD straw tube (1.6 cm).

first pass of the DC reconstruction and identified by TRD during matching. Then we can refit this track adding the Q_{brem} matrix calculated above to the process noise of Kalman filter. While the initial direction of the electron is determined rather well, unfortunately, the initial momentum resolution is quite poor: $\sigma(p)/p \sim 15\%$ (see Fig. 3.21).

In case an electron trajectory was broken into several pieces during the first pass of DC reconstruction and only the last segment was identified as being an electron, we scan the track/vertex structure upstream and update the track type for all the segments if they are connected via vertices of a special type.

In order to improve the momentum resolution another method can be tried which consists in using recursively a breakpoint search algorithm for the identified electron trajectory. One should point out that another track model should be used in this case, since the track model which takes into account brem energy losses destroys the information needed for the breakpoint search algorithm. Thus, we were obliged to introduce one more track model which assumes the electron mass and no brem energy losses. The new approach works in the following way. First, we create a chained track/vertex structure breaking the original trajectory at the most probable breakpoint locations (which correspond to emission of relatively hard bremsstrahlung photons) and joining new segments with vertices of special (BREM) type. Second, we associate when possible to these vertices bremsstrahlung photons reconstructed either from standalone ECAL clusters or from reconstructed conversions in the DC fiducial volume. Let us point out that additional tools to deal with neutral tracks were needed in order to develop this approach. An example of application of this more sophisticated technique to an event from real data is given in Fig. 3.22 and Fig. 3.23.

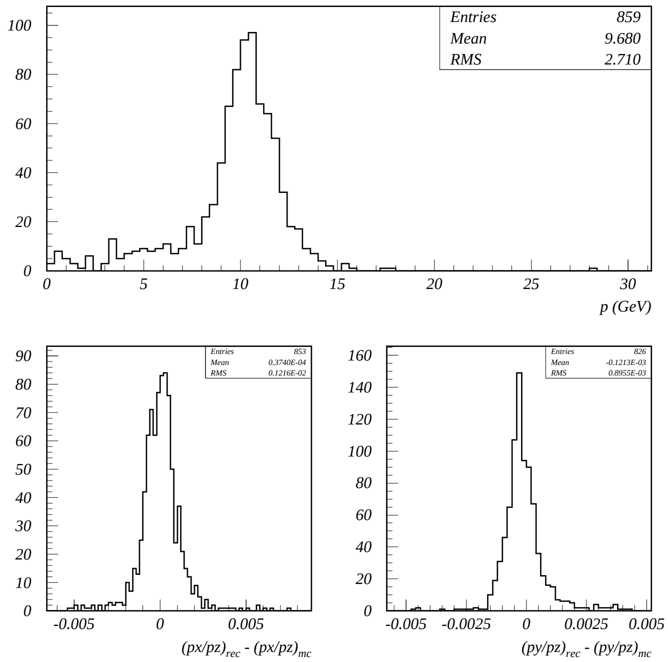

Figure 3.21: Simulated 10 GeV electrons reconstructed using special track model ("electron" hypothesis) which takes into account brem energy losses during the track fit. The primary electron direction is better reconstructed compared to the "pion" track model (see Fig. 3.15). The reconstructed initial electron momentum is also closer to the simulated value while the momentum resolution is rather poor.

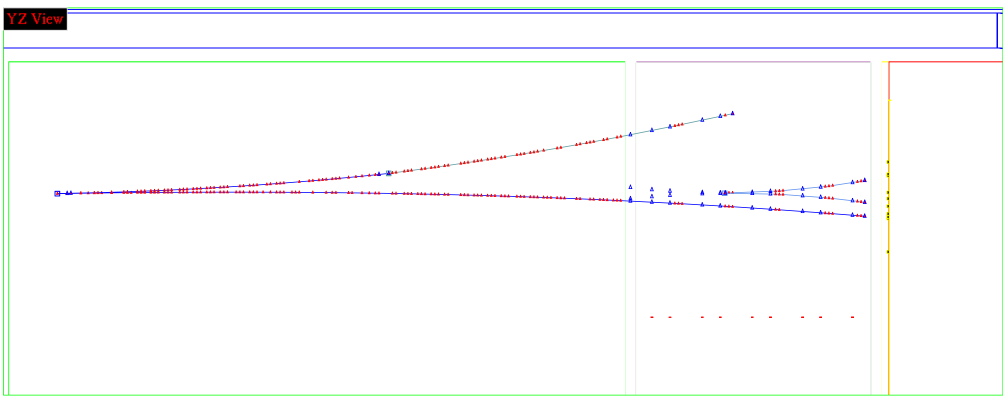

Figure 3.22: Run 10409 Event 22765 (YZ view) from real data before an attempt to apply breakpoint search algorithm. The track at the bottom was identified as an electron by TRD.

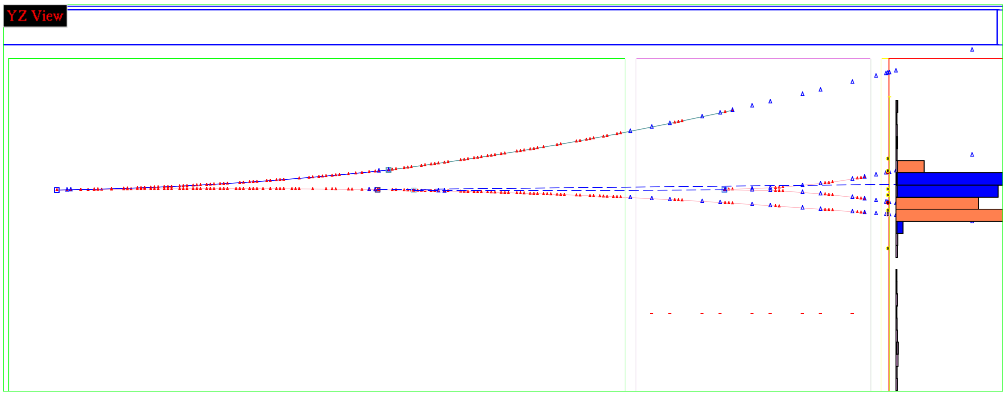

Figure 3.23: Run 10409 Event 22765 (YZ view) after applying a recursive breakpoint search algorithm. Two breakpoints were found along the electron trajectory and they were associated with two photons: one built out of a conversion inside the DC fiducial volume and the other from a standalone ECAL cluster.

3.4.2 Neutral tracks

As it was mentioned above, neutral tracks are important ingredients of the NOMAD reconstruction program since:

- they allow to provide a unified way for calculation of the event kinematics;
- can be a given type of identified "V^0" vertices in order to perform analysis of strange particles production. The criteria used for the identification of the vertices of V^0 type are described in [86];
- they allow to resolve some of the problems in reconstruction of the event kinematics (such as missing momentum in the transverse plane) by attaching neutrals to other vertices than the primary;
- they allow the representation of electron/positron trajectory in the NOMAD detector as a chain of charged track/vertex/(charged & neutral tracks) and help in the determination of
  - the initial direction of electrons using the information from the first charged segment;
  - the initial momentum summing up all the electromagnetic energy seen in the ECAL associated to the chain of charged segments and neutral tracks representing bremsstrahlung photons (which could be built out of identified conversions or ECAL clusters);
  - the proper ECAL energy association avoiding the double counting of brem clusters and electron momentum.

Special tools have been developed within the framework of the DC reconstruction program to build, extrapolate and draw neutral tracks. In the current implementation neutral tracks are created during the matching procedure and the decision about the attachment of these tracks to vertices is taken by the corresponding matching routines. We build neutral tracks out of

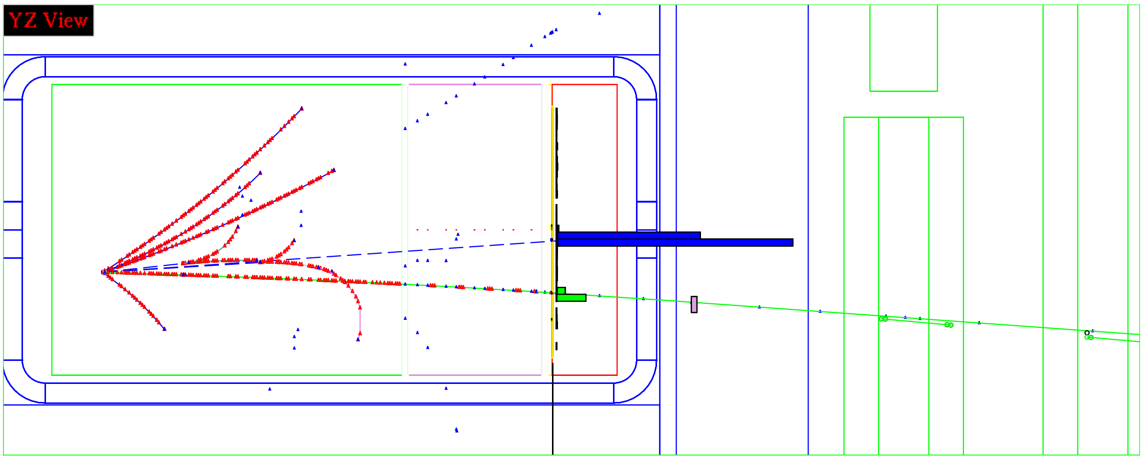

Figure 3.24: A fully reconstructed ν_μ-CC candidate (run 9753 event 81). The longest track at the bottom is a muon matched to the segments in muon chambers; small triangles are track extrapolations. Three photons (dashed lines) were built: one out of the standalone ECAL cluster, the two others from conversions inside the DC fiducial volume.

- clusters in the electromagnetic calorimeter not associated to any charged track;
- vertices of V^0 type consistent with the hypothesis of K_S^0 or Λ^0 decays or photon conversions if they point to a vertex;
- secondary vertices with no incoming charged track which could be interpreted as an interaction of a neutral hadron;
- hanging single charged tracks pointing to the primary vertex which represent asymmetric photon conversions.

An example of an event from real data containing three photons (one built out of the standalone ECAL cluster and the two others from conversions inside the DC fiducial volume) is shown in Fig. 3.24.

3.4.3 Breakpoint search

Another ingredient of the proposed method for the electron reconstruction is a breakpoint search algorithm allowing to find the most probable location of hard brem photon emission. Let us consider this problem in a more general way.

We define a kink (or a "breakpoint") to be a sudden change of the state vector, that is a point where one or more of the track parameters has a measurable discontinuity, and we consider three physical processes which may have different signatures:

- an electron emitting a bremsstrahlung photon generally changes only $1/R$ since this photon is collinear with the electron direction;
- a pion under a hard elastic scattering may have $1/R$ unchanged while changing $\tan\lambda$ and ϕ;

- a charged pion or kaon decaying to muon changes $1/R$, $\tan\lambda$ and ϕ.

The main purpose of the breakpoint search is to allow the detection and proper handling of these physical processes.

The information provided by the filter and smoother after the DC track fit is sufficient to allow the construction of a fast and relatively efficient kink finding algorithm. At the end of the track fit a significant amount of information exists at every hit on the track: track parameters estimated from the upstream segment, from the downstream segment and from the whole track.

If the kink occurs somewhere between measurements k and $k+1$ we may expect that the state vector $\widetilde{x}_k$ obtained from the upstream track segment $\{m_1, ..., m_k\}$ is different from the backward extrapolation $\widetilde{x}_k^{k+1\ (b)}$ of the downstream track segment $\{m_{k+1}, ..., m_n\}$. In order to decide whether a kink has occurred between measurements k and $k+1$ we can test if the difference

$$\Delta_k = \widetilde{x}_k^{k+1\ (b)} - \widetilde{x}_k$$

is significantly different from 0 by means of the χ^2 statistics [102]:

$$\chi^2_{k,\Delta} = \Delta_k^T (cov\{\Delta_k\})^{-1}\Delta_k = \Delta_k^T (C_k + C_k^{k+1\ (b)})^{-1}\Delta_k = \Delta_k^T C_k^{-1}(C_k - C_k^n) C_k^{-1}\Delta_k$$

The equivalent but easier way to calculate $\chi^2_{k,\Delta}$ is:

$$\chi^2_{k,\Delta} = \chi^2_n - \chi^2_k - \chi^{2\ (b)}_{k+1}\ ,$$

where χ^2_n, χ^2_k and $\chi^{2\ (b)}_{k+1}$ are the total chi-squared of the whole track, of the first segment and of the second segment respectively.

If there is no kink, $\chi^2_{k,\Delta}$ follows a χ^2 distribution with the number of degrees of freedom equal to the dimension of Δ_k.

This test, however, is not robust against an outlier somewhere along the track. Another possibility would be to modify this test requiring that both track segments $\{m_1, ..., m_k\}$ and $\{m_{k+1}, ..., m_n\}$ have small total χ^2 and that $\chi^2_{k,\Delta}$ is large. The combination of this information into one variable gives:

$$F_{k,\Delta} = \frac{(\chi^2_{k,\Delta}/n_{df})}{[(\chi^2_k + \chi^{2\ (b)}_{k+1})/n_k]}\ ,$$

where n_k is the sum of the respective number of degrees of freedom for the first and second segments.

Unfortunately, neither criteria gives a correct answer if there are several breakpoints or outliers along the trajectory. On top of that the $\chi^2_{k,\Delta}$ and $F_{k,\Delta}$ criteria mix all the parameter mismatch information together and are insensitive to the arithmetic sign of the difference between parameters and thus are not optimal for our case.

A different approach [122] was tried in order to obtain and examine the result one would get by doing a traditional fit which uses all hits, but which allows one or more of the track parameters to be discontinuous at a particular hit k. Corresponding to the three physical processes mentioned above, we consider describing the track at hit k with 7, 8 or 9 parameters:

- 7 parameters: $\{x, y, 1/R_F, 1/R_B, \tan\lambda, \phi, t_0\}$
- 8 parameters: $\{x, y, 1/R, \tan\lambda_F, \tan\lambda_B, \phi_F, \phi_B, t_0\}$
- 9 parameters: $\{x, y, 1/R_F, 1/R_B, \tan\lambda_F, \tan\lambda_B, \phi_F, \phi_B, t_0\}$

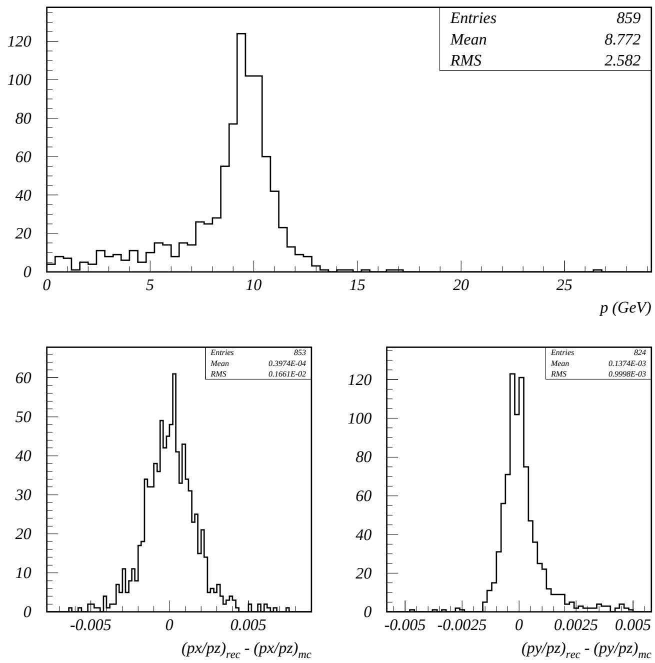

Figure 3.25: Simulated 10 GeV electrons reconstructed using a track model which assumes an electron mass and no brem energy losses and considering only the 30 first hits during the track fit.

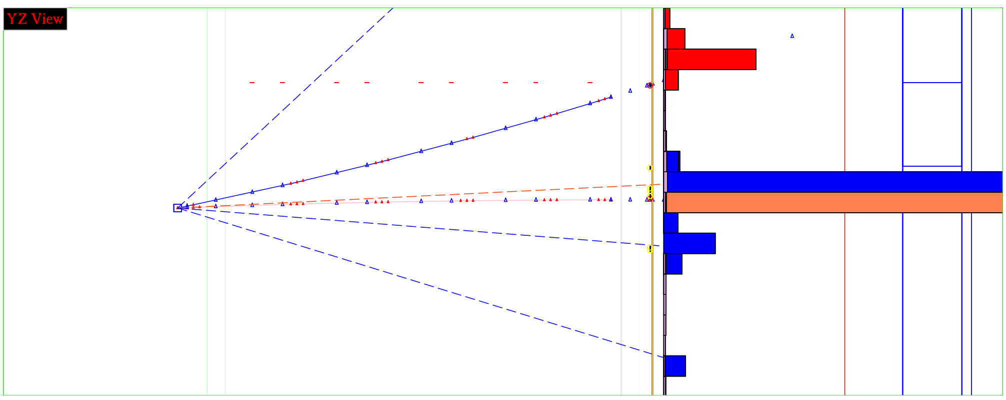

Figure 3.26: Run 10037 Event 2084 (YZ view) from real data showing the limitation of the breakpoint search algorithm. There are only 18 hits in the electron track which is clearly not enough.

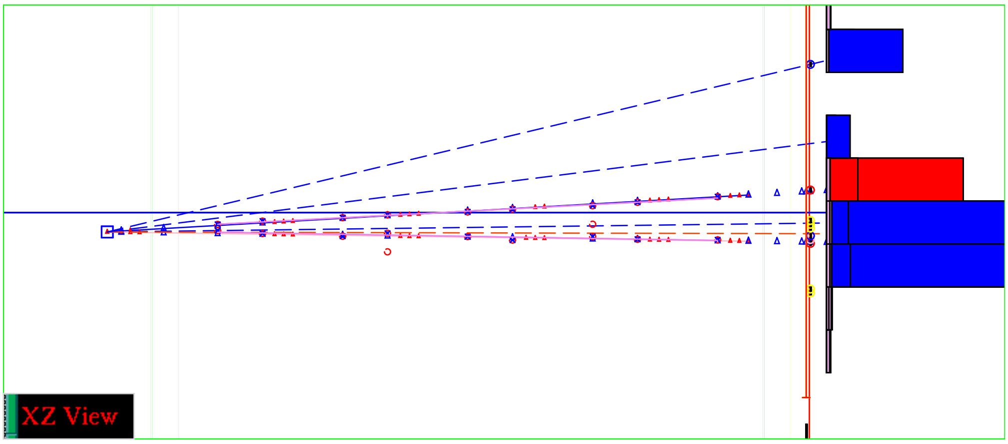

Figure 3.27: Run 10037 Event 2084 (XZ view) from real data showing the limitation of the breakpoint search algorithm. There are only 18 hits in the electron track which is clearly not enough.

where subscripts $_F$ and $_B$ denote the parameters forward and backward of hit k.

This method provides a large amount of useful information. But the decision upon the correct variables to use and the possible cut position is not easy. It requires additional studies, preferably using the real data rather than simulation.

We have implemented the algorithm to treat an electron trajectory in the following way. For identified electrons a recursive breakpoint search algorithm is applied. If the most upstream segment is still longer than 40 hits we will force a break after 30 hits to estimate the initial electron direction in a better way (see Fig. 3.25). Brem photons built out of identified conversions inside the DC fiducial volume and from standalone ECAL clusters will, whenever possible, be attached to the corresponding vertices along the electron trajectory. The electron momentum is then determined by summing all the energy downstream in the electromagnetic calorimeter while the initial electron direction is taken from the first DC segment.

The limitation of this approach is illustrated with an event from real data (Fig. 3.26 and Fig. 3.27). There are only 18 hits in the electron trajectory which is clearly not enough to perform a breakpoint analysis. Consequently a hard brem photon is attached to the primary vertex and is associated to the hadronic jet messing up the calculation of the event kinematics.

In order to overcome this problem we decided to associate all the photons (built out of the reconstructed conversions or from the clusters in ECAL) with the electron/positron candidate if they are emitted in a cone of 2.5 degrees with respect to the charged track identified as an electron by TRD. The final momentum resolution obtained ($\frac{\sigma_p}{p} \approx 5\%$) is shown in Fig. 4.11 (see later).

A complementary algorithm to the one used for the tracking of electron candidate was developed for the electron energy reconstruction in the electromagnetic calorimeter [124]. The energy is obtained as the sum of the energies of the primary electron candidate (using nonet, that is 3×3 cell matrix centered around the electron impact point) and of the associated brem photons using the so-called brem strip algorithm (the electromagnetic energy deposition in the bending plane consistent with converted or unconverted brem photons emitted by the primary electron). The performance of this method is illustrated in Fig. 3.28. The brem strip algorithm provides very good electron energy resolution of $\sim 2.3\%$ for isolated primary electrons, while the performance of this method in case of overlaps between

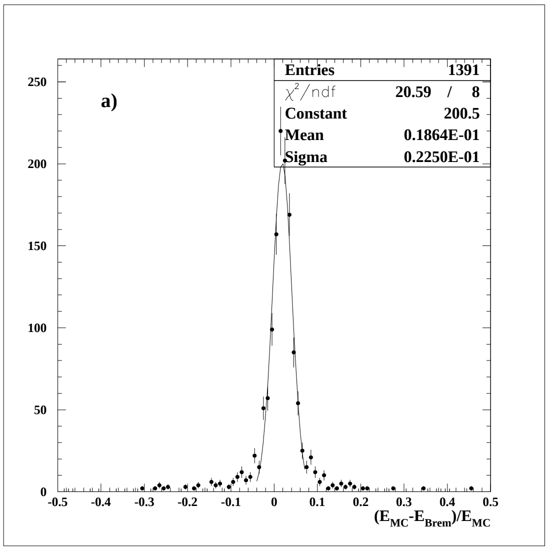

Figure 3.28: Distribution of $\frac{\Delta E}{E} = \frac{E_{MC}-E_{BREM}}{E_{MC}}$ for simulated ν_e CC events.

electron candidate and the hadronic jet is still under study.

In what follows we will be using the algorithm described earlier which combines the breakpoint search technique with the reconstruction of associated brem photons in the electromagnetic calorimeter. The reason is that we want to know whether that approach is applicable to large data samples where the behaviour of the algorithm on the tails of the distributions could become more important than its ability to reconstruct correctly the central value.

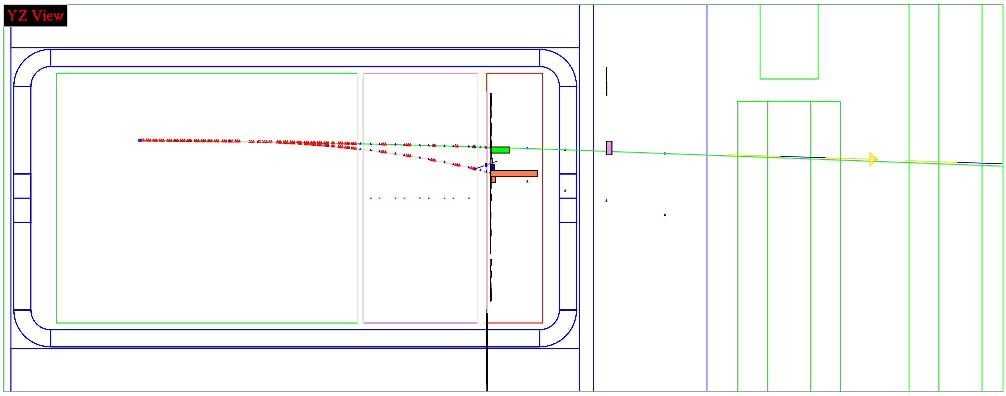

Figure 3.29: Run 8246 Event 20299 from real data shows a muon producing a delta electron in the NOMAD setup.

3.5 Tests of algorithms using electrons from real data

The algorithms developed for electron identification and reconstruction were tested under running conditions using δ-electrons produced by straight-through muons ($5 < p_\mu(GeV) < 50$) crossing the NOMAD detector during the flat top between two neutrino spills. An example of such event is given in Fig. 3.29.

The selection of muons giving δ-rays is done with the help of the matching technique requiring two tracks to be reconstructed in the DC fiducial volume, one of which is positively identified as a muon. The second track is assumed to be an electron. This hypothesis is confirmed by the momentum and angular distributions of the corresponding tracks.

This sample of selected electrons from real data was used to check the subdetectors (TRD, PRS and ECAL) responses compared to simulations, to tune breakpoint search criteria taking into account the effect of DC alignment quality (see Fig. 3.30) and to test the electron tracking algorithm.

The TRD simulation has also been extensively tested in-situ using this event sample [93]. Figure 3.31 shows the distribution of the energy deposited in straw tubes by 5 GeV muons (ionization losses only) and by δ-ray electrons (emitted by muons) with a mean momentum of about 2 GeV (a sum of ionization losses and absorbed TR photons).

We want to stress here that a track of a charged particle can be broken at the emission point of a delta electron. That is why special care was taken in order to propagate the particle ID information in such a case (this is implemented at the level of matching for muons and electrons).

3.6 Reconstruction in the ECAL

In order to provide good measurement of the total energy flow in neutrino interactions it is important to perform correctly the reconstruction in the electromagnetic calorimeter.

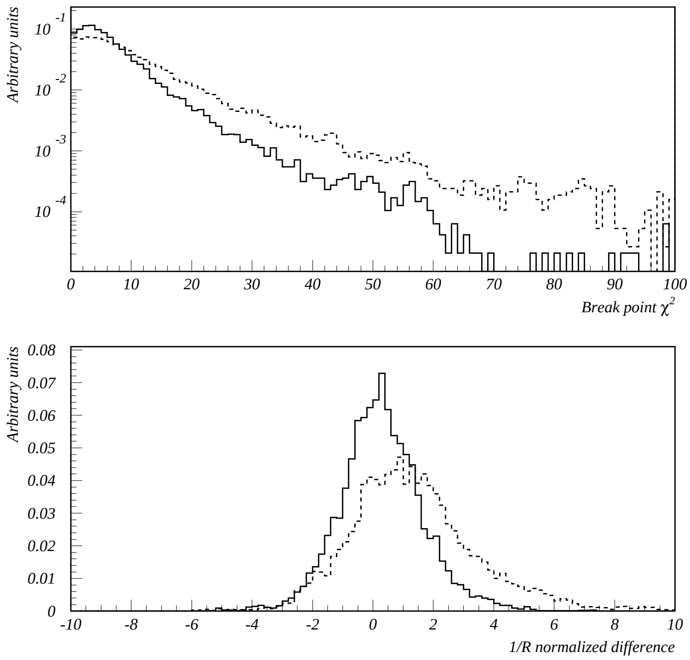

Figure 3.30: Test of breakpoint search criteria using the experimental data (muons producing δ-electrons). Comparison of breakpoint chi-squared ($\chi^2_{k,\Delta}$) and normalized difference between curvatures in backward and forward directions ($\frac{1/R_B-1/R_F}{\sigma_{1/R}}$) for muons (solid line) and electrons (dashed line). One can see the presence of potential breakpoints for electrons (high positive values in both distributions). The typical values of the cuts to actually break a track are 25 and 3 respectively.

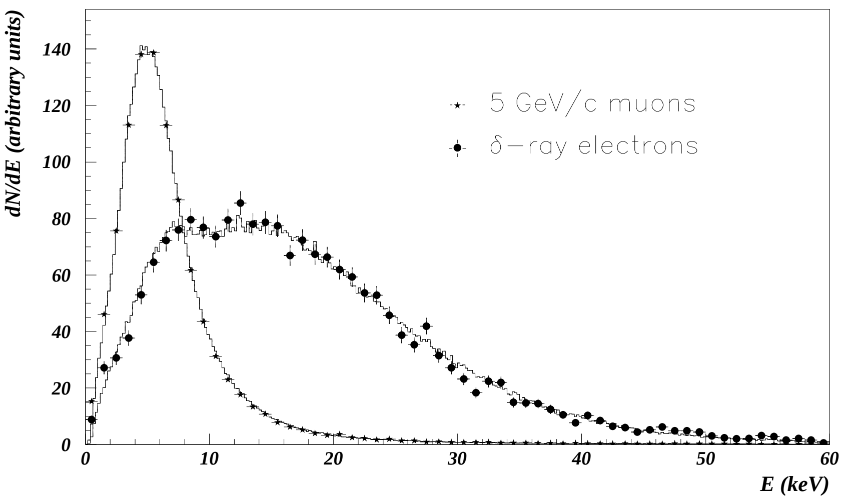

Figure 3.31: Comparison of experimental (points with error bars) and simulated (solid lines) distributions of the energy deposited in the TRD straw tubes by 5 GeV muons and 2 GeV electrons.

When designing a clusterization algorithm, one should keep in mind that for the oscillation search the underestimation of the hadronic energy is preferable. Overestimation of the hadronic vector would create signal-like topology since it introduces a fake missing transverse momentum in the direction of a lepton candidate.

The major problem consists in finding clusters induced by neutral particles entering the calorimeter front face and determining their energy. That is why it was decided to use charged track driven algorithm for the reconstruction in the ECAL. The main idea consists in finding and building clusters associated with charged particles first and performing special clusterization of left over cells using also the information provided by the preshower to indicate the positions of converted photons. This approach allows in some cases to resolve overlaps between charged and neutral particles and even between two neutral clusters.

A diagram showing the algorithm used for the reconstruction in the ECAL is presented in Fig 3.32.

The clusterization in the electromagnetic calorimeter is performed at the level of matching (as soon as the particle ID is known) via the following steps:

- create muon clusters;
- perform the electron clusterization, compute χ^2 for the electromagnetic shower profile;
- find compact electromagnetic clusters corresponding to the photons converted in the PRS;
- perform a hadron subtraction [113] for charged tracks and associate this fraction of energy to charged tracks;
- clusterize the remaining energy to build final photon clusters.

More detailed information on the implementation of this algorithm can be found in [123].

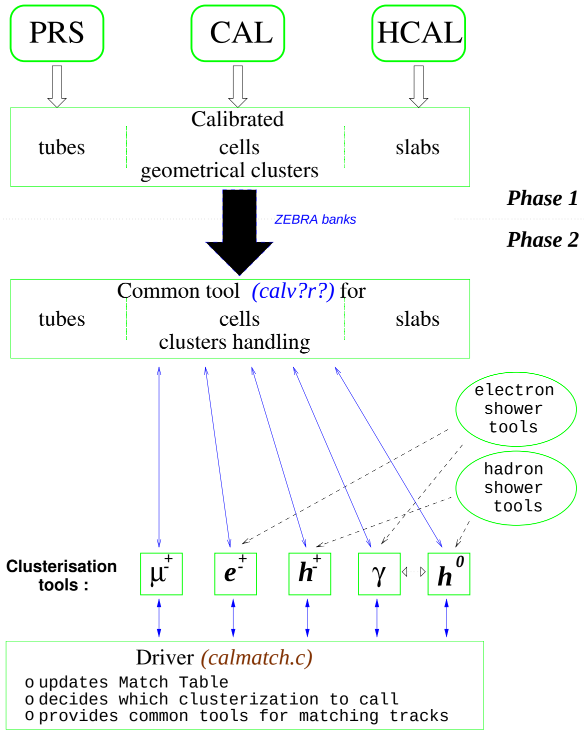

Figure 3.32: Diagram showing the algorithm used for the reconstruction in the ECAL.

3.7 Summary

Algorithms developed for the event reconstruction in the NOMAD experiment were presented.

Charged track reconstruction is done with the help of the system of drift chambers. It provides an overall efficiency of better than 95% and a momentum resolution of $\sim 3.5\%$ in the momentum range of interest. The track model used for the charged track reconstruction was described in detail.

Reconstructed charged tracks are used to perform pattern recognition in the other NOMAD subdetectors. The developed TRD identification algorithm uses the information provided by extrapolated DC tracks and allows to obtain a rejection factor of 10^3 against charged hadrons keeping the electron identification efficiency at the level of 90% (for isolated tracks). An additional hadron rejection power is provided by the system of the preshower and the electromagnetic calorimeter. They are also used to reconstruct electromagnetic showers induced by photons.

The particle identification is done via the developed subdetector matching package. The muon identification efficiency is better than 97% for muon momenta greater than 5 GeV.

Several different approaches to treat an electron trajectory in the NOMAD setup have been tried. The most sophisticated one uses breakpoint search algorithm implemented on the basis of information provided by the Kalman filter and tries to find bremsstrahlung photons either from reconstructed vertices of V^0 type of from neutral clusters in the electromagnetic calorimeter.

The usage of the information provided by the reconstruction program to compute the event kinematics will be discussed in the next chapter.

Chapter 4

Reconstruction of event kinematics

The technique chosen for the oscillation search in the NOMAD experiment relies strongly on the usage of event kinematics to separate a possible signal from background events. That is why it is extremely important to demonstrate that the detector is capable of reconstructing correctly the kinematics of neutrino interactions. Moreover, the efficiency of τ^- detection and the background rejection power are determined using mainly Monte-Carlo simulation. So, we have also to question the reliability of the Monte-Carlo simulation of neutrino interactions in the NOMAD setup.

4.1 Event simulation in NOMAD

A brief reminder on the neutrino-nucleon deep inelastic scattering (DIS) is given below.

4.1.1 Neutrino scattering from a nucleon target

In the Standard Model, the charged current reactions

$$\nu_l N \to l^- X$$
$$\bar{\nu}_l N \to l^+ X$$

are considered to proceed via the exchange of a charged intermediate vector boson. This process is presented by the diagram of Fig. 4.1. In this figure $k = (E, \vec{k})$ represents the 4-momentum of the incident neutrino (antineutrino), $k' = (E, \vec{k}')$ that of the outgoing charged lepton, and $P = (M, 0)$, $p' = (E_h, \vec{p}_h)$ and $q = (q_0, \vec{q})$ the 4-momenta of the target nucleon, hadron final state and exchanged boson respectively.

Let us define the kinematical variables in terms of which lepton-nucleon scattering is generally discussed. The following Lorentz scalars are commonly used:

$$\nu = \frac{P \cdot q}{M}$$
$$Q^2 = -q \cdot q > 0$$

In the laboratory frame ν is simply the energy transfer $(E - E')$ from the neutrino to the charged lepton, and Q^2 is given by

$$Q^2 = 2(EE' - \vec{k}\vec{k}') - m_l^2 - m_{l'}^2 \approx 4EE' \sin^2 \frac{\theta}{2}$$

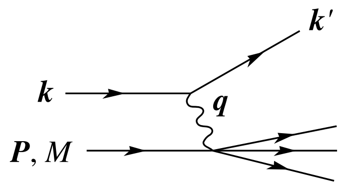

Figure 4.1: Diagram showing the variables used for the description of the kinematics of lepton-nucleon scattering.

where m_l^2 ($m_{l'}^2$) is the initial (final) lepton mass and θ is the lepton scattering angle in the laboratory.

Two further variables are the so-called Bjorken scaling variables:

$$x = \frac{Q^2}{2M\nu}$$

(in the quark-parton model x is the measure of the fractional momentum of the nucleon carried by the struck quark)
and

$$y = \frac{\nu}{E}$$

is the fraction of the lepton energy lost in the laboratory frame (called inelasticity). The invariant mass squared of the hadronic system is given by

$$W^2 = (P+q)^2 = M^2 + 2M\nu - Q^2 = M^2 + Q^2(\frac{1}{x} - 1)$$

The total energy squared in the centre of mass frame is

$$s = (k+P)^2 = 2ME + M^2 = \frac{Q^2}{xy} + M^2$$

In terms of x and y the differential cross section of (anti-)neutrino - nucleon scattering can be written as

$$\frac{d^2\sigma^{\nu,\bar{\nu}}}{dxdy} = \frac{G^2ME}{\pi}\cdot(\frac{m_W^2}{m_W^2+Q^2})^2\cdot[2xF_1^{\nu,\bar{\nu}}(x,Q^2)\frac{y^2}{2}+F_2^{\nu,\bar{\nu}}(x,Q^2)(1-y-\frac{Mxy}{2E})\pm xF_3^{\nu,\bar{\nu}}(x,Q^2)y(1-\frac{y}{2})]$$

The introduction of the superscripts ν, $\bar{\nu}$ emphasises that the structure functions F_i are different for neutrino-nucleon and antineutrino-nucleon scattering, and the explicit dependence of the structure functions on the variables x and Q^2 is shown. These three structure functions describe the properties of a nucleon as seen by leptons. In the parton model they are weighted density distributions associated with partons inside the nucleon.

For low momentum transfer Q^2 (which is the case for existing neutrino beams) the propagator term $(\frac{m_W^2}{m_W^2+Q^2})^2$ can be neglected since it is very close to unity. The term $\frac{Mxy}{2E} = \frac{Q^2}{4E^2}$ is $\ll 1$.

In the hypothesis of scaling [125] (which is a consequence of the assumption of scattering on point-like objects) the dependence on Q^2 disappears and we get:

$$\frac{d^2\sigma^{\nu,\bar{\nu}}}{dxdy} = \frac{G^2ME}{\pi} \cdot [xy^2F_1^{\nu,\bar{\nu}}(x) + (1-y)F_2^{\nu,\bar{\nu}}(x) \pm y(1-\frac{y}{2})xF_3^{\nu,\bar{\nu}}(x)]$$

If the partons have spin $\frac{1}{2}$ the Callan-Gross relation [126] holds: $2xF_1 = F_2$ and the expression for the cross section takes a simpler form:

$$\frac{d^2\sigma^{\nu,\bar{\nu}}}{dxdy} = \frac{G^2ME}{\pi} \cdot [(1-y+\frac{y^2}{2})F_2^{\nu,\bar{\nu}}(x) \pm y(1-\frac{y}{2})xF_3^{\nu,\bar{\nu}}(x)]$$

Defining $q(x) = \frac{1}{2}[F_2(x)+xF_3(x)]$ and $\bar{q}(x) = \frac{1}{2}[F_2(x)-xF_3(x)]$ one then obtains

$$\frac{d^2\sigma^{\nu}}{dxdy} = \frac{G^2ME}{\pi} \cdot [q(x) + (1-y)^2 \cdot \bar{q}(x)]$$

$$\frac{d^2\sigma^{\bar{\nu}}}{dxdy} = \frac{G^2ME}{\pi} \cdot [(1-y)^2 \cdot q(x) + \bar{q}(x)]$$

The function $q(x)$ ($\bar{q}(x)$) can be interpreted as the distribution of momentum of the left-handed partons (right-handed antipartons) in the nucleon.

Integrating over x one finds

$$\frac{d\sigma^{\nu}}{dy} = \frac{G^2ME}{\pi} \cdot [\mathcal{Q} + (1-y)^2 \cdot \bar{\mathcal{Q}}]$$

$$\frac{d\sigma^{\bar{\nu}}}{dy} = \frac{G^2ME}{\pi} \cdot [(1-y)^2 \cdot \mathcal{Q} + \bar{\mathcal{Q}}]$$

The total cross section is obtained by integrating over y

$$\sigma^{\nu} = \frac{G^2ME}{\pi} \cdot [\mathcal{Q} + \frac{1}{3} \cdot \bar{\mathcal{Q}}]$$

$$\sigma^{\bar{\nu}} = \frac{G^2ME}{\pi} \cdot [\frac{1}{3} \cdot \mathcal{Q} + \bar{\mathcal{Q}}]$$

As can be seen from the formulae above, if scaling holds, the neutrino and antineutrino cross sections grow lineary with the energy E and the slopes of the rising cross section are determined by the integrals over the structure functions. In the absence of antipartons (antiquarks) in the nucleon the ratio of antineutrino to neutrino total cross section should be equal to $\frac{\sigma^{\bar{\nu}}}{\sigma^{\nu}} = \frac{1}{3}$.

Measurements of (anti-)neutrino-nucleon cross sections in the energy region above 10 GeV yield

$$< \sigma^{\nu}/E > \approx 0.67 \times 10^{-38}\ cm^2/GeV$$

$$< \sigma^{\bar{\nu}}/E > \approx 0.33 \times 10^{-38}\ cm^2/GeV$$

The measured ratio of antineutrino to neutrino charged current cross section is

$$r = \frac{\sigma_{CC}^{\bar{\nu}}}{\sigma_{CC}^{\nu}} = 0.49 \pm 0.01$$

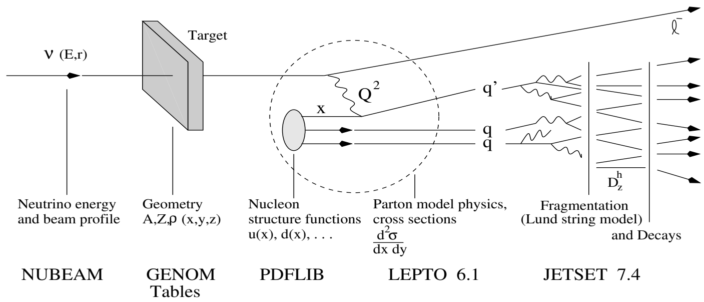

Figure 4.2: Overview of the different packages used for the simulation of neutrino interactions in the NOMAD setup (from [89]).

confirming the presence of an antiquark component in the nucleon.

The neutral current reactions

$$\nu_l N \to \nu_l X$$

$$\bar{\nu}_l N \to \bar{\nu}_l X$$

also take place.

The ratio of neutral current to charged current cross section for neutrinos and antineutrinos was measured to be

$$R = \frac{\sigma^{\nu}_{NC}}{\sigma^{\nu}_{CC}} = 0.309 \pm 0.003$$

$$\bar{R} = \frac{\sigma^{\bar{\nu}}_{NC}}{\sigma^{\bar{\nu}}_{CC}} = 0.39 \pm 0.01$$

It is important to note that the y-distributions for neutrino neutral current and charged current reactions are similar. This fact was confirmed experimentally [127].

4.1.2 Event simulation

Fig. 4.2 shows the overview of the different packages used for the simulation of the neutrino interactions in the NOMAD setup.

The computation of the incoming neutrino beam (NUBEAM package [128]) is performed via the simulation of proton interactions in the beryllium target using the FLUKA package [129] and a full GEANT simulation of the secondary particle transport through the beam-line.

The NOMAD event generator (NEGLIB package [130]) is used to simulate charged and neutral current neutrino (including ν_τ) deep inelastic interactions in the quark-parton model approximation with QCD-evolved structure functions. It is a package based on the LEPTO 6.1 physics simulation program [131] with the following additions and corrections [132]:

- produced charged lepton mass and target mass are taken into account (Fig. 4.3);
- produced charged lepton polarization;
- simulation of polarized τ decays;

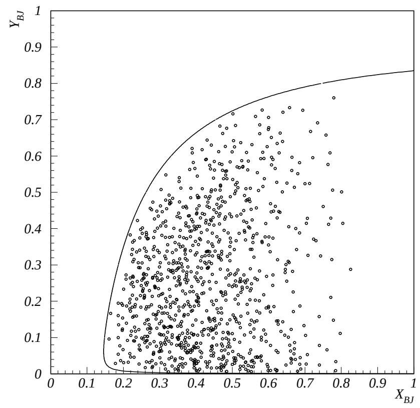

Figure 4.3: The kinematically allowed region of Bjorken variables x and y due to the presence of the massive τ lepton in the final state in ν_τ CC interactions for the energy in the centre of mass region $(s - M^2)$ below 25 GeV^2 (to the right from the solid line) and ν_τ CC events simulated with the NOMAD event generator (dots). See [132] for details.

- removed kinematical cut-offs (Q^2, W^2, ν). The better agreement between data and the MC simulation was obtained by extending the kinematical domain in which the neutrino interactions are described in terms of the DIS formalism. Q^2 is allowed to go down to zero;
- different parametrizations for the Fermi motion of the nucleon inside the nucleus were implemented (Fig. 4.4).

This program generates a complete event starting from the energy spectra of the incident neutrino. The hadronization of the produced partons into observable hadrons is performed with the Lund string hadronization model [135] via the JETSET 7.4 program [136]. To define the parton content of the nucleon for the cross-section calculation, the parton density functions are needed. We have been using the GRV-HO parametrization [137] available in PDFLIB [138] which is valid in the range $10^{-5} \leq x < 1$ and $0.3 \leq Q^2 \leq 10^8$ (GeV^2).

It was realized that the energy limit E_{min} at which the fragmentation stops creating quark-antiquark pairs from the color field has to be lowered down to 0.2 GeV to describe in a better way the hadronic jet behaviour observed in the NOMAD real data [139, 140].

The tracking of secondary particles through the detector setup, their interactions and decays, the digitization of the subdetector responses are implemented with the help of the GENOM package [110] based on the general purpose physics simulation GEANT program [80].

Simulated events can be passed through the NOMAD reconstruction program as if they were real data.

4.1.3 Event selection

In order to compare the simulation with reality we have to select genuine neutrino interactions in the NOMAD active target. At the first stage of the real data event selection all the NOMAD $\bar{V}T_1T_2$ triggers were passed through a special filter [141] since at this level the data are largely contaminated by straight-through muons from veto inefficiencies, cosmic ray muons and neutrino interactions in the surrounding

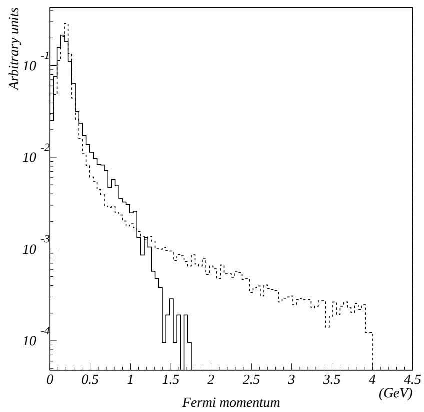

Figure 4.4: Two parametrizations of Fermi motion of the nucleon inside the nucleus used in the NEGLIB package: Guoju - Irvine [133] (solid line) and Bodek - Ritchie [134] (dashed line). Let us point out that the first parametrization does not have a long tail compared to the second one, but predicts a larger fraction of events in the interval [0.4, 1] (GeV).

materials (coil, front I, C's). The purpose of this filter based on the first pass of the DC reconstruction was to reject the largest possible fraction of background keeping essentially 100% of events suitable for analysis. The rejection power and the efficiency of this filter were evaluated by visual scanning and by using MC samples and turned out to be: rejection factor ~ 10, efficiency $\sim 99\%$.

The output of this filter was passed through the NOMAD reconstruction program and was saved in the form of data summary tape (DST) [142].

To ensure that the sample of events chosen for analysis constitutes a reliable sample of desired events, as free as possible from experimental biases not present in the simulated events, a number of selection criteria were applied to the data. These cuts are described below:

- **Fiducial cuts:** the primary vertex of all events was required to lie within the following fiducial volume

$$-120 < x, y < 120 \ (cm) \qquad 5 < z < 395 \ (cm)$$

  that is to be well within the drift chambers system;

- **Quality cuts:** requiring the event to be well reconstructed

$$-2 \leq \text{Sum of charges at the primary vertex} \leq 3$$

  to suppress events with several non-reconstructed primary charged tracks;

$$\text{Number of unmatched TRD tracks} \leq 10$$

  to get rid of events containing non-reconstructed secondary hadron interactions;

$$E^{tot}_{HCAL}/E^{tot}_{visible} \leq 0.75$$

  to suppress events with energetic neutral hadron escaping detection;

- **Multiplicity cut:** ≥ 2 charged tracks fitted to the primary vertex.

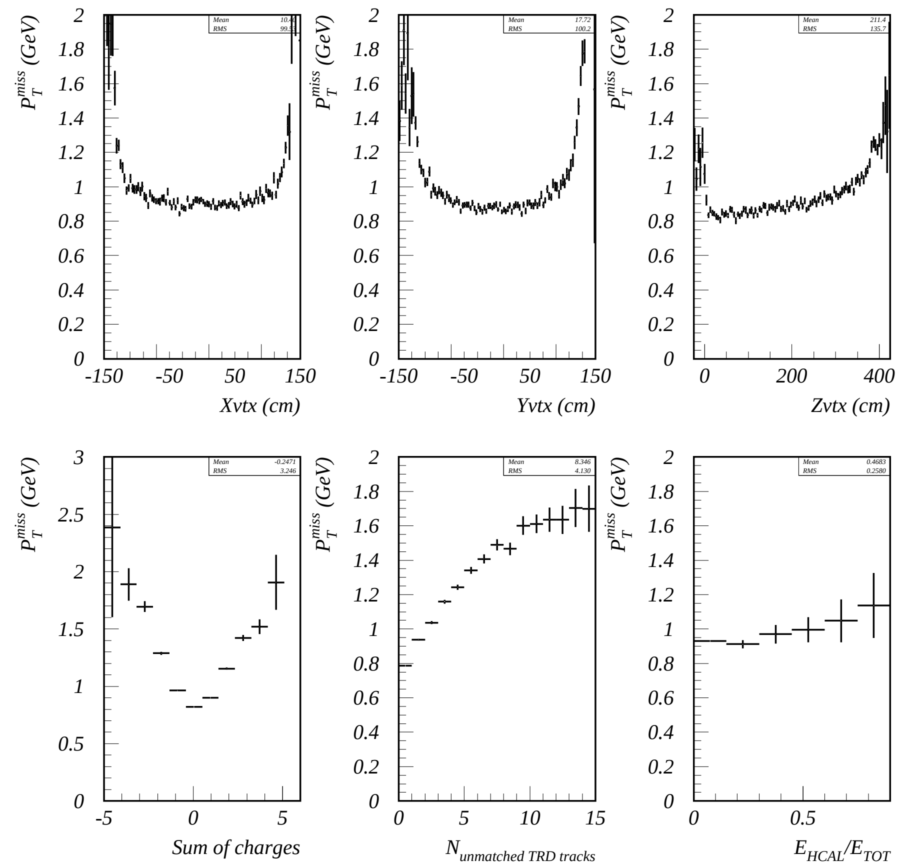

Figure 4.5: The dependence of the missing transverse momentum in ν_μ CC candidates from real data '96 on the primary vertex position (X_{vtx}, Y_{vtx}, Z_{vtx}), the sum of charges at the primary vertex, the number of unmatched TRD tracks and the fraction of energy deposited in the HCAL over the total visible energy in an event.

The necessity of these cuts can be easily seen from the Fig. 4.5 showing the dependence of the missing transverse momentum in the identified ν_μ CC candidates[1] from real data on the primary vertex position (X_{vtx}, Y_{vtx}, Z_{vtx}), sum of charges at the primary vertex, number of unmatched TRD tracks and fraction of energy deposited in the HCAL over the total visible energy in an event. The missing transverse momentum is a good measure of the quality of the event reconstruction. If we want to obtain a good quality of the reconstruction of event kinematics it is important to keep the missing transverse momentum as small as possible.

We have estimated using MC samples that these cuts reject approximately 10% of good events.

In the following we will always apply the above mentioned selection criteria to both MC and real data samples to ensure the validity of the comparison.

[1] Requiring a μ^- connected to the primay vertex.

4.2 Comparison of reconstructed and simulated kinematics

Contrary to many analyses performed within the NOMAD collaboration we have decided to use the reconstructed primary vertex and only tracks (charged or neutral) fitted to this vertex to calculate the event kinematics. This is especially important for the selection of the primary electron candidate since we want to suppress as much as possible all backgrounds coming from non-prompt electrons (like conversions near the primary vertex). The alternative would be to use a box of 5 cm size around the primary vertex and all the tracks which have a starting point within this box [86, 100].

The parameters which are rather well measured in ν_μ CC neutrino interactions are the momentum of the outgoing muon (p_μ) and its scattering angle in the laboratory frame (θ). For the calculation of the kinematical quantities describing neutrino interactions one has to know a third parameter, the incoming neutrino energy (E_ν), for example. We have been using an approximation which consists in setting the incoming neutrino energy equal to the total visible energy in an event (E_{tot}). The total visible energy is computed by summing up the energies of all the particles (charged and neutral) emerging from the primary vertex (particle ID, if known, is used for the energy calculation):

$$E_{tot} = E_{lepton} + \sum E_{primary\ charged\ tracks} + \sum E_{primary\ neutral\ tracks}$$

The first important check which was made consists in making a comparison of simulated and reconstructed kinematical quantities using Monte-Carlo events.

4.2.1 ν_μ CC events

Let us look at the ν_μ CC events first and compare the generated and reconstructed kinematical variables (Fig. 4.6). We see a clear correlation smeared by escaping neutral particles and detector resolution.

Having selected ν_μ CC candidates from the real data requiring a μ^- candidate connected to the primary vertex, we can proceed by comparing the reconstructed kinematical variables between data and MC (see Fig. 4.7). This plot shows a clear disagreement which is due to the presence of the quasielastic events and resonance production in the real data. These events were not simulated by our neutrino-nucleon deep inelastic scattering (DIS) Monte-Carlo program. Having applied a set of cuts allowing to choose the deep inelastic kinematic region we find a reasonable agreement between data and MC (Fig. 4.8).

A serious problem appears when we try to compare the behaviour of the real data and MC events in the plane perpendicular to the incoming neutrino direction. This can be seen in the missing transverse momentum distribution (Fig. 4.9). The average missing transverse momentum in ν_μ CC MC events is $< p_T^{miss} >= 0.6\ GeV$, while in ν_μ CC candidates from the real data it is $< p_T^{miss} >= 0.74\ GeV$. Possible reasons for the difference in the p_T^{miss} distributions were carefully studied, namely:
- lower reconstruction efficiency for real data;
- incorrect description of the hadronic interactions in the simulation program;
- nuclear effects (Fermi-motion tail, nuclear reinteractions, etc.).

Using MC simulation and the real data with simple topologies (two charged track events) different contributions to the p_T^{miss} have been studied [143]. It was found that the largest contribution comes from escaping neutrals ($\sim 375\ MeV$) while Fermi motion contributes ($\sim 200\ MeV$). The effect of the detector resolution was found to be $\sim 330\ MeV$ and the contribution due to reconstruction inefficiencies was estimated to be $\sim 300\ MeV$.

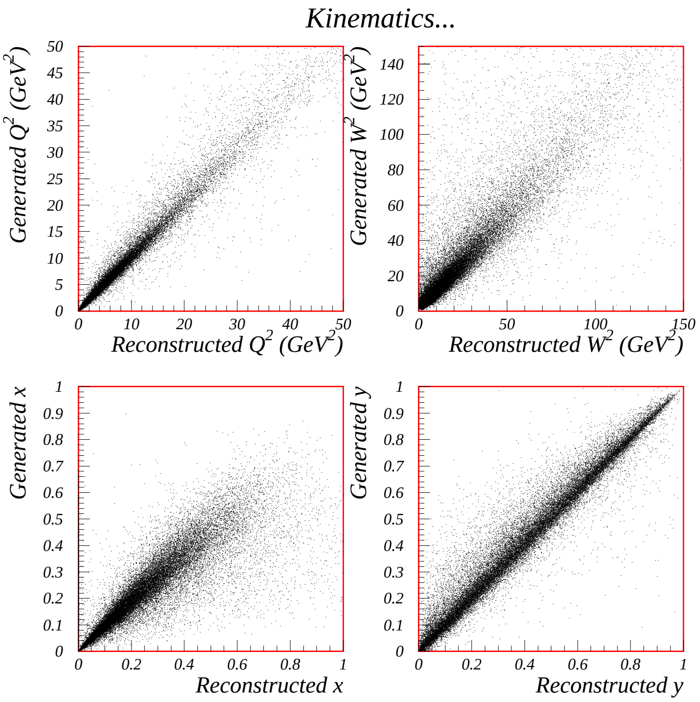

Figure 4.6: Comparison of generated and reconstructed kinematical quantities for ν_μ CC simulated events.

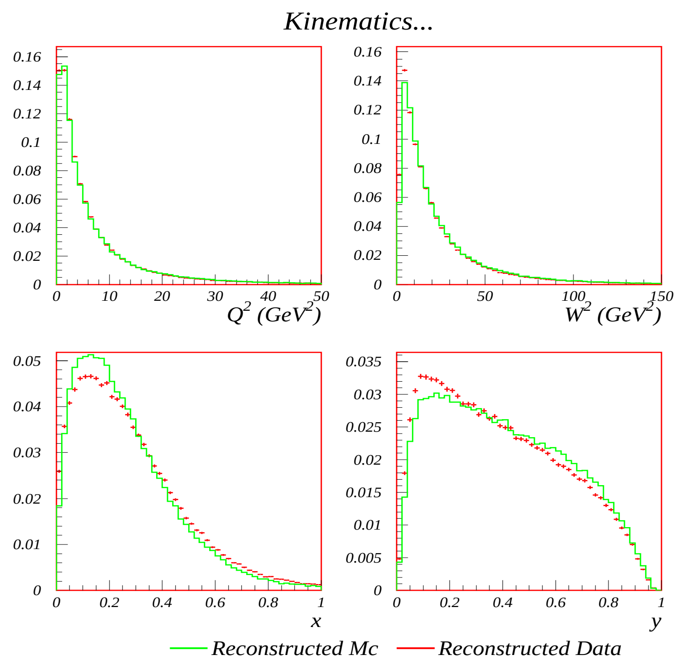

Figure 4.7: Comparison of the reconstructed kinematical quantities for the identified ν_μ CC MC (solid line) and the real data (crosses) events. The disagreement is due to the presence of the quasielastic events and resonance production in the real data while these events were not simulated in our deep-inelastic Monte-Carlo.

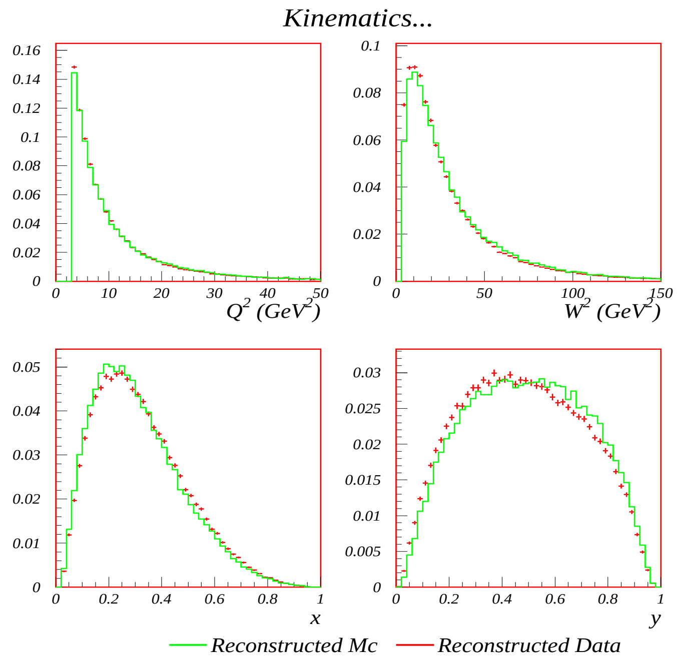

Figure 4.8: Comparison of the reconstructed kinematical quantities for the identified ν_μ CC MC (solid line) and the real data (crosses) events (kinematical cuts applied to select events from the DIS region: $Q^2 > 3\ GeV^2$ and $W^2 > 3\ GeV^2$).

Intranuclear cascades can take place in nuclear target where the primary hadrons may undergo successive hadronic interactions with the nucleons of the target nucleus before exiting it. It was shown in [139] that nuclear reinteractions are not causing too large kinematical distortions on top of the existing smearing from Fermi motion. However, they tend to send particles at higher angles and softer momenta where the acceptance of the NOMAD detector is reduced. That is why a $\sim 50 \div 100\ MeV$ effect on the $< p_T^{miss} >$ can be expected. This conclusion is consistent with the result of independent studies presented in [144]. In addition, a possible excess of protons in the hadronic jet in the NOMAD real data reinforces the studies of nuclear reinteractions since this observation can be explained by the effect of intranuclear cascades and these measurements can be used to tune the MC predictions.

Data simulator

Unfortunately, no solution to the problem of $< p_T^{miss} >$ was found up to now. In other words we did not manage to find a way to degrade our MC simulation so that it would reproduce what we observe in the real data.

Nevertheless, there is still a way out which consists is using simulations based on the real data whenever possible. For example:
- to simulate ν_τ CC events with subsequent τ^- decay one can take ν_μ CC events from the real data and replace the μ^- by a τ^- decay. The procedure is not straightforward due to the difference in masses between the μ and the τ which can cause energy/momentum non-conservation;
- to simulate ν_μ NC events one can use ν_μ CC events from the real data with μ^- removed. But one should beware of a bias in the y distribution caused by the momentum threshold in the muon identification and a bias in the total charge of the hadronic jet;

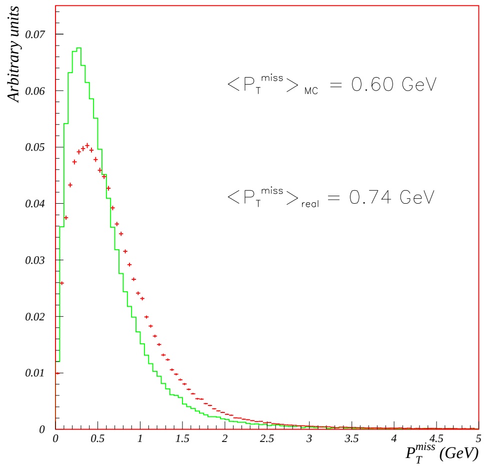

Figure 4.9: Missing transverse momentum p_T^{miss} distribution in the identified ν_μ CC MC (solid line) and the real data (crosses) events. A difference of the order of 140 MeV is observed.

- to simulate ν_e CC events one can replace the μ^- by an e^- in ν_μ CC events from the real data and reweight events according to the different neutrino energy spectra. However, the detector effects (such as overlaps in the NOMAD subdetectors) cannot be easily simulated.

4.2.2 ν_e CC events

Let us look now at the quality of the reconstruction for ν_e CC MC events. We start from the primary electron identification and reconstruction.

Fig. 4.10 shows the efficiency of the primary electron identification and connection to the primary vertex as a function of the primary vertex position and incoming neutrino energy. The average efficiency is $\sim 55\%$. The clear Z dependence of the efficiency is due to the requirement that the electron candidate should point to the electromagnetic calorimeter.

The quality of the reconstruction of the initial electron momentum and direction is illustrated in the Fig. 4.11. The electron momentum resolution achieved with the proposed method for electron reconstruction is $\frac{\sigma_p}{p} \approx 5\%$.

Having checked that the electron momentum (Fig. 4.12) and the total visible energy (Fig. 4.13) in ν_e CC MC events are reasonably well reconstructed we can compare other kinematical variables (Fig. 4.14).

Finally, we can state that the quality of the reconstruction of the event kinematics is not crucially different for ν_e CC MC events compared to ν_μ CC MC events.

The higher value of the average missing transverse momentum in the ν_e CC MC events is due to the higher mean energy of interacting neutrinos. The other variables describing the kinematics of neutrino interactions are reconstructed with a resolution of the order of $\sim 15 \div 30\%$.

4.3 Summary

It was illustrated that the NOMAD detector is able to reconstruct the kinematics of neutrino interactions with a good precision. We have shown also that the detector

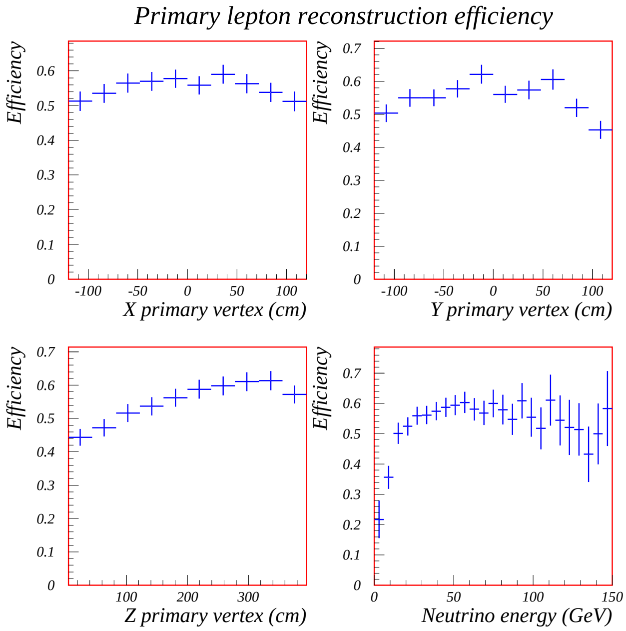

Figure 4.10: Efficiency of the primary electron identification and connection to the primary vertex as a function of the primary vertex position and the incoming neutrino energy.

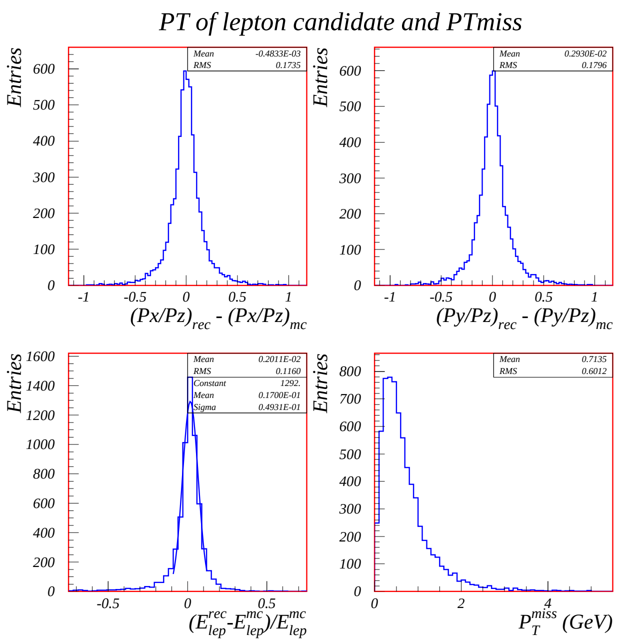

Figure 4.11: Quality of the primary electron reconstruction: determination of the initial electron direction and momentum; missing transverse momentum p_T^{miss} in reconstructed ν_e CC MC events.

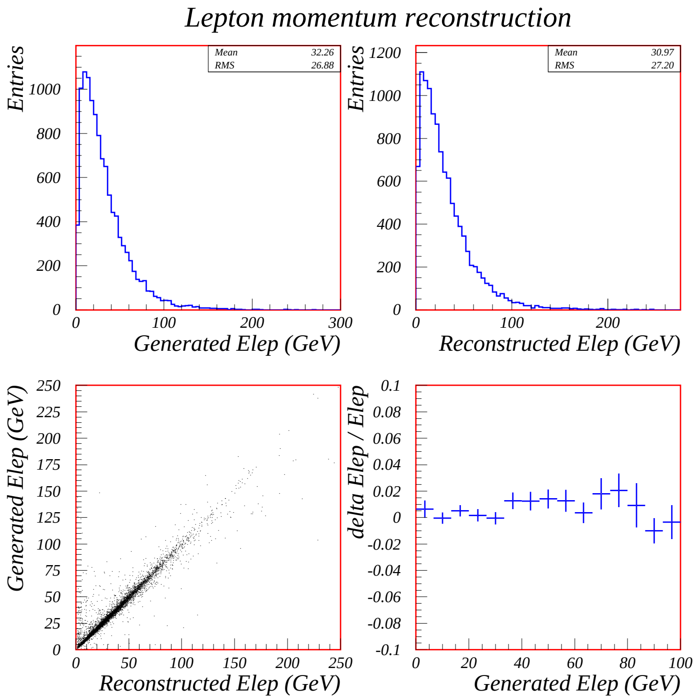

Figure 4.12: Reconstruction of the initial electron momentum in ν_e CC MC events.

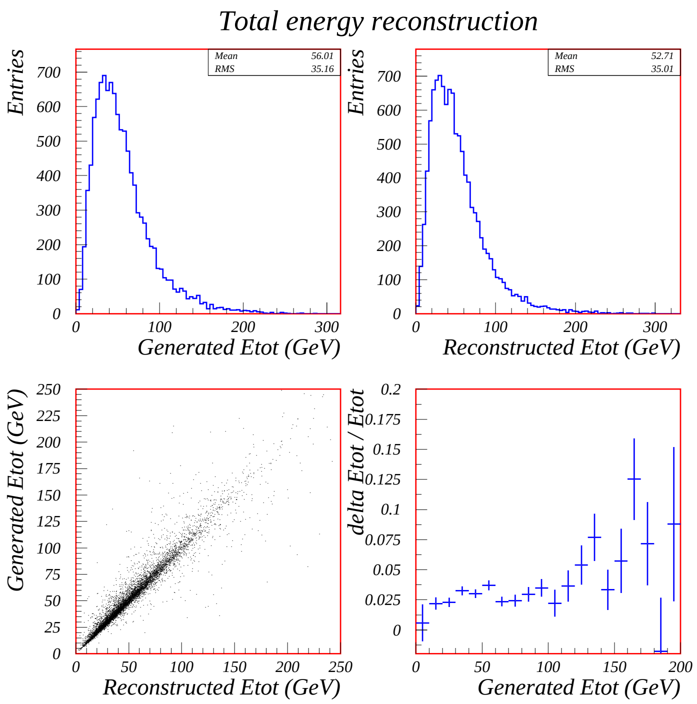

Figure 4.13: Reconstruction of the total visible energy in ν_e CC MC events.

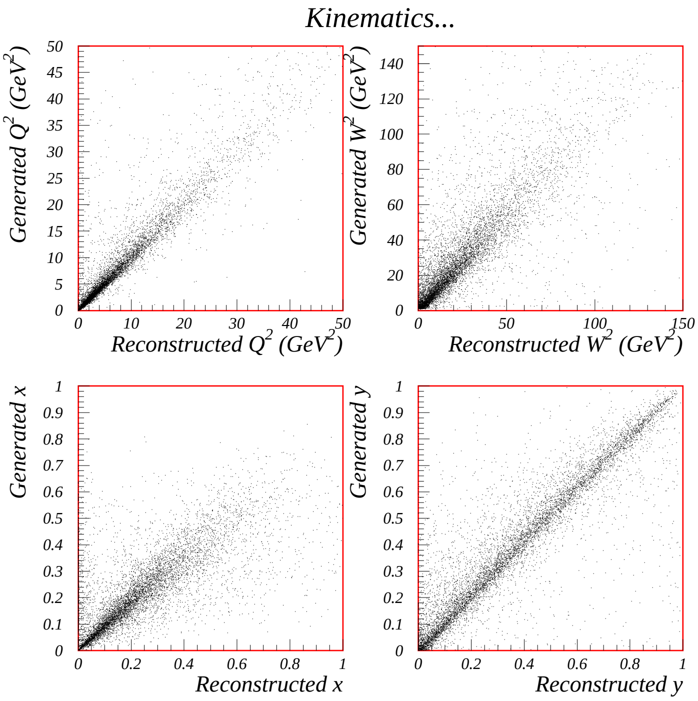

Figure 4.14: Comparison of generated and reconstructed kinematical quantities for ν_e CC MC events.

simulation program cannot reproduce precisely the behavior of the hadronic jet observed in the NOMAD real data especially in the plane perpendicular to the incoming neutrino direction. Let us point out that this discrepancy affects less the search for possible τ^- decays into leptonic modes than in the hadronic ones. The proposed way out consists in using the simulation based on the real data whenever possible.

The simulation of the τ production and decay takes into account the produced charged lepton mass and polarization. The effect of Fermi motion of the nucleon inside the nucleus is also simulated, while the smearing of the hadronic jet due to the effect of intranuclear cascades is currently under study.

In the next chapter we will perform a selection of ν_e CC candidates and we will present our approach to the $\nu_\mu \to \nu_\tau$ oscillation search in the $\tau^- \to e^- \bar{\nu}_e \nu_\tau$ decay channel.

Chapter 5

Analysis

This chapter consists of two main parts. We start with the description of the method used for the selection of ν_e CC candidates from the NOMAD real data, and we finish by presenting the current state of the analysis devoted to the $\nu_\mu \to \nu_\tau$ oscillation search in the $\tau^- \to e^-\bar{\nu}_e\nu_\tau$ decay channel.

The purpose of the ν_e CC selection is two-fold. First of all, we want to establish a set of cuts which would allow to get rid of background originating from neutral current events (conversions near the primary vertex and misidentified primary hadrons) and will serve for the $\nu_\mu \to \nu_\tau$ oscillation search in the $\tau^- \to e^-\bar{\nu}_e\nu_\tau$ decay channel. Second, we want to verify that the selection efficiency and the reconstructed kinematical quantities of ν_e CC events are well reproduced by the MC simulation program. This comparison is crucial for the usage of ν_e CC simulated events to estimate background in the $\tau^- \to e^-\bar{\nu}_e\nu_\tau$ decay search.

5.1 Selection of ν_e CC candidates

The procedure which was applied in order to select ν_e CC candidates from the NOMAD real data is described below.

5.1.1 Data sample

The real data sample which is presently available for analysis in NOMAD corresponds to two years of data taking ('95 and '96 runs)[1]. Due to a delay in the drift chambers construction schedule, the '95 run is divided into three periods, corresponding to different target configurations - 4, 8 and 11 (full target) modules of DC inside the magnet, while the whole '96 run corresponds to data taking in the full target configuration.

The following data samples were used for this analysis:

- **Real Data** (see Table 5.1):
  - the subsample of data from the '95 run (the total exposure corresponds to 0.86×10^{19} p.o.t.) containing events from 8- and 11-modules periods. Unfortunately, normalization to the number of protons on target cannot be done for this subsample due to uncontrolled losses of events during data reprocessing for this particular analysis. Nevertheless, this data set was very useful to build the analysis chain and it will be used for cross-checks;
  - the full data set corresponding to the '96 run (1.4×10^{19} p.o.t.);

[1]The data from the '97 run corresponding to 1.5×10^{19} p.o.t. are currently being processed through the $\bar{V}T_1T_2$ filter mentioned in section 4.1.3.

Table 5.1: The real data samples used for this analysis.

Data sample	N of events inside FV	N of events identified as ν_μ CC
'95 run	145909	85432
'96 run	514061	256074

Table 5.2: The Monte-Carlo samples used for this analysis. The number of ν_μ CC events in the last column of this table can be directly compared to the last column of the Table 5.1.

Monte-Carlo event type	N of generated events	N of events with generated vertex inside FV	N of events with reconstructed vertex inside FV	N of events identified as ν_μ CC
ν_μ CC	484302	391977	377423	275644
ν_μ NC	148132	117772	108481	602
$\bar{\nu}_\mu$ CC	13127	9824	9590	158
ν_e CC	19775	15114	13892	67
$\bar{\nu}_e$ CC	2717	1971	1883	11
$\tau^- \to e^- \bar{\nu}_e \nu_\tau$	28460	23361	21891	103

- **Monte-Carlo** (see Table 5.2):
  - ν_μ CC & NC, $\bar{\nu}_\mu$ CC, ν_e CC and $\bar{\nu}_e$ CC events simulated with the following versions of the NOMAD simulation programs: NEGLIB 5.06 and GENOM 5.12.6. The primary vertex for the Monte-Carlo events is generated in the following volume: $|x| < 140$ cm, $|y| < 140$ cm and $0 < z < 405$ (cm). The statistics of ν_μ CC & NC MC and $\bar{\nu}_\mu$ CC MC samples corresponds roughly to the one expected in the '96 data set, while the ν_e CC and $\bar{\nu}_e$ CC MC samples represent approximately 3 times the number of expected events from the '96 run;
  - $\tau^- \to e^- \bar{\nu}_e \nu_\tau$ events containing proper simulation of τ^- production[2] and decay (NEGLIB 5.07.1 and GENOM 5.12.12 versions). Let us point out that Guoju - Irvine [133] parametrization of Fermi motion of the nucleon inside the nucleus was used for ν_τ CC simulation, while all the other MC samples were generated using Bodek - Ritchie [134] parametrization (see Fig. 4.4);
  - additional samples of MC events are used to cross-check selection efficiencies and background rejection power. They are referred to as test samples.

5.1.2 Event selection

The following set of cuts was used for the event preselection:

- **Fiducial cuts:**
  the primary vertex of all events was required to lie within the following fiducial volume
  $$-120 < x, y < 120 \ (cm) \qquad 5 < z < 395 \ (cm)$$
- **Quality cuts** requiring the event to be well reconstructed:

[2]It was shown in [132] that the suppression factor $(1 - \frac{m_\tau^2}{s})^2$ in the ν_τ CC cross-section calculation is not needed.

  - ($-2 \leq$ Sum of charges at the primary vertex ≤ 3)
  - Number of unmatched TRD tracks < 10
  - $E^{tot}_{HCAL}/E^{tot}_{visible} < 0.75$
  - Z coordinate of the first hit of the lepton candidate $< 400\ cm$
  - momentum of the lepton candidate $> 1.5\ GeV$

- **Multiplicity cut:** ≥ 2 charged tracks fitted to the primary vertex

The event reduction flow of the '96 run is as follows: out of ~ 8 million $\bar{V}T_1T_2$ triggers, 807123 events survive the $\bar{V}T_1T_2$ filter and 514061 the fiducial volume requirements before entering the analysis chain.

5.1.3 Method

Throughout this analysis we have been extensively using an especially developed procedure to discriminate a signal from a background [145]. Since the likelihood ratio provides in certain cases an optimal separation between signal and background, it has been chosen for the current implementation.

Let us consider a discriminating random variable $\vec{x}$ (can be multidimensional) and call $\mathcal{S}$ the likelihood distribution of $\vec{x}$ under the signal hypothesis and $\mathcal{B}$ the likelihood distribution of $\vec{x}$ under the background hypothesis. The one-dimensional variable (likelihood ratio) $z = \frac{\mathcal{S}(\vec{x})}{\mathcal{B}(\vec{x})}$ which is a function of the random variable $\vec{x}$ is a good discriminator between the signal and the background populations.

Some remarks about the likelihood ratio are needed:

- any monotonic function of the likelihood ratio has the same properties. Two such transformations are often used: $\log(\frac{\mathcal{S}}{\mathcal{B}})$ and $\frac{\mathcal{S}}{(\mathcal{S}+\mathcal{B})}$, the latter being bounded by [0,1];
- when the likelihood ratio of a 1-dimensional variable is monotonic as a function of this variable, then cutting on the likelihood ratio rather than on the original variable does not make any difference in the efficiency versus purity figures.

The $\mathcal{S}$ and $\mathcal{B}$ distributions can be built using both MC simulation and the real data (see later). To avoid discontinuities due to the lack of statistics in the tails of the relevant distributions they are parametrized with the help of the HQUAD subpackage available in HBOOK [146]. It provides a sufficiently flexible parametrization technique (referred to as multiquadric radial basis functions) which can be used for our application. We limit our likelihood modelization to a product of 1- or 2-dimensional distributions, i.e we neglect part of the possible correlations between different components of the multidimensional variable $\vec{x}$. If the variables (components) x_1 and x_2 are assumed to be independent then their joint likelihood $f(x_1, x_2)$ can be factorized as $g(x_1) \times h(x_2)$, that is the independency reduces the dimension of variables whose likelihoods are to be modeled.

Let us consider an example of building a discriminant variable

$$X_{pa} = \frac{\mathcal{S}}{(\mathcal{S}+\mathcal{B})}$$

and illustrate the advantage of this variable. Defining σ and β to be the distributions of X_{pa} for signal and background respectively:

$$\begin{aligned} \sigma(y) &= \int \mathcal{S}(x)\delta(y - \frac{\mathcal{S}(x)}{\mathcal{S}(x)+\mathcal{B}(x)})dx \\ \beta(y) &= \int \mathcal{B}(x)\delta(y - \frac{\mathcal{S}(x)}{\mathcal{S}(x)+\mathcal{B}(x)})dx \end{aligned}$$

and evaluating $\frac{\sigma(y)}{y}$, one finds:

$$\begin{aligned}\frac{\sigma(y)}{y} &= \int \frac{\mathcal{S}(x)}{y}\delta(y-\frac{\mathcal{S}(x)}{\mathcal{S}(x)+\mathcal{B}(x)})dx \\ &= \int \frac{\mathcal{S}(x)}{\mathcal{S}(x)}(\mathcal{S}(x)+\mathcal{B}(x))\delta(y-\frac{\mathcal{S}(x)}{\mathcal{S}(x)+\mathcal{B}(x)})dx \\ &= \int (\mathcal{S}(x)+\mathcal{B}(x))\delta(y-\frac{\mathcal{S}(x)}{\mathcal{S}(x)+\mathcal{B}(x)})dx \\ &= \sigma(y)+\beta(y)\end{aligned}$$

or

$$\frac{\sigma(y)}{\sigma(y)+\beta(y)} = y \tag{5.1}$$

From the above equation we can deduce that

- considering $y = X_{pa}(x)$ as a random variable and evaluating $X_{pa}(y)$, one would find that $X_{pa}(y) = y$. That is, repetition of the transformation does not yield any additional discriminating power (as expected);
- The $\mathcal{S}$ and $\mathcal{B}$ functions inside the δ-functions are the modeled distributions (the ones that are used to transform x into $X_{pa}(x)$), while the other ones are the true distributions. The equality (5.1) holds if both sets coincide, and, as a result, it can be used to check the goodness of the parametrization. In practice, if one fills the histograms **s** and **b** of $X_{pa}(x)$ for signal and background and evaluates bin by bin $\mathbf{s}/(\mathbf{s}+\mathbf{b})$, a straight line fit ($y = \alpha x + \beta$) to the resultant histogram should yield $\alpha = 1$ and $\beta = 0$ within uncertainties. When the parametrization does not account for correlations, this test can be used to feel the importance of this approximation.

As an illustration, we show here some distributions obtained by simulating both signal and background as 2-dimensional Gaussian random variables with sigma of 1 and 50% correlation coefficient; signal and background only differ by their average: (1,1) and (-1,-1). When parametrizing these spectra, one can account (*cor*) or not (*uncor*) for correlations, and compare the results of both. In Fig. 5.1 one can see the poor performance the uncorrelated (*uncor*) parametrization exhibits when fitting the **s**/(**s**+**b**) distribution. Fig. 5.2 shows a comparison of the rejection power for correlated (*cor*) and uncorrelated (*uncor*) parametrizations. As one can see for this particular case it becomes relevant only if a rejection factor better than 10^{-3} is required.

We can summarize by saying that the variable X_{pa} takes values in the $[0,1]$ interval. The larger the value the more signal-like the event is. X_{pa} also provides a way to test the quality of the parametrizations obtained for $\mathcal{S}$ and $\mathcal{B}$. Nevertheless, it was still found very useful to check the quality of these parametrizations "by eye".

Let us introduce the following notations. In case of 3 variables a, b, c:
− the notation $\{a,b,c\}$ means that the discriminant variable is built through parametrizations that assume independence of a, b and c, that is the joint likelihood is a product of individual likelihoods;
− the notation $\{[a,b],c\}$ (or $\{\mathrm{HQ}[a,b],c\}$) means that the discriminant variable is built by evaluating the joint likelihood for a and b and combining it with the independent likelihood for c.

5.1.4 Electron identification

For the selection of the primary electron candidate the standard electron identification by means of TRD (pion contamination $< 10^{-3}$) was required first. Another

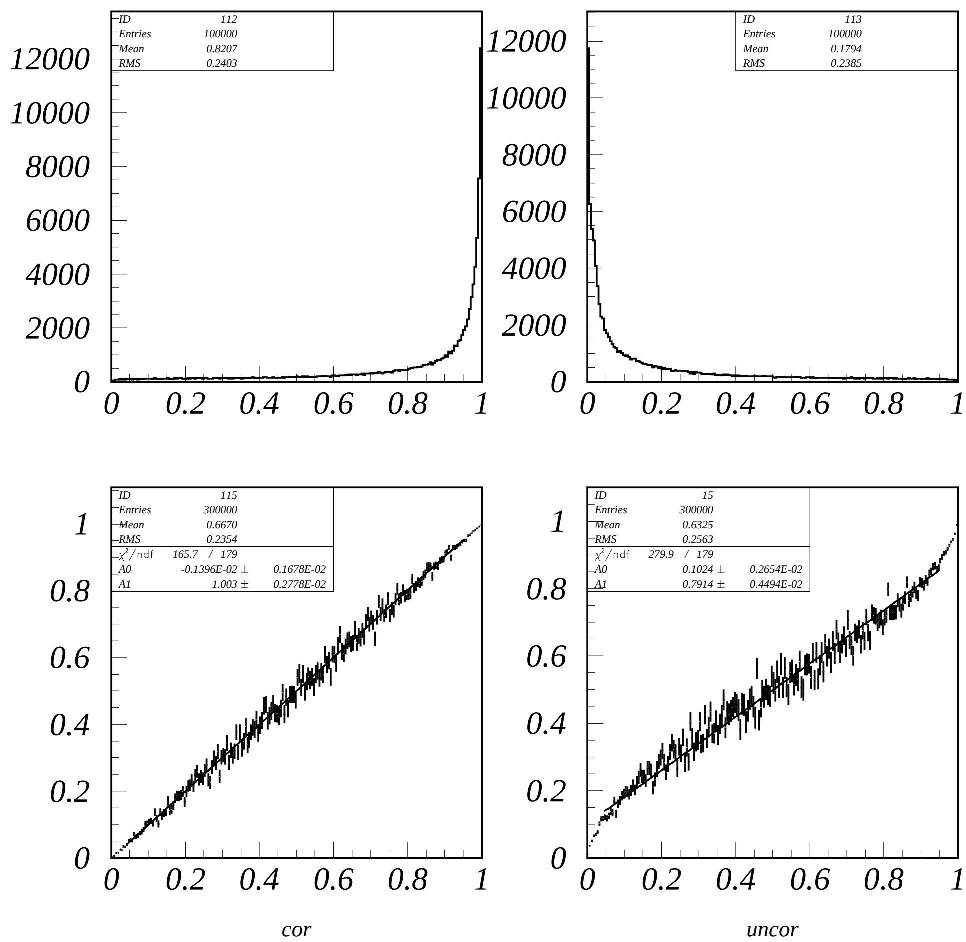

Figure 5.1: Illustration of the X_{pa} transformation applied to a 2-dimensional variable (signal and background are both 2d-Gaussians and both have a 50% correlation coefficient). Top: distributions of X_{pa} for signal **s** (left) and background **b** (right). Down left: **s**/(**s**+**b**) distribution taking into account the correlations with superimposed straight line fit. The parameters are compatible with 0 and 1. Down right: the same as on the left but when one parametrizes projections as if they were independent, the straight line fit parameters depart very significantly from 0 and 1.

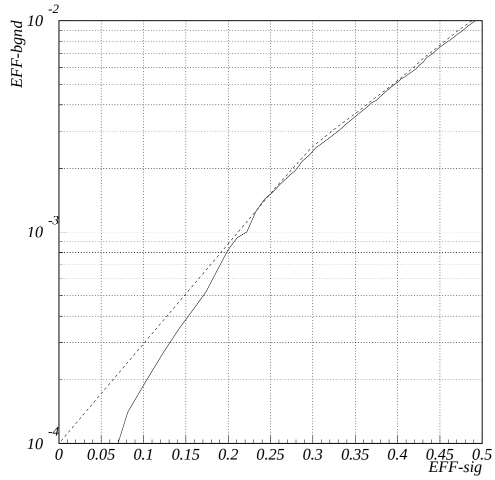

Figure 5.2: The rejection power versus efficiency for the previous example with 2 Gaussians taking into account the correlations (solid line) and neglecting the correlations (dashed line). Accounting for the correlations becomes important if a rejection power better than 10^{-3} is required.

(independent) identification criterion was built using the information from PRS and ECAL based on the real data measurements in both subdetectors. Signal and background samples were extracted from the data themselves. To select true electrons we have used the kinematical selection allowing to make a pure sample of ν_e CC candidates. To build an orthogonal (background) sample we applied a special pass of reconstruction to the real data events treating each track as a possible electron/positron candidate and selecting those which do not look like electrons from the TRD point of view (pion contamination distribution in the region > 0.1 is almost flat). Let us stress that a small contribution of the signal in the background distribution should not be considered as a problem in this case.

A discriminant variable was built in the following way:

```
eleid = {HQ[eop,HQ[prsx,prsy]],cxy=HQ[chix,chiy]},
```

where we tried to combine the information about pulse height in both preshower planes $(prsx, prsy)$ with a consistent energy/momentum measurement by DC and ECAL ($eop = \frac{E_{CAL}-P_{DC}}{E_{CAL}+P_{DC}}$) requiring also a reasonable shape of the electromagnetic shower profile in both projections $(chix, chiy)$. These criteria allowed to reach a rejection factor of $\sim 4 \times 10^{-2}$ against primary hadrons which deposit more than $0.75\ GeV$ in the ECAL keeping the electron identification efficiency at the level of $\sim 90\%$. The efficiency versus purity curve for this discriminant variable is shown in Fig. 5.3. The rejection factor against all hadrons is 1/4 of the number given here and is compatible with the test beam result presented in the section 3.3.1.

Having two electron identification algorithms: one based on the TRD response (1) and one which uses PRS and ECAL information (2), an attempt can be made to measure the background rejection power of both algorithms (ε_1^π and ε_2^π) assuming that they are independent and that the efficiency for each of them (ε_1^e and ε_2^e) is known. In case we have N tracks out of which N_e are genuine electrons we can

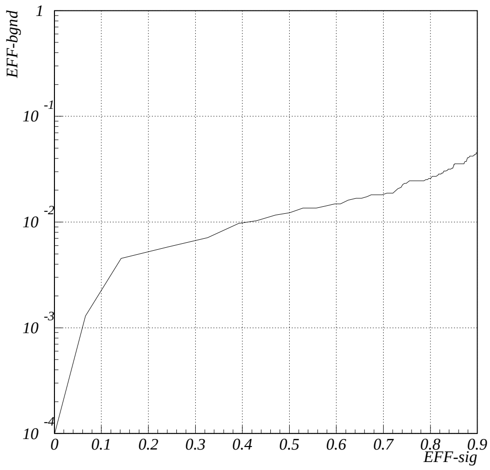

Figure 5.3: Electron identification algorithm using the information from PRS and ECAL: rejection power versus efficiency (for tracks depositing more than 0.75 GeV in the ECAL)

state that the number of tracks identified as electrons by the first algorithm is

$$N_1 = \varepsilon_1^e \cdot N_e + \varepsilon_1^\pi \cdot (N - N_e)$$

while the number of tracks identified as electrons by the second algorithm is

$$N_2 = \varepsilon_2^e \cdot N_e + \varepsilon_2^\pi \cdot (N - N_e)$$

and, finally, the number of tracks identified as electrons by both algorithms is

$$N_{12} = \varepsilon_1^e \cdot \varepsilon_2^e \cdot N_e + \varepsilon_1^\pi \cdot \varepsilon_2^\pi \cdot (N - N_e)$$

The system above can be solved in order to extract the values we are interested in. This check is important for the evaluation of the rejection power of the TRD in an independent way under running conditions (which are quite different from the ideal test beam conditions).

If one uses this approach to estimate the TRD rejection power (against hadrons leaving more than 0.75 GeV in ECAL) in the real data one gets $\varepsilon_{TRD}^\pi \sim 0.7\%$ requiring no overlaps in the TRD[3] and $\varepsilon_{TRD}^\pi \sim 7\%$ allowing overlaps in the TRD. This is compatible with our expectations.

Unfortunately, when applied to MC events this procedure did not give sensible results for the TRD rejection factor ($\varepsilon_{TRD}^\pi \sim 10\%$ even in case of no TRD overlaps). Since we were using only the real data to parametrize signal and background this could reveal a possible discrepancy between the simulated and the true response of the subdetectors. This discrepancy could be amplified by the necessary dependence of the identification algorithms on the reconstruction. For example, the special electron clusterization is performed only for tracks identified by the TRD and it is extremely difficult to decide which portion of the energy should be attributed to the electron candidate in case of overlaps in the calorimeter. This discrepancy was not investigated further yet.

[3]Overlap in the TRD happens when there are several particles crossing the same set of TRD straw tubes in a given event.

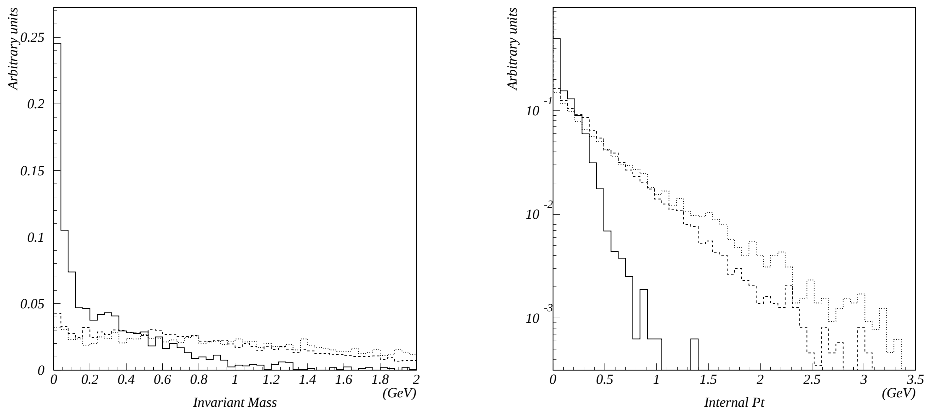

Figure 5.4: Comparison of invariant mass and internal p_T distributions for a pair of tracks (primary $e^{\pm}$ candidate and another track of the opposite charge making the smallest opening angle in YZ plane with the first one) for ν_μ NC (solid line), $\tau \to e$ (dashed line) and ν_e CC (dotted line) Monte-Carlo events. A contribution from conversions near the primary vertex is clearly visible (peaks near zero in both distributions).

5.1.5 Electron reconstruction

Only tracks fitted to the primary vertex are considered as primary electron candidates. For the electron reconstruction in the NOMAD setup we have been using the algorithm combining the information from the drift chambers (segment reconstruction and interconnection via vertices, breakpoint search) and the electromagnetic calorimeter (clusters corresponding to charged tracks and bremsstrahlung photons emitted by the electron candidate).

The loss of efficiency due to a small fraction of events containing a primary electron identified by the TRD and not attached to the primary vertex by the reconstruction program is estimated (using MC) to be less than 2%.

5.1.6 Selection of the current lepton

The selection of the current lepton is done in the following way. In case we have only one identified primary lepton l ($\mu^{\pm}$ or $e^{\pm}$) the event is considered as a $\overset{(-)}{\nu}_l$ CC candidate. If there are two primary leptons of different flavours and one of them is a μ^- the event is assumed to be a ν_μ CC candidate and it is also used to build the so-called fake NC events - identified ν_μ CC events with the primary muon removed. In case of two primary leptons of the same flavour the selection of the current lepton is made by taking the largest p_T track among the lepton candidates. If there are more than two identified primary leptons the event is not used for the analysis presented here.

5.1.7 Kinematical selection

Only events passing through fiducial, quality and multiplicity cuts are considered. The absence of identified muon in an event is required.

We decided to use a sample of ν_e CC MC events to build all the signal distributions, while fake NC (data) sample was used for background parametrization. In

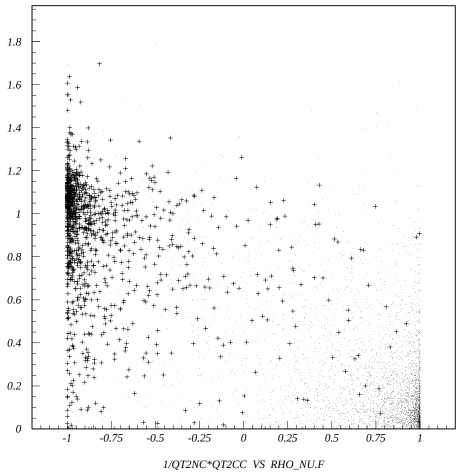

Figure 5.5: Comparison of *qt2ratio* vs *rho_nu* distribution for ν_e CC MC events (dots) and ν_μ NC MC with primary electron candidate (crosses). See text for details.

order to separate ν_e CC candidates from ν_μ CC and NC background we proceed in several steps.

First, cuts are applied to get rid of conversions near the primary vertex where one of the tracks is fitted to the primary vertex while the partner is reconstructed but not associated to the first track. We choose the opposite charge partner[4] making the smallest opening angle in YZ plane[5] with the primary electron candidate (oyz) and apply standard invariant mass (xm_yz), internal p_T (ptp_yz) (see Fig. 5.4) and opening angle (in space (op_yz) and in XZ plane (oxz_yz)) cuts computed for this pair of tracks:

```
conv = {ptp_yz,xm_yz,oyz,op_yz,oxz_yz}
```

Second, we try to reject NC events in which one of the primary hadrons was misidentified as an electron using the fact that this hadron still belongs to the hadronic jet. This cut consists of two parts.

The first one is the criterion proposed in [100] to separate CC and NC events and to check that the track which was identified as an electron is consistent with the hypothesis of being the current lepton. The idea of this criterion consists in checking the average Q_T^2 of the hadronic jet behaviour under two hypothesis: neutral current event - $Q_T^2(NC)$ (all the visible tracks emerging from the primary vertex belong to the hadronic jet) and charged current event - $Q_T^2(CC)$ (in this case we compute the Q_T^2 assuming that the track under consideration is the current lepton and we remove it from the hadronic jet). When taking the ratio $\frac{Q_T^2(CC)}{Q_T^2(NC)}$ for a given event one observes the following: this ratio tends to be close to 1 for true NC events since a randomly removed track does not change the hadronic jet behaviour. While it is

[4]When looking for a partner we allow the difference between the Z positions of the first hit of the $e^\pm$ candidate and the first hit of the other track to be within 100 cm. This is essential because two tracks from a conversion are usually well aligned and hits belonging to the second track could be masked by the first one.

[5]Since we know that the quality of track reconstruction is much better in YZ plane compared to XZ plane.

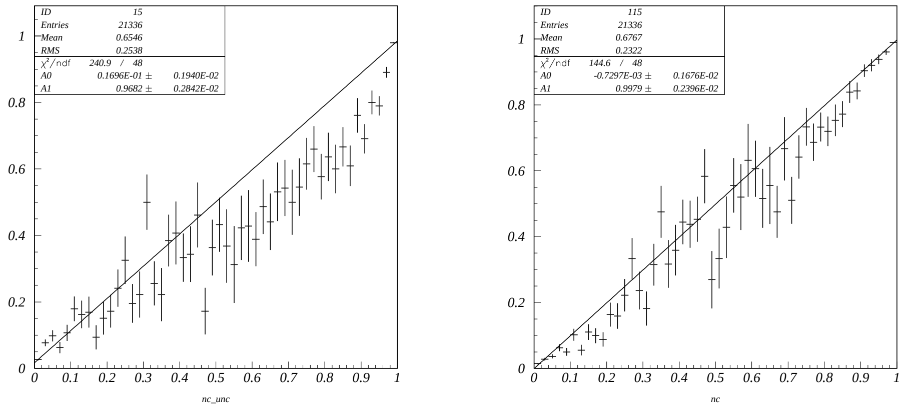

Figure 5.6: The $\mathbf{s/(s{+}b)}$ distribution which allows to check the quality of the parametrization for the *nc* discriminant variable neglecting the correlation between *qt2ratio* and *rho_nu* (left) and accounting for the correlation (right). The parameters of the straight line fit show that we obtain better result taking into account the correlation.

getting close to 0 for CC events due to the fact that the current lepton increases significantly the Q_T^2 of the jet when included in it. That is $Q_T^2(NC) > Q_T^2(CC)$ for true CC events when we correctly pick up the current lepton (see Fig. 5.5 as an illustration).

The discriminant variable is built in the following way:

```
nc = HQ[qt2ratio,rho_nu]
```

An example of $\mathbf{s/(s{+}b)}$ distribution is given in Fig. 5.6. It allows to check the quality of the parametrization for the *nc* discriminant variable and confirms that one should take into account the correlation between *qt2ratio* and *rho_nu*. One should keep in mind that neglecting correlations or using bad parametrizations lead to some loss in background rejection power compared to an optimal separation.

The second cut is a combination of the smallest opening angle with respect to any other charged track in an event (*opanch*) and the transverse momentum of the electron candidate with respect to the hadronic jet (*qtisol*). This criterion also tends to distinguish CC from NC events since the current lepton is usually well separated from the rest of the hadrons.

```
ang = HQ[opanch,qtisol]
```

Finally, the kinematical selection based on other variables such as the total visible energy in an event (*etot*), the momentum of the electron candidate (*plep*), the missing transverse momentum in an event (*ptmis*), the transverse mass (*xmt*) built out of $\vec{p}_T^{\,e}$ and $\vec{p}_T^{\,miss}$ and variables describing the event kinematics in the transverse plane (*rho_nu*, *rho_mu*) is applied:

```
kin1={xmt,etot,plep,qtisol,rho_nu,rho_mu,ptmis}
```

The formulae used to compute the above mentioned variables are given here:

$$\vec{q}_T = \vec{p} - \frac{(\vec{p}\cdot\vec{P}_h)}{P_h^2}\vec{P}_h$$

$$Q_T^2(NC) = \frac{1}{n}\sum_i q_T^2(i)$$

Table 5.3: Rejection power of the proposed cuts (combination of *eleid*, *conv*, *nc*, *ang* and *kin*1) against ν_μ CC and NC events. Please, note, that the 20 "$-$" events in the fake NC from ν_e CC (MC) category are in fact genuine ν_e CC interactions containing a μ^- from hadron decay which was removed to build fake NC (see text for details).

Event type	N of raw events	N of gen. events in FV	N of rec. events in FV	N of bgnd in "$-$"	N of bgnd in "+"
ν_μ CC (MC)	484302	391977	377423	3	9
ν_μ NC (MC)	148132	117772	108481	3	4
ν_μ NC (MC) test	150000	119527	110178	5	4
$\bar{\nu}_\mu$ CC (MC)	13127	9824	9590	0	-
fake NC from ν_μ CC (MC)	-	-	275644	4	17
fake NC from ν_e CC (MC)	19775	15114	13892	20	-
fake NC (data '96)	-	-	256074	18	33
fake NC (data total)	-	-	341510	23	41

$$Q_T^2(CC) = \frac{1}{n-1} \sum_{i \neq lepton} q_T^2(i)$$

$$qt2ratio = \frac{Q_T^2(CC)}{Q_T^2(NC)}$$

$$\rho_\nu = rho\_nu = \frac{p_T^{lep} - p_T^{miss}}{p_T^{had}}, \qquad \rho_\mu = rho\_mu = \frac{p_T^{lep} + p_T^{miss} - p_T^{had}}{p_T^{lep} + p_T^{miss} + p_T^{had}}$$

$$M_T = xmt = \sqrt{(p_T^{lep} \ + \ p_T^{miss})^2 \ - \ (\vec{p}_T^{\,lep} \ + \ \vec{p}_T^{\,mis})^2}$$

5.1.8 Efficiency and background estimations

Having applied a combination of the above mentioned cuts we obtain a selection efficiency[6] of $(38.5 \pm 0.5)\%$ for ν_e CC events. A check with an independent sample (not used for the parametrization of the likelihood functions) gave a consistent value: $\varepsilon_{\nu_e\ CC} = (39.0 \pm 0.4)\%$.

For the simulated backgrounds we are left with a small number of events in each category (Table 5.3). From these low statistical samples we can only estimate the rejection factor against ν_μ NC MC events to be in the range $(2 \text{ to } 5) \times 10^{-5}$ for negative ("$-$") and positive ("+") primary electron/positron candidates, and the rejection factor against ν_μ CC MC events in the range $(3 \text{ to } 13) \times 10^{-6}$ for "$-$" and $(1 \text{ to } 3) \times 10^{-5}$ for "+". The "+"/"$-$" background symmetry from ν_μ NC sample was expected, while a much worse rejection power against positives compared to negatives in ν_μ CC is explained by the presence of semileptonic charmed meson decays ($c \to he^+\nu_e$). One of these events is shown in Fig. 5.7.

To cross-check these results, obtained using MC samples, we built fake NC out of ν_μ CC MC, ν_e CC MC and data events. The large "+"/"$-$" asymmetry from charm decays is clearly visible in fake NC made from ν_μ CC. Thus we decided not to build fake NC out of events containing μ^+ in order to keep our negative sample unbiased by a small contribution of anticharm decays in $\bar{\nu}_\mu$ CC.

Two classes of potential problems are linked to the use of fake NC to predict the background expectations from real NC events.

[6] Efficiencies and rejection power are calculated with respect to the number of events with the reconstructed primary vertex in the fiducial volume (FV).

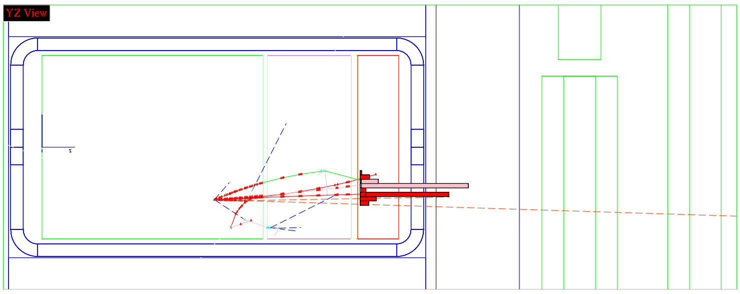

Figure 5.7: Run 212013 event 27069 (YZ view): surviving "+" candidate from ν_μ CC MC sample containing $D^0 \to e^+\nu_e K^-$ decay ($p_{e^+} = 5.3\ GeV$, $p_{\nu_e} = 4.3\ GeV$, $p_{K^-} = 14.7\ GeV$).

The first class originates from our current lepton selection algorithm and it is only present in the real data. If in a genuine ν_e CC event a negative hadron decays into muon, this event will appear in the fake NC sample. Among the 18 "$-$" events in the fake NC (data '96) category ~ 7 events are attributed to this mechanism as it follows from the studies of ν_e CC MC events (see line "fake NC from ν_e CC MC" in Table 5.3). The remaining 11 "$-$" events are compatible with our MC prediction ($[(2 \text{ to } 5) \times 10^{-5}] \times 256074$).

The second class is present in both real and simulated samples and is inherent to the procedure to build fake NC.
The kinematics of fake NC events is biased since the μ^- had to be identified in order to be removed. Moreover, the average charge of the hadronic jet is 3/2 instead of 1/2 biasing the leading particle charge. Finally, because of the drift chambers double track resolution, when removing the muon one cannot decide which hits should be removed and which should be attributed to nearby tracks. As an example, if a muon emits a δ-electron near the primary vertex, the electron could be connected to it using leftover muon hits. The event may not be rejected by the opening angle cut (ang) since the muon was removed. Another example is related to overlap of the identified muon and a hadron in the TRD which could cause the hadron to be identified as an electron.

Nevertheless, $\overset{(-)}{\nu_e}$ CC background sensitive to the jet kinematics or to its charge is only due to hadron misidentification which is independent of the hadron kinematics itself. Thus, the possible bias in the background estimation from fake NC is of second order. About the detector related problems, they are rare enough not to degrade significantly the purity of our selection. They could, however, become important when searching for $\nu_\mu \to \nu_\tau$ oscillation in the $\tau \to e$ decay channel.

The comparison of relevant kinematical variables between ν_μ NC MC events, fake NC made out of the simulated (Fig. 5.8 and Fig. 5.9) and the real data events (Fig. 5.10 and Fig. 5.11) shows a reasonable agreement. This agreement together with the remarks made above justify the possibility of using fake NC (data) events as a background sample to build likelihood functions. For this particular selection we have been using both positive and negative electron/positron candidates from fake NC (data) to parametrize the background distributions.

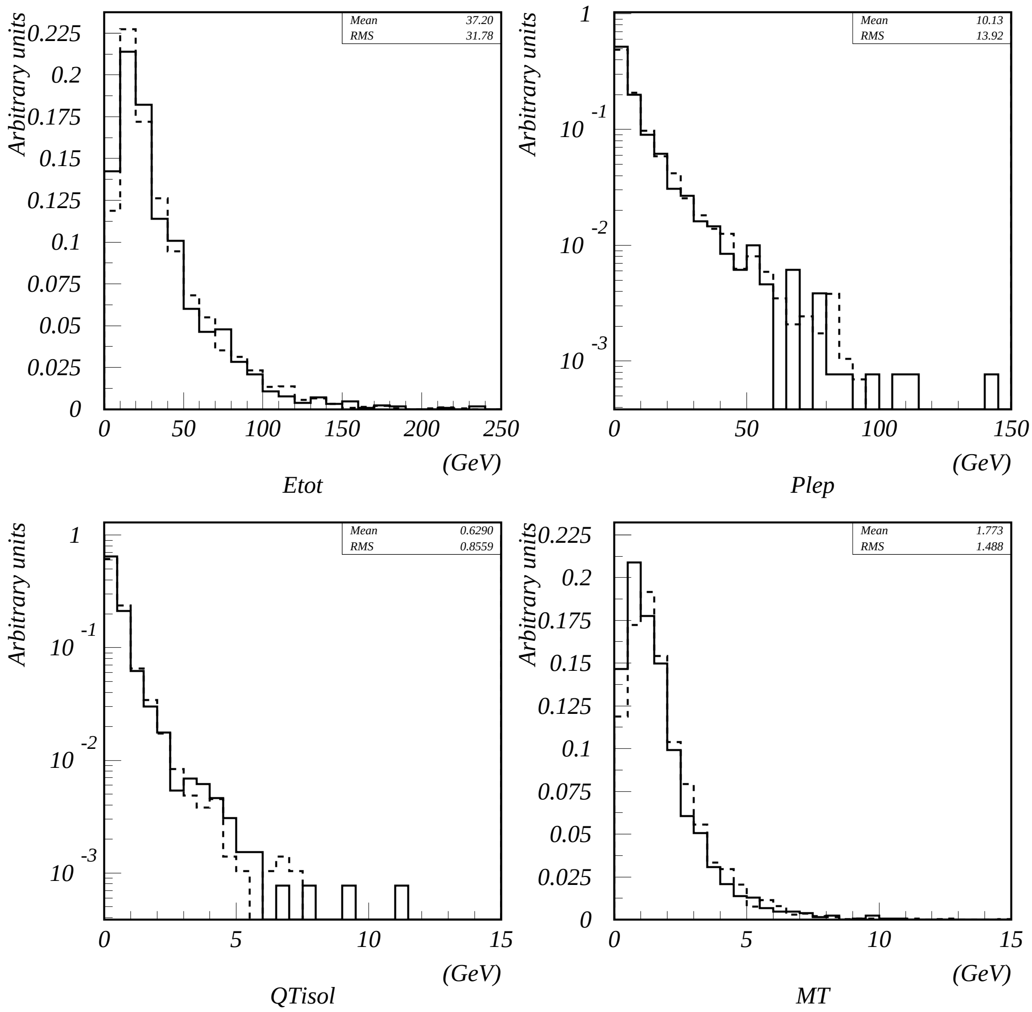

Figure 5.8: Comparison of the total visible energy, the initial electron momentum, the transverse momentum of the electron with respect to the hadronic jet and the transverse mass for events containing primary $e^{\pm}$ candidate: ν_μ NC MC events (solid line) and fake NC made from ν_μ CC MC events (dashed line).

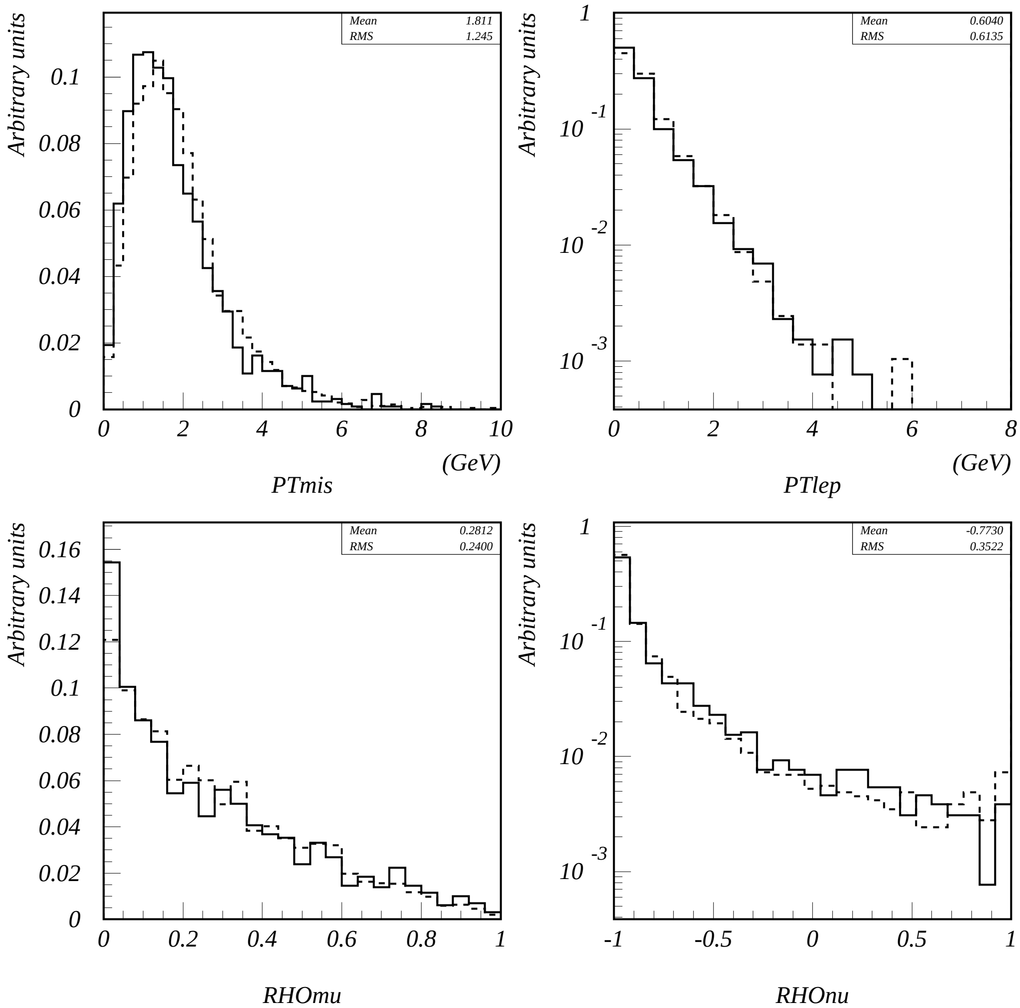

Figure 5.9: Comparison of the missing transverse momentum, P_T of the electron candidate, ρ_μ and ρ_ν for events containing primary $e^\pm$ candidate: ν_μ NC MC events (solid line) and fake NC made from ν_μ CC MC events (dashed line).

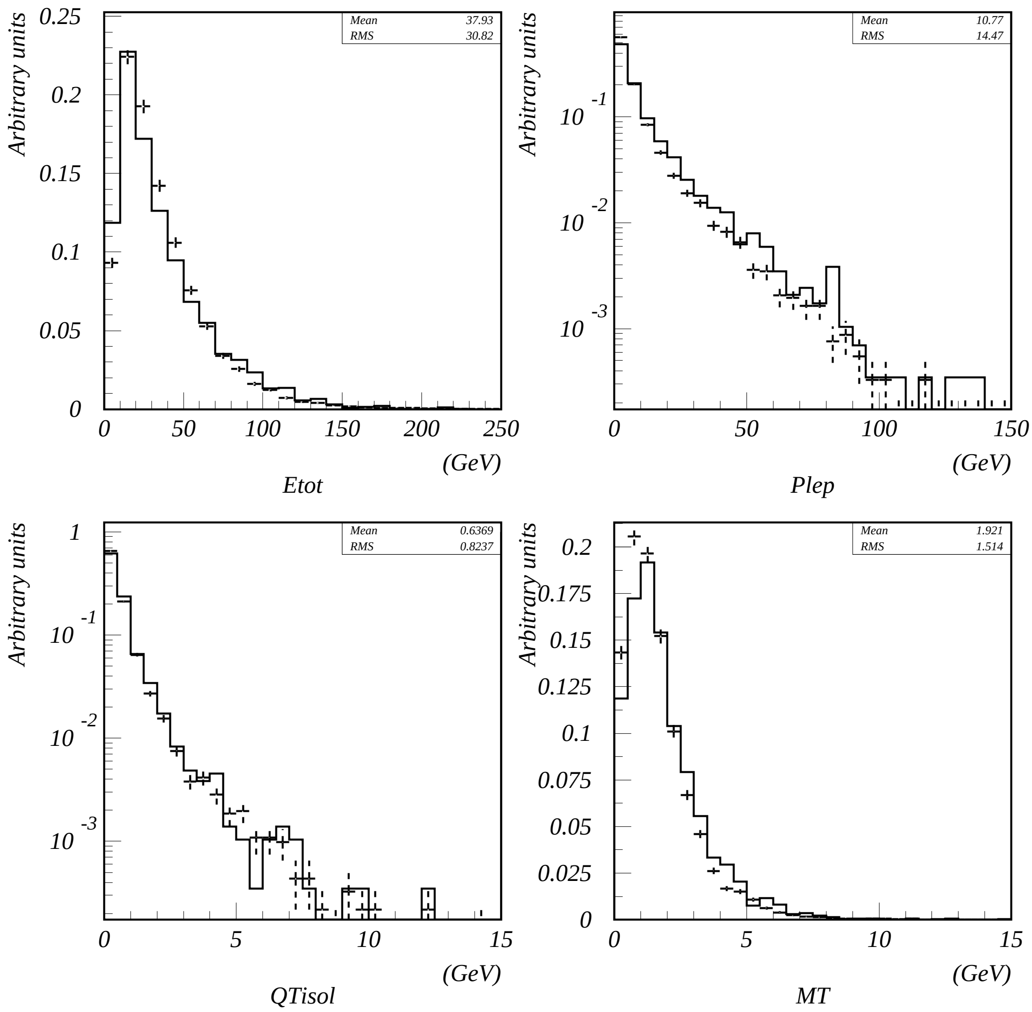

Figure 5.10: Comparison of the total visible energy, the initial electron momentum, the transverse momentum of the electron with respect to the hadronic jet and the transverse mass for events containing primary $e^{\pm}$ candidate: fake NC made from ν_μ CC MC events (solid line) and fake NC made from the '96 data (crosses).

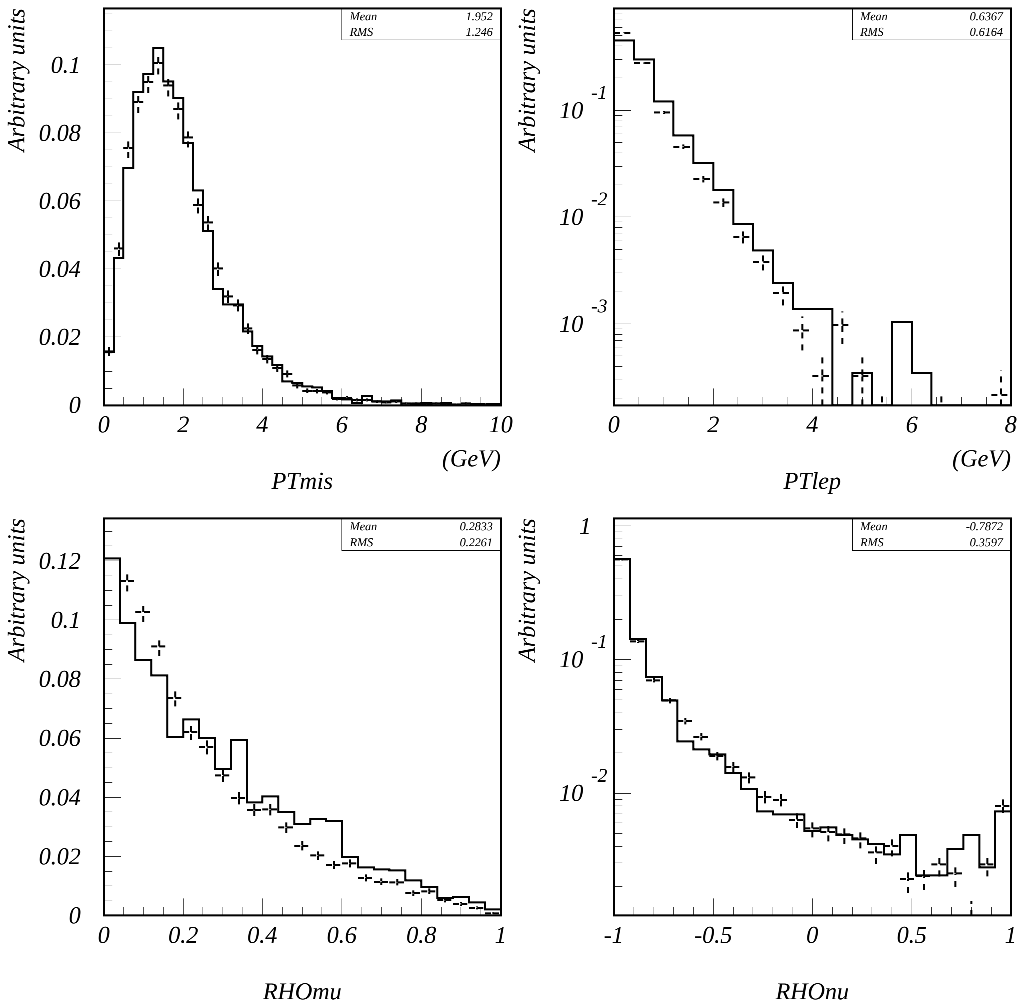

Figure 5.11: Comparison of the missing transverse momentum, P_T of the electron candidate, ρ_μ and ρ_ν for events containing primary $e^\pm$ candidate: fake NC made from ν_μ CC MC events (solid line) and fake NC made from the '96 data (crosses).

5.1.9 Results and checks

When applied to the '96 data sample our selection gives 1842 ν_e CC candidates with an estimated background contamination of ~ 5 (or < 9 at 90% CL) events from ν_μ NC and ~ 3 (or < 7 at 90% CL) events from ν_μ CC.

The comparison (between ν_e CC MC events and candidates from real data) of the kinematical variables used for the selection is given in Fig. 5.12 and Fig. 5.13. Reasonable agreement is obtained for the longitudinal variables while the transverse ones reflect the difference already seen in the p_T^{miss} distribution for ν_μ CC events (see Fig. 4.9). Let us stress however that the use of fake NC from real data to estimate the background partially compensates for these discrepancies.

One can make a prediction on the expected number of identified ν_e CC events in the '96 data sample. Using the observed number of ν_μ CC events inside FV (256074) corrected for the identification efficiency ($\varepsilon_{\nu_\mu\ CC} = (73.0 \pm 0.2)\%$) and the MC prediction for the relative beam composition ($\nu_e/\nu_\mu \sim 1.4\%$) we can assess the expected number of ν_e CC events: $1891 \pm 25(stat) \pm 95(syst)$. Which is in agreement with the number of observed events.

We checked that using the same technique we were able to select a clean sample of $\bar{\nu}_e$ CC events. 240 events were observed with a background contamination of ~ 5 (or < 9 at 90% CL) events from ν_μ NC and ~ 9 events (or < 14 at 90% CL) from ν_μ CC. The efficiency estimated using a sample of $\bar{\nu}_e$ CC MC events ($\varepsilon_{\bar{\nu}_e\ CC} = (38.4 \pm 1.4)\%$) is similar to the one obtained for ν_e CC identification. Taking the ratio of $\bar{\nu}_e$ CC over ν_e CC events we got a value of $(12 \pm 1)\%$ which is again consistent with our MC expectations.

We further checked that we are dealing with primary $e^\pm$ candidates comparing the ΔZ distributions (difference between the Z position of the primary vertex and the Z coordinate of the first hit of the lepton candidate) for ν_e CC and ν_μ CC events in the real data (see Fig. 5.14). The distributions are in reasonable agreement which confirms that the contamination of non-prompt electrons from conversions near the primary vertex is small in our ν_e CC real data sample.

5.1.10 Usage of selected events

Using the ν_e CC candidates selected from the NOMAD real data we can make some simple checks.

First of all, we can test the hypothesis of $\nu_\mu \to \nu_e$ oscillation with the probability of $(0.31 \pm 0.12 \pm 0.05)\%$ suggested by the LSND result in the region of large Δm^2. The presence of such oscillations would manifest itself as an excess of ν_e CC events compared to the MC expectations especially at low energies due to the difference between ν_e and ν_μ spectra in the original beam.

In order to reduce the systematic uncertainties it is preferable to study the ratio of the number of ν_e CC interactions over the number of ν_μ CC interactions as a function of the incoming neutrino energy (see Fig. 5.15). No oscillation signal is seen in the NOMAD data. The computation of the limit on the probability of $\nu_\mu \to \nu_e$ oscillation requires a careful study of systematic errors. This is the subject of an independent analysis [147]. When applied to the '95 data sample such an analysis [148] allowed the NOMAD collaboration to establish a 90% CL limit of 2×10^{-3} on $\sin^2(2\theta)$ for large Δm^2.

A strange behaviour of the total visible energy for ν_e CC candidates was observed in our data at high energies. In the region of $\sim 120\ GeV$ we see an excess of events at the level of 2 standard deviations (see Fig. 5.16). Scanning of the real data events corresponding to this bump did not allow to establish its origin while confirming the correct interpretation of these events as candidates for ν_e CC interactions.

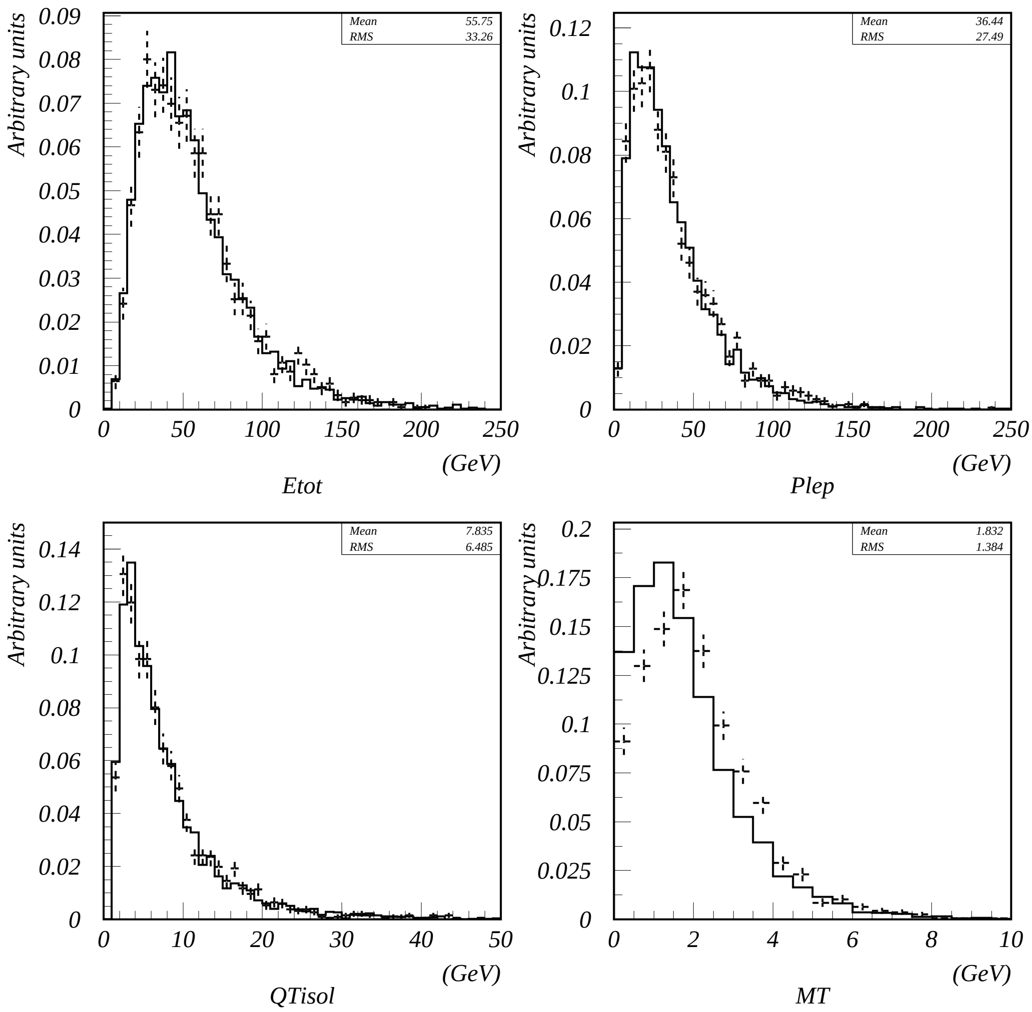

Figure 5.12: Comparison of the total visible energy, the initial electron momentum, the transverse momentum of the electron with respect to the hadronic jet and the transverse mass for ν_e CC MC events (solid line) and ν_e CC candidates selected from the '96 data (crosses).

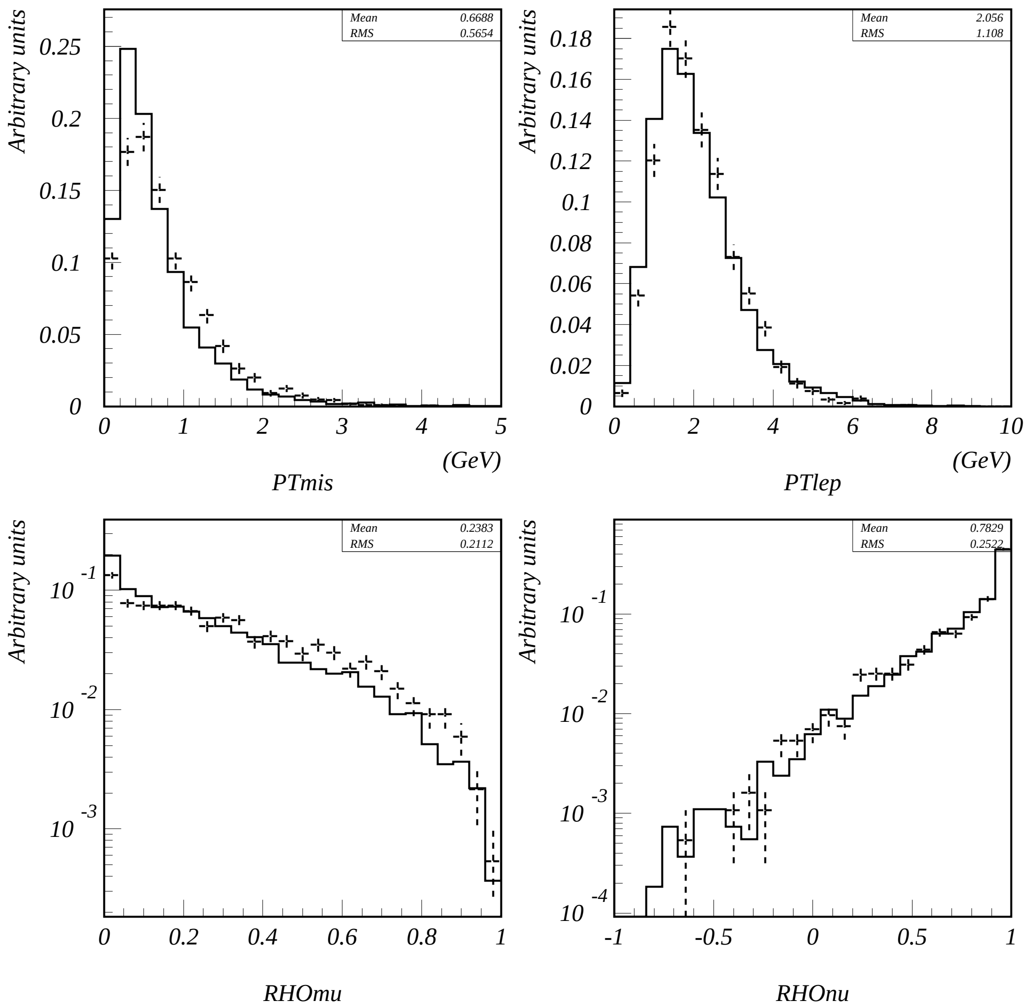

Figure 5.13: Comparison of the missing transverse momentum, P_T of the electron candidate, ρ_μ and ρ_ν for ν_e CC MC events (solid line) and ν_e CC candidates selected from the '96 data (crosses).

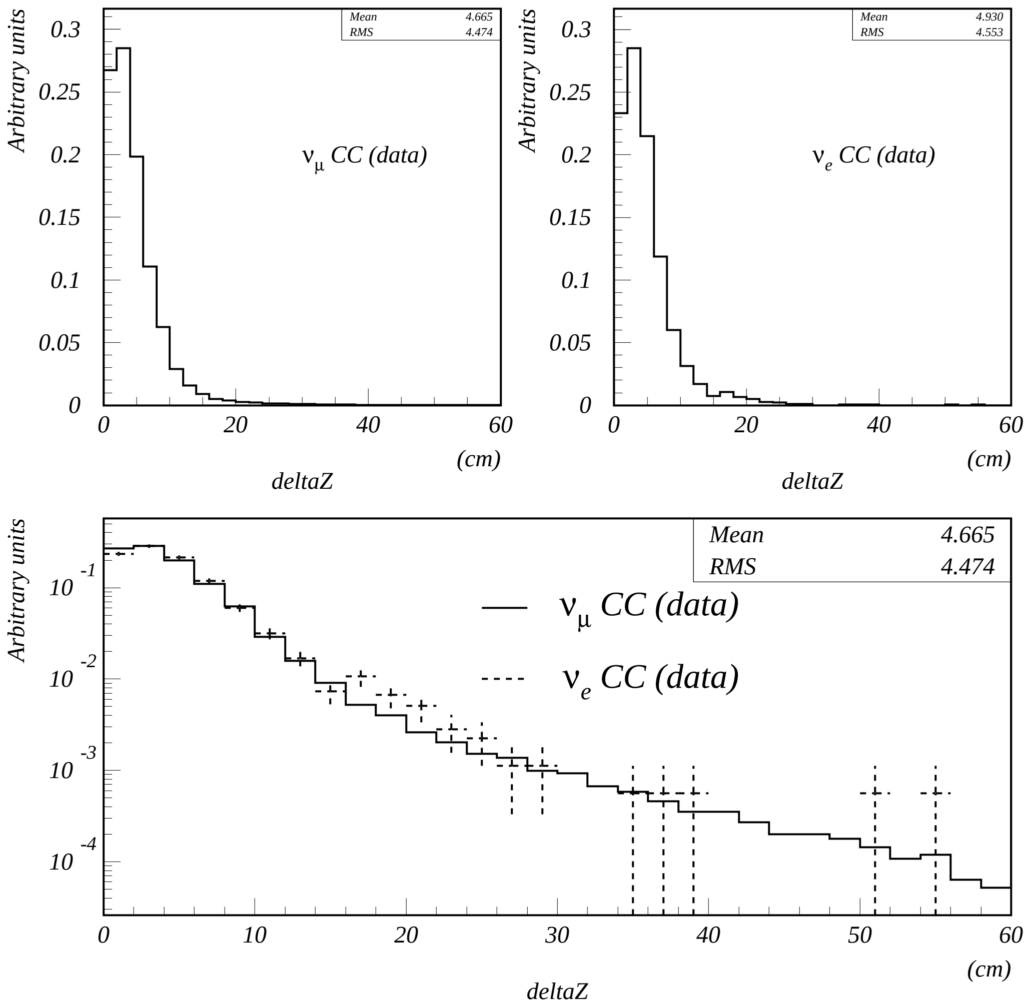

Figure 5.14: Comparison of the ΔZ distributions (difference between the Z position of the primary vertex and the Z coordinate of the first hit of the lepton candidate) for ν_μ CC and ν_e CC real data events.

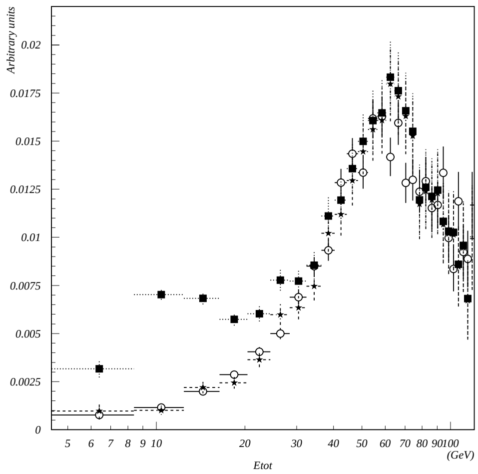

Figure 5.15: Ratio of the number of ν_e CC interactions over the number of ν_μ CC interactions as a function of the incoming neutrino energy (only statistical errors are shown). Open circles represent the expected distribution from the beam simulation program in the absence of $\nu_\mu \rightarrow \nu_e$ oscillations. Stars are NOMAD data from the '96 run. Black boxes show the distribution in case of the $\nu_\mu \rightarrow \nu_e$ oscillations with the parameters favoured by the LSND result: $\sin^2(2\theta) = 6 \times 10^{-3}$ and $\Delta m^2 = 19\ eV^2$.

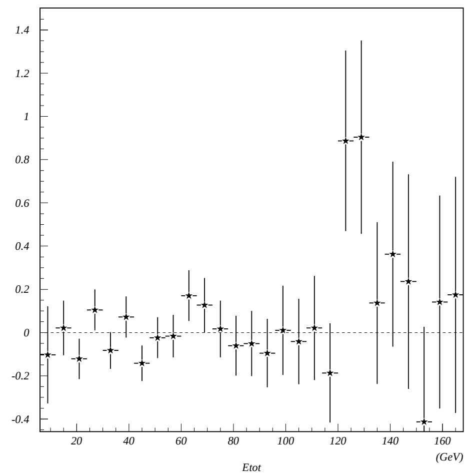

Figure 5.16: Ratio of the number of ν_e CC interactions ($\frac{REAL-MC}{MC}$) as a function of the incoming neutrino energy (only statistical errors are shown). $REAL$ represents the NOMAD data from the '96 run. MC is the expectation from the beam simulation program.

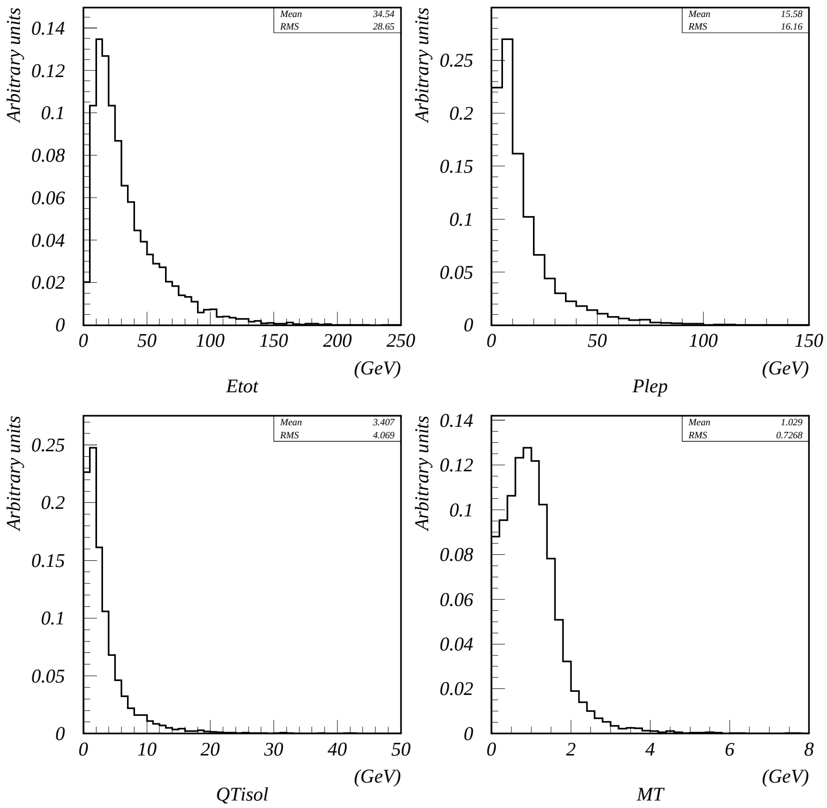

Figure 5.17: Total visible energy, initial electron momentum, transverse momentum of the electron with respect to the hadronic jet and transverse mass for ν_τ CC MC events with an identified primary electron from $\tau^- \to e^- \bar{\nu}_e \nu_\tau$ decay.

5.2 Oscillation search

Having shown that we reached a good level of understanding of our data and of the analysis tools we can address the main question of this work which is the $\nu_\mu \to \nu_\tau$ oscillation search in the $\tau^- \to e^- \bar{\nu}_e \nu_\tau$ decay channel.

5.2.1 Approach

As illustrated in Fig. 5.12 and Fig. 5.13 the reconstructed longitudinal kinematical quantities for ν_e CC interactions correspond to our MC expectations. However, the discrepancies in the variables which describe an event in the transverse plane (p_T^{miss}, M_T) are not fully understood yet. We will try to compensate for the observed differences using simulations based on real data whenever possible.

The kinematical variables of ν_τ CC events with an identified primary electron from $\tau^- \to e^- \bar{\nu}_e \nu_\tau$ decay are shown in Fig. 5.17 and Fig. 5.18. In order to select this topology we have to fight against two main sources of background - the first one coming from ν_e CC events and the second one originating from NC events and CC events with a lost lepton. The τ^- signal lies somewhere in between (see Fig 5.19 as

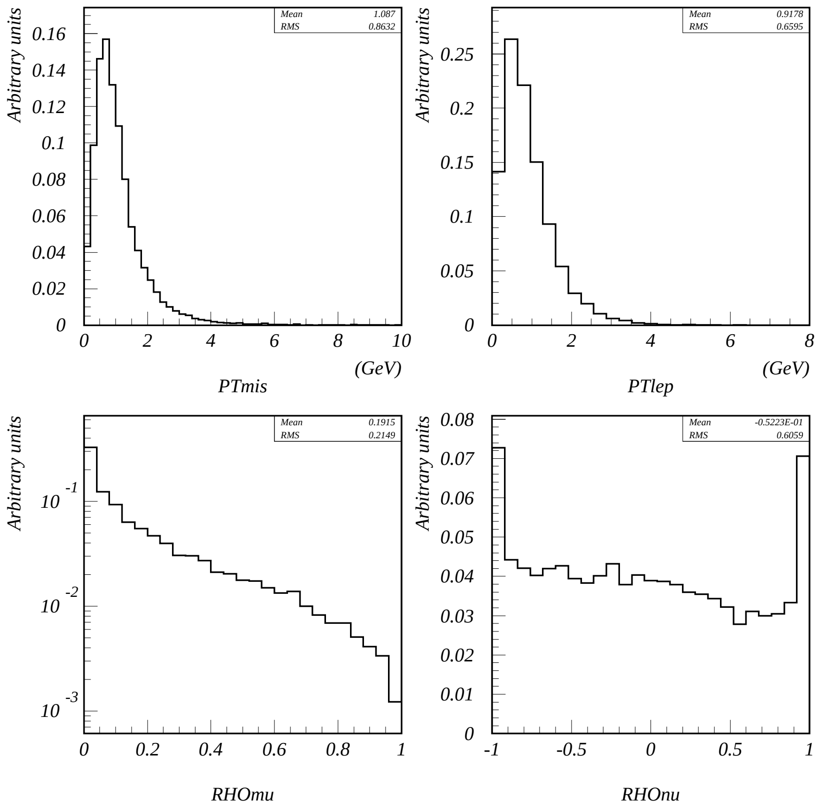

Figure 5.18: Missing transverse momentum, P_T of the electron candidate, ρ_μ and ρ_ν for ν_τ CC MC events with an identified primary electron from $\tau^- \to e^- \bar{\nu}_e \nu_\tau$ decay.

an illustration).

An approach similar to the one described for the ν_e CC selection can be used for the oscillation search in the $\tau^- \to e^-$ decay channel. The only change which is made consists in using a different kinematical selection (trying to take into account the correlations between different variables) to separate the $\tau^- \to e^-$ signal from the ν_e CC background:

```
kin = {etot,xmt,plep,ptmis,qtrr=HQ[qtisol,rr=HQ[rho_mu,rho_nu]]}
```

The efficiency versus the rejection power curve for this discriminant variable is shown in Fig. 5.20. The usage of other kinematical variables has also been explored. No gain in the background rejection power has been obtained.

The rejection of NC background is done in exactly the same way (using *nc*, *conv* and *ang* discriminant variables) as was described for the ν_e CC selection except that we were using only negative electron candidates for the parametrization of the background distributions from (fake) neutral current events. The positive samples are then independent and can be used for cross-checks. It was essential also to apply stricter cuts in order to suppress the NC background down to the required level.

To be precise, we have been applying the procedure to discriminate the signal

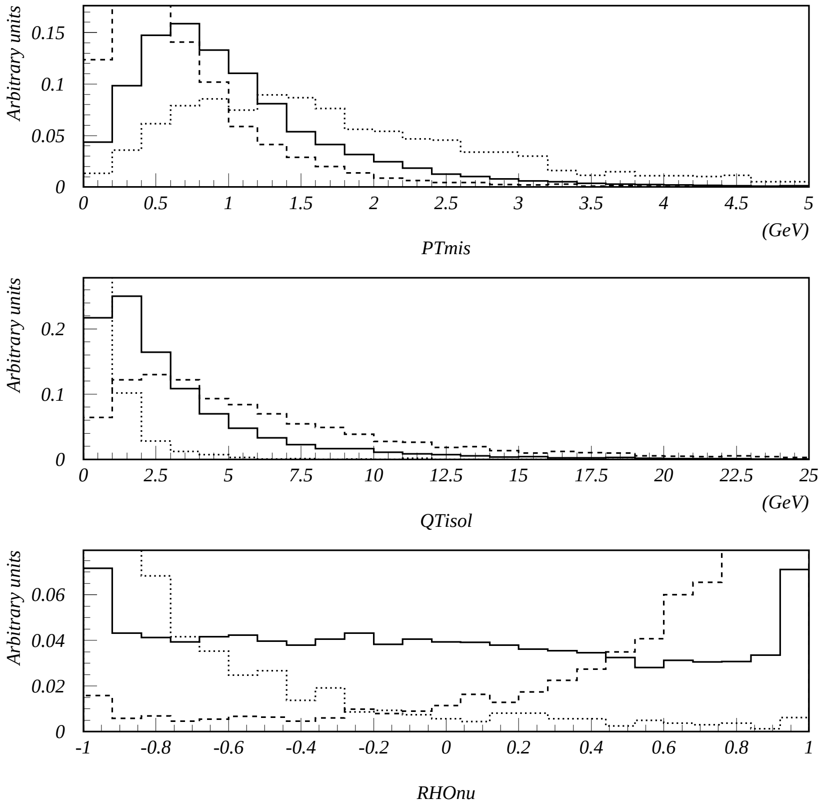

Figure 5.19: Missing transverse momentum, transverse momentum of the electron with respect to the hadronic jet and ρ_ν variable for ν_τ CC MC events (solid line), ν_e CC MC events (dashed line) and ν_μ NC MC events (dotted line). The signal is in between the two backgrounds.

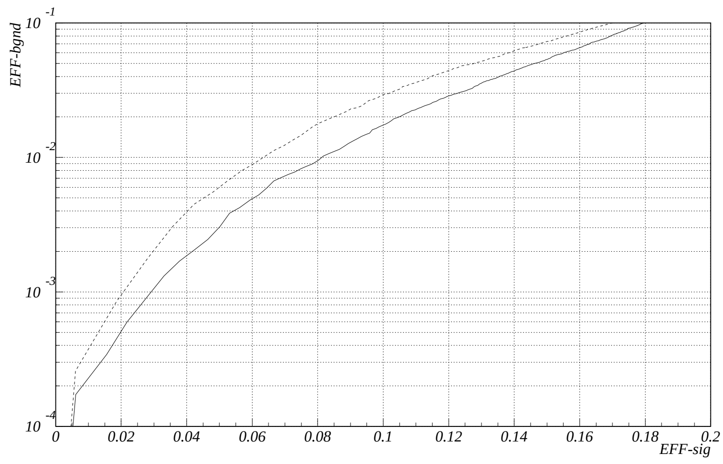

Figure 5.20: The efficiency versus rejection power curve for the kin discriminant variable (solid line) built to separate $\tau^- \rightarrow e^-\bar{\nu}_e\nu_\tau$ decays from the ν_e CC background. Dashed curve represents the result one would get not taking into account the correlations between variables, that is $kin\prime = \{etot, xmt, plep, ptmis, qtisol, rho\_mu, rho\_nu\}$. The behaviour of the curve below 1×10^{-4} is not shown because we cannot predict it given the statistics of the ν_e CC MC sample used.

from the background in two steps. First, we have rejected the ν_μ NC background introducing a bias in the kinematics for both $\tau^- \rightarrow e^-\bar{\nu}_e\nu_\tau$ and ν_e CC samples. Second, we have built the kin discriminant variable to separate the signal from the ν_e CC background using only events which survive the first selection.

It was checked that the order of the rejection of these two major backgrounds does not influence the final result.

An attempt was made to mix two backgrounds in the right proportion and to apply the rejection procedure against both of them at the same time. This approach did not give satisfactory results yet. The reason is that we had to reduce significantly the number of considered ν_e CC MC events to avoid introducing weights which could be a problem for building parametrizations with the help of HQUAD.

5.2.2 Strategy

When looking for the $\nu_\mu \rightarrow \nu_\tau$ oscillation signal in the $\tau^- \rightarrow e^-\bar{\nu}_e\nu_\tau$ decay channel one is interested in studying a possible excess of events compatible with the $\tau^- \rightarrow e^-$ decay signature compared to the estimated background. An additional handle on the background evaluation is provided by the "+" topology since we do not expect to see any $\bar{\nu}_\tau$ in the beam (prompt or from $\bar{\nu}_\mu \rightarrow \bar{\nu}_\tau$ oscillations). However, the background conditions are not symmetric for "+" and "−" because of semileptonic charm decays in ν_μ CC interactions.

A subsample of the '95 data was used to establish and check the analysis chain. That is why we have allowed ourselves to scan interesting events from the '95 run and MC samples in order to understand the major problems, while it was forbidden to look at the events from the '96 run (in order to avoid a bias caused by the introduction of additional cuts which would reject surviving events one by one).

Table 5.4: Rejection power of proposed cuts (combination of *eleid*, *conv*, *nc*, *ang* and *kin*). Samples marked by a star (*) are independent (not used for building likelihood parametrizations) and are used as a cross-check.

Criterion	ν_μ CC (MC)		ν_μ NC (MC)		fake NC (MC)		fake NC (data '96)		fake NC (data total)	
	$-$	$+^\star$	$-$	$+^\star$	$-$	$+^\star$	$-$	$+^\star$	$-$	$+^\star$
Initial	484302		148132		-		-		-	
Rec. in FV	377423		108481		275644		256074		341506	
EleID	183	296	496	522	922	1241	841	1165	1067	1463
anti ν_μ NC	3	16	6	9	10	28	37	44	43	58
anti ν_e CC	1	2	0	1	1	2	3	7	4	8

Criterion	ν_μ NC (MC)*		$\bar{\nu}_\mu$ CC (MC)*	ν_e CC (MC)	ν_e CC (MC)*	$\bar{\nu}_e$ CC (MC)*	$\tau^- \to e^-\bar{\nu}_e\nu_\tau$	$\tau^- \to e^-\bar{\nu}_e\nu_\tau{}^\star$
	$-$	$+$	$-$	$-$	$-$	$+$	$-$	$-$
Initial	150000		13127	19775	40940	2712	28460	20654
Rec. in FV	110178		9590	13892	28687	1883	21891	15921
EleID	503	491	12	6070	12737	815	6665	4940
anti ν_μ NC	4	11	0	4685	9733	653	4305	3191
anti ν_e CC	0	1	0	12	30	2	685	480

5.2.3 Results

Monte-Carlo samples

Having applied a combination of cuts against ν_μ NC & CC and ν_e CC backgrounds we have obtained the following results for the Monte-Carlo samples (see Table 5.4):

- 3 survivors (1 "$-$" and 2 "$+$") from 377423 ν_μ CC events with reconstructed vertex inside FV;
- 1 survivor ("$+$") from 108481 ν_μ NC events in the FV. It was found that if we do not apply electron identification a primary charged hadron has a probability to fake an oscillation signal of $\sim 2 \times 10^{-5}$ for negatives and of $\sim 1 \times 10^{-4}$ for positives;
- no survivors from 9590 $\bar{\nu}_\mu$ CC MC events with reconstructed vertex in the FV.
- 12 "$-$" events out of 13892 ν_e CC MC events with reconstructed vertex in the FV. Using independent sample one gets 30 out of 28687 events in FV. One can realize immediately that this is the dominant background for the oscillation search in the $\tau \to e$ decay channel for this particular analysis;
- 2 "$+$" events out of 1883 $\bar{\nu}_e$ CC MC event with reconstructed vertex in the FV;
- 3 events (1 "$-$" and 2 "$+$") from 275644 thousand fake NC (MC) events;
- 12 events (4 "$-$" and 8 "$+$") from fake NC (data) events (subsample of '95 & data '96 corresponding in total to 341506 thousand events in the FV);

Table 5.5: Rejection power of the proposed cuts (combination of *eleid*, *conv*, *nc*, *ang* and *kin*) when applied to real data samples.

Criterion	data '95		data '96	
	$-$	$+$	$-$	$+$
Inside FV	145909		514061	
EleID	912	329	2991	1166
NC rejection	565	71	1640	226
CC rejection	2	0	10	3

- an efficiency for $\tau^- \to e^-$ decay detection: $\varepsilon_{\tau^- \to e^-} = (3.1 \pm 0.1)\%$. When estimated using an independent event sample this efficiency is found to be $(3.0 \pm 0.1)\%$. The distributions of the kinematical variables for the surviving ν_τ CC events are shown in Fig. 5.21.

These results should be considered as an illustration of the data reduction flow in this analysis. The surviving events will be used to understand the possible background sources.

Real data
If we apply this selection to the real data samples we find the following number of surviving events (see Table 5.5 for details):
'95 : 2 "$-$" and 0 "$+$";
'96 : 10 "$-$" and 3 "$+$";

5.2.4 Interpretation of results

In the most general case, taking into account several τ decay channels, the upper limit on the oscillation probability can be written as

$$P_{osc} < \frac{N_\tau}{(N_\mu/\varepsilon_\mu) \times (\sigma_\tau/\sigma_\mu) \times \Sigma_i(Br_i \times \varepsilon_i)}$$

where N_τ is an upper limit on the possible number of τ decays, N_μ is the observed number of ν_μ CC interactions inside the fiducial volume, ε_μ is the identification efficiency for ν_μ CC events, (σ_τ/σ_μ) the kinematical suppression factor due to the difference in the τ and μ masses, Br_i is the branching ratio and ε_i is the selection efficiency for the i-th decay mode of τ.

The preliminary limit on the probability of $\nu_\mu \to \nu_\tau$ oscillations using the NOMAD '95 data sample and combining all the studied decay channels of τ was established:

$$P_{osc}(\nu_\mu \to \nu_\tau) < 2.1 \times 10^{-3}$$

which corresponds to $\sin^2 2\theta_{\mu\tau} < 4.2 \times 10^{-3}$ for large Δm^2 at 90% CL [149].

The contribution of the DIS analysis of $\tau \to e$ decay channel to this result is $(N_\mu/\varepsilon_\mu) \times (\sigma_\tau/\sigma_\mu) \times (Br \times \varepsilon) = 635$ with 0 events observed while the expected background amounts to $0.6^{+0.7}_{-0.6}$. This result corresponds to the limit on the probability of $\nu_\mu \to \nu_\tau$ oscillations $P_{osc}(\nu_\mu \to \nu_\tau) < 4 \times 10^{-3}$ at 90% CL. Let us say that the kinematical suppression factor (σ_τ/σ_μ) is equal to 0.48 in the DIS region and the branching ratio of the $\tau^- \to e^- \bar{\nu}_e \nu_\tau$ decay channel is 17.8%.

The larger statistics of the '96 data sample did not allow us to improve the limit on the probability of $\nu_\mu \to \nu_\tau$ oscillations using $\tau^- \to e^- \bar{\nu}_e \nu_\tau$ decay channel due to the presence of background events in our analysis.

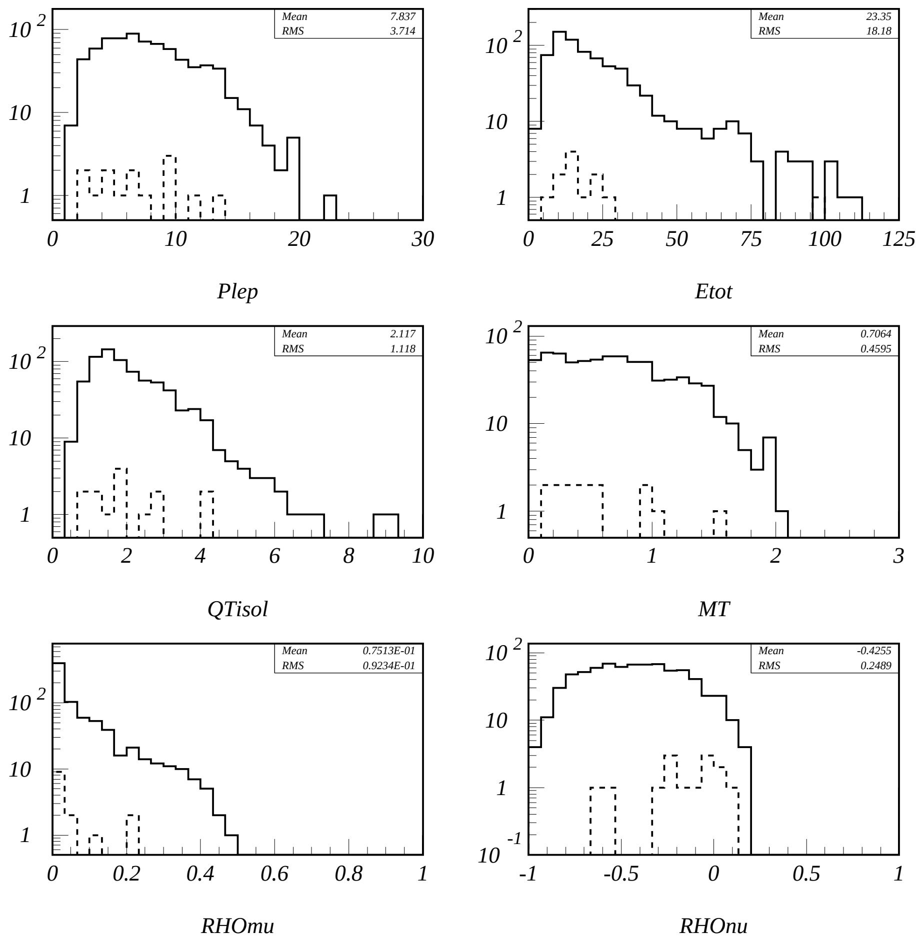

Figure 5.21: Distributions of kinematical variables for the surviving ν_τ CC events (solid line) and ν_e CC events (dashed line).

Table 5.6: For a given τ detection efficiency the average number of expected background events ($<\mu_B>$), the number of events seen in the '96 data (N_{DATA}), the systematic correction factor, the upper limit at 90% CL on the number of signal events (N_{signal}), the sensitivity of the analysis and the limit on the probability of the oscillations at 90% CL are presented.

τ efficiency (%)	$<\mu_B>$ "–"	N_{DATA} "–"	Systematic correction	90% CL on N_{signal}	Sensitivity (a.u.)	Probability ($\times 10^{-3}$)
15.0	295.3 ± 7.3	316	1.00	45.9	0.873	10.2
10.0	67.3 ± 3.6	96	1.07	38.1	1.181	12.7
9.0	51.0 ± 3.2	77	1.10	33.6	1.203	12.4
8.5	43.5 ± 2.9	61	1.11	24.1	1.224	9.5
8.0	38.0 ± 2.8	52	1.12	20.1	1.225	8.4
7.5	32.5 ± 2.6	43	1.13	16.4	1.236	7.3
7.0	27.9 ± 2.4	35	1.14	13.1	1.241	6.2
6.5	24.2 ± 2.3	29	1.15	11.0	1.234	5.6
6.0	21.2 ± 2.2	27	1.16	11.5	1.210	6.4
5.0	15.3 ± 1.9	19	1.17	9.3	1.185	6.2
4.0	9.8 ± 1.7	12	1.18	7.4	1.179	6.2
3.0	6.4 ± 1.5	9	1.18	7.3	1.094	8.1
2.0	3.4 ± 1.3	6	1.19	6.7	0.990	11.2
1.0	1.7 ± 1.2	5	1.19	7.3	0.697	24.2

Table 5.7: For a given τ detection efficiency the average number of expected background "+" events and the number of "+" events seen in the '96 data are presented.

τ eff. (%)	Exp. "+"	Obs. "+"
15.0	56.9 ± 5.6	62
10.0	20.5 ± 3.6	21
9.0	15.1 ± 3.0	15
8.0	10.3 ± 2.5	13
7.0	9.0 ± 2.4	10
6.0	7.1 ± 2.1	9
5.0	5.6 ± 2.0	8
4.0	5.3 ± 2.0	7
3.0	4.0 ± 1.7	3
2.0	3.4 ± 1.7	2
1.0	1.4 ± 1.2	2

Using the number of observed events in the studied MC samples one can derive the expectation for the number of events in our data from different background sources. In order to make a prediction on the expected number of background events μ_B we have been using the following procedure:

$$\mu_B = \hat{p} \cdot N_{DATA} = \sum_i (n_i + \frac{1}{2}) \cdot \frac{N_{DATA_i}}{N_{MC_i}}$$

where n_i is the number of surviving background events in the i-th category of MC events with statistics N_{MC_i}; N_{DATA_i} is the number of events of the corresponding category in the data sample. When n_i is small and when the statistics of the corresponding MC sample is of the same order as the data sample ($\frac{N_{DATA_i}}{N_{MC_i}} \sim 1$) the knowledge of μ_B is poor and could be biased towards low values, especially if $n_i = 0$. The term $\frac{1}{2}$ was introduced in order to take into account the relatively low statistics of the MC samples used for this analysis. However, in our case -where the dominant background is predicted rather well and as long as μ_B is greater than a few units- it does not make any significant difference.

Let us stress that independent MC samples were used for the calculation of the number of expected background events.

We defined the sensitivity of the analysis as the ratio of the τ^- detection efficiency over the square root of the number of expected background events. We varied the positions of our cuts in order to find the highest sensitivity region of this analysis which turned out to contain a significant number of expected background events (see Table 5.6). This fact shows that some of our background events are so signal-like that when trying to reject them we loose more in efficiency than we gain in rejection power.

This study also confirms that we can predict rather well the number of observed data events in both "$-$" and "$+$" topologies (see Table 5.7).

The upper limit on the number of the expected signal events is computed using the procedure described in the Review of Particle Properties and in [150] assuming that the predicted background is known with negligible error. This assumption is valid for the statistical error on the predicted background since the dominant contribution is known rather well. However, it is extremely difficult to take into account the systematic error on the predicted number of background events given the fact that our knowledge of the effects which cause the discrepancy between MC simulation and the real data is rather poor. Nevertheless, we have tried to get an estimate of the systematic uncertainty using the following procedure. We have applied a combination of cuts (nc and ang) to select a sample of ν_μ CC candidates from the real data. This sample is expected to be 99.97% pure. Making an appropriate mixture of MC events we have applied the same selection criteria to this data set. We then studied the dependence of the ratio of the number of events surviving the cut against CC background (kin) as a function of this cut. From the Fig. 5.22 it is clear that in the signal-like region ($kin > 0.9$) the behaviour of the data and the simulated events differs. This difference cannot be interpreted in terms of $\nu_\mu \to \nu_\tau$ oscillations with a subsequent $\tau^- \to \mu^- \bar{\nu}_\mu \nu_\tau$ decay since such a signal would be two orders of magnitude more prominent in the $\tau^- \to e^- \bar{\nu}_e \nu_\tau$ decay channel due to the much better background conditions. We have checked also that the number of surviving ν_μ CC events (after reweighting to take into account the difference in energy spectra) is consistent with the corresponding number of ν_e CC survivors. That is why we can attribute the observed discrepancy to the difference in the hadronic jet behaviour between the simulated and the real data events and we can conclude that the systematic uncertainty varies from 5% to 20% in the region of interest.

To extract the limit on the probability of neutrino oscillations obtained in this

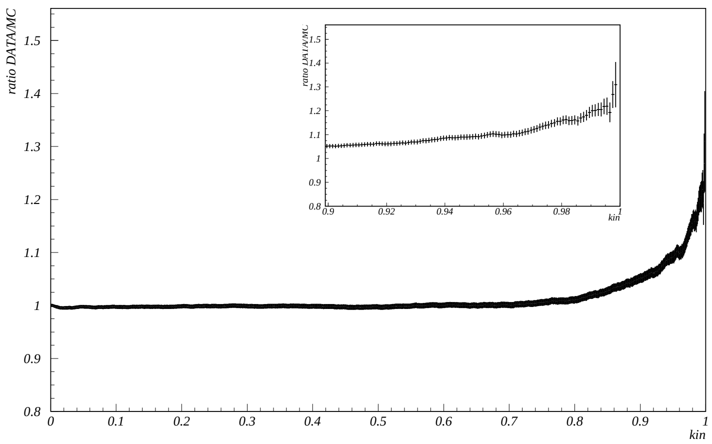

Figure 5.22: The ratio of the number of surviving ν_μ CC candidates in the real data over the appropriate mixture of simulated events as a function of the kin discriminant variable. In the signal region ($kin > 0.9$) the discrepancy varies from 5% to 20% which could be considered as an estimate of the systematic error due to the difference between the real data and the simulation. The region of the highest sensitivity to the oscillation signal corresponds to $kin = 0.98$.

analysis we use the number of events observed in the real data in the region of the highest sensitivity.

In contradiction to Murphy's principle, the region of highest sensitivity of this analysis corresponds to the best limit on the oscillation probability (Table 5.6):

$$P_{osc}(\nu_\mu \to \nu_\tau) < 6.2 \times 10^{-3} \quad \text{at 90\% CL.}$$

5.2.5 Study of background events

Some of the surviving events were carefully studied.

A spectacular background event was found in the ν_μ CC MC sample. It contains a μ^- decay within 40 cm from the primary vertex (see Fig. 5.23). The missing momentum carried away by neutrinos points in the direction of the identified electron from the decay and fakes the τ^- signature we are looking for.

The 2 "+" survivors from ν_μ CC MC sample contain semileptonic charmed meson decays. This is also the case for 1 out of 2 surviving events from fake NC (MC), while the other event from this category is due to a misidentified π^+.

The "$-$" survivor in the sample of fake NC (MC) is the event where the primary muon emits a delta electron near the primary vertex (Fig. 5.24). The same problem appears when scanning surviving "$-$" events from fake NC (data) sample (Fig. 5.25) representing non-physical background inherent to the method of constructing NC events by removing the identified muon from ν_μ CC.

The "+" event left after selection in the ν_μ NC MC sample originates from the π^0 Dalitz decay.

Studying the 12 survivors from ν_e CC MC sample we have found the following potential problems. Several events contain escaping photons or neutrons in the direction of the electron candidate (an example of such event is shown in Fig. 5.26 and Fig. 5.27). The reconstruction of the great majority of events is messed up by a

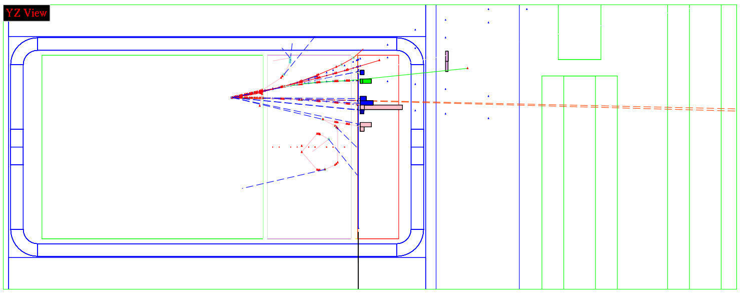

Figure 5.23: Run 212003 event 13655 (YZ view of the simulated event): surviving candidate from ν_μ CC MC. This event contains $\mu^- \to e^- \bar{\nu}_e \nu_\mu$ decay with $p_{\mu^-} = 15\ GeV$ and $p_{e^-} = 2.8\ GeV$. The remaining momentum is taken away by two neutrinos (long dashed lines).

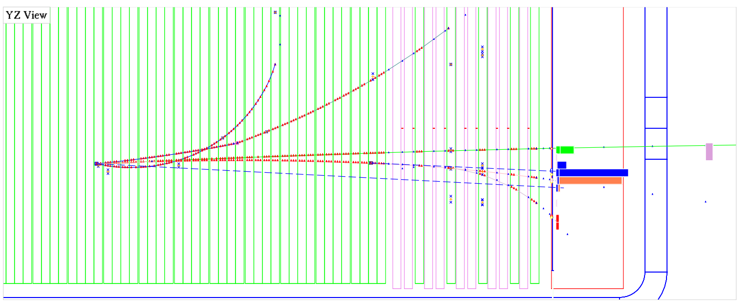

Figure 5.24: Run 212011 event 19660 (DC view of the reconstructed event): surviving candidate from fake NC (MC). This event contains μ^- emitting a delta electron near the primary vertex. The electron track is the one closest to the muon (shown as the line which extends out of the DC fiducial volume).

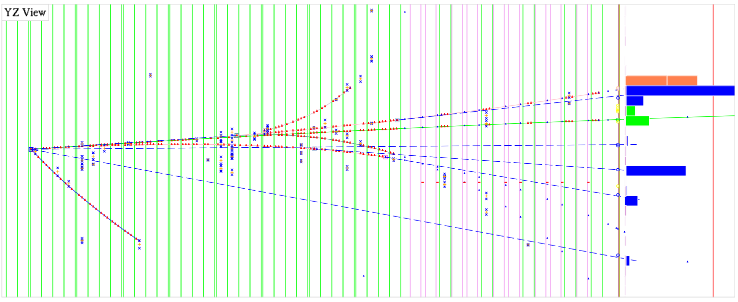

Figure 5.25: Run 13312 event 3003 (DC view of the reconstructed event): surviving candidate from fake NC (data). This event most probably contains μ^- emitting a delta electron near the primary vertex.

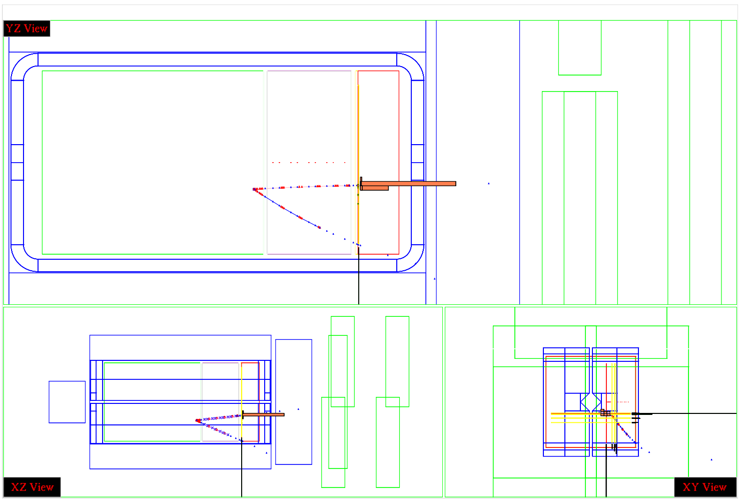

Figure 5.26: Run 232001 event 2971 (General view of the reconstructed event): dangerous event from ν_e CC MC.

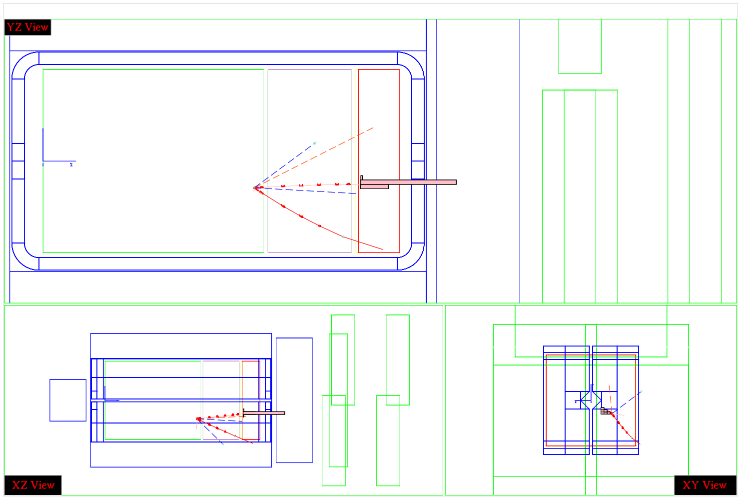

Figure 5.27: Run 232001 event 2971 (General view of the simulated event): dangerous event from ν_e CC MC. Primary neutron escaping detection is seen as a dashed grey line ($p_n = 0.8\ GeV$).

secondary hadron interaction causing double counting when adding neutral particles to the list of primary tracks. This overestimation of the hadronic vector fakes the tau decay signature. One should point out that in all the surviving ν_e CC MC events the primary electron is correctly identified and its momentum is reasonably well reconstructed (see Table 5.8) with the exception of one event (16507) where a hard brem photon escapes detection at the edge of the ECAL. The Fermi momentum of surviving events is biased towards larger values: 5 events have $p_F > 0.35\ GeV$. We checked also that in all these 5 events the $\vec{p}_F$ vector is opposite to the $\vec{p}_e$ vector in the transverse plane introducing missing transverse momentum in the direction of the electron candidate and, thus, faking the τ^- decay topology.

We found a dangerous "+" event in the fake NC (data) sample which is quite interesting since this event is simple and well reconstructed (see Fig. 5.28 and Fig. 5.29). The probability that this event is caused by a conversion near the primary vertex is low (there is no single hit near the primary vertex which could be attributed to the negative partner of the e^+ candidate which is also well separated from the rest of the hadrons). The easiest interpretation of this event is a semileptonic charmed meson decay but it seems quite improbable because of the low hadronic activity.

Let us look at one more event from the fake NC (data) sample (see Fig. 5.30). The event becomes dangerous as soon as the muon is removed. Scanning of this event shows that it contains a conversion near the primary vertex and the positive partner was not reconstructed because of its low momentum ($< 50\ MeV$). This event cannot be easily rejected by the set of cuts against NC background because of the low multiplicity and the low hadronic activity (as a result the direction of the hadronic jet is not well defined).

Let us consider one of the signal-like events from the '95 subsample (Fig. 5.31). This event illustrates another potential source of background: a hadron interacting

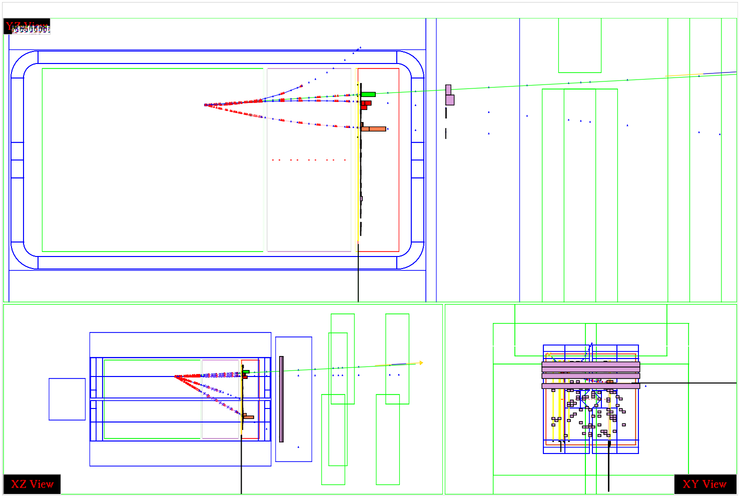

Figure 5.28: Run 8746 event 3736 (General view): a dangerous event from the fake NC (data). Positron ($p_{DC} = 2\ GeV$, $E_{ECAL} = 1.4\ GeV$, $E_{PRS\ X} = 36.9\ mip$, $E_{PRS\ Y} = 45.3\ mip$ and the average energy deposition in TRD straw tubes is $< E_{TRD} >= 23.7\ keV$) is the largest angle track in both YZ (top) and XZ (bottom left) views.

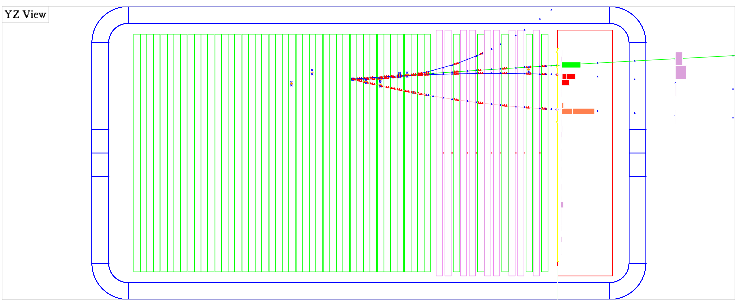

Figure 5.29: Run 8746 event 3736 (DC view): a dangerous "+" event from the fake NC (data). There are no leftover hits near the primary vertex which could be attributed to non-reconstructed negative partner of this e^+ candidate.

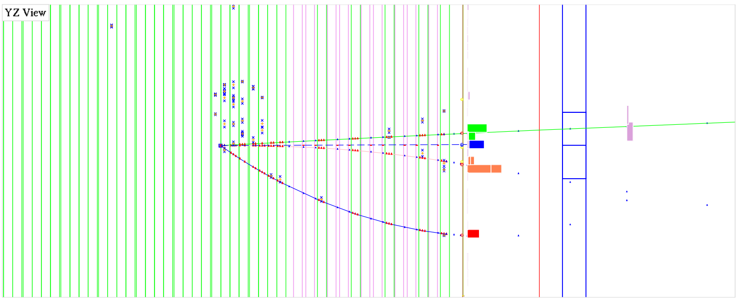

Figure 5.30: Run 13132 event 27820 (DC view): a dangerous "−"event from the fake NC (data). There are hits near the primary vertex which could be attributed to the non-reconstructed positive partner of this e^- candidate.

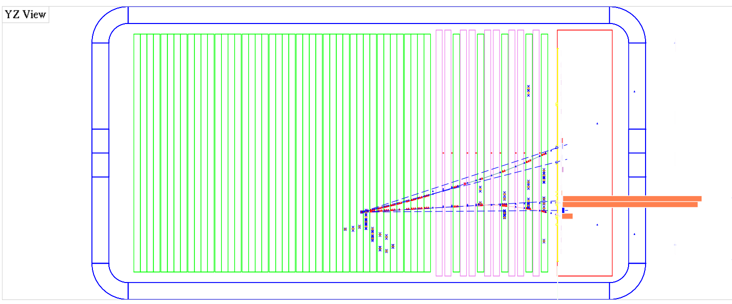

Figure 5.31: Run 9288 event 14549 (DC view): the event from the '95 run which is suspected to contain a negative hadron interacting in the TRD region.

Table 5.8: The quality of the initial momentum reconstruction for electron candidates in the surviving ν_e CC MC events. The value of Fermi momentum in each event is also given.

RUN	EVT	ELEP_MC	PLEP_REC	FERMI
232001	14005	6.6469	6.5928	0.17697
232001	16507	23.983	13.033	0.16529
232001	2525	7.3583	7.3478	0.76017
232001	21336	3.7789	4.0056	0.49693
232001	2900	5.9707	4.9491	0.19862
232001	2971	5.1870	5.6199	0.13800
232001	22972	6.5169	6.1317	0.13853
232001	17907	11.022	9.6290	0.53216
232001	19245	5.8481	6.2265	1.5624
232001	20281	2.7344	2.4591	0.39115
232001	20294	4.2814	4.5042	0.16111
232001	25962	6.6770	6.5326	0.19074

in the TRD region. A careful investigation of the TRD track associated to the primary electron candidate shows a strange behaviour: it looks like a *mip* when entering the TRD and suddenly changes its nature:

```
Long Interactive Dump **** Reconstructed Track number :     3
 Parameters :  0:     -114.6836    1:       -4.2941
 First last planes  1  9 , nhits  9
chi2, incremental :      13.0233 , global :      13.0232
 plane  1  rec    1  geant    0 x -112.10  residual -0.7619 energy     0.60 keV
 plane  2  rec    1  geant    0 x -111.21  residual  0.6378 energy     8.76 keV
 plane  3  rec    1  geant    0 x -113.51  residual -0.7511 energy     6.70 keV
 plane  4  rec    1  geant    0 x -112.78  residual  0.4859 energy    40.11 keV
 plane  5  rec    1  geant    0 x -113.62  residual  0.5468 energy    20.62 keV
 plane  6  rec    1  geant    0 x -114.57  residual  0.1087 energy    31.98 keV
 plane  7  rec    1  geant    0 x -115.24  residual  0.3468 energy    30.98 keV
 plane  8  rec    1  geant    0 x -115.97  residual  0.1245 energy    36.49 keV
 plane  9  rec    1  geant    0 x -117.73  residual -0.7376 energy    83.48 keV
```

A similar behaviour can be found in a MC event (see Fig. 5.32) containing a π^- which interacts in the TRD region and produces an energetic π^0 leaving an electromagnetic shower in the ECAL. The dump of the TRD track looks familiar to us (after 3 hits in the TRD which are consistent with a *mip* an abrupt change occurs which is confirmed by the change in the GEANT ID of the corresponding MC track):

```
Long Interactive Dump **** Reconstructed Track number :     3
 Parameters :  0:      -78.8620    1:        1.9082
 First last planes  1  9 , nhits  8
chi2, incremental :      10.9934 , global :      10.9933
 plane  1  rec    3  geant    3 x  -79.67  residual  0.6765 energy    12.34 keV
 plane  3  rec    3  geant    3 x  -79.52  residual  0.1992 energy     6.09 keV
 plane  4  rec    3  geant    3 x  -80.38  residual -0.8859 energy     7.10 keV
 plane  5  rec    3  geant    7 x  -79.62  residual -0.5281 energy    32.30 keV
 plane  6  rec    3  geant    7 x  -78.91  residual -0.0432 energy    38.37 keV
```

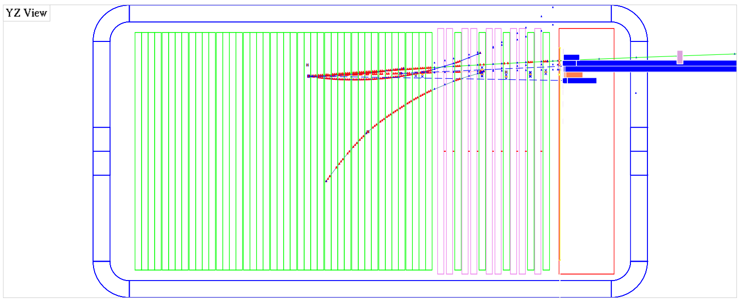

Figure 5.32: Run 212001 event 20498 (DC view): π^- interacts in the TRD region and produces an energetic π^0 leaving an electromagnetic shower in the ECAL. This configuration fakes a primary electron signature. Unfortunately, the backward going track is not associated to the interaction vertex and cannot be used to recognize the hadronic interaction.

plane	7	rec	3	geant	7	x	-78.00	residual	0.4646	energy	159.16	keV
plane	8	rec	3	geant	7	x	-78.71	residual	-0.4705	energy	43.88	keV
plane	9	rec	3	geant	7	x	-77.25	residual	0.5873	energy	472.22	keV

Unfortunately, the currently implemented TRD identification algorithm [93] does not take into account the order of TRD hits in a TRD track. That is why the identification of such a topology (hadron interacting in the TRD region) cannot be done on a solid ground.

As a result, the scanning of the surviving events shows that there is a number of events which could be rejected by using improved reconstruction and identification algorithms. While there are also events representing irreducible background for the $\nu_\mu \to \nu_\tau$ oscillation search in the $\tau \to e$ decay channel.

5.2.6 Conclusion

Despite of all our efforts to improve the reconstruction quality and the sensitivity of the analysis we are still unable to reach the detection efficiency for the $\tau \to e$ decay channel declared in the proposal of the experiment while keeping the needed background rejection power [77].

Nevertheless, the preliminary analysis presented here shows that some improvements both in the reconstruction and in the analysis technique are still possible. We hope that with an improved reconstruction some background events will disappear.

The MC simulation of neutrino interactions in the NOMAD detector has been improved in both the generation of the primary kinematics and the description of the jet fragmentation together with a detailed simulation of the detector response. However, we still observe a discrepancy in the transverse plane between the data and the simulation which currently limits the predicting power of our MC. The use of the data simulator allows to correct for some of these differences but only in a restricted kinematic region. Besides, since we are dealing with large data samples and want to reach high sensitivity we need to understand all the possible background sources to the oscillation search down to the level of $10^{-5} \div 10^{-6}$. The data simulator has by definition the same statistics as the data sample and thus has a limited precision for the ν_μ induced backgrounds. For other background sources the correct simulation of detector effects (such as overlaps in different subdetectors) when substituting a muon by an electron implies the mixture of both simulated and real information which is not at all straightforward. Finally, this approach could also introduce some additional background leading to a lower efficiency for the signal detection. For example, building a fake NC event from an event where the primary muon emits a delta electron close to the primary vertex may fake the expected tau decay topology once the muon is removed.

This analysis is the first attempt to use the '96 data for the oscillation search in the $\tau^- \to e^-\bar{\nu}_e\nu_\tau$ decay channel. Other analyses performed within the NOMAD collaboration using the '95 data sample declare better sensitivity to the signal and higher level of background rejection [151, 152]. We are currently trying to understand these differences. The serious limitation of the analysis presented here is a lack of MC statistics. Clearly larger samples of simulated events are needed to perform better parametrizations of the signal and the background distributions. On the other side, we have tried to use mainly kinematical quantities which are well reproduced by the MC simulation to build discriminant variables.

To conclude, we can state that the most dangerous background for the $\tau^- \to e^-$ search is due to ν_e CC interactions. In these events the major problem is not related to the proper electron reconstruction but to the understanding of the hadronic jet. Other backgrounds, such as muon decays or conversions near the primary vertex, can be suppressed -at some loss of efficiency- with either a lower bound on the transverse mass or with specialized cuts against conversions for the low multiplicity events.

Summary

This work has been done in the framework of the NOMAD experiment at CERN. It is devoted to the $\nu_\mu \to \nu_\tau$ oscillation search in the $\tau^- \to e^- \bar{\nu}_e \nu_\tau$ decay channel.

After a brief reminder on the neutrino properties and a short review of the experimental searches for neutrino oscillations, the description of the NOMAD experiment is given.

The event reconstruction in the NOMAD experiment is presented with a special emphasis put on the electron identification and reconstruction. The track model used for the charged track reconstruction is described in details. The algorithm developed to treat electron trajectories in the NOMAD setup based on the subdetector matching technique and the breakpoint search algorithm is presented.

The quality of the reconstruction of the kinematics of neutrino interactions is illustrated. It is shown that the currently used detector simulation program cannot reproduce precisely the behavior of the hadronic jet observed in the NOMAD real data especially in the plane perpendicular to the incoming neutrino direction. To overcome this problem simulations based on the real data are used whenever possible.

The method based on the likelihood ratio is developed to discriminate a signal from a background. A selection of ν_e CC candidates from the NOMAD '96 data set is performed using this technique. 1842 events are extracted with a selection efficiency of $(38.5 \pm 0.5)\%$ while the background contamination is estimated to be less than 0.5%. This number of events is compatible with our expectations: $1891 \pm 25(stat) \pm 95(syst)$. No sign of possible $\nu_\mu \to \nu_e$ oscillation signal corresponding to the LSND solution in the large Δm^2 region is observed in the NOMAD data.

Finally, the preliminary analysis of the $\nu_\mu \to \nu_\tau$ oscillation search in the $\tau^- \to e^- \bar{\nu}_e \nu_\tau$ decay channel using the data collected during the '96 run is presented. It is shown that currently the contribution of this decay channel to the sensitivity of the experiment for this particular analysis is limited by the presence of a dominant background from ν_e CC interactions. In the region of the highest sensitivity of this analysis we obtain the 90% CL limit on the oscillation probability:

$$P_{osc}(\nu_\mu \to \nu_\tau) < 6.2 \times 10^{-3}$$

Résumé

Cette thèse décrit une recherche d'oscillations de neutrinos dans le faisceau de haute énergie du CERN avec le détecteur NOMAD qui permet de sélectionner des candidats d'interactions du ν_τ.

Le premier chapitre dresse un panorama de la physique des neutrinos avec une discussion du problème de leurs masses et de leurs mélanges. En particulier sont presentées les diverses indications provenant du déficit des neutrinos solaires, de l'anomalie des neutrinos atmospheriques et du résultat de l'expérience LSND. Les différents aspects tant théoriques qu'expérimentaux sont abordés, et l'importance des oscillations qui permet d'atteindre la region des très petites masses est soulignée.

Le deuxieme chapitre décrit le dispositif expérimental utilisé: tout d'abord le faisceau du CERN essentiellement composé de ν_μ puis le détecteur NOMAD dont les caractéristiques ont été spécialement choisies pour cette recherche. Les performances des divers éléments de l'appareillage sont presentées de manière critique.

Le troisième chapitre discute le problème fondamental de la reconstruction des traces dans NOMAD, l'ambition du détecteur étant de reconstruire avec le maximum de précision l'ensemble des interactions. Les algorithmes utilisés sont décrits tant pour les traces chargées que pour les traces neutres. En particulier la reconstruction des traces chargées dans le système des chambres à dérives est presentée, puis l'association des information des sous-élements du détecteur nécessaires pour l'identification des particules est détaillée. L'accent est mis sur le cas des électrons dont le comportement spécial donne lieu à un développement particulier.

Le quatrième chapitre parle de la simulation des interactions du neutrino dans le détecteur qui permet d'évaluer les qualités de reconstruction de la cinématique des interactions en comparant les grandeurs engendrées et leurs valeurs obtenues après reconstruction. On montre que le programme de simulation ne reproduit pas précisément le comportement du jet hadronique observé dans les données réelles, particulièrement dans le plan transverse à la direction du faisceau. Pour pallier à ce problème, des simulations basées sur les données elles-mêmes sont utilisées partout où cela est possible.

Le dernier chapitre résume les divers éléments de cette étude. La méthode de rapport de vraisemblance a été mise au point pour distinguer le signal et le bruit de fond. La sélection des candidats d'interactions du ν_e est faite à l'aide de cette technique. Dans les données 1996 on obtient 1842 événements avec une efficacité de $(38.5 \pm 0.5)\%$ et la contamination du bruit de fond estimée à moins de 0.5%. Le nombre des événements attendu est $1891 \pm 25(stat) \pm 95(syst)$. Dans cette analyse il n'y a pas d'évidence de l'oscillation $\nu_\mu \to \nu_e$ pour l'indication de l'expérience LSND correspondant à des grands Δm^2.

La recherche des candidats d'interactions du ν_τ dans le canal de désintégration électronique du τ est faite en utilisant la même méthode. Les résultats préliminaires basés sur l'analyse des données accumulées en 1996 sont présentés. La limite obtenue pour l'oscillation $\nu_\mu \to \nu_\tau$ à 90% niveau de confiance dans la région de meilleure sensibilité est

$$P_{osc}(\nu_\mu \to \nu_\tau) < 6.2 \times 10^{-3}$$

List of Figures

List of Tables

Bibliography

[1] W.Pauli, Public letter to the group of the Radioactives at the district society meeting in Tübingen, 4 Dec. 1930

[2] C.L.Cowan et al., Science 124 (1956) 103
F.Reines, C.L.Cowan, Nature 178 (1956) 446

[3] G.Danby et al., Phys. Rev. Lett. 9 (1962) 36

[4] B.Pontecorvo, JETP 37 (1959) 1751

[5] M.Schwartz, Phys. Rev. Lett. 4 (1960) 306

[6] M.Perl et al., Phys. Rev. Lett. 35 (1975) 1489

[7] see, for example, Review of Particle Properties, Phys. Rev. D54 (1996) 256

[8] C.Albajar et al., Phys. Lett. B185 (1987) 233

[9] Review of Particle Properties, Phys. Rev. D54 (1996)
ALEPH, DELPHI, L3, OPAL Collaborations

[10] S.L.Glashow, Nucl. Phys. 22 (1961) 579
S.Weinberg, Phys. Rev. Lett. 19 (1967) 1264
A.Salam, J.C.Ward, Phys. Lett. 13 (1964) 168

[11] M.Goldhaber, L.Grodzins, A.W.Sunyar, Phys. Rev. 109 (1958) 1015

[12] R.P.Feynman, Photon and Hadron Interactions, Benjamin ed. (1972)

[13] F.J.Hasert et al., Phys. Lett. 46B (1973) 121
F.J.Hasert et al., Phys. Lett. 46B (1973) 138

[14] V.M.Lobashev, Proc. of Neutrino '96, World Scientific, Singapore (1996)
A.Belesev et al., Phys. Lett. B350 (1995) 263

[15] K.Assamagan et al., Phys. Rev. D53 (1996) 6065
K.Assamagan et al., Phys. Lett. B335 (1994) 231

[16] A.Gregorio, ALEPH Collaboration, Proc. of Neutrino '96, World Scientific, Singapore (1996)
D.Buskulic et al., ALEPH Collaboration, Phys. Lett. B349 (1995) 585

[17] see, for example, P.Binetruy, "Neutrino properties beyond the Standard Model", VIII Rencontres de Blois "Neutrinos, Dark Matter and the Universe" (1996)

[18] B.Kayser, "The physics of massive neutrinos", World Scientific, 1989

[19] K.Fujikawa, R.E.Shrock, Phys. Rev. Lett. 45 (1980) 963

[20] M.Gell-Mann, P.Ramond, R.Slansky, "Supergravity", North Holland, Amsterdam, 1979
T.Yanagida, Proc. of the Workshop on Unified Theory and the Baryon Number of the Universe, KEK, Japan, 1979
S.Weinberg, Phys. Rev. Lett. 43 (1979) 1566

[21] H.Harari, Y.Nir, Nucl. Phys. B292 (1987) 251
H.Harari, Phys. Lett. B216 (1989) 413

[22] S.M.Bilenky, S.T.Petcov, Rev. of Mod. Phys. vol.59, No.3 (1987) 671

[23] G.Gyak, M.S.Turner, Nucl. Phys. B (Proc. Suppl.) 38 (1995) 13

[24] B.Pontecorvo, JETP 33 (1957) 549

[25] Z.Maki et al., Prog. Theor. Phys. 28 (1962) 870

[26] X.Shi et al., Phys. Rev. Lett. 69 (1992) 717

[27] Review of Particle Properties, Phys. Rev. D54 (1996) 287

[28] J.N.Bahcall, M.H.Pinsonneault, Rev. Mod. Phys. 64 (1992) 885

[29] S.Turck-Chiéze, I.Lopes, Astrophys. J. 408 (1993) 347

[30] J.N.Bahcall, M.H.Pinsonneault, Rev. Mod. Phys. 67 (1995) 781

[31] A.Dar, G.Shaviv, Astrophys. J. 468 (1996) 933

[32] R.Davis, Prog. Part. Nucl. Phys. 32 (1994) 13
R.Davis Jr., Nucl. Phys. B (Proc. Suppl.) 48 (1996) 284

[33] B.Pontecorvo, Chalk River Laboratory report PD-205, Canada (1946)

[34] V.A.Kuzmin, JETP 49 (1965) 1532

[35] W.Hampel et al., GALLEX Collaboration, Phys. Lett. B388 (1996) 384
P.Anselmann et al., GALLEX Collaboration, Phys. Lett. B357 (1995) 237
P.Anselmann et al., GALLEX Collaboration, Phys. Lett. B361 (1996) 235

[36] P.Anselmann et al., GALLEX Collaboration, Phys. Lett. B342 (1995) 440
W.Hampel et al., GALLEX Collaboration, to appear in Phys. Lett. B, December 1997

[37] J.N.Abdurashitov et al., Phys. Lett. B328 (1994) 234

[38] J.N.Abdurashitov et al., Phys. Rev. Lett. 77 (1996) 4708

[39] G.Ewan et al., SNO proposal, SNO 87-12

[40] G.Arpesella et al., BOREXINO proposal, University of Milan (1991)

[41] Y.Suzuki et al., Proc. of Neutrino '96, World Scientific, Singapore (1996)
Y.Fukuda et al., KAMIOKANDE Collaboration, Phys. Rev. Lett. 77 (1996) 1683

[42] S.Mikheev, A.Smirnov, Sov. J. Nucl. Phys. 42 (1985) 913

[43] L.Wolfenstein, Phys. Rev. D17 (1978) 2369; D20 (1979) 2634

[44] N.Hata, P.Langacker, Phys. Rev. D56 (1997) 6107

[45] Y.Totsuka, Neutrino physics (nonaccelerator), contribution to the Lepton Photon Symposium 1997, Hamburg, July 1997

[46] T.K.Gaisser et al., Phys. Rev. D54 (1996) 5578

[47] Y.Fukuda et al., KAMIOKANDE Collaboration, Phys. Lett. B335 (1994) 237
K.S.Hirata et al., KAMIOKANDE Collaboration, Phys. Lett. B280 (1992) 146

[48] R.Becker-Szendy et al., IMB Collaboration, Phys. Rev. D46 (1992) 3720

[49] K.Daum et al., FREJUS Collaboration, Z. Phys. C66 (1995) 417

[50] M.Aglietta et al., NUSEX Collaboration, Europhys. Lett. 8 (1989) 611

[51] W.Allison et al., SOUDAN 2 Collaboration, Phys. Lett. B391 (1997) 491

[52] B.Achkar et al., Nucl. Phys. B434 (1995) 503

[53] G.S.Vidyakin et al., JETP Lett. 59 (1994) 364

[54] C.Athanassopoulos et al., LSND Collaboration, Phys. Rev. C54 (1996) 2685

[55] C.Athanassopoulos et al., LSND Collaboration, nucl-ex/9709006, nucl-ex/9706006

[56] K.Eitel et al., KARMEN Collaboration, hep-ex/9706023

[57] K.Eitel, private communication

[58] N.Ushida et al., E531 Collaboration, Phys. Rev. Lett. 57 (1986) 2897

[59] C.Birnbaum et al., Phys. Lett. B397 (1997) 143

[60] R.E.Shrock, Phys. Rev. D24 (1981) 1232

[61] F.Bergsma et al., Phys. Lett. B128 (1983) 361,
J.Dorenbosch et al., Phys. Lett. B166 (1986) 473

[62] G.Bernardi et al., Phys. Lett. B166 (1983) 479, Phys. Lett. B203 (1988) 332

[63] A.M.Cooper-Sarcar et al., Phys. Lett. B160 (1985) 207

[64] S.Baranov et al., Phys. Lett. B302 (1993) 336

[65] J.Hellmig, “The Heidelberg-Moscow double beta decay experiment”, VIII Rencontres de Blois “Neutrinos, Dark Matter and the Universe” (1996)

[66] E.Eskut et al., CHORUS Collaboration, CERN-PPE-97-033 (1997)
E.Eskut et al., CHORUS Collaboration, Nucl. Instr. and Meth. A401 (1997) 7

[67] E.Eskut et al., CHORUS Collaboration, CERN-PPE-97-149 (1997), submitted to Phys. Lett. B

[68] COSMOS Collaboration, P803 proposal to Fermilab (1993)

[69] A.S.Ayan et al., A high sensitivity short baseline experiment to search for $\nu_\mu \to \nu_\tau$ oscillation, CERN-SPSC-97-05 (1997)

[70] D. Autiero et al., A medium baseline facility for ν_μ oscillations, CERN-SPSC-97-23 (1997)

[71] H.de Kerret et al., CHOOZ Collaboration, The CHOOZ Experiment, Proposal, LAPP report (1993)

[72] M.Apollonio et al., CHOOZ Collaboration, hep-ex 9711002 (1997)
M.Apollonio et al., CHOOZ Collaboration, Phys. Lett. B420 (1998) 397

[73] G.Gratta, Palo Verde Collaboration, Proc. of Neutrino '96, World Scientific, Singapore (1996)

[74] K.Nishikawa et al., Proposal for a Long Baseline Neutrino Oscillation Experiment, using KEK-PS and Super-Kamiokande (1995)

[75] M.Goodman et al., MINOS Collaboration, ANL-HEP-CP-97-49 (1997)
S.G.Wojcicki, Proc. of Neutrino '96, World Scientific, Singapore (1996)

[76] A. Rubbia et al., ICARUS Collaboration, "A search program of explicit neutrino oscillations with ICARUS detector at long distances", CERN-SPSLC-96-58 (1996)

[77] P.Astier et al., "Search for the Oscillation $\nu_\mu \to \nu_\tau$", CERN-SPSLC/91-21, CERN-SPSLC/91-48, CERN-SPSLC/91-53

[78] J.Altegoer et al., NOMAD Collaboration, CERN-PPE-97-059 (1997)
J.Altegoer et al., NOMAD Collaboration, Nucl. Instr. and Meth. A404 (1998) 96

[79] C.H.Albright, R.E.Shrock, Phys. Lett. B84 (1979) 123

[80] GEANT : Detector Description and Simulation Tool, CERN Programming Library Long Writeup W5013, GEANT version 3.21

[81] G.Ambrosini et al., SPY Collaboration, CERN-SPSLC/96-01 (1996)

[82] M.C.Gonzalez-Garcia, J.J.Gomez-Cadenas, CERN-TH/96-220 (1996)
M.C.Gonzalez-Garcia, J.J.Gomez-Cadenas, Phys. Rev. D55 (1997) 1297

[83] B.Van de Vyver, P.Zucchelli, CERN-PPE/96-113 (1996)
B.Van de Vyver, Nucl. Instr. and Meth. A385 (1997) 91

[84] J.-P.Meyer, "Drift Chamber chemical composition", NOMAD memo # 96-003

[85] P.Astier, J.Dumarchez, A.Letessier-Selvon, B.Popov, K.Schahmaneche, "Drift Chamber global alignment: status report", NOMAD memo # 73

[86] K.Schahmaneche, Ph.D. Thesis, Paris VI (1997)

[87] C.Hagner, "Drift Chamber Efficiency", NOMAD memo # 97-024

[88] C.Hagner, "A Study of Afterpulses", NOMAD memo (unpublished)

[89] B.Schmidt, Ph.D. Thesis, Dortmund (1997)

[90] G.Bassompierre et al., "A large area Transition Radiation Detector for the NOMAD experiment", LAPP-EXP-97-05 (1997), Nucl. Instr. and Meth. A403 (1998) 363
G.Bassompierre et al., "Performance of the NOMAD Transition Radiation Detector", LAPP-EXP-97-06 (1997), submitted to Nucl. Instr. and Meth. A

[91] G.M.Garibian, JETP 6 (1958) 1079, JETP 10 (1960) 372
K.A.Barsukov, JETP 10 (1960) 787
G.M.Garibian et al., Nucl. Instr. and Meth. 125 (1975) 133

[92] V.C.Ermilova, L.P.Kotenko, G.J.Merzon, Nucl. Instr. and Meth. 145 (1977) 555

[93] T.Fazio, J.-P.Mendiburu, P.Nedelec, D.Sillou, S.Valuev, "NOMAD TRD Electron Identification: Method and First Results", NOMAD memo # 95-041
P.Nedelec, D.Sillou, S.Valuev. "NOMAD TRD Identification of Overlapping Tracks", NOMAD Memo # 96-005

[94] D.Autiero et al., Nucl. Instr. and Meth. A373 (1996) 358

[95] D.Autiero et al., to be published in Nucl. Instr. and Meth. A

[96] D.Autiero et al., Nucl. Instr. and Meth. A372 (1996) 556

[97] K.Eggert et al., Nucl. Instr. and Meth. A176 (1980) 217

[98] P.Astier, E.Gangler, A.Letessier-Selvon, B.Popov, K.Schahmaneche, Nomad Reconstruction Software, "Drift Chamber Package".

[99] R.Brun, J.Zoll, "ZEBRA user guide", CERN computer centre program library write-up, Q100

[100] E.Gangler, Ph.D. Thesis, Paris VI (1997)

[101] P.Astier, E.Gangler, A.Letessier-Selvon, Nomad Reconstruction Software, "DC-TRD package"

[102] Application of Filter Methods to the Reconstruction of Tracks And Vertices in Events of Experimental High Energy Physics. by R. Frühwirth, HEPHY-PUB 516/88 Vienna, December 1988.

[103] P. Billoir et al., Nucl. Instr. and Meth. A241 (1985) 115

[104] "Database Management Package", CERN program library long write-up, Q180

[105] A.Baldisseri, Th.Stolarczyk, "Drift Chamber Database - Reference Guide", NOMAD memo # 95-019

[106] P.Astier et al., Nomad Reconstruction Software, "UTIL package"

[107] Review of Particle Properties, Phys. Rev. D54 (1996) 134

[108] A.C.Hearn, REDUCE reference manual, RAND-CD-162 (1989)

[109] Review of Particle Properties, Phys. Rev. D54 (1996) 132

[110] J.Altegoer et al., "GENOM: NOMAD GEANT off-line manual"

[111] P.Astier, P.Cattaneo, A.Letessier-Selvon, B.Popov, Nomad Reconstruction Software, "Extrapolator Package".

[112] I.G.Bird, "Vertex finding and fitting package", NOMAD memo # 96-019

[113] S.Gninenko, A.Toropin, "Subtraction of energy deposited by charged hadrons in the ECAL", NOMAD memo # 95-040

[114] P.Astier, E.Gangler, A.Letessier-Selvon, B.Popov, M.Serrano, S.Valuev, M.Vo, Nomad Reconstruction Software, "Subdetector matching package"

[115] M.Serrano, Nomad Reconstruction Software, "Generic package"

[116] G.Barrand, OnX version 5r1, available from *lalftp.in2p3.fr*

[117] C.Arnault, Ci version 3r3, available from *lalftp.in2p3.fr*

[118] M.Vo, Ph.D. Thesis, Paris VII (1996)

[119] M.Mezetto, D.Gibin, A.Guglielmi, M.Laveder, "π/e rejection with Calo and Prs modules at T9 test beam",

[120] P.Astier, E.Gangler, A.Letessier-Selvon, E.Manola, P.Nedelec, B.Popov, S.Valuev, Nomad Reconstruction Software, "TRD first stage package"

[121] R.Petti, "Parametrization of e and gamma initiated showers in the NOMAD lead-glass calorimeter", NOMAD memo # 97-018

[122] R.Cousins, "Some Extended Tools for Track Breakpoint Analysis", NOMAD memo # 96-016

[123] S.Gninenko et al., "Calorimeter matching general layout, tools and the algorithm", NOMAD Reconstruction Software, NOMAD memo # 96-033
S.Gninenko et al., "Clusterization of Charged Hadron Energy Release in Cal", NOMAD Reconstruction Software, NOMAD memo # 96-034
S.Gninenko et al., "Gammas and Neutrals Finding and Fitting Package", NOMAD Reconstruction Software, NOMAD memo # 96-035

[124] M.Contalbrigo, D.Gibin, S.Lacaprara, "A bremsstrahlung algorithm implemented within the NOMAD software", NOMAD memo # 97-010

[125] J.D.Bjorken, Phys. Rev. 179 (1969) 1547

[126] C.Callan, D.Gross, Phys. Rev. Let. 21 (1968) 311

[127] K.Kleinknecht, CERN yellow report, CERN 78-10 (1978)

[128] "NUBEAM: NOMAD neutrino beam generator"

[129] A.Fasso et al., FLUKA92, in Workshop on Simulating Accelerator Radiation Environments, Santa Fe, USA (1993)

[130] J.-P.Meyer, A.Rubbia, "NEGLIB: NOMAD event generator off-line manual"

[131] G.Ingelman, LEPTO version 6.1, "The Lund Monte-Carlo for Deep Inelastic Lepton-Nucleon Scattering", TSL-ISV-92-0065 (1992)
G.Ingelman, A.Edin, J.Rathsman, LEPTO version 6.5, Comp. Phys. Comm. 101 (1997) 108, hep-ph/9605286

[132] J.-M.Levy, "Neutrino-nucleon CC scattering with non-zero lepton mass", NOMAD memo # 97-051

[133] H.Guoju, J.M.Irvine, J. Phys. G: Nucl. Part. Phys. 15 (1989) 147

[134] A.Bodek, J.L.Ritchie, Phys. Rev. D23 (1981) 1070

[135] B.Anderson, G.Gustafson, G.Ingelman, T.Sjöstrand, Phys. Rep. 97 (1983) 31

[136] T.Sjöstrand, "PYTHIA 5.7 and JETSET 7.4: physics and manual", LU-TP-95-20 (1995), hep-ph/9508391
T.Sjöstrand, Comp. Phys. Comm 39 (1986) 347, 43 (1987) 367

[137] M.Glück, E.Reya, A.Vogt, Z. Phys. C53 (1992) 127

[138] H.P.Besch, Comp. Phys. Comm. 75 (1993) 396

[139] A.Rubbia, "NEGLIB status report", in the minutes of the NOMAD collaboration meeting, September and December 1997

[140] D.Allasia et al., Phys. Lett. B154 (1985) 231

[141] A.Geiser, P.Nedelec, R.Petti, "The 1996 $\bar{V}T_1T_2$ filter", NOMAD memo # 97-008

[142] K.Varvell, Nomad Reconstruction Software, "Nomad DST package", NOMAD memo # 97-034

[143] A.Bueno, A.Rubbia, "Considerations about the missing Pt for events with two tracks at the primary vertex", NOMAD memo # 96-009

[144] G.Battistoni et al., "Simulation of nuclear effects in quasi elastic and resonant neutrino interactions", hep-ph/9801426 (1998)

[145] P.Astier, E.Gangler, A.Letessier-Selvon, B.Popov, Nomad Analysis Software, "LIKE package"

[146] "HBOOK reference manual", CERN computer centre program library write-up, Y250

[147] S.Valuev, Ph.D. Thesis, Paris VII (1998)

[148] A.De Santo, NOMAD Collaboration, Proceedings of the XXXIInd RENCONTRES DE MORIOND, March 15-22, 1997

[149] J. Altegoer et al., NOMAD Collaboration, CERN-EP/98-57, to be published in Phys. Lett. B.

[150] O.Helene, Nucl. Instr. and Meth. 212 (1983) 319

[151] M.Mezzetto et al., "Results of the $\rightarrow$ e d.i.s. analysis of the 1995 data", NOMAD memo # 97-043

[152] R.Petti, G.Polesello, "Results of the $\rightarrow$ e analysis", in the minutes of the NOMAD analysis meetings

Acknowledgements

First of all, I would like to thank Prof. F.Vannucci for inviting me to LPNHE (Paris) and for giving me a chance to start, accomplish and, finally, present this work.

It was a pleasure to work with all the members of neutrino group in LPNHE (which has proved its right to be called the Paris group inside the NOMAD collaboration): Pierre Astier, Marcel Banner, Alain Castera, Jacques Dumarchez, Emmanuel Gangler, Cyril Lachaud, Antoine Letessier-Selvon, Jean-Michel Levy, Kyan Schahmaneche, Maria Serrano, Anne-Marie Touchard, Victor Uros, Francois Vannucci and Mai Khanh Vo (I take a liberty of including her while she officially belonged to the Saclay group). Especially I am grateful to Pierre, Antoine, Jacques, Emmanuel, Kyan, Maria and Mai for common creative activities.

Friendly attitude of all the other members of LPNHE is very much appreciated.

Special thanks to Francois and Antoine for the careful reading of this manuscript. I'm greatful to Antoine for his guidance and help and also for his efforts in trying to present this work in a complete and readable way.

I am indebted to the referees of this manuscript - Jacques Bouchez and Serguey Petcov for useful discussions and critical comments.

I would like also to thank Antoine and Anne, Jacques, Kyan, Victor and Mai for their friendship and for their help in discovering France and western style of life (while I hope it was still a cultural exchange...).

It is important for me to express my gratitude to the leader of the Elementary Particles Physics Department, Laboratory of Nuclear Problems (JINR, Dubna) Prof. S.A.Bunyatov for his guidance and support.

It is also a pleasure to mention all the members of the Dubna group in the NOMAD collaboration: S.A.Bunyatov, O. Klimov, A. Krasnoperov, V. Kuznetsov, Yu. Nefedov, V. Tereshchenko, V. Valuev and to thank all of them for friendship and amicable atmosphere of real community which exists outside science and which is always supported and reinforced by our charming secretary Irina Sidorkina.

I am indebted also to all the members of the NOMAD collaboration for our experiment which was not perfect but which will stay in memory forever since it was my first experience to work in an international collaboration.

I would like to thank especially Jean Gosset and Jean-Pierre Meyer (DAPNIA, Saclay), Juan-Jose Gomez-Cadenas and Andre Rubbia (CERN), Patrick Nedelec and Daniel Sillou (LAPP, Annecy), Robert Cousins (UCLA), Burkhard Schmidt (Dortmund) and Alexander Kovzelev (INR, Moscow) for sharing with me their knowledge and useful discussions.

I am indebted to Sylvie Soulie and Patrick Nedelec for processing 1.5×10^5 ν_μ NC MC events which allowed to use this independent sample for background prediction.

Friendly relations with Patrick Nedelec, Daniel Sillou and their families at the early stage of the NOMAD experiment are very much appreciated.

This work would be impossible without financial support of IN2P3, French Ministère de l'Education Nationale (Réseau de Formation et de Recherche JINR-Dubna, LAPP-Annecy, and LPNHE-Paris VI and VII) and my home institute.

Finally, I must say that I cannot imagine this work being done without support of my family where I was always able to find new forces and inspiration. I'm grateful to my mother, father, sister and two nieces - Dasha and Lyuba - for their understanding and for keeping up our good soviet traditions.